

Cover Page



Universiteit Leiden



The handle <http://hdl.handle.net/1887/30224> holds various files of this Leiden University dissertation.

Author: Neshati, Zeinab

Title: Cellular models and viral vectors for skeletal and cardiac muscle research

Issue Date: 2014-12-23

Cellular models and viral vectors for skeletal and cardiac muscle research

Colophon

The studies described in this thesis were performed at the department of Molecular Cell Biology and department of Cardiology of the Leiden University Medical Center, Leiden, The Netherlands.

Financial support by the Ministry of Science, Research and Technology of Iran for the studies described in this thesis is gratefully acknowledged.

Copyright © Zeinab Neshati, Mashhad, Iran. All rights reserved.

No part of this book may be reproduced or transmitted in any form or by any means, without prior written permission of the author.

Cover: Troponin I-stained human skeletal myoblasts (top) and α -actinin-stained and GFP-positive neonatal rat cardiomyocyte (bottom) photographed by Zeinab Neshati. Schematic picture of a lentiviral vector (middle) drawn by Antoine A.F. de Vries.

Cover design and layout: Mohammad Tayyebi

Printed by: Gildeprint BV, Enschede

ISBN/EAN: 978-90-9028708-9

Cellular models and viral vectors for skeletal and cardiac muscle research

Proefschrift

ter verkrijging van

de graad van Doctor aan de Universiteit Leiden,

op gezag van Rector Magnificus prof. mr. C.J.J.M. Stolker,

volgens besluit van het College voor Promoties

te verdedigen op dinsdag 23 december 2014

klokke 15:00 uur

door

Zeinab Neshati

geboren te Mashhad

in 1982

PROMOTIECOMMISSIE

Promotor

Prof. dr. M.J. Schalijs

Co-promotores

Dr. A.A.F. de Vries

Dr. D.A. Pijnappels

Overige leden

Prof. dr. M.J.Th.H. Goumans

Prof. dr. D.E. Atsma

Dr. P. van der Meer (University Medical Center Groningen)

List of Contents

Chapter 1	General Introduction and Outline of Thesis	7
Chapter 2	Development of a Lentivirus Vector-Based Assay for Non-Destructive Monitoring of Cell Fusion Activity <i>PLoS One</i> . 2014;9:e102433.	27
Chapter 3	Evaluating the Biodegradability of Gelatin/Siloxane/Hydroxyapatite (GS-Hyd) Complex <i>in vivo</i> and its Ability for Adhesion and Proliferation of Rat Bone Marrow Mesenchymal Stem Cells <i>Cytotechnology</i> . 2012;64:485-495.	63
Chapter 4	Investigation of the Pro-arrhythmic Features of Pathological Cardiac Hypertrophy in Neonatal Rat Ventricular Cardiomyocyte Cultures	89
Chapter 5	An <i>In Vitro</i> Model of Early- or No-Reperfusion Scars to Explain How Clinical Reentrant Arrhythmia Characteristics May Relate to Therapeutic Efficacy	113
Chapter 6	Atrium-Specific Kir3.x Determines Inducibility, Dynamics, and Termination of Fibrillation by Regulating Restitution-Driven Alternans <i>Circulation</i> . 2013;128:2732-2744.	137
Chapter 7	Summary, Conclusions and Future Perspectives	185
List of Publications		199
Acknowledgements		203
Curriculum Vitae		207

Chapter 1

General Introduction

Background

Skeletal and cardiac muscle disorders are associated with substantial morbidity and mortality. Collectively, these diseases affect millions of people worldwide and enormous amount of time, effort and money have been spent to identify and improve recuperative strategies for prevention and treatment of such disorders. Although many striated muscle diseases manifest themselves only in the heart or skeletal musculature, others affect both tissues although the moment of onset, progression, severity of disease and specific disease symptoms may differ between skeletal and cardiac muscle tissue.¹ The existence of a large number of disorders with both skeletal and cardiac muscle involvement is a direct consequence of the large overlap in gene expression profile between skeletal and cardiac myocytes, which relates to commonalities in their contractile systems. In many striated muscle diseases loss of functional myocytes eventually exceeds the tissue's regenerative capacity. This causes gradual replacement of these parenchymal cells by adipocytes and/or (myo)fibroblasts leading to progressive wasting and pathological remodelling of skeletal and cardiac muscle tissue, respectively.

Skeletal muscle wasting

A common feature of many skeletal muscle disorders is gradual muscle degeneration leading to impairment or loss of mobility. In healthy individuals, skeletal muscle damage triggers the activation of a population of muscle-resident stem cells called satellite cells. Following their activation, satellite cells start to proliferate giving rise to myoblasts, which are responsible for skeletal muscle repair and regeneration by fusion with injured myofibers or formation of new myofibers. Hence, fusion plays a key role in the regeneration process.²⁻⁴ In muscular dystrophies, because of the repetitive cycles of degeneration and regeneration the myoregenerative potential of skeletal muscle tissue becomes progressively exhausted. As a consequence, damaged myofibers are gradually replaced by fibroblasts and adipocytes. One of the therapeutic options to overcome this problem is cell transplantation. The success rate of transplantation is highly dependent on the ability of the donor cells to fuse with each other and/or with the recipient's skeletal myocytes in order to produce new myofibers and repair existing ones, respectively.⁵ Mechanistic studies on (myogenic)

cell fusion may thus be of great help to further optimize cell-based therapies for degenerative skeletal muscle diseases.

Pathological cardiac remodelling

Cardiac diseases are usually associated with distinct alterations of the expression and function of ion channels, Ca^{2+} -handling proteins, metabolic enzymes and structural proteins including sarcomeric components, and intercellular adhesion molecules. These changes are often accompanied by pathological cardiac hypertrophy (PCH) and fibrosis leading to electrophysiological and structural remodelling, which have been identified to increase pro-arrhythmic risk.⁶⁻⁸

An increase in cardiac demand due to physiological or pathological changes in hemodynamics makes the heart respond in several ways, including by the enlargement of cardiomyocytes. Such cardiac hypertrophy is essentially a beneficial compensatory process as it decreases wall stress, while increasing cardiac output.⁹ This adaptation by growth occurs under physiological conditions like exercise and pregnancy, but also in response to myocardial infarction and other cardiac pathologies (e.g. hypertension, aortic stenosis, aortic coarctation, valvular regurgitation, septal defects and arteriovenous fistulae).¹⁰ Physiological hypertrophy typically is a reversible process to fulfill a temporary need for additional cardiac output. Pathological hypertrophy, on the other hand, is essentially an irreversible process involving permanent changes in cardiac structure and function that initially secure but subsequently reduce cardiac output. Besides an increase in cardiomyocyte size, diseased hearts usually also display a decrease in cardiomyocyte number together with a (compensatory) fibrotic response. The changes in cardiac geometry, myocardial tissue composition and cardiomyocyte biology increase the risk of cardiac arrhythmias and thus both directly and indirectly contribute to a reduction in the pumping capacity of the heart, which may ultimately lead to heart failure.^{11,12} The exact pro-arrhythmic mechanisms of PCH are not well understood, partly because of the concurrent presence of fibrosis which is a pro-arrhythmic feature by itself.

Adult heart displays limited regenerative capacity.¹³ In case of cardiac injury, fibroblasts get activated, proliferate and form myofibroblasts, which secrete large

amounts of extracellular matrix.¹⁴ This process, which is called fibrosis, helps to maintain the heart's integrity; but negatively affects heart function due to the replacement of contractile by non-contractile tissue, an increase in myocardial stiffness and disturbed impulse generation and propagation. The disturbances in the heart's electrical activity are caused by the (electrical) isolation of cardiomyocytes by newly deposited extracellular matrix resulting in slowing or even block of conduction. Coupling of cardiomyocytes with (myo)fibroblasts may also add to disturbed impulse generation and propagation in fibrotic hearts. Taken together, structural and electrical remodelling in the heart could provide both the substrates and triggers for cardiac arrhythmias.^{15,16}

Cardiac arrhythmias

Proper electrical cardiac function relies on coordinated and well-timed generation of electrical impulses (*i.e.* action potentials) by cardiomyocytes and propagation of these impulses from cell to cell through gap junctions. Disturbances in electrical impulse generation and propagation could contribute to cardiac arrhythmias.¹⁷ Such heart rhythm disturbances concern any type of condition in which the atrial and/or ventricular rhythm is irregular, slower than normal (bradycardia) or faster than normal (tachycardia). In general, tachyarrhythmias are maintained by reentrant electrical activity or high-frequency electrical signals originating from focal sources. The most dangerous types of cardiac arrhythmias are those which are maintained by fibrillatory conduction (*i.e.* by chaotic activation patterns) especially when this happens in ventricular myocardium. Although our understanding of heart rhythm disturbances has surely improved over time, more insight, especially related to the underlying molecular and cellular mechanisms, is needed in order to improve the diagnosis and treatment of these disorders.

Focal tachyarrhythmias

Disturbances in repolarization can lead to prolongation of action potential duration (APD) and, when occurring at the earlier phases of repolarization (between -40 and 0 mV), may favor formation of aberrant electrical signals, referred to as early afterdepolarizations (EADs). These EADs, in combination with other pro-arrhythmic

conditions could give rise to focal or reentrant tachyarrhythmias. EADs are mainly Ca^{2+} -dependent and can be induced by anachronistic reactivation of the L-type Ca^{2+} channel, sarcoplasmic Ca^{2+} release and inward $\text{Na}^+/\text{Ca}^{2+}$ exchanger activity.¹⁸⁻²⁰ EADs can occur during phase 2 (*i.e.* the plateau phase) or phase 3 of the cardiac action potential. The mechanisms involved in the generation of phase-2 and phase-3 EADs are not the same as reflected by their different responsiveness to pharmacological inhibitors of ion channels. Since at the depolarized membrane voltages of phase 2, most Na^+ channels are inactivated, the L-type Ca^{2+} current (I_{CaL}) and the $\text{Na}^+/\text{Ca}^{2+}$ exchanger current (I_{NCX}) are the main currents responsible for phase-2 EADs. During the plateau phase of the action potential, L-type Ca^{2+} channels can undergo transitions between closed and open states. An increase in I_{CaL} in this phase can provide enough depolarizing force for EAD formation. At the same time, the cardiac $\text{Na}^+/\text{Ca}^{2+}$ exchanger generates a net inward current by coupling the export of a single Ca^{2+} ion to the import of three Na^+ ions, thereby resisting repolarization. The increase in the I_{CaL} further increases the inward current of the $\text{Na}^+/\text{Ca}^{2+}$ exchanger, and thereby may increase the probability of an EAD-triggered action potential.²¹ Forward mode of $\text{Na}^+/\text{Ca}^{2+}$ exchanger activity and possibly I_{Na} can promote phase-3 EAD generation. Finally, recent evidences suggest that electrotonic current flow in response to large voltage gradients resulting from heterogeneous repolarization are an important cause of phase-3 EADs.^{21,22}

Reentrant arrhythmias

Reentrant arrhythmias are those electrical impulses which are propagated in self-sustaining circuits that do not follow the normal cardiac conduction pattern, in which action potentials generated in the sinoatrial node move through the atrial myocardium and to the atrioventricular node and, after some delay, via the bundle of His and Purkinje fibers through the ventricular myocardium. Under normal conditions, impulses disappear automatically after the entire heart has been activated because the duration of the refractory period exceeds that of the excitation wave. However, if the heart contains an area of inexcitable tissue causing local conduction block and at the same time the tissue around this area shows large heterogeneity in repolarization or conduction, unidirectional block may develop forcing the wavefront of excitation to move in one direction which based on the timing may reenter the original site of excitation, establishing a reentrant circuit.

Reentry can occur in the presence (anatomical reentry),²³ or absence (functional reentry)²⁴ of an anatomical obstruction (e.g. myocardial scar tissue) or can be the result of both structural and functional disturbances in electrical impulse propagation.^{25,26} While anatomical reentry in many cases leads to reentrant circuits of constant wavelength and position, rotors caused by functional reentry often meander throughout the tissue.^{27,28}

Challenges in skeletal and cardiac muscle research

Research in the field of skeletal and cardiac muscle diseases mainly focuses on unravelling the underlying pathogenic mechanisms and on developing (better) therapeutic interventions. Despite many improvements in the medical and surgical management of skeletal and cardiac muscle disorders, development of effective and durable treatments has proven to be challenging. In cardiac muscle disorders, device therapies and interventional procedures such as catheter ablation have multiple limitations and are associated with a risk of complications.^{29,30} Pharmacological therapies for skeletal and cardiac muscle diseases are largely directed toward palliation of the symptoms of the disease rather than targeting the underlying causes.³¹⁻³³ Improvement in therapeutic modalities requires better understanding of molecular pathways involved in the initiation and progression of these diseases. Much of the available information about the underlying mechanisms of skeletal and cardiac muscles disorders is obtained from *in vivo* studies. These studies are, however, complicated by the complexity of three-dimensional (3D) tissues, the occurrence of disease symptoms secondary to the primary condition, primary causes directly affecting other organs besides the heart and skeletal muscles and the interplay between different organ systems. For example, Duchenne muscular dystrophy (DMD), the most common inherited myopathy affects different skeletal muscles to a different extent but may also impair cardiac and brain function to various degrees depending on the specific mutation involved.³⁴⁻³⁷ Also, the coincident presence of e.g. inflammation, hypoxia and fibrosis in PCH makes it very hard to determine its specific/mechanistic contribution to the occurrence of arrhythmias.^{38,39}

The development and use of dedicated cellular experimental models to study the mechanisms underlying skeletal and cardiac muscle diseases in combination with

genetic interventions to investigate the role of specific factors, may resolve these limitations and lay the basis for the development of novel treatment options.

Cellular models

Cultures of skeletal myoblasts or cardiomyocytes offer the possibility to analyse cellular functions and molecular pathways in a highly specific and controllable manner, which is difficult to accomplish *in vivo*. Given the ease with which *in vitro* models can be established and manipulated to mimic physiological or pathological conditions, they are ideally suited for proof-of-concept studies and testing new therapeutic interventions targeting specific aspects of disease. Indeed, cellular models have greatly contributed to our current understanding of skeletal and cardiac muscle diseases.^{40,41} Although their relative simplicity facilitates data interpretation, cells in culture are not subjected to the complex regulatory systems controlling organ function *in vivo*. Accordingly, results obtained in *in vitro* experiments will always need to be validated in clinical studies. In spite of their shortcomings, *in vitro* models keep on being highly useful for mechanistic and therapy-directed skeletal and cardiac muscle research. This is particularly true when cell culture models are combined with genetic interventions to investigate the involvement of specific genes in physiological and pathophysiological processes.

Genetic interventions

Recently, there has been considerable interest in the application of gene therapy in the field of skeletal and cardiac muscle diseases. Many of these genetic interventions have focussed on counteracting the pathological processes in failing myocytes either directly by correction of the underlying genetic defect if applicable or indirectly by inhibition of pathogenic mechanisms or stimulation of physiological processes. Gene therapy has, for example, been used to complement gene mutations causing various types of muscular dystrophy including DMD as well as defects in several sarcomeric protein genes linked to PCH.^{42,43} Genetic intervention can be also employed for overexpression of a protein like sarcoplasmic reticulum Ca^{2+} -ATPase pump (Serca2a) to improve cardiac function⁴⁴ or downregulation of a protein like the acetylcholine-activated K^+ channel Kir3.4 to terminate atrial fibrillation (AF).⁴⁵ Clinical and preclinical studies have shown beneficial effects of myocardial

gene transfer in neovascularization of ischemic myocardium, increasing myocardial contractility, induction of cardiac repair and reduction of AF and ventricular tachycardia vulnerability.⁴⁶⁻⁵¹ Gene therapy has also demonstrated improvements in skeletal muscle disorders.⁵²⁻⁵⁴ The safe and successful delivery of a gene is very important in order to gain high therapeutic efficacy. A large number of gene delivery methods have been developed using both viral and non-viral vectors, each of which have their own pros and cons. Non-viral methods include using naked DNA alone or in combination with cationic liposomes or polymers.^{55,56} Non-viral vectors are typically easy to synthesize and can be used for the transfer of genetic material of all kind of different sizes. Additional advantages of non-viral vectors are their safety and the ease with which they can be modified e.g. to alter their cell tropism. By applying non-viral gene delivery one can avoid disadvantages intrinsic to the use of viral vectors such as limited genetic payloads and expensive/laborious production methods. Also, nonviral vectors are generally less immunogenic and have a lower risk of insertional oncogenesis than viral vectors.⁵⁷ Major limitations of non-viral vectors are their very low *in vivo* gene transfer activity and their difficulty to efficiently transduce differentiated cells both *in vitro* and *in vivo*. Viral vectors are much better suited for this purpose especially when high transduction rates and transgene expression levels are required.⁵⁸

Viral vectors

Viral vectors are commonly used for the genetic modification of skeletal and cardiac muscle cells and tissues because they transfer genes much more efficiently than any of the non-viral vectors. The most commonly used viral vectors are derived from retroviruses (including lentiviruses), adenoviruses and adeno-associated virus, which belongs to the parvoviruses. These potentially harmful viruses are converted into innocuous viral vectors by the replacement of one or more essential viral genes by heterologous gene expression units, which renders the viral vectors replication-deficient but still allows introduction and expression of their genetic cargo into target cells. The production of these vectors requires the missing viral genes to be provided *in trans* through packaging plasmids, complementing cell lines or helper viruses.

Retroviral vectors

The first retroviral vectors were derived in the 1980s from gammaretroviruses. Since these vectors require cell division for efficient transduction, they are not suitable for the genetic modification of differentiated cell types like skeletal and cardiac myocytes. Unlike gammaretroviral vectors, lentivirus vectors (LVs) do not depend on cell division for efficient transduction of target cells. Following target cell entry, the LV genome, which consists of a positive-sense, single-stranded linear RNA molecule, is reverse transcribed into cDNA and subsequently integrated into the host cell genome. LV vectors can accommodate a fair amount of foreign DNA due to the absence of a strict upper packaging limit. There is, however, an inverse relationship between LV yields and genome lengths⁵⁹ which practically restricts insert sizes to ± 5 kb. LVs are generally produced in human embryonic kidney (HEK) 293T cells by a simple transfection procedure involving a LV shuttle plasmid and two or three so-called helper or packaging plasmids. These features and the ease with which LVs can be generated may explain why LVs have become such popular gene delivery vehicles for the permanent *ex vivo* genetic modification of both differentiated and proliferating cell populations.^{60,61} LVs are much less suitable for *in vivo* gene therapies due to their large diameter, which hampers their spreading through tissues, and the preferential integration of LV genomes into transcriptionally active chromosome loci imposing a certain risk of insertional oncogenesis.^{62,63} Currently, much effort is put in the improvement of lentiviral vector design to reduce as much as possible the risk of insertional oncogenesis.^{64,65}

Adenoviral vectors

Adenoviral vectors (AdVs) have the capacity to carry large DNA molecules (± 37 kb for human adenovirus type 5), can be produced in very large quantities and very efficiently transduce all kinds of cells, irrespective of their cell cycle status. AdV genomes are linear double-stranded DNA molecules covalently linked at their 5' ends to the so-called terminal protein.⁶⁶ These genomes normally do not integrate to the host chromosomal DNA but reside in the nucleus of the target cells as nonreplicating episomes, which causes transient expression especially in dividing cell populations but simultaneously limits concerns related to oncogene activation. The main disadvantages of AdVs are their large size limiting their dissemination through tissue and their relatively high immunogenicity, which may result in the *in*

in vivo elimination of transduced cells by cell-mediated immune responses. This latter problem especially applies to first- and second-generation AdVs, which in contrast to their third-generation counterparts still contain adenoviral genes that are expressed at low levels in target cells. As a consequence, severe inflammation leading to toxicity and even, in very rare cases, organ failure has been reported following *in vivo* administration of early-generation AdVs.⁶⁷ In recent years, AdV vector development has mainly focussed on lowering the immunogenicity of the adenovirus particle, reducing unintended interactions with host proteins and increasing target cell specificity by chemical or genetic modification of the adenoviral capsid/coat proteins.^{68,69}

Adeno-associated virus vectors

Adeno-associated virus vectors (AAVs) carry a single-stranded DNA genome with a T-shaped hairpin at both termini. Following their delivery in the target cell nucleus most AAV DNA is converted into highly stable double-strand circular monomers and concatemers. Moreover, AAVs are significantly less immunogenic than AdVs, which is partially explained by the absence in the vector genome of parvoviral genes. Because of these properties AAVs can mediate long-term albeit not permanent gene expression.⁷⁰ Another advantage of AAVs is their small diameter, which allows them to easily penetrate tissues. The downside of their small size is their limited packaging capacity, which does not allow incorporation of transgene > 4.7 kb. Other disadvantages of AAVs include the time-consuming and expensive procedures needed for their production and purification and their relatively low gene transfer activity requiring high amount of AAV particles to achieve efficient transduction.⁷¹ In addition, due to the slow onset of transgene expression AAVs cannot be used for studies with a short time course. Still, at present AAVs are the only viral vectors that can transduce entire organs, including the heart.⁷² Therefore, currently, much effort is put in improving AAV production methods and in modifying the vector genome and capsid to increase the specific gene transfer activity of AAVs and to overcome their limited packaging capacity.⁷³

Aim an outline of the thesis

The limited suitability of existing experimental models for acquiring a thorough understanding of the mechanisms underlying skeletal and cardiac muscle diseases and the lack of efficiency and specificity of many of the currently available therapeutic interventions have made efficient treatment of these diseases challenging. Therefore, the aim of this thesis is to establish dedicated cellular models and use viral vector systems to study the biology of skeletal and cardiac muscles in healthy and diseased states and thereby identify potential targets for future therapeutic interventions.

Chapter I of this thesis explains the common pathological features of skeletal and cardiac muscle diseases, the limitations of current therapies and advantages of cellular models and genetic interventions in improved treatment of these diseases.

The successful deployment of cell transplantation in skeletal muscle disorders depends on the potential of the donor cells to engage in myotube formation (myogenesis), which is amongst others determined by the ability of the transplanted cells to fuse with cells present in the host tissue.^{5,74} Cell fusion also plays an important role in fertilization, syncytiotrophoblast production, bone remodelling, eye lens development and certain forms of tissue repair.⁷⁵ Different methods can be used for monitoring cell fusion activity. These methods and a newly developed non-destructive quantitative cell fusion assay are described in **chapter II**.

Efficient engraftment of transplanted cells is another factor which determines the success rate of transplantation. Scaffolds provide a framework for cells to attach, proliferate, and form extracellular matrix *in vivo*. The scaffolds may also serve as carriers for cells, growth factors, and/or other biomolecular signals. Ideally, scaffolds should be degraded *in vivo* at an appropriate rate to allow its gradual replacement by regenerated host tissue. Therefore, the *in vivo* biodegradability of Gelatin/Siloxane/Hydroxyapatite scaffolds and their ability to support adhesion and proliferation of rat bone marrow mesenchymal stem cells have been studied in **chapter III**.

Employment of 2D cell culture models makes it possible to study the contribution of PCH per se to arrhythmogenicity, which cannot be easily done *in vivo* due to the simultaneous presence of other pro-arrhythmic features. Induction of hypertrophy-related pathological changes in cardiomyocyte cultures can be achieved by exposing

the cells to a variety of different peptide and non-peptide hormones and growth factors. It has been shown that phorbol 12-myristate 13-acetate (PMA), which activates protein kinases C and D, induces a gene expression program in cardiac muscle cells resembling that of cardiomyocytes in pathologically hypertrophied hearts.⁷⁶⁻⁷⁸ In **chapter IV**, the use of the PMA to establish an *in vitro* model of PCH based on ventricular neonatal rat cardiomyocytes is described and its pro-arrhythmic features are studied.

Early- and no-reperfusion after myocardial infarction (MI) leads to formation of patchy and compact scars, respectively. These post MI scars facilitate circular conduction of the impulses in the heart. How scar composition affects arrhythmogenicity and arrhythmic phenotype has been investigated in an *in vitro* model in **chapter V**.

Atrium-selective drugs and interventions with higher efficacy in AF rhythm control but fewer side effects such as ventricular pro-arrhythmia are paramount needs in AF treatment. In **chapter VI**, the role of acetylcholine-activated K⁺ channels, whose expression in mammalian hearts is largely restricted to the atria, has been studied in AF initiation, dynamics and termination in a cell culture and whole-heart model of AF. Finally, **chapter VII** summarizes the findings of this thesis and provides future perspectives based on the conclusions drawn from each study.

References

1. Limongelli G, D'Alessandro R, Maddaloni V, Rea A, Sarkozy A, McKenna WJ. Skeletal muscle involvement in cardiomyopathies. *J Cardiovasc Med (Hagerstown)*. 2013;14:837-861.
2. Morgan JE, Partridge TA. Muscle satellite cells. *Int J Biochem Cell Biol*. 2003;35:1151-1156.
3. Horsley V, Pavlath GK. Forming a multinucleated cell: Molecules that regulate myoblast fusion. *Cells Tissues Organs*. 2004;176:67-78.
4. Wagers AJ, Conboy IM. Cellular and molecular signatures of muscle regeneration: Current concepts and controversies in adult myogenesis. *Cell*. 2005;122:659-667.
5. Skuk D, Roy B, Goulet M, Chapdelaine P, Bouchard JP, Roy R, Dugre FJ, Lachance JG, Deschenes L, Helene S, Sylvain M, Tremblay JP. Dystrophin expression in myofibers of Duchenne muscular dystrophy patients following intramuscular injections of normal myogenic cells. *Mol Ther*. 2004;9:475-482.
6. Coronel R, Wilders R, Verkerk AO, Wiegerinck RF, Benoist D, Bernus O. Electrophysiological changes in heart failure and their implications for arrhythmogenesis. *Biochim Biophys Acta*. 2013;1832:2432-2441.
7. Lou Q, Fedorov VV, Glukhov AV, Moazami N, Fast VG, Efimov IR. Transmural heterogeneity and remodelling of ventricular excitation-contraction coupling in human heart failure. *Circulation*. 2011;123:1881-1890.
8. Tomaselli GF, Marban E. Electrophysiological remodelling in hypertrophy and heart failure. *Cardiovasc Res*. 1999;42:270-283.
9. Grossman W, Jones D, McLaurin LP. Wall stress and patterns of hypertrophy in the human left ventricle. *J Clin Invest*. 1975;56:56-64.
10. Bernardo BC, Weeks KL, Pretorius L, McMullen JR. Molecular distinction between physiological and pathological cardiac hypertrophy: experimental findings and therapeutic strategies. *Pharmacol Ther*. 2010;128:191-227.
11. Weber KT, Brilla CG. Pathological hypertrophy and cardiac interstitium. Fibrosis and renin-angiotensin-aldosterone system. *Circulation*. 1991;83:1849-1865.
12. Burchfield JS, Xie M, Hill JA. 013 Pathological ventricular remodelling: mechanisms: part 1 of 2. *Circulation*. 2;128:388-400.

13. Senyo SE, Steinhauser ML, Pizzimenti CL, Yang VK, Cai L, Wang M, Wu TD, Guerquin-Kern JL, Lechene CP, Lee RT. Mammalian heart renewal by pre-existing cardiomyocytes. *Nature*. 2013;493:433-436.
14. Kong P, Christia P, Frangogiannis NG. The pathogenesis of cardiac fibrosis. *Cell Mol Life Sci*. 2014;71:549-574.
15. de Bakker JM, van Capelle FJ, Janse MJ, Tasseron S, Vermeulen JT, de Jonge N, Lahpor JR. Slow conduction in the infarcted human heart. 'Zigzag' course of activation. *Circulation*. 1993;88:915-926.
16. Gomez JF, Cardona K, Martinez L, Saiz J, Trenor B. Electrophysiological and structural remodelling in heart failure modulate arrhythmogenesis. 2d simulation study. *PLoS One*. 2014;9:e103273.
17. Gaztanaga L, Marchlinski FE, Betensky BP. Mechanisms of cardiac arrhythmias. *Rev Esp Cardiol (Engl Ed)*. 2012;65:174-185.
18. Qi M, Shannon TR, Euler DE, Bers DM, Samarel AM. Downregulation of sarcoplasmic reticulum Ca(2+)-ATPase during progression of left ventricular hypertrophy. *Am J Physiol*. 1997;272:H2416-2424.
19. Qu Z, Xie LH, Olcese R, Karagueuzian HS, Chen PS, Garfinkel A, Weiss JN. Early afterdepolarizations in cardiac myocytes: beyond reduced repolarization reserve. *Cardiovasc Res*. 2013;99:6-15.
20. Peters NS, Cabo C, Wit AL: Arrhythmogenic mechanisms: automaticity, triggered activity, and reentry. In Zipes DP, Jalife J, editors: *Cardiac electrophysiology: from cell to bedside*, ed 3, Philadelphia, 2000, Saunders, pp 345–355..
21. Weiss JN, Garfinkel A, Karagueuzian HS, Chen PS, Qu Z. Early afterdepolarizations and cardiac arrhythmias. *Heart Rhythm*. 2010;7:1891-1899.
22. Maruyama M, Lin SF, Xie Y, Chua SK, Joung B, Han S, Shinohara T, Shen MJ, Qu Z, Weiss JN, Chen PS. Genesis of phase 3 early afterdepolarizations and triggered activity in acquired long-QT syndrome. *Circ Arrhythm Electrophysiol*. 2011;4:103-111.
23. Mehra R, Zeiler RH, Gough WB, El-Sherif N. Reentrant ventricular arrhythmias in the late myocardial infarction period. 9. Electrophysiologic-anatomic correlation of reentrant circuits. *Circulation*. 1983;67:11-24.

24. Allesie MA, Bonke FI, Schopman FJ. Circus movement in rabbit atrial muscle as a mechanism of tachycardia. *Circ Res*. 1973;33:54-62.
25. Kleber AG, Rudy Y. Basic mechanisms of cardiac impulse propagation and associated arrhythmias. *Physiol Rev*. 2004;84:431-488.
26. Lim ZY, Maskara B, Aguel F, Emokpae R, Jr., Tung L. Spiral wave attachment to millimeter-sized obstacles. *Circulation*. 2006;114:2113-2121.
27. Otani NF. A primary mechanism for spiral wave meandering. *Chaos*. 2002;12:829-842.
28. Comtois P, Kneller J, Nattel S. Of circles and spirals: bridging the gap between the leading circle and spiral wave concepts of cardiac reentry. *Europace*. 2005;7 Suppl 2:10-20.
29. Daubert JP, Zareba W, Cannom DS, McNitt S, Rosero SZ, Wang P, Schuger C, Steinberg JS, Higgins SL, Wilber DJ, Klein H, Andrews ML, Hall WJ, Moss AJ. Inappropriate implantable cardioverter-defibrillator shocks in MADIT II: frequency, mechanisms, predictors, and survival impact. *J Am Coll Cardiol*. 2008;51:1357-1365.
30. Tokuda M, Kojodjojo P, Epstein LM, Koplán BA, Michaud GF, Tedrow UB, Stevenson WG, John RM. Outcomes of cardiac perforation complicating catheter ablation of ventricular arrhythmias. *Circ Arrhythm Electrophysiol*. 2011;4:660-666.
31. Leung DG, Wagner KR. Therapeutic advances in muscular dystrophy. *Ann Neurol*. 2013;74:404-411.
32. Epstein SE, Rosing DR. Verapamil: its potential for causing serious complications in patients with hypertrophic cardiomyopathy. *Circulation*. 1981;64:437-441.
33. Arshad A, Mandava A, Kamath G, Musat D. Sudden cardiac death and the role of medical therapy. *Prog Cardiovasc Dis*. 2008;50:420-438.
34. Mosqueira M, Zeiger U, Forderer M, Brinkmeier H, Fink RH. Cardiac and respiratory dysfunction in Duchenne muscular dystrophy and the role of second messengers. *Med Res Rev*. 2013;33:1174-1213.
35. Mercuri E, Muntoni F. Muscular dystrophy: new challenges and review of the current clinical trials. *Curr Opin Pediatr*. 2013;25:701-707.
36. Sekiguchi M. The role of dystrophin in the central nervous system: a mini review. *Acta Myol*. 2005;24:93-97.

37. Anderson JL, Head SI, Rae C, Morley JW. Brain function in Duchenne muscular dystrophy. *Brain*. 2002;125:4-13.
38. McLenachan JM, Dargie HJ. Determinants of ventricular arrhythmias in cardiac hypertrophy. *J Cardiovasc Pharmacol*. 1991;17 Suppl 2:S46-49.
39. Amano Y, Kitamura M, Tachi M, Takeda M, Mizuno K, Kumita S. Delayed enhancement magnetic resonance imaging in hypertrophic cardiomyopathy with Basal septal hypertrophy and preserved ejection fraction: relationship with ventricular tachyarrhythmia. *J Comput Assist Tomogr*. 2014;38:67-71.
40. Goetsch KP, Myburgh KH, Niesler CU. *In vitro* myoblast motility models: investigating migration dynamics for the study of skeletal muscle repair. *J Muscle Res Cell Motil*. 2013;34:333-347.
41. Parameswaran S, Kumar S, Verma RS, Sharma RK. Cardiomyocyte culture - an update on the *in vitro* cardiovascular model and future challenges. *Can J Physiol Pharmacol*. 2013;91:985-998.
42. Mendell JR, Rodino-Klapac L, Sahenk Z, Malik V, Kaspar BK, Walker CM, Clark KR. Gene therapy for muscular dystrophy: lessons learned and path forward. *Neurosci Lett*. 2012;527:90-99.
43. Seidman JG, Seidman C. The genetic basis for cardiomyopathy: from mutation identification to mechanistic paradigms. *Cell*. 2001;104:557-567.
44. Kawase Y, Ladage D, Hajjar RJ. Rescuing the failing heart by targeted gene transfer. *J Am Coll Cardiol*. 2011;57:1169-1180.
45. Bingen BO, Neshati Z, Askar SF, Kazbanov IV, Ypey DL, Panfilov AV, Schalij MJ, de Vries AA, Pijnappels DA. Atrium-specific Kir3.x determines inducibility, dynamics, and termination of fibrillation by regulating restitution-driven alternans. *Circulation*. 2013;128:2732-2744.
46. Rubanyi GM. Mechanistic, technical, and clinical perspectives in therapeutic stimulation of coronary collateral development by angiogenic growth factors. *Mol Ther*. 2013;21:725-738.
47. Hajjar RJ, Schmidt U, Matsui T, Guerrero JL, Lee KH, Gwathmey JK, Dec GW, Semigran MJ, Rosenzweig A. Modulation of ventricular function through gene transfer *in vivo*. *Proc Natl Acad Sci U S A*. 1998;95:5251-5256.
48. Donahue JK, Heldman AW, Fraser H, McDonald AD, Miller JM, Rade JJ, Eschenhagen T, Marban E. Focal modification of electrical conduction in the heart by viral gene transfer. *Nat Med*. 2000;6:1395-1398.

49. Lau DH, Clausen C, Sosunov EA, Shlapakova IN, Anyukhovskiy EP, Danilo P, Jr., Rosen TS, Kelly C, Duffy HS, Szabolcs MJ, Chen M, Robinson RB, Lu J, Kumari S, Cohen IS, Rosen MR. Epicardial border zone overexpression of skeletal muscle sodium channel SkM1 normalizes activation, preserves conduction, and suppresses ventricular arrhythmia: an *in silico*, *in vivo*, *in vitro* study. *Circulation*. 2009;119:19-27.
50. Sasano T, McDonald AD, Kikuchi K, Donahue JK. Molecular ablation of ventricular tachycardia after myocardial infarction. *Nat Med*. 2006;12:1256-1258.
51. Igarashi T, Finet JE, Takeuchi A, Fujino Y, Strom M, Greener ID, Rosenbaum DS, Donahue JK. Connexin gene transfer preserves conduction velocity and prevents atrial fibrillation. *Circulation*. 2012;125:216-225.
52. Wang B, Li J, Xiao X. Adeno-associated virus vector carrying human minidystrophin genes effectively ameliorates muscular dystrophy in *mdx* mouse model. *Proc Natl Acad Sci U S A*. 2000;97:13714-13719.
53. Romero NB, Braun S, Benveniste O, Leturcq F, Hogrel JY, Morris GE, Barois A, Eymard B, Payan C, Ortega V, Boch AL, Lejean L, Thioudellet C, Mouroit B, Escot C, Choquel A, Recan D, Kaplan JC, Dickson G, Klatzmann D, Molinier-Frenckel V, Guillet JG, Squiban P, Herson S, Fardeau M. Phase I study of dystrophin plasmid-based gene therapy in Duchenne/Becker muscular dystrophy. *Hum Gene Ther*. 2004;15:1065-1076.
54. Glascock JJ, Shababi M, Wetz MJ, Krogman MM, Lorson CL. Direct central nervous system delivery provides enhanced protection following vector mediated gene replacement in a severe model of spinal muscular atrophy. *Biochem Biophys Res Commun*. 2012;417:376-381.
55. Lin H, Parmacek MS, Morle G, Bolling S, Leiden JM. Expression of recombinant genes in myocardium *in vivo* after direct injection of DNA. *Circulation*. 1990;82:2217-2221.
56. Nabel EG, Plautz G, Nabel GJ. Site-specific gene expression *in vivo* by direct gene transfer into the arterial wall. *Science*. 1990;249:1285-1288.
57. Yin H, Kanasty RL, Eltoukhy AA, Vegas AJ, Dorkin JR, Anderson DG. Non-viral vectors for gene-based therapy. *Nat Rev Genet*. 2014;15:541-555.

58. Katz MG, Fagnoli AS, Williams RD, Bridges CR. Gene therapy delivery systems for enhancing viral and nonviral vectors for cardiac diseases: current concepts and future applications. *Hum Gene Ther.* 2013;24:914-927
59. Kumar M, Keller B, Makalou N, Sutton RE. Systematic determination of the packaging limit of lentiviral vectors. *Hum Gene Ther.* 2001;12:1893-1905
60. Giry-Laterriere M, Verhoeyen E, Salmon P. Lentiviral vectors. *Methods Mol Biol.* 2011;737:183-209
61. Lewis PF, Emerman M. Passage through mitosis is required for oncoretroviruses but not for the human immunodeficiency virus. *J Virol.* 1994;68:510-516
62. Hacein-Bey-Abina S, Hauer J, Lim A, Picard C, Wang GP, Berry CC, Martinache C, Rieux-Laucat F, Latour S, Belohradsky BH, Leiva L, Sorensen R, Debre M, Casanova JL, Blanche S, Durandy A, Bushman FD, Fischer A, Cavazzana-Calvo M. Efficacy of gene therapy for X-linked severe combined immunodeficiency. *N Engl J Med.* 2010;363:355-364
63. Hacein-Bey-Abina S, Von Kalle C, Schmidt M, McCormack MP, Wulffraat N, Leboulch P, Lim A, Osborne CS, Pawliuk R, Morillon E, Sorensen R, Forster A, Fraser P, Cohen JI, de Saint Basile G, Alexander I, Wintergerst U, Frebourg T, Aurias A, Stoppa-Lyonnet D, Romana S, Radford-Weiss I, Gross F, Valensi F, Delabesse E, Macintyre E, Sigaux F, Soulier J, Leiva LE, Wissler M, Prinz C, Rabbitts TH, Le Deist F, Fischer A, Cavazzana-Calvo M. LMO2-associated clonal T cell proliferation in two patients after gene therapy for SCID-X1. *Science.* 2003;302:415-419
64. Pluta K, Kacprzak MM. Use of HIV as a gene transfer vector. *Acta Biochim Pol.* 2009;56:531-595
65. Pauwels K, Gijsbers R, Toelen J, Schambach A, Willard-Gallo K, Verheust C, Debyser Z, Herman P. State-of-the-art lentiviral vectors for research use: risk assessment and biosafety recommendations. *Curr Gene Ther.* 2009;9:459-474
66. Goncalves MA, de Vries AA. Adenovirus: from foe to friend. *Rev Med Virol.* 2006;16:167-186
67. Muruve DA. The innate immune response to adenovirus vectors. *Hum Gene Ther.* 2004;15:1157-1166

68. Thacker EE, Timares L, Matthews QL. Strategies to overcome host immunity to adenovirus vectors in vaccine development. *Expert Rev Vaccines*. 2009;8:761-777.
69. Ahi YS, Bangari DS, Mittal SK. Adenoviral vector immunity: its implications and circumvention strategies. *Curr Gene Ther*. 2011;11:307-320.
70. Flotte TR, Afione SA, Conrad C, McGrath SA, Solow R, Oka H, Zeitlin PL, Guggino WB, Carter BJ. Stable *in vivo* expression of the cystic fibrosis transmembrane conductance regulator with an adeno-associated virus vector. *Proc Natl Acad Sci U S A*. 1993;90:10613-10617.
71. Dong JY, Fan PD, Frizzell RA. Quantitative analysis of the packaging capacity of recombinant adeno-associated virus. *Hum Gene Ther*. 1996;7:2101-2112.
72. Prasad KM, Xu Y, Yang Z, Acton ST, French BA Robust cardiomyocyte-specific gene expression following systemic injection of AAV: *in vivo* gene delivery follows a Poisson distribution. *Gene Ther*. 2011;18:43-52.
73. Kotterman MA, Schaffer DV. Engineering adeno-associated viruses for clinical gene therapy. *Nat Rev Genet*. 2014;15:445-451.
74. Cossu G, Sampaolesi M. New therapies for muscular dystrophy: cautious optimism. *Trends Mol Med*. 2004;10:516-520.
75. Shinn-Thomas JH, Mohler WA. New insights into the mechanisms and roles of cell-cell fusion. *Int Rev Cell Mol Biol*. 2011;289:149-209.
76. Dunnmon PM, Iwaki K, Henderson SA, Sen A, Chien KR. Phorbol esters induce immediate-early genes and activate cardiac gene transcription in neonatal rat myocardial cells. *J Mol Cell Cardiol*. 1990;22:901-910.
77. Shubeita HE, Martinson EA, Van Bilsen M, Chien KR, Brown JH. Transcriptional activation of the cardiac myosin light chain 2 and atrial natriuretic factor genes by protein kinase c in neonatal rat ventricular myocytes. *Proc Natl Acad Sci U S A*. 1992;89:1305-1309.
78. Prasad AM, Inesi G. Regulation and rate limiting mechanisms of Ca²⁺ ATPase (SERCA2) expression in cardiac myocytes. *Mol Cell Biochem*. 2012;361:85-96.

Chapter 2

Development of a Lentivirus Vector-Based Assay for Non-Destructive Monitoring of Cell Fusion Activity

Zeinab Neshati, Jia Liu, Guangqian Zhou, Martin J. Schalij, Antoine A. F. de Vries

PLoS One. 2014;9:e102433.

Abstract

Cell-to-cell fusion can be quantified by endowing acceptor and donor cells with latent reporter genes/proteins and activators of these genes/proteins, respectively. One way to accomplish this goal is by using a bipartite lentivirus vector (LV)-based cell fusion assay system in which the cellular fusion partners are transduced with a flippase-activatable *Photinus pyralis luciferase* (*PpLuc*) expression unit (acceptor cells) or with a recombinant gene encoding FLPe^{NLS+}, a nuclear-targeted and molecularly evolved version of flippase (donor cells). Fusion of both cell populations will lead to the FLPe-dependent generation of a functional *PpLuc* gene. *PpLuc* activity is typically measured in cell lysates, precluding consecutive analysis of one cell culture. Therefore, in this study the *PpLuc*-coding sequence was replaced by that of *Gaussia princeps luciferase* (*GpLuc*), a secretory protein allowing repeated analysis of the same cell culture. In myotubes the spread of FLPe^{NLS+} may be limited due to its nuclear localization signal (NLS) causing low signal outputs. To test this hypothesis, myoblasts were transduced with LVs encoding either FLPe^{NLS+} or an NLS-less version of FLPe (FLPe^{NLS-}) and subsequently co-cultured in different ratios with myoblasts containing the FLPe-activatable *GpLuc* expression cassette. At different times after induction of cell-to-cell fusion the *GpLuc* activity in the culture medium was determined. FLPe^{NLS+} and FLPe^{NLS-} both activated the latent *GpLuc* gene but when the percentage of *FLPe*-expressing myoblasts was limiting, FLPe^{NLS+} generally yielded slightly higher signals than FLPe^{NLS-} while at low acceptor-to-donor cell ratios FLPe^{NLS-} was usually superior. The ability of FLPe^{NLS+} to spread through myofibers and to induce reporter gene expression is thus not limited by its NLS. However, at high FLPe concentrations the presence of the NLS negatively affected reporter gene expression. In summary, a rapid and simple chemiluminescence assay for quantifying cell-to-cell fusion progression based on *GpLuc* has been developed.

Introduction

During cell-to-cell fusion, plasma membranes of individual cells merge to form a multinucleated structure called a syncytium. Plasma membrane fusion is a crucial event during, for example, fertilization, syncytiotrophoblast production, skeletal muscle formation, bone remodeling, eye lens development and certain forms of tissue repair.¹ In general, cell fusion is a tightly regulated and highly selective process involving specific cell types. Inappropriate cell fusion has been implicated in tumor development and progression.²

Cell fusion can be easily observed using microscopic techniques and in many studies the extent of cell fusion is expressed as fusion index, which either stands for the percentage of cells with two or more nuclei or the percentage of nuclei present in syncytia.³ However, without continuous monitoring, it is impossible to decide by microscopy alone whether multinucleation is caused by cell fusion or the result of karyokinesis without cytokinesis. In addition, cells growing on top of each other can be mistaken for syncytia. Furthermore, as fusion index determinations are generally carried out manually, they are laborious, error-prone and often inaccurate. This has led to the development of methods for quantifying cell fusion independent of microscopic inspection. Nearly all these methods are based on systems of two components that interact to create a novel detectable signal only after cell fusion.³ Mohler and Blau, for example, developed a quantitative cell fusion assay based on functional complementation between two biologically inactive β -galactosidase deletion mutants.⁴ Another possibility to produce fusion-dependent signals is by applying site-specific recombination systems such as Cre-loxP and FLP-FRT. In these systems, a latent reporter gene is activated by the action of the site-specific DNA recombinase Cre from bacteriophage P1 or flippase/FLP from *Saccharomyces cerevisiae*, which catalyze the excision and inversion of DNA flanked by 34-base pair (bp) recognition sequences (loxP for Cre and FRT for FLP) in a direct or inverted repeat configuration, respectively.^{5,6}

Gonçalves *et al.* previously developed a bipartite lentivirus vector (LV)-based cell fusion assay system in which the cellular fusion partners are endowed with a FLP-activatable *Photinus pyralis luciferase* (*PpLuc*) expression unit/"gene switch" (acceptor cells) or with a recombinant gene encoding a molecularly evolved version of FLP (FLPe) with a nuclear localization signal (NLS) derived from the simian virus

40 large T antigen (donor cells).⁷ Fusion between acceptor and donor cells led to the FLPe-dependent generation of a functional episomal *PpLuc* expression module. This cell fusion monitoring system was successfully used to study the role of the p38 MAPK signaling pathway in myoblast fusion/myotube formation. However, since PpLuc is a cytoplasmic protein and its substrate D-luciferin is poorly membrane-permeable, this assay requires lysis of the cells prior to luminometry and does not allow repeated analysis of the same cell culture. This prompted us to develop a nondestructive method to quantify cell fusion using the bipartite LV-based cell fusion assay system described by Gonçalves and colleagues as starting point.

The key difference between the new and “old” version of the LV-based cell fusion assay system is the replacement of the *PpLuc* open reading frame (ORF) in the “original” gene switch construct by the humanized coding sequence of *Gaussia princeps* luciferase (GpLuc), which is a secretory protein converting the substrate coelenterazine into coelenteramide plus light. GpLuc also displays a much higher specific luciferase activity than PpLuc and is exceptionally resistant to exposure to heat and strongly acidic and basic conditions.⁸ In addition, we hypothesized that in myotubes the spread of nuclear-targeted FLPe (FLPe^{NLS+}) beyond the direct surroundings of donor nuclei may be limited due to the presence of the NLS. This would result in the activation of only a fraction of the reporter genes especially in hybrid myotubes containing a relatively low percentage of *FLPe* gene-positive donor nuclei compared to GpLuc-encoding acceptor nuclei. To test this hypothesis, we generated an LV encoding an NLS-less version of FLPe (FLPe^{NLS-}) and compared, in myogenic fusion assays, its ability to activate latent *GpLuc* genes with that of FLPe^{NLS+}.

Materials and Methods

Plasmids

DNA constructions were carried out with enzymes from Fermentas (Fisher Scientific, Landsmeer, the Netherlands) or from New England Biolabs (Bioké, Leiden, the Netherlands) by using established procedures⁹ or following the instructions provided with specific reagents.

To generate a bicistronic self-inactivating (SIN) human immunodeficiency virus type 1 (HIV1) vector shuttle plasmid coding for *Streptomyces alboniger* puromycin N-

acetyl transferase (PurR) and FLPe^{NLS-}, pLV.FLPe.PurR (⁷; GenBank accession number: GU253314; hereinafter referred to as pLV.hCMV-IE.FLPe^{NLS+}.IRES.PurR.hHBVPRE; Figure 1A) was digested with BshT1 and Eco81I and the 9.6-kb DNA fragment containing the vector backbone was purified from agarose gel. The hybridization product of oligodeoxyribonucleotides 5' CCGGTACCATGAGTCAATTTGATATATTATGTAAAAC-ACCACC 3' and 5' TTAGGTGGTGTGTTTTACATAATATATCAAATTGACTCATGGTA 3' (both from Eurofins MWG Operon, Ebersberg, Germany) was combined with the 9.6-kb BshT1xEco81I fragment of pLV.hCMV-IE.FLPe^{NLS+}.IRES.PurR.hHBVPRE by ligation with bacteriophage T4 DNA ligase producing pLV.hCMV-IE.FLPe^{NLS-}.IRES.PurR.hHBVPRE (Figure 1B).

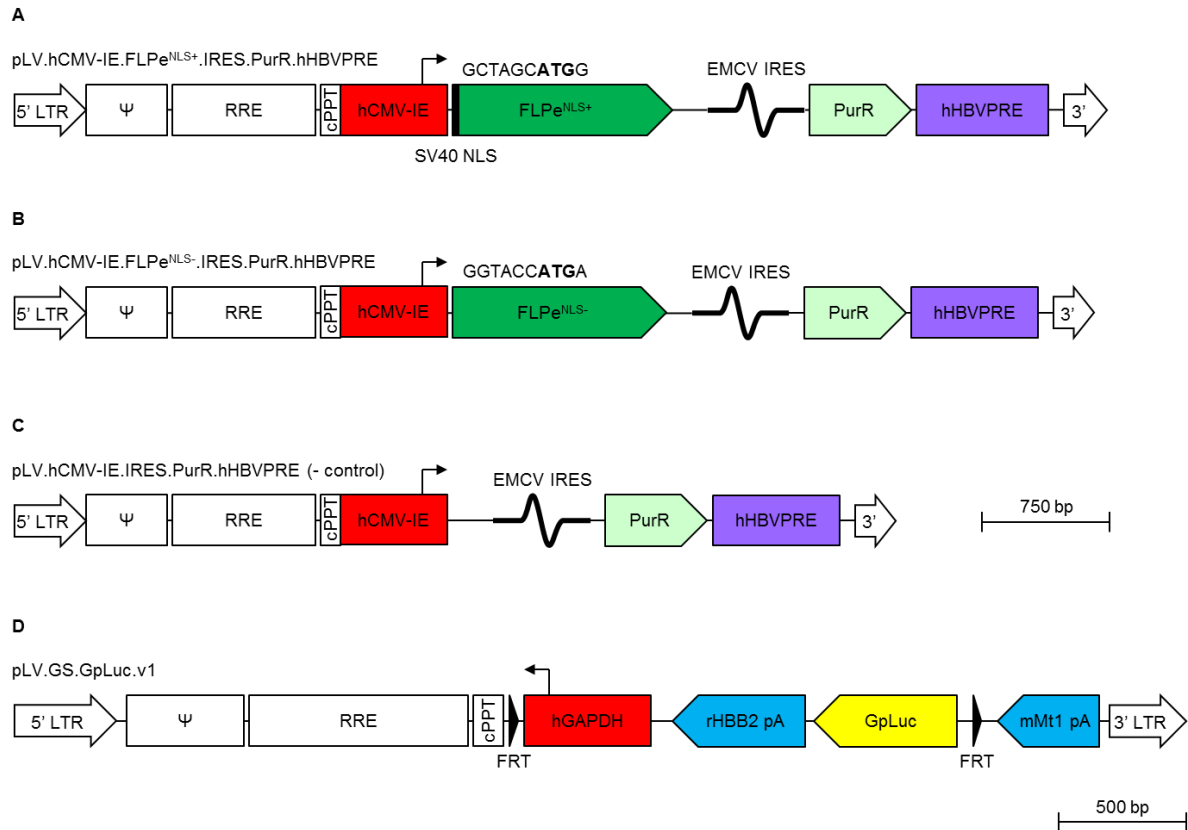


Figure 1. Structure of the LV DNA in the LV shuttle plasmids. **(A):** pLV.hCMV-IE.FLPe^{NLS+}.IRES.PurR.hHBVPRE **(B):** pLV.hCMV-IE.FLPe^{NLS-}.IRES.PurR.hHBVPRE **(C):** pLV.hCMV-IE.IRES.PurR.hHBVPRE and **(D):** pLV.GS.GpLuc.v1. The start codons of the FLPe^{NLS+} and FLPe^{NLS-} ORFs are shown in boldface. 5' LTR, chimeric 5' long terminal repeat containing the Rous sarcoma virus U3 region and the HIV1 R and U5 regions; Ψ, HIV1 packaging signal; RRE, HIV1 Rev-responsive element; cPPT, HIV1 central polypurine tract and termination site; hCMV-IE, human cytomegalovirus *immediate early* gene promoter; FLPe^{NLS+}, molecularly evolved flippase with simian virus 40 (SV40) nuclear localization signal (NLS; black bar); FLPe^{NLS-}, molecularly evolved flippase without NLS; EMCV IRES, encephalomyocarditis virus internal ribosomal entry site; PurR; *Streptomyces alboniger* puromycin N-acetyl transferase-coding sequence; hHBVPRE, human hepatitis B virus posttranscriptional regulatory element; black triangle/FRT, flippase recognition target sequence; hGAPDH, human *glyceraldehyde 3-phosphate dehydrogenase* gene promoter; rHBB2 pA, rabbit β -hemoglobin gene polyadenylation signal; GpLuc, *Gaussia princeps* luciferase-coding sequence; mMT1 pA, mouse *metallothionein 1* gene polyadenylation signal; 3' LTR, 3' HIV1 long terminal repeat containing a deletion in the U3 region to render the LV self-inactivating.

To generate a SIN-LV shuttle plasmid carrying a silent *GpLuc* gene that can be activated by FLP, cloning vector pR6K.MCS was digested with XmaJI and NotI, the 2.2-kb DNA fragment containing the vector backbone was purified from agarose gel and combined with the 0.6-kb *GpLuc*-encoding XmaJI×NotI fragment of phGluc.dBamHI yielding construct pR6K.GpLuc. The cloning vector pR6K.MCS was derived from construct pA1.GFP.A2 (¹⁰; GenBank accession number: GQ380658) by combining its 2.0-kb Sall×AflII fragment with the 0.3-kb Sall×AflII fragment of pMOLUC (¹¹; Addgene, Cambridge, MA; plasmid number: 12514). Plasmid phGluc.dBamHI was made from the mammalian expression vector phGluc (¹²; Addgene; plasmid number: 22522) by self-ligation of its 2.9-kb BamHI fragment. The *GpLuc* ORF was excised from pR6K.GpLuc by digestion with XmaJI and MluI and combined with the 7.2-kb BcuI×MluI fragment of pLV.GS.DsRed.dKpnI to generate pLV.GS.GpLuc.v1 (Figure 1D). The LV shuttle plasmid pLV.GS.DsRed.dKpnI was derived from pLV.pA+.GS.DsRed (⁷; GenBank accession number: GU253312) by self-ligation of its 7.9-kb KpnI fragment. The SIN-LV shuttle plasmid pLV.GS.GpLuc.v6 is a derivative of construct pLV.pA+.GS.Luc (⁷, hereinafter referred to as pLV.GS.PpLuc), in which the sequences interspersed between the rabbit *β-hemoglobin* gene polyadenylation signal (rHBB pA) and the mouse *metallothionein 1* gene (mMT1) pA (*i.e.* the *PpLuc* ORF and an FRT sequence) are replaced by a synthetic DNA fragment comprising the *GpLuc* ORF and an FRT sequence. More details about the genetic makeup of pLV.GS.GpLuc.v1, pLV.GS.GpLuc.v6 and pLV.GS.PpLuc and about the nucleotide sequences located in between the mMT1 pA and *Luc* ORFs of these three SIN-LV plasmids are provided in Figures 2 and 3.

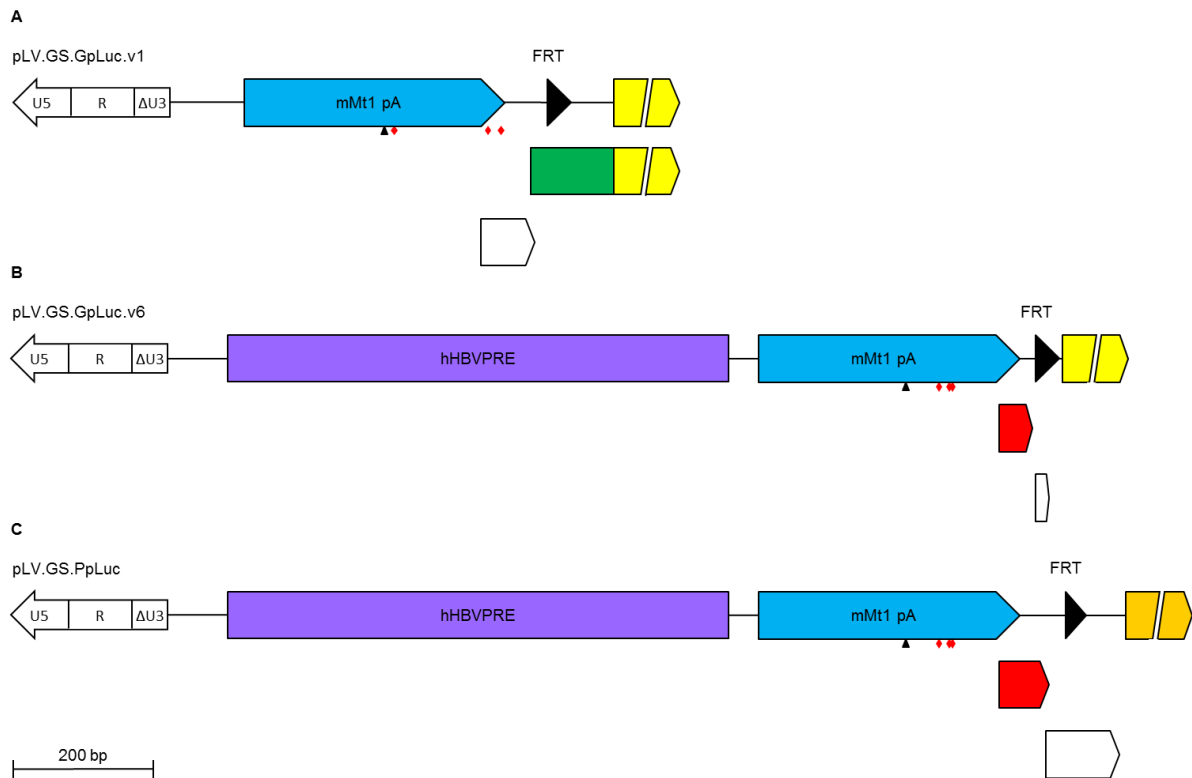


Figure 2. Improved design of the *GpLuc* gene switch cassette. (A-C): Detailed structure of the areas upstream of the *Luc* ORFs in pLV.GS.GpLuc.v1 (A), pLV.GS.GpLuc.v6 (B) and pLV.GS.PpLuc (C) starting at the HIV1 3' LTR. U5, HIV1 LTR unique 5' region; R, HIV1 LTR repeat region; ΔU3, enhancer- and promoterless HIV1 LTR unique 3' region; blue arrow, mouse *metallothionein 1* gene polyadenylation signal (mMT1 pA); small black triangle, AATAAA motif in mMT1 pA; red diamonds, stop codons in frame with *Luc* ORFs; large black triangle, minimal FRT sequence; light yellow arrow, *GpLuc* ORF; green box, 5' in-frame extension of the *GpLuc* ORF; white arrows, out-of-frame ORFs preceding *Luc* ORFs; red arrows, in-frame ORFs preceding *Luc* ORFs; dark yellow arrow, *PpLuc* ORF.

GpLuc.v1	GGGTAATGTCTTTGGG <u>TAA</u> AGCCAAGCTATCCCA <u>TAA</u> GCTCTGCAGGTCAAACATTTATC	60
PpLuc	GGGTAATGTCTTTGGGTAAGCCAAGCTATCCATAAGCTCTGCAGGTCAAACATTTATC	60
GpLuc.v6	GGGTAATGTCTTTGGGTAAGCCAAGCTATCCATAAGCTCTGCAGGCCGGGTAAACC	60
	***** * * *	
GpLuc.v1	GATCGCGCGCAGATCTGTCA <u>TGATGATCATTGAAGTTACTATTCC</u> GAAGTTCCTATTCTC	120
PpLuc	GATCGCGCGCAGATCTGTCA <u>TGATGATCATTGAAGTTACTATTCC</u> GAAGTTCCTATTCTC	120
GpLuc.v6	-----ATCGAAGTTCCTATTCTC	78

GpLuc.v1	<u>TAGAAAGTATAGGAACTTC</u> AAAGCTGGCTAACGTTGATCCACTAGGCTTTTGCAAAAGCT	180
PpLuc	<u>TAGAAAGTATAGGAACTTC</u> AAAGCTGGCTAACGTTGATCCACTAAGCTTGGCATTCCGGTA	180
GpLuc.v6	<u>TAGAAAGTATAGGAACTTC</u> -----	97

GpLuc.v1	TGATTGGGATCCAGCCACC <u>ATGG</u>	203
PpLuc	CTGTTGGTAA--AGCCACC <u>ATGG</u>	201
GpLuc.v6	-----CACC <u>ATGG</u>	105

Figure 3. Alignment of the nucleotide sequences immediately upstream of the *Luc* ORFs in pLV.GS.GpLuc.v1, pLV.GS.PpLuc and pLV.GS.GpLuc.v6. Blue box, 3' end of the mMT1 pA; underlined sequences, out-of-frame ORFs preceding *Luc* ORFs; boxed TAA sequences, in-frame stop codons preceding *Luc* ORFs; red letters, in-frame ORFs preceding *Luc* ORFs; green letters, 5' in-frame extension of the *GpLuc* ORF in pLV.GS.GpLuc.v1; black box, minimal FRT sequence; boxed ATG sequences, *Luc* initiation codons; light yellow box, 5' end *GpLuc* ORF; dark yellow box, 5' end *PpLuc* ORF.

The ligation mixtures were introduced in chemocompetent cells of *Escherichia coli* strain GeneHogs (Life Technologies Europe, Bleiswijk, the Netherlands) or GT115 (InvivoGen, San Diego, CA). Large-scale plasmid purifications were performed using JETSTAR 2.0 Plasmid Maxiprep kits (Genomed, Löhne, Germany) according to the manufacturer's instructions.

Cells

The culture and differentiation conditions of the murine Bmi1- and human TERT-immortalized human myoblasts (iDMD myoblasts) have been described previously.¹³

Viral vectors

The vesicular stomatitis virus G protein-pseudotyped SIN-LVs LV.FLPe^{NLS+}.PurR, LV.FLPe^{NLS-}.PurR, LV.PurR (negative control vector), LV.GS.GpLuc.v1, LV.GS.PpLuc and LV.GS.GpLuc.v6 were generated in 293T cells with the aid of the LV shuttle plasmids pLV.hCMV-IE.FLPe^{NLS+}.IRES.PurR.hHBVPRE, pLV.hCMV-

IE.FLPe^{NLS-}.IRES.PurR.hHBVPRE, pLV.CMV.IRES.PURO (¹⁴, hereinafter referred to as pLV.hCMV-IE.IRES.PurR.hHBVPRE; Figure 1C), pLV.GS.GpLuc.v1, pLV.GS.PpLuc and pLV.GS.GpLuc.v6, respectively. The 293T cells were transfected with one of the LV shuttle constructs and the packaging plasmids psPAX2 (Addgene; plasmid number: 12260) and pLP/VSVG (Life Technologies Europe) at a molar ratio of 2:1:1. To concentrate and purify the LV particles, producer cell supernatants were layered onto 5-ml cushions of 20% (wt/vol) sucrose in phosphate-buffered saline (PBS) and centrifuged at 15,000 rotations per minute for 2 h at 4°C in an SW32 rotor (Beckman Coulter Nederland, Woerden, the Netherlands). Prior to ultracentrifugation, producer cell supernatants were clarified by low speed centrifugation and filtration through 0.45-µm pore-sized cellulose acetate filters (Pall Netherlands, Mijdrecht, the Netherlands). For more details about the SIN-LV production method, see ¹⁵. The titers of the resulting LV stocks were determined using the RETROTEK HIV-1 p24 Antigen ELISA kit (ZeptoMetrix, Franklin, MA) following the instructions provided by the manufacturer. To derive functional titers from these measurements a conversion factor of 2.5 transducing units (TUs) per pg of HIV-1 p24 protein was used.

Cell transductions

Cryopreserved LV.FLPe^{NLS+}.PurR-transduced iDMD myoblasts (⁷; hereinafter referred to as myoblasts-FLPe^{NLS+}) were thawed and cultured in the presence of puromycin (Life Technologies Europe) at a final concentration of 0.4 µg/ml to prevent transgene silencing. FLPe^{NLS-}-expressing iDMD myoblasts were generated by overnight (\pm 20 h) exposure of 10^5 cells in a well of a 24-well cell culture plate (Greiner Bio-One, Alphen aan den Rijn, the Netherlands) to 30 TUs of LV.FLPe^{NLS-}.PurR per cell in 500 µl of growth medium in a humidified atmosphere of 5% CO₂/95% air at 37°C. The next day, the cell monolayer was rinsed three times with 1 ml of PBS after which fresh culture medium was added. At 3 days post transduction, the culture of LV.FLPe^{NLS-}.PurR-treated cells (hereinafter referred to as myoblasts-FLPe^{NLS-}) as well as a control culture of untransduced iDMD myoblasts were given medium containing 0.8 µg/ml of puromycin. Within a week, all cells in the culture of untransduced iDMD myoblasts had died while the cells in the LV.FLPe^{NLS-}.PurR-treated culture were nicely expanding. The myoblasts-FLPe^{NLS-} were passaged once a week (split ratio 1:3) in growth medium containing 0.4 µg/ml of puromycin. Myoblasts^{GS.GLuc}, myoblasts^{GS.PLuc} and myoblasts^{GS.GLuc+} were generated likewise by

exposure of iDMD myoblasts to LV.GS.GpLuc.v1, LV.GS.PpLuc and LV.GS.GpLuc.v6, respectively. Before being used for co-culture experiments, the cells were passaged at least three times to rule out secondary transduction of the *FLPe*-expressing myoblasts in the co-cultures with luciferase-encoding SIN-LVs.¹⁶

Co-culture establishment and maintenance

Co-cultures containing a total number of 2×10^5 cells were established in wells of 24-well culture plates by mixing myoblasts-*FLPe*^{NLS+} or myoblasts-*FLPe*^{NLS-} with myoblasts^{GS.GLuc} at the indicated ratios. Following an incubation period of about 72 h when the cell monolayers had reached 90-100% confluency, the growth medium was substituted by 400 μ l of either differentiation medium or fresh growth medium. At specified time points thereafter, the culture medium (400 μ l) was collected and stored at -80°C for luciferase assay. The co-cultures were then either terminated or further incubated at 37°C in a water-saturated atmosphere of 5% CO₂/95% air.

To compare the performance of the newly developed LV.GS.GpLuc.v1-based cell fusion assay system with that of the previously described LV.GS.PpLuc-based cell fusion quantification method⁷, myoblasts^{GS.GLuc} or myoblasts^{GS.PLuc} were co-cultured with myoblasts-*FLPe*^{NLS+} in different ratios in 24-well culture plates containing 2×10^5 cells per well. Samples (culture fluid for cultures containing myoblasts^{GS.GLuc} and cell lysates for cultures containing myoblasts^{GS.PLuc}) were harvested 96 h and 120 h after induction of myogenic differentiation. Exactly the same approach was used to compare the LV.GS.GpLuc.v1- and LV.GS.GpLuc.v6-based cell fusion assays.

Immunocytology

At different time points after the initiation of differentiation, 1:1 co-cultures of myoblasts-*FLPe*^{NLS-} and myoblasts^{GS.GLuc} were fixed by incubation for 30 minutes at room temperature (RT) in PBS containing 4% formaldehyde. To permeabilize the cells, they were exposed for 10 minutes at RT to 0.1% Triton X-100 in PBS. Next, cells were incubated overnight at 4°C with mouse anti-skeletal muscle troponin I (skTnI) primary antibody (HyTest, Turku, Finland; clone 12F10) diluted 1:100 in PBS + 0.1% donkey serum (Santa Cruz Biotechnology, Santa Cruz, CA) followed by a 2-h incubation at RT with Alexa Fluor 568-conjugated donkey anti-mouse IgG (H+L) secondary antibody (Life Technologies Europe) diluted 1:400 in PBS + 0.1% donkey serum. Counterstaining of nuclei was performed with 10 μ g/ml Hoechst 33342 (Life

Technologies Europe) in PBS. Cells were washed three times with PBS after fixation, permeabilization and incubation with primary antibody, secondary antibody and DNA-binding fluorochrome. To minimize photobleaching, coverslips were mounted in Vectashield mounting medium (Vector Laboratories, Burlingame, CA). Pictures were taken with a fluorescence microscope equipped with a digital color camera (Nikon Eclipse 80i; Nikon Instruments Europe, Amstelveen, the Netherlands) using NIS Elements software (Nikon Instruments Europe).

Subcellular fractionation and western blotting

Myoblasts-FLPe^{NLS+} and myoblasts-FLPe^{NLS-} were cultured separately in 24-well cell culture plates at a density of 2×10^5 cells per well. Following an incubation period of 72 h when the cell monolayers had reached 90-100% confluency, the growth medium was substituted by 400 μ l of either differentiation medium or fresh growth medium. Ninety-six h later, cell fractionation was carried out as described by Suzuki *et al.*¹⁷ with the following modifications. Cell pellets were suspended in 97.5 μ l of ice-cold 0.1% NP40 in PBS. One-third of the lysate was removed as “whole cell lysate” and mixed with 5 μ l of 10 \times NuPAGE Sample Reducing Agent and 12.5 μ l of 4 \times NuPAGE LDS Sample Buffer (both from Life Technologies Europe). The rest of the lysate was briefly centrifuged at 4°C after which 32.5 μ l of the supernatant was removed as “cytosolic fraction” and supplemented with 5 μ l of 10 \times NuPAGE Sample Reducing Agent and 12.5 μ l of 4 \times NuPAGE LDS Sample Buffer. The remaining supernatant was removed and the pellet was washed with and suspended in 30 μ l PBS, after which 5 μ l of 10 \times NuPAGE Sample Reducing Agent and 12.5 μ l of 4 \times NuPAGE LDS Sample Buffer were added to produce the “nuclear fraction”. Nuclear fractions and whole cell lysates were sonicated for 2 times 10 seconds at 200 Hz using a Soniprep 150 ultrasonic disintegrator (Measuring and Scientific Equipment, London, United Kingdom). After incubating the samples for 1 minute at 100°C, 10 μ l of whole cell lysate, 10 μ l of cytosolic fraction and 5 μ l of nuclear fraction were applied to a NuPAGE Novex 12% Bis-Tris gel (Life Technologies Europe). Following electrophoretic separation, the proteins were transferred to a polyvinylidene difluoride membrane (Amersham Hybond P; GE Healthcare Europe, Diegem, Belgium) by wet electroblotting. Next, the membrane was incubated with 2% ECL AdvanceTM blocking agent (GE Healthcare Europe) in PBS-0.1% Tween 20 (PBST) for 1 h at RT and probed with rabbit anti-FLP (1:200; Diagenode, Seraing, Belgium;

CS-169-100), mouse anti-glyceraldehyde 3-phosphate dehydrogenase (GAPDH; 1:10,000; Merck Millipore, Billerica, MA; clone 6C5) or rabbit anti-lamin A/C (1:10,000; Santa Cruz Biotechnology; sc-20681) primary antibodies overnight at 4°C, followed by a 1-h incubation with appropriate horseradish peroxidase-conjugated secondary antibodies (Santa Cruz Biotechnology). GAPDH served as cytoplasmic marker protein and lamin A/C antibody was used as nuclear marker protein. Target protein signals were visualized using the SuperSignal West Femto Maximum Sensitivity Substrate Kit (Thermo Scientific, Rockford, IL) and chemiluminescence was measured with the ChemiDoc XRS imaging system (Bio-Rad Laboratories, Veenendaal, the Netherlands).

FLPe functionality test

To test the functionality of the FLPe molecules encoded by LV.FLPe^{NLS+}.PurR and LV.FLPe^{NLS-}.PurR, myoblasts^{GS.GLuc} were transduced with LV.FLPe^{NLS+}.PurR, LV.FLPe^{NLS-}.PurR or LV.PurR. Myoblasts^{GS.GLuc} were seeded in a 24-well cell culture plate at a density of 10⁵ cells per well and exposed for 20 h to 75 µl per well of concentrated vector stock diluted in growth medium to a final volume of 500 µl. Next, the cell monolayers were rinsed three times with 1 ml of PBS after which 400 µl fresh growth medium was added. At 24 h after the removal of the inoculum, the culture medium was collected and transiently stored at -80°C for subsequent analysis of luciferase activity. The cells were overlaid with 400 µl of fresh growth medium, which was harvested 24 h later for storage at -80°C until luciferase activity measurement.

Luciferase assay

After thawing the GpLuc-containing samples on ice, 50 µl of each sample was transferred to a well of a white opaque 96-well flat-bottom microtiter plate (OptiPlate-96; PerkinElmer, Groningen, the Netherlands) for chemiluminescence measurements. The native coelenterazine (Promega Benelux, Leiden, the Netherlands) stock solution (5 mg/ml in acidified methanol) was diluted 1,000 times in phenol red-free Dulbecco's modified Eagle's medium (Life Technologies Europe) and equilibrated for 1 h in the dark at RT before starting the measurements. The luciferase activity was measured at RT with the aid of a Wallace 1420 VICTOR 3 multilabel plate reader with automatic injection system (PerkinElmer). Immediately after automated addition of 20 µl of substrate to a well, substrate and sample were

mixed by shaking for 1 second (double orbital, 0.1 mm, normal speed). PpLuc activity was measured in cell lysates as previously described.⁷ For each condition, three independent samples were measured in three series of measurements.

Statistical analysis

Different experimental groups were compared using the independent samples *t*-test. Differences among means were considered significant at $P \leq 0.05$. Graphs were prepared in GraphPad Prism version 5 (GraphPad Software, La Jolla, CA).

Results

Microscopic analysis of cell fusion kinetics

Cultured myoblasts can be prompted to fuse with each other by withdrawing mitogens from the culture medium. This causes a time-dependent accumulation of nuclei in syncytial structures called myotubes or myosacs depending on whether these structures are elongated or rounded. To get a first impression of the cell-to-cell fusion kinetics of the genetically modified iDMD myoblasts, 1:1 co-cultures of myoblasts-FLPe^{NLS-} and myoblasts^{GS.GLuc} were exposed to myogenic differentiation conditions. As shown in the upper panel of Figure 4, the myoblasts started to fuse 48 h after serum withdrawal resulting in the formation of myotubes/sacs. Both the percentage of nuclei present in myotubes/sacs as well as the size of the syncytia increased with time until 120 h following serum removal, after which the cells started to detach from the surface of the culture plates. The fusion process was accompanied by the accumulation of sarcomeric proteins as evinced by the results of the skTnI-specific immunostaining depicted in the lower panel of Figure 4.

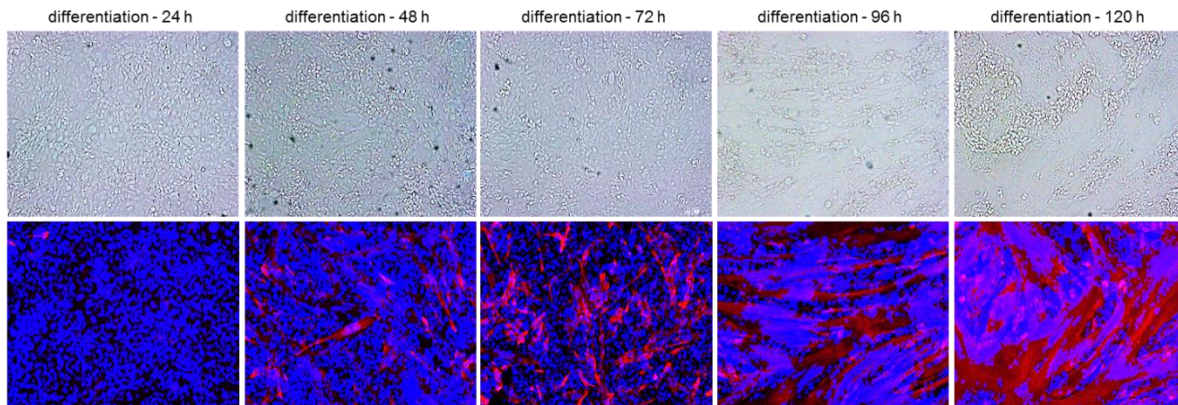


Figure 4. Microscopic analysis of cell fusion kinetics in 1:1 co-cultures of myoblasts-FLPe^{NLS-} and myoblasts^{GS.GLuc} after maintenance for 72 h in growth medium and subsequent exposure to differentiation medium. At 24, 48, 72, 96 or 120 h after initiation of differentiation the cells were fixed and immunostained for skTnl (red fluorescence). The blue fluorescence corresponds to nuclei labeled with the karyophilic dye Hoechst 33342. The upper and lower row of pictures show phase-contrast images and fluoromicrographs, respectively. The first syncytia appeared at \pm 48 h after serum removal. The cell cultures displayed a time-dependent increase in frequency and size of myotubes/sacs until the cells started to detach from the surface of the culture plates. In parallel cultures of myoblasts kept in normal growth medium the cells remained firmly attached to their support and only few small syncytia were observed at late times after culture initiation (data not shown).

Immunodetection of FLPe in LV.FLPe^{NLS+/-}.PurR-transduced iDMD myoblasts

To compare FLPe protein level and intracellular distribution between myoblasts-FLPe^{NLS+} and myoblasts-FLPe^{NLS-}, western blot analysis was performed on whole cell lysates as well as on nuclear and cytosolic cell fractions (Figure 5A). As expected from the presence at its amino terminus of the SV40 NLS, FLPe^{NLS+} (predicted molecular weight: 49.7 kilodaltons) had a slightly lower gel mobility than FLPe^{NLS-} (predicted molecular weight: 48.6 kilodaltons). Both under growth and differentiation conditions, the steady-state level of FLPe^{NLS+} was considerably higher than that of FLPe^{NLS-} even though the nucleotide sequences upstream of the FLPe start codon are very similar and both proteins contain a “destabilizing” amino acid residue (serine in FLPe^{NLS-} versus alanine in FLPe^{NLS+;}¹⁸) immediately downstream of the initiator methionine. Figure 5A also reveals that a larger fraction of FLPe^{NLS+} molecules than of FLPe^{NLS-} molecules resides in the nucleus (nuclear-to-cytosolic ratios under differentiation conditions of 8.4 and 3.1, respectively) consistent with the presence in FLPe^{NLS+} of an SV40 NLS.

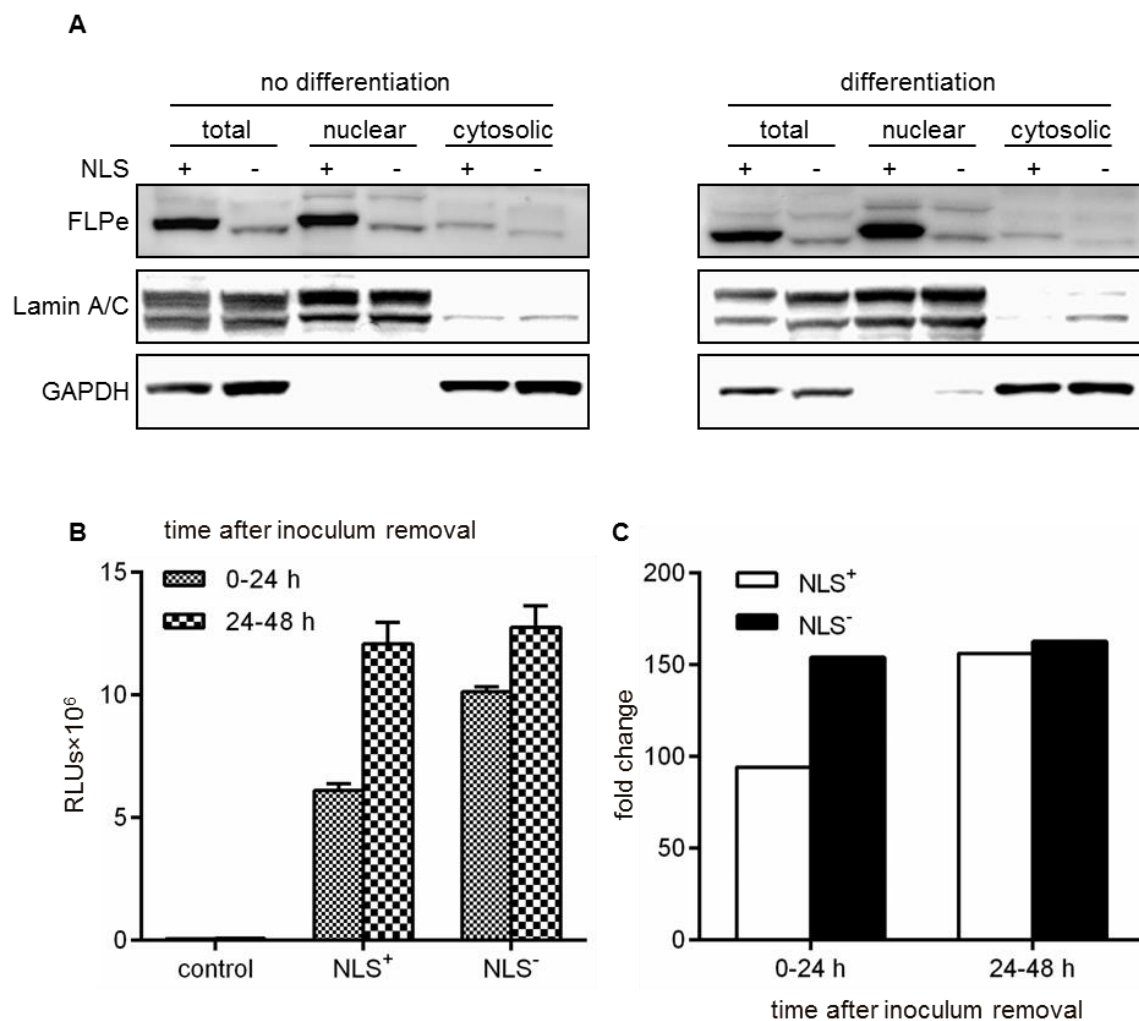


Figure 5. Analysis of FLPe^{NLS+/-} level, intracellular localization and enzymatic activity. **(A):** Western blotting analysis of whole protein lysates, nuclear cell fractions and cytosolic cell fractions of myoblasts-FLPe^{NLS+} (+) and of myoblasts-FLPe^{NLS-} (-) maintained in growth medium (no differentiation) or exposed to differentiation conditions for 96 h (differentiation). **(B):** Luciferase activity measurements in culture media of myoblasts^{GS.GLuc} transduced with LV.FLPe^{NLS+}.PurR, LV.FLPe^{NLS-}.PurR or LV.PurR (negative control vector) representing different intervals (*i.e.* 0-24 h and 24-48 h) post transduction. Bars show mean \pm standard error of the mean ($n=3$). **(C):** Fold change in luciferase activity calculated on the basis of the data presented in **(B)**. The average light production by samples of LV.PurR-transduced myoblasts^{GS.GLuc} was the denominator and the mean of the RLUs produced by LV.FLPe^{NLS+}.PurR-transduced myoblasts^{GS.GLuc} (NLS⁺) or by LV.FLPe^{NLS-}.PurR-transduced myoblasts^{GS.GLuc} (NLS⁻) was the numerator. NLS, nuclear localization signal; FLPe, molecularly evolved flippase; GAPDH, glyceraldehyde 3-phosphate dehydrogenase; RLUs, relative light units.

Assessment of FLPe^{NLS+/-} functionality

To investigate the functionality of the FLPe molecules encoded by LV.FLPe^{NLS+}.PurR and LV.FLPe^{NLS-}.PurR, myoblasts^{GS.GLuc} were transduced with either of these FLPe-encoding SIN-LVs or with LV.PurR (negative control vector). Production of functional recombinases by the FLPe-encoding SIN-LVs should result in activation of the *GpLuc* gene switch cassettes incorporated into the genomes of the myoblasts^{GS.GLuc} and the secretion of active GpLuc molecules in their culture medium (Figure 6). Analysis of the culture media harvested at 24 h after vector removal showed strong luciferase activity in the samples derived from the LV.FLPe^{NLS+}.PurR- and LV.FLPe^{NLS-}.PurR-transduced myoblasts^{GS.GLuc}, while hardly any luciferase activity was detected in the culture medium of LV.PurR-transduced myoblasts^{GS.GLuc} (Figure 5B). During the next 24-h interval the luciferase activity in the culture media of LV.FLPe^{NLS+}.PurR- and LV.FLPe^{NLS-}.PurR-transduced myoblasts^{GS.GLuc} further increased whereas the luciferase activity in the negative control samples remained very low. As a result, luciferase activity was 94/154- and 156/162-fold higher in 0-24 h and 24-48 h culture medium of LV.FLPe^{NLS+}.PurR- and LV.FLPe^{NLS-}.PurR-transduced myoblasts^{GS.GLuc}, respectively, than in the corresponding culture media of LV.PurR-infected cells (Figure 5C). These findings confirm the presence of FLP recombinase-activatable *GpLuc* expression units in myoblasts^{GS.GLuc} and demonstrate that LV.FLPe^{NLS+}.PurR and LV.FLPe^{NLS-}.PurR both code for functional FLPe molecules.

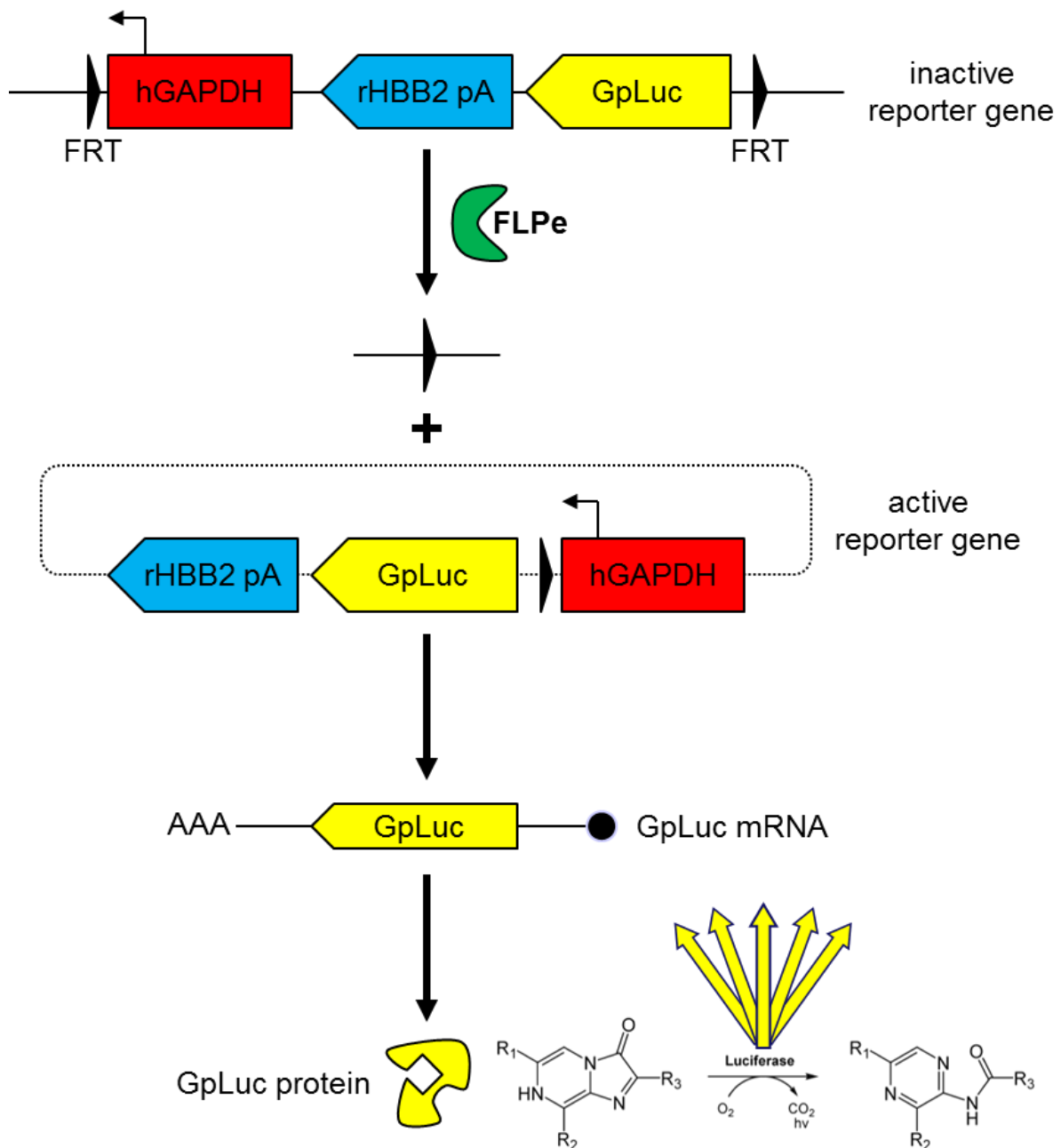


Figure 6. Schematic overview of the activation of the *GpLuc* gene switch cassette. Recognition of the FRT sites in chromosomally integrated copies of the LV.GS.*GpLuc* genome by FLPe leads to the activation of the latent *GpLuc* gene through the formation of circular episomes positioning the *hGAPDH* gene promoter upstream of the *GpLuc* ORF. Black triangle/FRT, flippase recognition target sequence; *hGAPDH*, human *glyceraldehyde 3-phosphate dehydrogenase* gene promoter; *rHBB2* pA, rabbit *β-hemoglobin* gene polyadenylation signal; *GpLuc*, *Gaussia princeps* luciferase-coding sequence; FLPe, molecularly evolved flippase.

Validation of the LV.FLPe^{NLS+/-}.PurR/LV.GS.GpLuc-based cell fusion assay system

To compare the ability of FLPe^{NLS+} and FLPe^{NLS-} to activate the *GpLuc* gene switch upon cell fusion, myoblasts^{GS.GLuc} were co-cultured with myoblasts-FLPe^{NLS+} or myoblasts-FLPe^{NLS-} at different ratios (*i.e.* 95:5, 90:10, 75:25, 50:50, 25:75, 10:90 and 5:95). Monocultures of myoblasts-FLPe^{NLS+}, myoblasts-FLPe^{NLS-} or myoblasts^{GS.GLuc} exposed to growth or differentiation medium and co-cultures of *FLPe*-expressing myoblasts and myoblasts^{GS.GLuc} maintained in growth medium served as negative controls. Based on the results of the microscopic analysis of cell fusion activity (Figure 4), the culture medium was harvested 96 h after induction of myogenic differentiation. It should be noted, however, that the kinetics of cell fusion progression slightly differed between individual experiments probably reflecting small differences in the myoblast populations used for different experiments. Luciferase activity in the medium of the fusogenic cell cultures depended on the ratio of myoblasts^{GS.GLuc} and myoblasts-FLPe, showed a similar trend for myoblasts-FLPe^{NLS+}- and myoblasts-FLPe^{NLS-}-containing co-cultures and was highest when co-cultures contained 50-95% myoblasts^{GS.GLuc} (Figure 7A). The peak of *GpLuc* activity was reached at myoblast^{GS.GLuc}:myoblast-FLPe ratios of 90:10 and 75:25 for myoblasts-FLPe^{NLS+} and myoblasts-FLPe^{NLS-}, respectively (Figure 7A). Interestingly, at low myoblast^{GS.GLuc}:myoblast-FLPe ratios (*i.e.* 10:90 and 5:95) the luciferase activity was significantly higher for myoblasts-FLPe^{NLS-} than for myoblasts-FLPe^{NLS+} (Figure 7A). Myoblast cultures kept under growth conditions and myoblast-FLPe monocultures maintained in differentiation medium yielded luminescence signals close to or at background levels. The monocultures of myoblasts^{GS.GLuc} did, however, secrete detectable amounts of *GpLuc* under differentiation conditions although the signal intensity was much lower than that produced by serum-deprived co-cultures containing 50-90% myoblasts^{GS.GLuc}. For the co-cultures containing 50-90% myoblasts^{GS.GLuc} shifting from growth to differentiation medium resulted in a >100-fold increase in luciferase activity (Figure 7B).

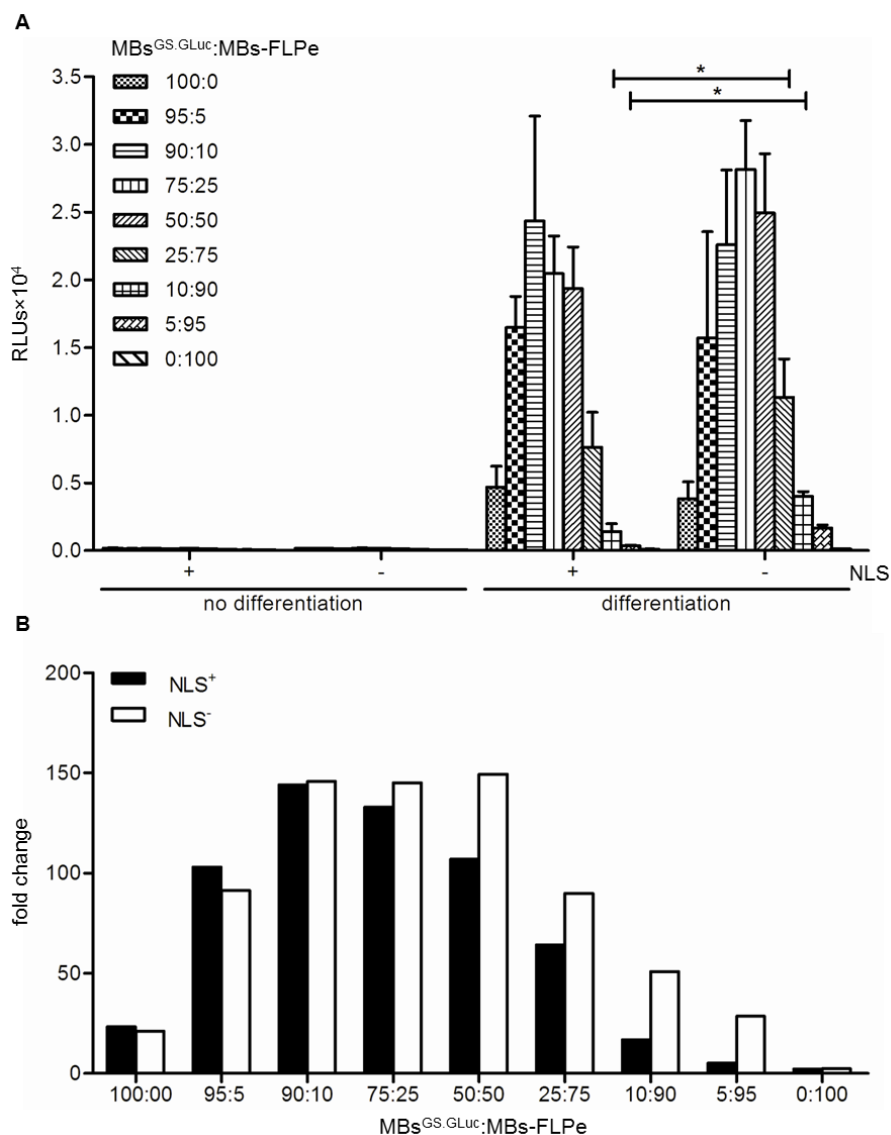


Figure 7. Validation of the LV.FLPe^{NLS+/-}.PurR/LV.GS.GpLuc.v1-based cell fusion assay system. **(A):** Luminometric analysis of culture medium of myoblasts^{GS.GLuc} co-cultured with myoblasts-FLPe^{NLS+} (+) or with myoblasts-FLPe^{NLS-} (-) at the indicated ratios. At 72 h after cell seeding, the culture fluid in each well was replaced by fresh culture medium with (growth conditions, no differentiation) or without (differentiation conditions) serum. Ninety-six h later the culture media were collected and subjected to luciferase activity measurements. Bars represent mean \pm standard error of the mean (n=3). **(B):** Fold change in luciferase activity calculated on the basis of the data presented in (A). For each culture composition the average light production under growth conditions was the denominator and the mean of the RLUs produced under differentiation conditions was the numerator. RLUs, relative light units; MBs^{GS.GLuc}, myoblasts^{GS.GLuc}; MBs-FLPe, myoblasts-FLPe; NLS, nuclear localization signal.

Use of the LV.FLPe^{NLS+/-}.PurR/LV.GS.GpLuc-based cell fusion assay system to analyse cell fusion progression

To investigate the utility of the LV.FLPe^{NLS+/-}.PurR/LV.GS.GpLuc-based cell fusion assay system to follow cell fusion progression, myoblasts^{GS.GLuc} were mixed with myoblasts-FLPe^{NLS+} or with myoblasts-FLPe^{NLS-} at a ratio of 50:50. After the cell cultures had become nearly confluent, they were either given fresh growth medium or exposed to differentiation medium. This was followed by the periodic collection of culture fluid for luciferase measurements using two different approaches. In one experiment, the culture medium was left on the cells for different time periods (*i.e.* from 0-24, 0-36, 0-48, 0-60, 0-72, 0-84, 0-96, 0-108 and 0-120 h) before being harvested for luminometry (“cumulative assay”; Figure 8). In the other experiment, the culture fluid was refreshed every 24 h and the amount of biologically active luciferase that had been secreted between 0-24, 24-48, 48-72, 72-96 and 96-120 h after the start of the differentiation process was determined (“kinetics assay”; Figure 9). As shown in Figure 8A, following an initial slow increase, the luciferase activity in the culture medium of the serum-deprived co-cultures rose sharply at late times (>72 h) after initiation of differentiation. Co-cultures of myoblasts^{GS.GLuc} and myoblasts-FLPe^{NLS-} produced better results than the combination of myoblasts^{GS.GLuc} and myoblasts-FLPe^{NLS+} (Figure 8A,B) in spite of the much higher FLPe concentration in myoblasts-FLPe^{NLS+} than in myoblasts-FLPe^{NLS-} (Figure 5A). These findings were corroborated by the data derived from the “kinetics assay” (Figure 9).

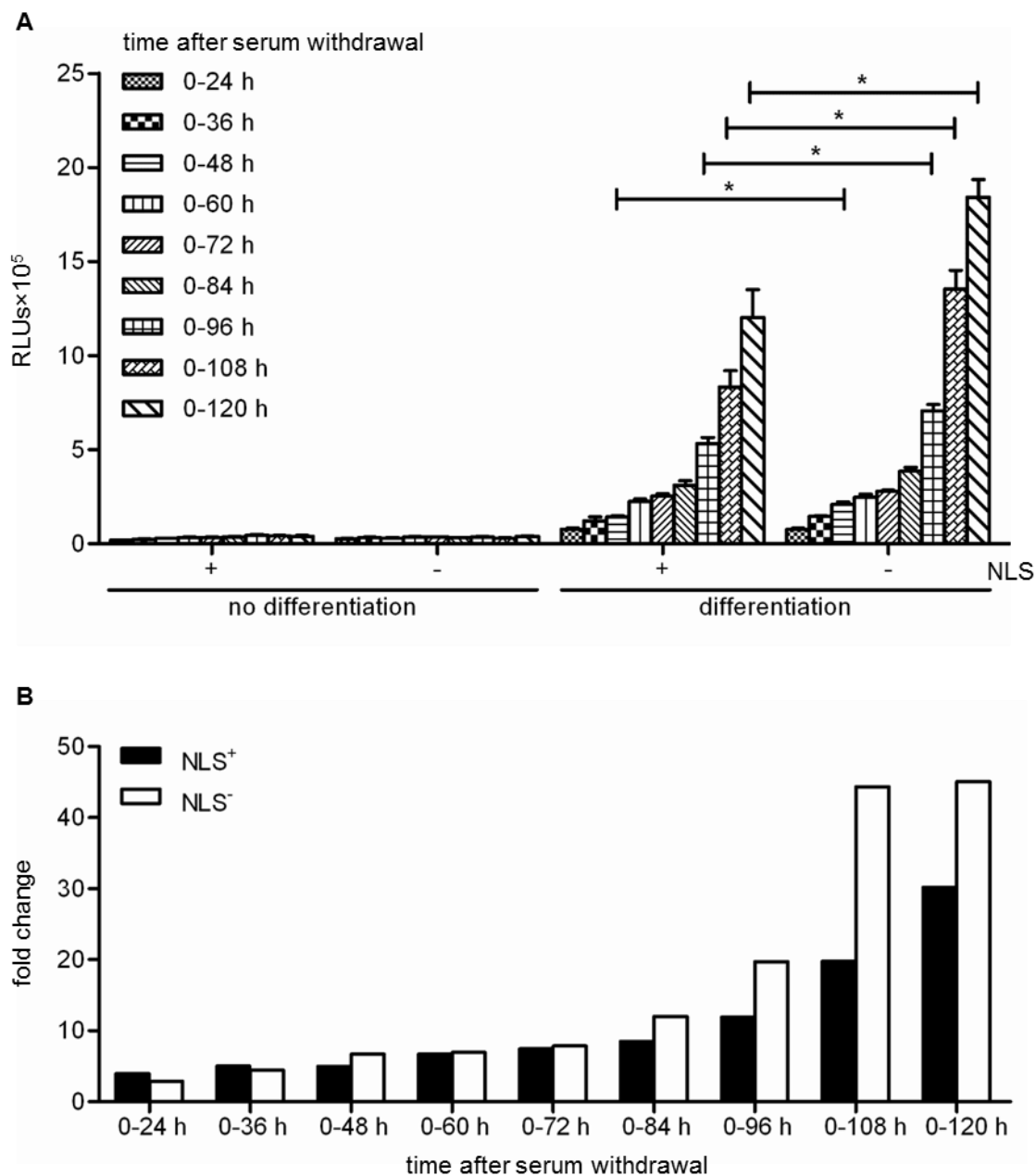


Figure 8. Analysis of GpLuc accumulation in proliferating and differentiating 1:1 co-cultures of myoblasts^{GS.GLuc} and either myoblasts-FLPe^{NLS+} or myoblasts-FLPe^{NLS-}. **(A):** Luminometric analysis of culture medium of co-cultures of 50% myoblasts^{GS.GLuc} and 50% myoblasts-FLPe^{NLS+} (+) or 50% myoblasts-FLPe^{NLS-} (-). At 72 h after cell seeding, the culture fluid was replaced by fresh culture medium with (growth conditions, no differentiation) or without (differentiation conditions) serum, which was left on the cells for the indicated periods of time. Bars represent mean \pm standard error of the mean (n=3). **(B):** Fold change in luciferase activity calculated on the basis of the data presented in (A). For each sampling time the average light production under growth conditions was the denominator and the mean of the RLUs produced under differentiation conditions was the numerator. RLUs, relative light units; NLS, nuclear localization signal.

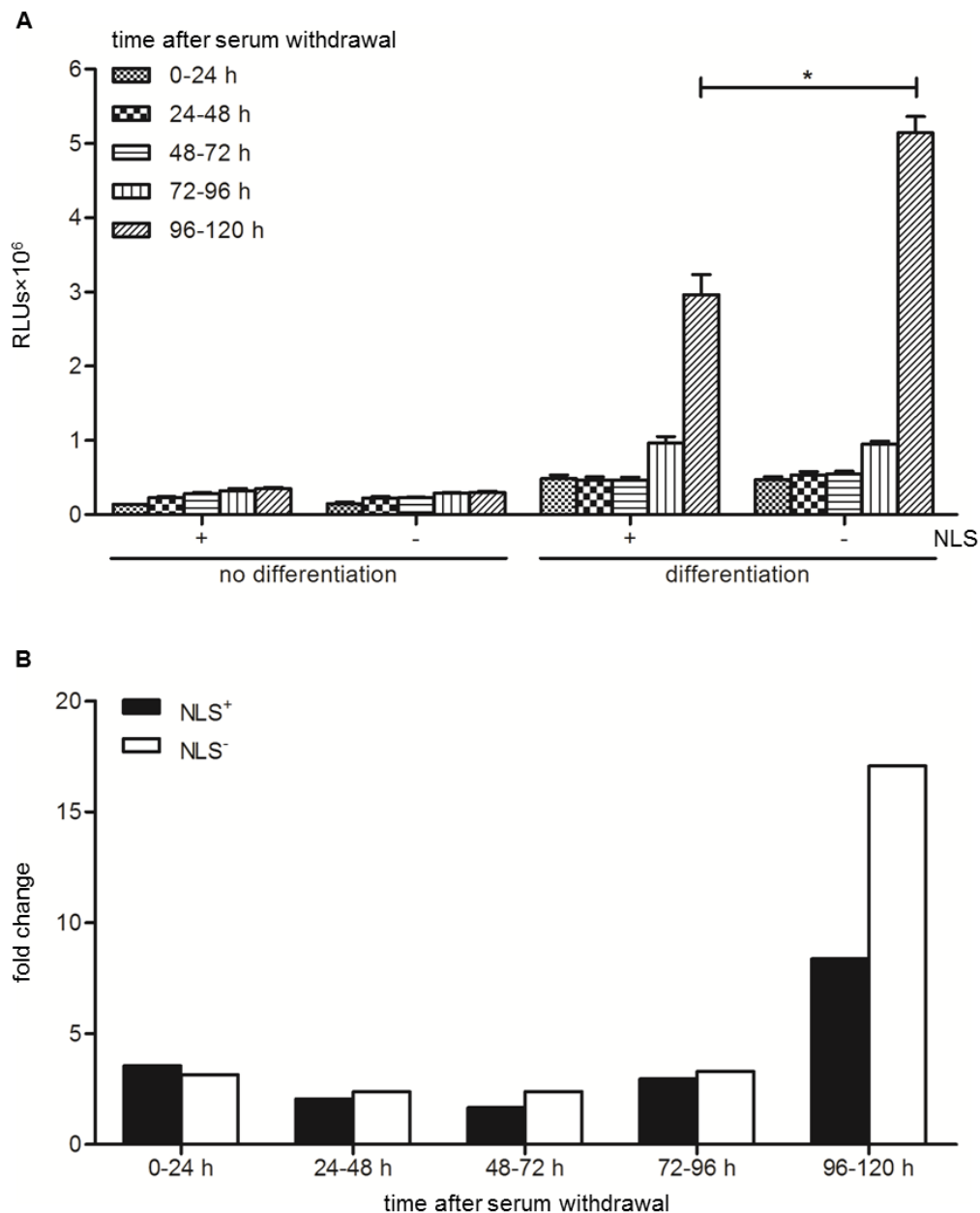


Figure 9. Analysis of GpLuc secretion in proliferating and differentiating 1:1 co-cultures of myoblasts^{GS,Gluc} and either myoblasts-FLPe^{NLS+} or myoblasts-FLPe^{NLS-}. **(A):** Luminometric analysis of culture medium of co-cultures of 50% myoblasts^{GS,Gluc} and 50% myoblasts-FLPe^{NLS+} (+) or 50% myoblasts-FLPe^{NLS-} (-). At 72 h after cell seeding, the culture fluid was replaced by fresh culture medium with (growth conditions, no differentiation) or without (differentiation conditions) serum, which was left on the cells for the indicated 24-h time intervals. Bars represent mean \pm standard error of the mean (n=3). **(B):** Fold change in luciferase activity calculated on the basis of the data presented in (A). For each sampling time the average light production under growth conditions was the denominator and the mean of the RLUs produced under differentiation conditions was the numerator. RLUs, relative light units; NLS, nuclear localization signal.

On the basis of the previous results, another experiment was carried out in which we directly compared the performance of FLPe^{NLS+} and FLPe^{NLS-} at different myoblast^{GS.GLuc}:myoblast-FLPe ratios (*i.e.* 95:5, 75:25, 25:75 and 5:95) and different time points (*i.e.* 72, 96 and 120 h after serum withdrawal). The culture medium was refreshed just before the start of the first sampling interval (*i.e.* at 48 h after serum removal) and after each round of sample collection. This experiment confirmed that at high myoblast^{GS.GLuc}:myoblast-FLPe ratios FLPe^{NLS-} was nearly as efficient as FLPe^{NLS+} at inducing reporter gene expression while at low myoblast^{GS.GLuc}:myoblast-FLPe ratios FLPe^{NLS-} gave rise to more RLU (Figure 10A) and to higher signal-to-noise ratios (Figure 10B). In accordance with the experiment presented in Figure 7, the co-cultures consisting of 75% myoblasts^{GS.GLuc} and 25% myoblasts-FLPe yielded the highest signals both in absolute (Figure 10A) and relative (Figure 10B) terms. Also in line with the previous experiments was the finding that most GpLuc accumulation takes place between 96 and 120 h after serum removal.

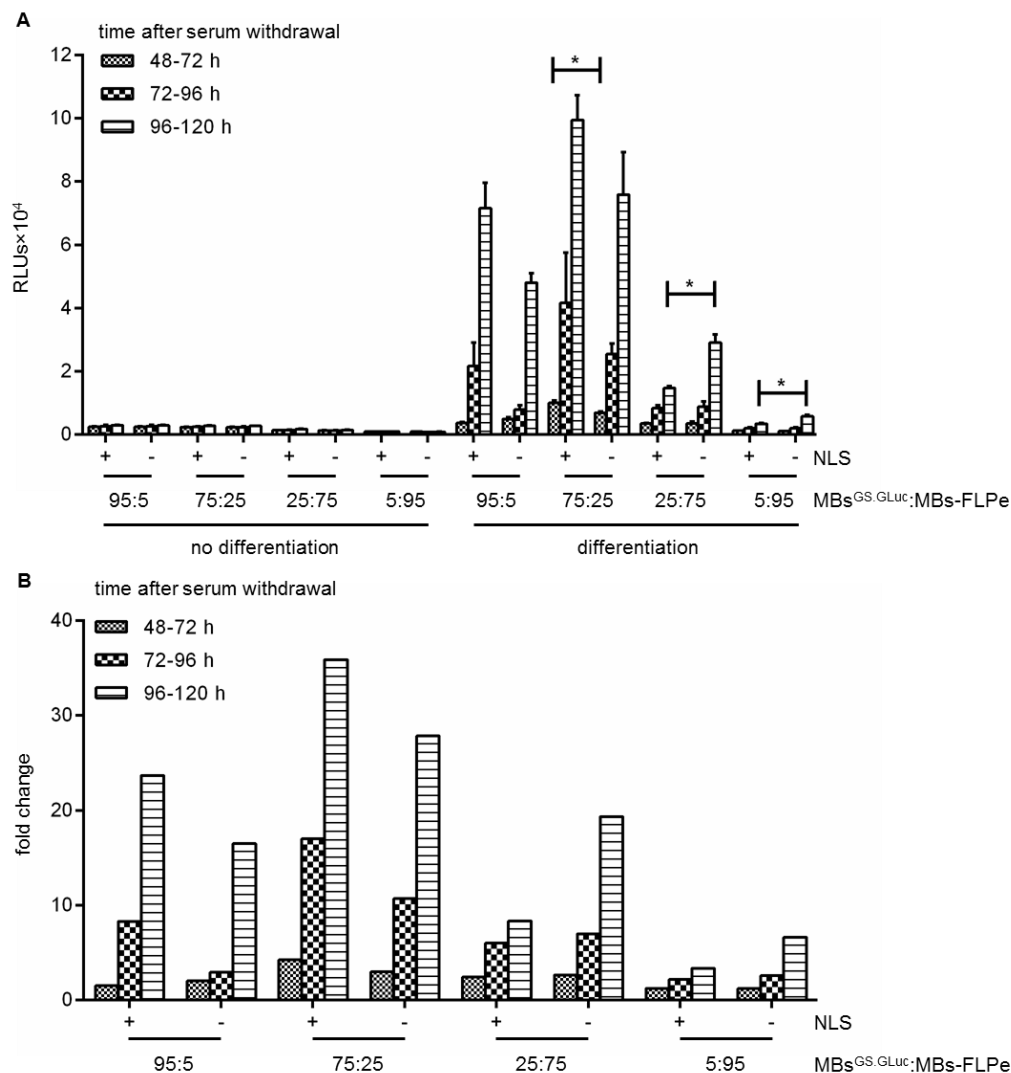


Figure 10. Performance of FLPe^{NLS+} and FLPe^{NLS-} at different acceptor-to-donor cell ratios and time points. **(A):** GpLuc release by proliferating or differentiating co-cultures of myoblasts^{GS.GLuc} and myoblasts-FLPe^{NLS+} (+) or myoblasts-FLPe^{NLS-} (-) at different time intervals after culture initiation. Myoblasts^{GS.GLuc} and myoblasts-FLPe were seeded in different ratios (*i.e.* 95:5%, 75:25%, 25:75% and 5:95%). At 72 h after cell seeding, the culture fluid was replaced by fresh culture medium with (growth conditions, no differentiation) or without (differentiation conditions) serum. Forty-eight h later the culture medium was refreshed once again. Twenty-four h later the culture fluid was harvested for luciferase activity measurement and replaced by the same volume of fresh culture medium. This procedure was repeated every 24 h until 120 h after the first medium change. Bars represent mean \pm standard error of the mean ($n=3$). **(B):** Fold change in luciferase activity calculated on the basis of the data presented in (A). For each experimental condition the average light production under growth conditions was the denominator and the mean of the RLUs produced under differentiation conditions was the numerator. RLUs, relative light units; MBs^{GS.GLuc}, myoblasts^{GS.GLuc}; MBs-FLPe, myoblasts-FLPe; NLS, nuclear localization signal.

Comparison of LV.GS.GpLuc.v1- and LV.GS.PpLuc-based cell fusion assay systems

In the next experiment, a direct comparison was made between the previously described LV.GS.PpLuc-based quantitative cell fusion assay system⁷ and the new LV.GS.GpLuc-based method to quantify cell-to-cell fusion. Consistent with the much higher light output of GpLuc than of PpLuc⁸, LV.GS.GpLuc yielded up to 23-fold higher signals than LV.GS.PpLuc (Figure 11A). However, the LV.GS.PpLuc-based cell fusion assay system appeared to be approximately twice as sensitive as its LV.GS.GpLuc-based counterpart at detecting myoblast-to-myoblast fusion at 120 h after initiation of differentiation (Figure 11B). The difference in sensitivity between the GS.GpLuc.v1- and LV.GS.PpLuc-based cell fusion assay systems was even bigger for the samples collected at 96 h after serum removal especially at the lowest two myoblast^{GS.Luc}:myoblast-FLPe^{NLS+} ratios (*i.e.* when FLPe levels are highest).

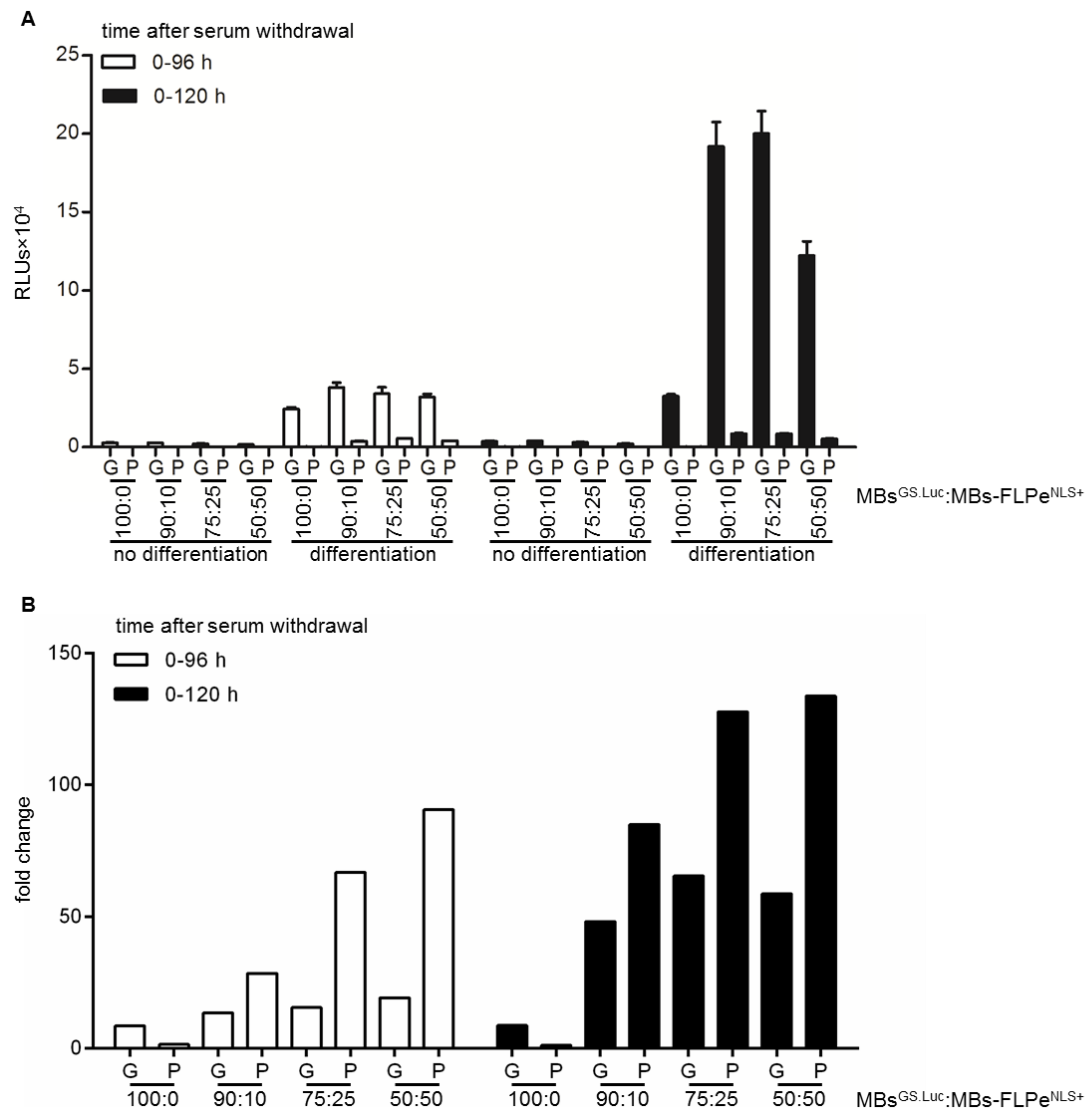


Figure 11. Comparison of LV.GS.GpLuc.v1- and LV.GS.PpLuc-based cell fusion assay systems. **(A):** GpLuc and PpLuc production by proliferating or differentiating co-cultures of myoblasts^{GS.GLuc} or myoblasts^{GS.PLuc} with myoblasts-FLPe^{NLS+} at different times after culture initiation. Cells were seeded in different ratios (*i.e.* 100:0%, 90:10%, 75:25% and 50:50%). At 72 h after cell seeding the culture fluid was replaced by fresh culture medium with (growth conditions, no differentiation) or without (differentiation conditions) serum. Ninety-six h and 120 h later samples (culture fluid for cultures containing myoblasts^{GS.GLuc} and cell lysates for cultures containing myoblasts^{GS.PLuc}) were harvested for luciferase activity measurements. Bars represent mean \pm standard error of the mean ($n=3$). **(B):** Fold change in luciferase activity calculated on the basis of the data presented in **(A)**. For each experimental condition the average light production under growth conditions was the denominator and the mean of the RLUs produced under differentiation conditions was the numerator. RLUs, relative light units; G, LV.GS.GpLuc.v1-based cell fusion assay; P, LV.GS.PpLuc-based cell fusion assay; MBs^{GS.Luc}, myoblasts^{GS.GLuc} or myoblasts^{GS.PLuc}; MBs-FLPe^{NLS+}, myoblasts-FLPe^{NLS+}.

Improvement of the GS.GpLuc-based cell fusion assay system

The results presented in Figures 7 and 11 identify the FLP-independent increase in GpLuc production when shifting from growth to differentiation medium as the main contributor to the reduced signal-to-noise ratio of the LV.GS.GpLuc-based cell fusion assay system as compared to its LV.GS.PpLuc-based counterpart. In search for a possible explanation for the high background signal produced by LV.GS.GpLuc.v1 in comparison to LV.GS.PpLuc, we compared their genetic organization upstream of the *Luc* start codon. As shown in Figures 2 A,B and 3 the *PpLuc* ORF in LV.GS.PpLuc is preceded by an out-of-frame ORF (uORF) starting with 2 ATG codons in a favourable context for translational initiation¹⁹ and ending with a highly efficient stop codon²⁰ separated by only 7 nucleotides from the *PpLuc* initiation codon. This specific genetic makeup will be effective in suppressing any *PpLuc* expression directed by mRNAs with 5' ends located upstream of the second ATG codon in the uORF. Oppositely, in LV.GS.GpLuc.v1 the previously mentioned tandem of ATG codons are in-frame with the *GpLuc* initiation codon allowing the synthesis of an N-terminally extended GpLuc fusion protein. Located further upstream of the *GpLuc* ORF in LV.GS.GpLuc.v1 is an out-of-frame ORF with suboptimal start and stop codons. LV.GS.GpLuc.v1 thus offers much more possibilities for “leaky” *Luc* expression than LV.GS.PpLuc. To solve this problem, we designed LV.GS.GpLuc.v6. In this construct, the distance between the mMT1 pA and *GpLuc* ORF is kept very short to minimize the chance of creating transcriptional start sites in the intervening region. As an additional measure to limit leaky *GpLuc* expression, LV.GS.GpLuc.v6 contains a 21-bp uORF starting immediately upstream of the FRT sequence and ending with an efficient stop codon provided by the FRT sequence. Between the stop codon of the uORF and the *PpLuc* initiation codon only 20 nucleotides are present comprising the remainder of the FRT sequence and an optimal start site for *GpLuc* translation.

LV.GS.GpLuc.v6 was used to generate myoblasts^{GS.GLuc+} carrying the optimized *GpLuc* gene switch cassette. Next, the performance of the LV.GS.GpLuc.v1- and LV.GS.GpLuc.v6-based cell fusion assay systems was compared in an experiment with the same setup as used for the comparison of LV.GS.GpLuc.v1 with LV.GS.PpLuc except for the omission of the 1:1 myoblast^{GS.GLuc(+)}:myoblast-FLPe^{NLS+} ratio. Luciferase activity in 0-96 h and 0-120 h culture medium of serum-

deprived myoblast^{GS.GLuc+} monocultures was \pm 3-fold lower than in culture medium of differentiating myoblast^{GS.GLuc} monocultures (Figure 12), demonstrating the effectiveness of the new gene switch design to inhibit leaky *GpLuc* expression. However, since the improved gene switch design also reduced FLPe-dependent signal output the fold increase in GpLuc activity during myogenic differentiation of myoblast^{GS.GLuc(+)}:myoblast-FLPe^{NLS+} co-cultures was quite similar for LV.GS.GpLuc.v1 and LV.GS.GpLuc.v6 (Figure 12B). Still, in comparison to LV.GS.GpLuc.v1 for LV.GS.GpLuc.v6 a much larger part of the increase in GpLuc activity observed in differentiating myoblast^{GS.GLuc(+)}:myoblast-FLPe^{NLS+} co-cultures is attributable to cell fusion.

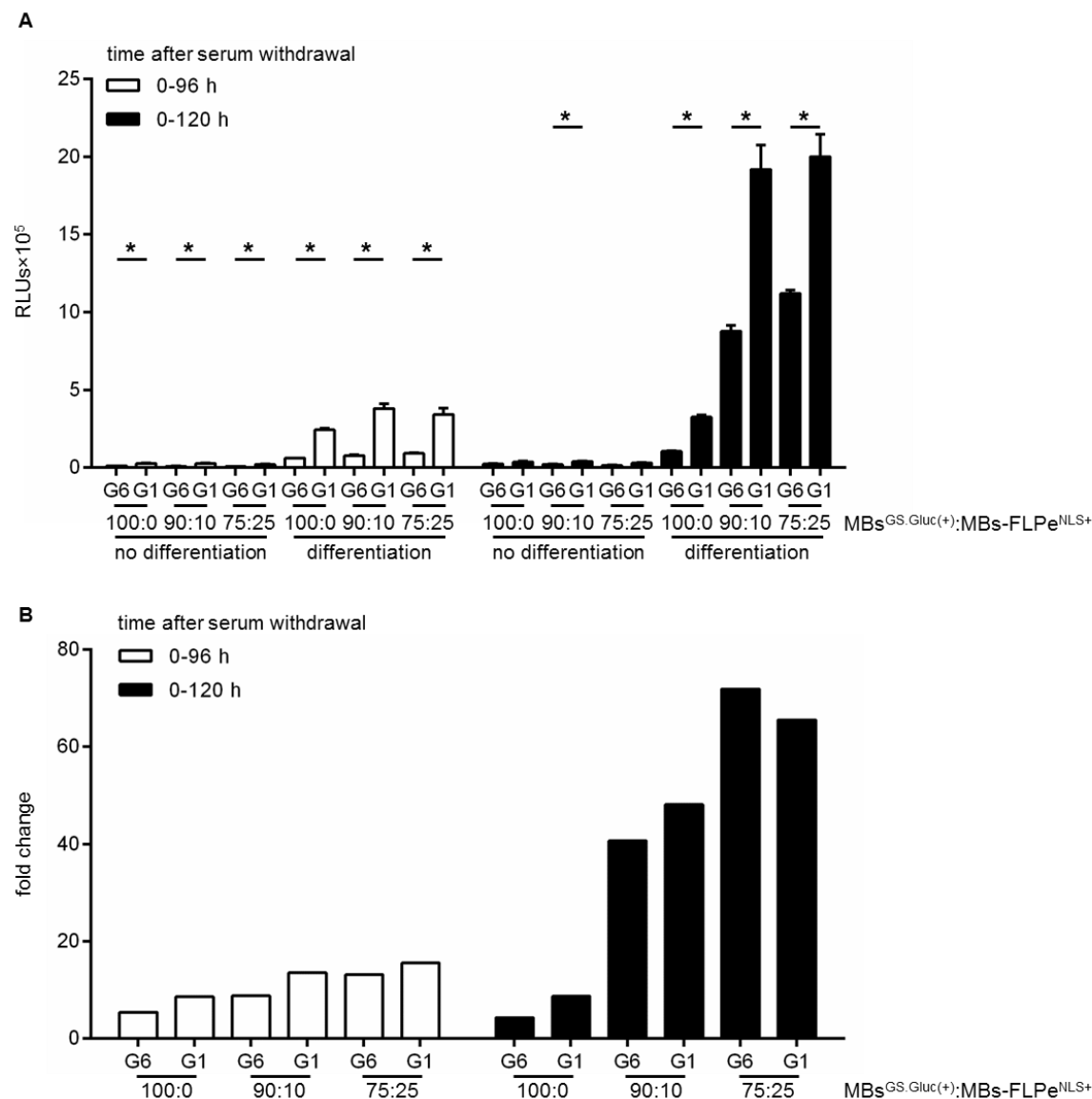


Figure 12. Comparison of LV.GS.GpLuc.v1- and LV.GS.GpLuc.v6-based cell fusion assay systems. **(A):** GpLuc production by proliferating or differentiating co-cultures of myoblasts^{GS.Gluc} or myoblasts^{GS.Gluc+} with myoblasts-FLPe^{NLS+} at different times after culture initiation. Cells were seeded in different ratios (*i.e.* 100:0%, 90:10% and 75:25%). At 72 h after cell seeding the culture fluid was replaced by fresh culture medium with (growth conditions, no differentiation) or without (differentiation conditions) serum. Ninety-six h and 120 h later culture medium collected for luciferase activity measurement. Bars represent mean \pm standard error of the mean ($n=3$). **(B):** Fold change in luciferase activity calculated on the basis of the data presented in **(A)**. For each experimental condition the average light production under growth conditions was the denominator and the mean of the RLUs produced under differentiation conditions was the numerator. RLUs, relative light units; G1, LV.GS.GpLuc.v1-based cell fusion assay; G6, LV.GS.GpLuc.v6-based cell fusion assay; MBs^{GS.Gluc(+)}, myoblasts^{GS.Gluc} or myoblasts^{GS.Gluc+}; MBs-FLPe^{NLS+}, myoblasts-FLPe^{NLS+}.

Discussion

Apart from being involved in the formation and maintenance of skeletal muscles, bones and the placenta, cell-to-cell fusion plays an important role in numerous other biological processes like fertilization. It has also been implicated in the initiation and progression of cancer² and as a driving force in evolution.²¹ Moreover, cell-to-cell fusion has been of great value to establish the chromosomal location of specific genes,²² can be used to induce cellular reprogramming^{23,24} and is indispensable for generating hybridomas.²⁵ The involvement of cell-to-cell fusion in a large variety of biological processes and its diverse biotechnological applications have prompted investigations into the mechanisms of cell fusion and the contribution of specific factors to this process. Instrumental to this research is the availability of robust assays to determine cell fusion kinetics and extent. However, most of the existing quantitative cell fusion assays do not allow consecutive analysis of the same cells/tissue. Accordingly, in this paper a new quantitative assay is presented to monitor cell-to-cell fusion. This assay is based on the activation of a latent *GpLuc* gene after fusion of cells containing this latent reporter gene with cells encoding a recombinase that activates the dormant *GpLuc* gene. The extent of cell-to-cell fusion is subsequently quantified by simply measuring the enzymatic activity of the luciferase molecules secreted by the cellular fusion products. To the best of our knowledge this is the first assay that allows quantification of cell fusion activity by medium sampling.

To validate the new cell fusion assay it was used to monitor the formation of myotubes/sacs in cultures of serum-deprived human myoblasts. In these experiments, several parameters were varied including the acceptor-to-donor cell ratio and the sample regimen(s) of the cell culture medium. In general, transgene expression increased with increasing fractions of myoblasts^{GS.GLuc} up to the point at which the number of active/nuclear FLPe molecules became limiting (*i.e.* at myoblast^{GS.GLuc}:myoblast-FLPe ratios of 90:10 for FLPe^{NLS-} and of 95:5 for FLPe^{NLS+}; Figure 7).

At high myoblast^{GS.GLuc}:myoblast-FLPe ratios LV.FLPe^{NLS+} was slightly more effective than LV.FLPe^{NLS-} in activating the latent *GpLuc* gene most likely due to fact that under differentiation conditions myoblasts-FLPe^{NLS+} contain \pm 5-fold more

nuclear FLPe molecules than myoblasts-FLPe^{NLS-} (Figure 5A). In contrast, at low myoblast^{GS.GLuc}:myoblast-FLPe ratios (*i.e.* when FLPe is no longer limiting) LV.FLPe^{NLS-} consistently outperformed LV.FLPe^{NLS+} (Figures 7 and 10). Collectively, these findings suggest that its NLS does not noticeably hamper the spreading of FLPe^{NLS+} through myofibers/sacs but that high nuclear FLPe levels may somehow limit reporter gene expression. A possible explanation for the higher *GpLuc* expression in differentiating co-cultures containing large percentages of myoblasts-FLPe^{NLS-} in comparison to those with large fractions of myoblasts-FLPe^{NLS+} may be the more frequent occurrence of secondary recombination events in the latter co-cultures leading to the deactivation of functional *GpLuc* expression modules.

While monocultures of myoblasts^{GS.GLuc} maintained in growth medium displayed very little if any leaky *GpLuc* expression, considerable amounts of GpLuc were produced by myoblast^{GS.GLuc} monocultures exposed to differentiation medium. There are several possible explanations for this finding. Firstly, growth and differentiation medium may differently affect light output *e.g.* by (i) causing different levels of coelenterazine “auto-oxidation”, (ii) containing different concentrations of chemiluminescence inhibitors or (iii) absorbing blue light to a different extent. Possibilities (i) and (iii) can be ruled out since mixing of coelenterazine substrate solution with fresh or myoblasts-FLPe^{NLS+}-conditioned growth or differentiation medium produced very similar signals (data not shown). This leaves us with the possibility that transcription termination by the mMT1 pA incorporated into the gene switch constructs is not very efficient or that differentiation conditions somehow stimulate transcription initiation in the region located in between the mMT1 pA and the *Luc* ORFs. For LV.GS.PpLuc and LV.GS.GpLuc.v6 the resulting transcripts may not lead to substantial luciferase production due to the presence of “decoy” ORFs immediately upstream of the *Luc* initiation codons (Figures 2 and 3). A similar favorable situation does not exist for LV.GS.GpLuc.v1, which may explain the high background signals produced by this construct under differentiation conditions. Even though the luciferase activity in culture medium of differentiating myoblast^{GS.GLuc+} monocultures is \pm 3-fold lower than in culture medium of differentiating myoblast^{GS.GLuc} monocultures LV.GS.GpLuc.v6 still gives rise to a higher background signal under differentiation conditions than LV.GS.PpLuc (compare Figure 11 with 12). Considering that the sequences in between the mMT1 pA and the *Luc* start codon in LV.GS.PpLuc and LV.GS.GpLuc.v1 are nearly identical this may suggest

that the GpLuc-coding sequence itself is the source of the relatively high luciferase activity detected in medium of differentiating LV.GS.GpLuc monocultures. If so, the problem could be overcome by switching to another secretory luciferase (e.g. *Vargula hilgendorffii* luciferase²⁶, Lucia luciferase (InvivoGen Europe, Toulouse, France) or secretory NanoLuc²⁷). Also the fact that GpLuc is a secretory protein with a long half-life (± 6 days in culture medium)²⁸ while Ppluc has a relatively short half-life (± 2 hours in cells)²⁹ may contribute to the higher background signals associated with LV.GS.GpLuc.v1 and LV.GS.GpLuc.v6 than with LV.GS.PpLuc.

Taken together, in this paper a new assay to quantify (the progression of) cell-to-cell fusion activity is described. Due to its nondestructive nature allowing repeated sampling of the same specimen, this assay will be an attractive alternative to existing quantitative cell fusion assays based on (i) light microscopic assessment of multinucleation, (ii) fluorescence dequenching, (iii) fluorescence resonance energy transfer, (iv) biochemical complementation or (v) activation of reporter genes different from *GpLuc* including *LacZ* and *PpLuc*.³ Other advantages of the LV.FLPe^{NLS+/-}.PurR/LV.GS.GpLuc-based cell fusion assay include the simplicity and speed of the analytical procedures and the ability to combine it with (immuno)cytology, real-time microscopy, cell function assays and other methods to study cell behavior.

The sensitivity of the current assay could be improved by changing the human *glyceraldehyde 3-phosphate dehydrogenase (hGAPDH)* gene promoter driving *GpLuc* expression for a promoter with higher activity in the cell type(s) under investigation. In addition, the sequences interspersed between the 3' long terminal repeat (LTR) and the *GpLuc* initiation codon of LV.GS.GpLuc.v6 may be further optimized to minimize leaky *GpLuc* expression.

Acknowledgments

The authors thank Martijn Rabelink (Department of Molecular Cell Biology, Leiden University Medical Center) for titrating the LV preparations.

References

1. Shinn-Thomas JH, Mohler WA. New insights into the mechanisms and roles of cell-cell fusion. *Int Rev Cell Mol Biol.* 2011;289:149-209.
2. Lu X, Kang Y. Cell fusion as a hidden force in tumor progression. *Cancer Res.* 2009;69:8536-8539.
3. Shinn-Thomas JH, Scranton VL, Mohler WA. Quantitative assays for cell fusion. *Methods Mol Biol.* 2008;475:347-361.
4. Mohler WA, Blau HM. Gene expression and cell fusion analyzed by *lacZ* complementation in mammalian cells. *Proc Natl Acad Sci USA.* 1996;93:12423-12427.
5. Holkers M, de Vries AA, Gonçalves MA. Modular and excisable molecular switch for the induction of gene expression by the yeast FLP recombinase. *Biotechniques.* 2006;41:711-713.
6. Turan S, Bode J. Site-specific recombinases: from tag-and-target- to tag-and-exchange-based genomic modifications. *FASEB J.* 2011;25:4088-4107.
7. Gonçalves MA, Janssen JM, Holkers M, de Vries AA. Rapid and sensitive lentivirus vector-based conditional gene expression assay to monitor and quantify cell fusion activity. *PLoS One.* 2010;5:e10954.
8. Tannous BA, Kim DE, Fernandez JL, Weissleder R, Breakefield XO. Codon-optimized Gaussia luciferase cDNA for mammalian gene expression in culture and *in vivo*. *Mol Ther.* 2005;11:435-443.
9. Sambrook J, Russell DW. *Molecular cloning: a laboratory manual*. New York: Cold Spring Harbor Laboratory Press. 2001.
10. van Nierop GP, de Vries AA, Holkers M, Vrijssen KR, Gonçalves MA. Stimulation of homology-directed gene targeting at an endogenous human locus by a nicking endonuclease. *Nucleic Acids Res.* 2009;37:5725–5736.
11. Feng T, Li Z, Jiang W, Breyer B, Zhou L, Cheng H, Haydon RC, Ishikawa A, Joudeh MA, He TC. Increased efficiency of cloning large DNA fragments using a lower copy number plasmid. *Biotechniques.* 2002;32:992, 994, 996 passim.
12. Pastrana DV, Tolstov YL, Becker JC, Moore PS, Chang Y, Buck CB. Quantitation of human seroresponsiveness to Merkel cell polyomavirus. *PLoS Pathog.* 2009;5:e1000578.

13. Cudré-Mauroux C, Occhiodoro T, König S, Salmon P, Bernheim L, Trono D. Lentivector-mediated transfer of Bmi-1 and telomerase in muscle satellite cells yields a Duchenne myoblast cell line with long-term genotypic and phenotypic stability. *Hum Gene Ther.* 2003;14:1525-1533.
14. Uil TG, de Vrij J, Vellinga J, Rabelink MJ, Cramer SJ, Chan OY, Pugnali M, Magnusson M, Lindholm L, Boulanger P, Hoeben RC. A lentiviral vector-based adenovirus fiber-pseudotyping approach for expedited functional assessment of candidate retargeted fibers. *J Gene Med.* 2009;11:990-1004.
15. Ramkisoensing AA, Pijnappels DA, Swildens J, Goumans MJ, Fibbe WE, Schalijs MJ, de Vries AA, Atsma DE. Gap junctional coupling with cardiomyocytes is necessary but not sufficient for cardiomyogenic differentiation of cocultured human mesenchymal stem cells. *Stem Cells.* 2012;30:1236-1245.
16. Ramkisoensing AA, de Vries AA, Schalijs MJ, Atsma DE, Pijnappels DA. Brief report: Misinterpretation of coculture differentiation experiments by unintended labeling of cardiomyocytes through secondary transduction: delusions and solutions. *Stem Cells.* 2012;30:2830-2834.
17. Suzuki K, Bose P, Leong-Quong RY, Fujita DJ, Riabowol K. REAP: A two minute cell fractionation method. *BMC Res Notes.* 2010;3:294.
18. Gonda DK, Bachmair A, Wüning I, Tobias JW, Lane WS, Varshavsky A. Universality and structure of the N-end rule. *J Biol Chem.* 1989;264:16700-16712.
19. Kozak M. Point mutations define a sequence flanking the AUG initiator codon that modulates translation by eukaryotic ribosomes. *Cell.* 1986;44:283-292.
20. McCaughan KK, Brown CM, Dalphin ME, Berry MJ, Tate WP. Translational termination efficiency in mammals is influenced by the base following the stop codon. *Proc Natl Acad Sci USA.* 1995;92:5431-5435.
21. Sinkovics JG. Horizontal gene transfers with or without cell fusions in all categories of the living matter. *Adv Exp Med Biol.* 2011;714:5-89.
22. Grzeschik KH. The role of somatic cell genetics in human gene mapping. *Experientia.* 1986;42:1128-1137.
23. Sanges D, Lluís F, Cosma MP. Cell-fusion-mediated reprogramming: pluripotency or transdifferentiation? Implications for regenerative medicine. *Adv Exp Med Biol.* 2011;713:137-159.

24. Serov OL, Matveeva NM, Khabarova AA. Reprogramming mediated by cell fusion technology. *Int Rev Cell Mol Biol.* 2011;291:155-190.
25. Köhler G, Milstein C. Continuous cultures of fused cells secreting antibody of predefined specificity. *Nature.* 1975;256:495-497.
26. Maguire CA, Bovenberg MS, Crommentuijn MH, Niers JM, Kerami M, Teng J, Sena-Esteves M, Badr CE, Tannous BA. Triple bioluminescence imaging for *in vivo* monitoring of cellular processes. *Mol Ther Nucleic Acids.* 2013;2:e99.
27. Hall MP, Unch J, Binkowski BF, Valley MP, Butler BL, Wood MG, Otto P, Zimmerman K, Vidugiris G, Machleidt T, Robers MB, Benink HA, Eggers CT, Slater MR, Meisenheimer PL, Klaubert DH, Fan F, Encell LP, Wood KV. Engineered luciferase reporter from a deep sea shrimp utilizing a novel imidazopyrazinone substrate. *ACS Chem Biol.* 2012;7:1848-1857.
28. Tannous BA. *Gaussia* luciferase reporter assay for monitoring biological processes in culture and *in vivo*. *Nat Protoc.* 2009;4:582-591.
29. Ignowski JM, Schaffer DV. Kinetic analysis and modeling of firefly luciferase as a quantitative reporter gene in live mammalian cells. *Biotechnol Bioeng.* 2004;86:827-834.

Chapter 3

Evaluating the Biodegradability of Gelatin/Siloxane/ Hydroxyapatite (GS-Hyd) Complex *in vivo* and its Ability for Adhesion and Proliferation of Rat Bone Marrow Mesenchymal Stem Cells

Zeinab Neshati, Ahmad Reza Bahrami, Hossein Eshtiagh-Hosseini,
Maryam M. Matin, Mohammad Reza Housaindokht, Taymaz Tabari,
Mohammad Amin Edalatmanesh

Cytotechnology. 2012;64:485-495.

Abstract

Recent studies have shown that the use of biomaterials and new biodegradable scaffolds for repair or regeneration of damaged tissues is of vital importance. Scaffolds used in tissue engineering should be biodegradable materials with three-dimensional structures, which can guide the growth and differentiation of the cells. They also should possess physical, chemical and biological properties that allow efficient supply of the cells to target tissues and have proper porosity along with minimal toxic effects. In this study, Gelatin/Siloxane/Hydroxyapatite (GS-Hyd) scaffold was synthesized and its morphology, *in vivo* biodegradability, cytotoxic effects and ability for cell adhesion were investigated using mesenchymal stem cells (MSCs). The cells were treated with different volumes of the scaffold suspension to evaluate its cytotoxic effects. The MSCs were also seeded on scaffolds and cultured for 2 weeks for assessing the scaffold's ability to promote cell adhesion and proliferation. To check the biodegradability of the GS-Hyd complex *in vivo*, scaffolds were implanted into the thigh muscle, testicle, and liver of rats and analyzed at 3, 7, 16 and 21 days after implantation by scanning electron microscopy (SEM) and weighing. The viability studies showed that the GS-Hyd scaffold exerted no cytotoxic effects on the cells and that the MSCs readily adhered to the scaffold with the expansion of their elongations and the formation of colonies. The rate of scaffold degradation as assessed by weighing was significant within each group at some time points along with significant differences between different tissues at the same time point. SEM micrographs indicated obvious changes at the surface of the scaffold particles and in the diameter of their pores through different stages of implantation. At 21 days after implantation the loss of scaffold was highest in the muscle and lowest in the liver.

Keywords

Tissue engineering, Gelatin/Siloxane/Hydroxyapatite scaffold, Biodegradability, Mesenchymal stem cells, Tissue regeneration

Introduction

Several strategies are employed to compensate for the loss of functional tissue in incurable diseases including cell, tissue and organ transplantation, surgical reconstruction, synthetic prostheses, and medical devices. However, each of these treatments, suffers from some problems or limitations. For example, organ transplantation is limited by donor shortage and usually requires lifelong consumption of immunosuppressive drugs, which may cause severe complications.¹ Although the other therapies are not limited by supply, they also have limitations. For example, synthetic prostheses and medical devices are generally not able to replace all the functions of damaged, diseased or lost tissue.

Tissue engineering has emerged as an expanding approach to address these problems and is now a major component of regenerative medicine.²⁻⁴ By combining engineering principles with material science and molecular biology, investigators seek to create novel constructs that will fully integrate into the host system and restore function of the lost tissues.⁵ The general principle of cell-based tissue engineering involves combining living cells with a natural/synthetic support or scaffold.⁶ The main roles of the porous three-dimensional (3D) scaffolds are to give structural support and to provide an optimal environment for the cells contained inside. Following their isolation from healthy tissue and *in vitro* expansion, the cells should adhere to the scaffold in all three dimensions, proliferate, differentiate and secrete their own extracellular matrices (ECMs), gradually replacing the scaffold.^{4,7} Therefore, in addition to permitting cell adhesion, promoting cell growth, and allowing retention of differentiated cell functions, the scaffold should be biocompatible, biodegradable, highly porous with a large surface to volume ratio, able to facilitate the necessary crosstalk with surrounding cells, mechanically strong, and capable of being formed into desired shapes with considerable stability.⁸⁻¹¹

A variety of hydrolytically degradable polymers have been developed for scaffold applications in tissue engineering. The majority of these polymers are composed of linear aliphatic polyesters with a high molecular weight and their copolymers. These materials often possess mechanical properties best suited for engineering of hard tissues.¹²⁻¹⁷ However, for engineering of soft tissues, flexible scaffolds are desirable.¹⁸ The biomaterials used to construct these porous scaffolds include synthetic biodegradable polymers such as polyglycolic acid (PGA), polylactic acid

(PLA), and their copolymer poly DL-lactic-co-glycolic acid (PLGA), and also polymers derived from natural materials such as collagen and inorganic hydroxyapatite.^{17,19,20} In this study, the GS-Hyd complex was synthesized by combining Gelatin, Siloxane and hydroxyapatite as will be explained below. Hydroxyapatite, mainly in a carbonated form, is the major inorganic constituent of natural bone.^{21,22} Synthetically made hydroxyapatite ($\text{Ca}_5(\text{PO}_4)_3(\text{OH})$) has long been used in medicine and dentistry due to its ability to chemically attach to bone. It has been used as a hard tissue replacement, usually in the form of fillers (pastes, powders), or as a bioactive agent in polymer composites.²¹ Pure, stoichiometrical hydroxyapatite is the least degradable form of calcium phosphate.²³ Often, other more soluble mineral phases of apatite are preferred as bone-substitute materials in order to combine calcium-ion release properties with chemical stability of the support.²⁴⁻²⁶ Amongst those are non-stoichiometrical hydroxyapatite (calcium-deficient hydroxyapatite (CDHA)), β -tricalcium phosphate (β -TCP), octacalcium phosphate (OCP), or biphasic hydroxyapatite (BCP, various hydroxyapatite/ β -TCP ratios).²⁴⁻²⁷ A number of synthetic routes towards the preparation of biologically active calcium phosphates, including different templating approaches, have been reported.²⁸⁻³² The presence of silica in many biocompatible and bioactive materials has generally been shown to improve their bioactivity.^{33,34} Studies show that introduced or already present silanol groups provide good nucleation sites for hydroxyapatite.³⁵ Silica is also one of the vital components in bioglass, but is also used in polymer composites and thin films.³⁶⁻⁴⁰ In addition, natural polymers like collagen, gelatin and chitosan are osteoconductive and biodegradable components that have been used in fabrication of scaffold materials for tissue engineering.^{41,42} Thus, combining these natural polymers with the inorganic species mentioned above may yield biodegradable and bioactive scaffolds for tissue engineering.⁴³ Scaffolds are normally analyzed by scanning electron microscopy (SEM) for their pore sizes, internal connections, and physical appearances. In the scaffold biodegradability process, both *in vitro* and *in vivo*, the pore diameters and volume of the scaffolds can be determined by SEM.⁴⁴

Development of a viable construct also requires a suitable supply of cells that are ideally non-immunogenic, highly proliferative, easy to harvest and have the ability to differentiate into a variety of cell types with specialized functions.⁴⁵⁻⁴⁷ Possible candidates for such purpose are bone marrow-derived mesenchymal stem cells (BM-MSCs), which have the potential to differentiate into various types of

mesenchymal tissues, including osteoblasts, chondroblasts, myoblasts and fibroblasts.⁴⁸ They are present in large quantities in animal and human bodies, can be easily obtained, and greatly expanded *in vitro*.^{49,50} Moreover, BM-MSCs are hypoimmunogenic cells that do not induce immune system response⁵¹ and have been successfully used to promote repair of different connective tissues, such as bone,⁵² cartilage,⁵³ tendon,⁵⁴ and ligament.⁵⁵ We have also shown in our previous studies, the capacity of MSCs to differentiate into insulin-producing and neural cells in animal models of diabetes and Huntington's disease, respectively.^{56,57}

In this study, the GS-Hyd complex was synthesized and the three main questions relevant for its use as scaffold were studied, *i.e.* (a) whether it affects cell viability, (b) whether it supports the cell adhesion and proliferation, and (c) whether it is biodegradable *in vivo*.

Materials and Methods

Scaffold preparation

Starting materials used in this investigation for synthesis of the scaffold, including analytical grade calcium nitrate tetrahydrate ($\text{Ca}(\text{NO}_3)_2 \cdot 4\text{H}_2\text{O}$), phosphoric pentoxide (P_2O_5) and tetraethoxyorthosilicate (TEOS) were purchased from Aldrich, Germany. All materials were used as received, without further purification.

Solutions of P_2O_5 (0.5 mol/L (absolute ethanol)) and solution of $\text{Ca}(\text{NO}_3)_2 \cdot 4\text{H}_2\text{O}$ (1.67 mol/L (absolute ethanol)) were prepared. They were mixed together in a Ca/P molar ratio of 1.67 to generate a calcium phosphate precursor solution. The mixture was then continuously stirred about 10 min at ambient temperature, followed by heating in a water bath at 60 °C for 1 h. A 12.5% solution of gelatin was prepared by dissolution in 0.1 M HCL. Addition of appropriate amount of calcium phosphate precursor solution to the gelatin solution resulted in the hybrid solution. After this ripening process, 5 ml TEOS was added to the mixture under continuous stirring, corresponding to 60% SiO_2 in the final SiO_2 /calcium phosphate material. The obtained gel was aged at room temperature for 20 h before calcination at 550 °C for 8 h (heating rate 1 K min⁻¹), to remove all organics from the material.

Animals

In all experiments, male Wistar rats with an average weight of 250 g were used. Rats were kept at standard conditions and subjected to 12-hour cycles of light and darkness.

BM-MSCs extraction and culture

Bone marrow (BM) was obtained from the femurs and tibias of rats. BM was flushed into Dulbecco's Modified Eagle's Medium (DMEM, Gibco, Scotland) supplemented with 15% fetal bovine serum (FBS, Gibco, Scotland), 100 units/ml penicillin, and 100 µg/ml streptomycin (Biosera, UK) and incubated in a humidified incubator at 37 °C with 5% CO₂. When cultures reached about 80% confluency, they were washed with phosphate-buffered saline (PBS) followed by a 5 min incubation with 0.05% trypsin solution at 37 °C. Cells were split weekly at a ratio of 1:3.

Cytotoxicity assay of GS-Hyd

5×10^3 of MSCs at passage 3 were seeded in each well of 96-well microplates and incubated for 48 h at 37 °C. Then, 80 mg of powdered scaffold was dissolved in 2 ml DMEM supplemented with 15% FBS, and cells were exposed to various volumes of the resulting GS-Hyd suspension (2, 4, 8, 16, 32, 64, 128 and 200 µl), with three repeats for each volume. Cells cultured in DMEM supplemented with 15% FBS without GS-Hyd were used as controls. Total volume in each well was 200 µl. The effect of GS-Hyd on cell viability was measured by 3-[4,5-dimethylthiazol-2-yl]-2,5-diphenyl tetrazolium bromide (MTT, Merck, Germany) staining. MTT assay was performed after 48 h of treatment. Cells in each well were incubated in 20 µl MTT solution (5 mg/ml MTT in PBS) for 4 h at 37 °C. The intense purple-colored formazan derivative formed via cell metabolism was then dissolved in 200 µl/well dimethylsulfoxide (DMSO, Merck, Germany) and the absorbance was measured at 570 nm by ELISA plate reader (Awareness Technology, USA). The cell viability in the presence of different volumes of GS-Hyd was calculated using the following formula: absorbance of each treated well/mean absorbance of control wells \times 100. The average cell viability for each volume of GS-Hyd was then calculated and presented in a graph using Microsoft Excel.

Seeding of MSCs on GS-Hyd scaffold

MSCs at passage 3 were trypsinized and suspended in DMEM followed by counting with a hemocytometer. The cell suspension was then centrifuged at $67.2 \times g$ for 5 min and the pellet was resuspended in DMEM, supplemented with 15% FBS, 100 units/ml penicillin and 100 $\mu\text{g/ml}$ streptomycin at a concentration of 10^7 cells/ml. After the scaffold had been cut into small pieces (5 mm \times 3 mm) and sterilized by autoclaving, the GS-Hyd pieces were placed on agarose-coated (1% agarose in sterile H_2O) 6-well culture plates (3 scaffolds/well), and divided into two test and control groups. The scaffolds received 100 μl medium without cells served as controls, while each scaffold in the test group was seeded with 10^6 cells in 100 μl medium. The scaffolds were incubated for 4 h in a humidified atmosphere at 37 $^\circ\text{C}$ and 5% CO_2 to allow cell attachment. Then 3 ml of the medium was added to each well and the scaffolds were incubated for 2 weeks. The medium was replaced every 2–3 days. On days 1, 7 and 14 the scaffolds were collected to be evaluated for cell attachment by SEM.

Preparation of the cell-seeded scaffolds for SEM

Scaffolds were fixed in 3% buffered glutaraldehyde for 24 h, dehydrated with a graded ethanol series, and dried. The dried samples were mounted on aluminum stubs and sputter-coated (SC7620 sputter coater) with gold for 2 min. SEM was used to take micrographs of the samples. The GS-Hyd scaffold was characterized mainly by Fourier transform infrared spectroscopy (FTIR), differential thermal analysis (DTA), and transmission electron microscopy (TEM). Simultaneous DTAs were carried out in the range of 20–1,000 $^\circ\text{C}$ in a Netzsch STA 409 $^\circ\text{C}$ instrument under air and at the rate of 10 $^\circ\text{C}/\text{min}$.

Preparation of scaffold for in vivo implantation

Another series of scaffolds were cut in small segments (5 mm \times 3 mm), submerged in 70% ethanol for 30 min, and washed with PBS. The scaffolds were then kept in PBS until the start of the surgery. Scaffolds were polished on the edges to ensure that they were not sharp. The weight of the scaffolds was recorded before the ethanol wash and placement in the PBS.

Preparation of animals for implantation surgery

All tests and experimental protocols were approved by the Ethics Committee of Ferdowsi University of Mashhad. Animals were anesthetized by a mixture of ketamine hydrochloride (100 mg/kg) and xylazine (5 mg/kg). The regions for the surgery (thigh muscle, testicles and liver) were sterilized with 70% ethanol after shaving.

For implantation of the scaffold in thigh muscle, a deep incision of 1 cm along the length of the muscle was made with a scalpel. Next, tampons were used to stop bleeding. If bleeding persisted, the site of incision was cauterized. The scaffold was then gently lowered in between the muscle fibers. After this step, the muscle was stitched layer by layer towards the surface. To implant the scaffold in a testicle, an incision was made in the scrotum. One of the testicles was exposed, and without applying too much pressure to the testicle, a hole with the exact size of the scaffold was made by scalpel. The scaffold was subsequently placed in the testicle and the testis and scrotum were stitched. For implantation of the scaffold in the liver, a deep incision of about 1 cm was made below the right side of the rib cage, until the visceral peritoneum of the liver appeared. Then, a small hole was made in the liver and the scaffold was placed inside and the peritoneum layers and skin were stitched separately.

At the end of each surgical procedure, the stitched tissues were sterilized with betadine and Lidocaine gel was applied to numb them. As extra measure against possible infections, every rat was injected intraperitoneally with 5,000 unit/kg penicillin. After surgery, the animals were moved to a recovery cage to regain their consciousness in a warm blanket. The conditions of the rats was monitored by checking their breathing, taking their pulse and measuring their body temperature. When the rats showed normal vital signs and movements, they were returned to their original cage.

Degradation assay of GS-Hyd

To analyze the degradability of the scaffold by weight changes, 3 rats per scaffold implantation site were anaesthetized at 3, 7, 16, and 21 days after implantation, and the scaffolds were removed from their bodies. On these days, the anatomical condition and histology of the surgery site were carefully studied. When each scaffold was removed from the body, it was immediately washed with normal saline

to remove blood and extra tissues. Each scaffold was placed into a separate test tube with specific identification number. The test tubes were then placed in oven at 50 °C for 30 min. After the scaffolds were completely dried, they were weighed with a sensitive electronic scale. The weight of the scaffolds after explantation were compared to their weight prior to surgery and the percentile weight loss was recorded. To check the rate of degradation using SEM, scaffold samples from each part of the body (thigh muscle, testicle and liver) were prepared using the same procedure. The number of connections between the pores of the scaffolds and the diameter and dispersion of the pores were assessed as indicators of scaffold degradation.

Statistical analysis

Data were analyzed using one way ANOVA. All group comparisons were analyzed using Tukey's *post hoc* test to determine which groups were significantly different from each other. *P* values ≤ 0.05 were considered to indicate statistical significance.

Results

Chemical and structural characteristics of GS-Hyd scaffold

GS-Hyd scaffold showed sharp absorption bands in FTIR that were attributed to hydroxyapatite: 3th vibration of PO_4^{3-} ($\nu_3\text{PO}_4^{3-}$) at 1,045–1,092 cm^{-1} and $\nu_2\text{PO}_4^{3-}$ at 474 cm^{-1} , $\nu_1\text{PO}_4^{3-}$ symmetric stretch at 963 cm^{-1} , $\nu_4\text{PO}_4^{3-}$ bending at 602 and 572 cm^{-1} . The broad absorption bands at 3,100–3,600 cm^{-1} belonged to OH stretching absorption bands. Extensive absorption around 630 cm^{-1} (structural OH stretching) was attributed to hydroxyapatite's crystalline structure. The silica layer showed weak absorption bands around 800 cm^{-1} corresponding to the Si–O–Si bonds. Some of the silica absorption bands were hard to identify due to stronger, overlapping absorption bands from hydroxyapatite. That is especially true in the area around 1,185 and at 1,000–1,085 cm^{-1} where the Si–O–Si vibration bands usually are the strongest, but also around 960 cm^{-1} where the Si–OH silanol groups absorb (data not shown).

Figure 1 shows the thermogram corresponding to simultaneous DTA at 70 °C/24 h. In the DTA curve of the precursor GS-Hyd scaffold (Figure 1), after dried in 70 °C, exothermic peaks assignable to organic combustion are visible. In order to

discard the presence of water occluded in the exhaustively dried sample after 150 °C, a simultaneous DTA was carried out due to its considerably higher sensibility. DTA showed the combustion peak of residual gelatin at 320 °C, and a very low peak at 590 °C. It can thus be concluded that the microporosity observed after calcination is originated by the elimination of gelatin macromolecules forming microdomains in the silica matrix.

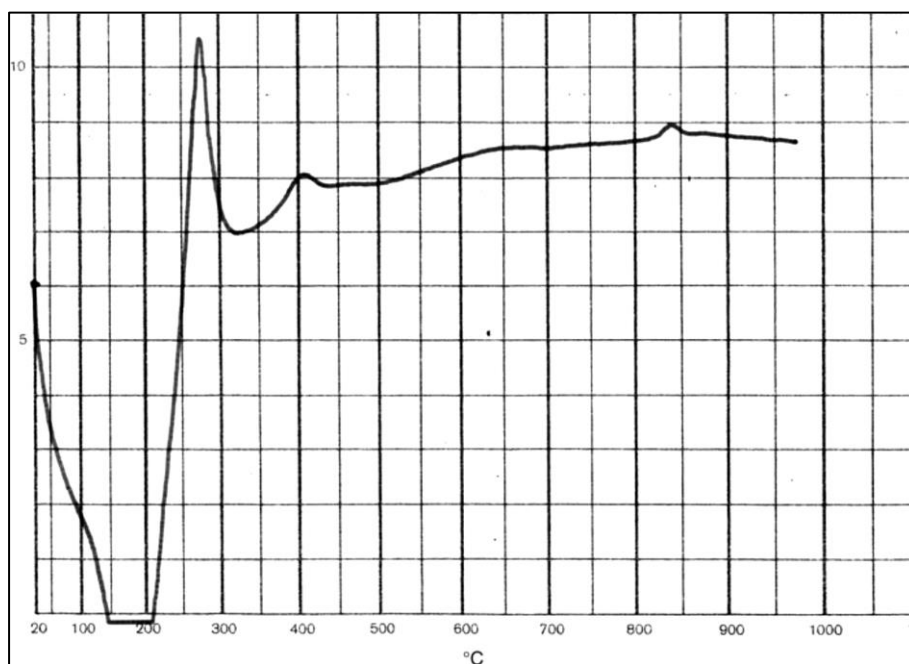


Figure 1. DTA thermogram of GS-Hyd.

The simple one-pot synthesis method resulted in a fairly homogeneous distribution of the mesoporous silica throughout the apatite crystal surface as demonstrated by the TEM micrograph (Figure 2). The crystalline size of the GS-Hyd scaffold is about 50 nm. This could be the reason for even distribution of hydroxyapatite over the surface of silica matrix. On the other hand, the material lacks a well-pronounced mesoporous long-range order in the silica layer.

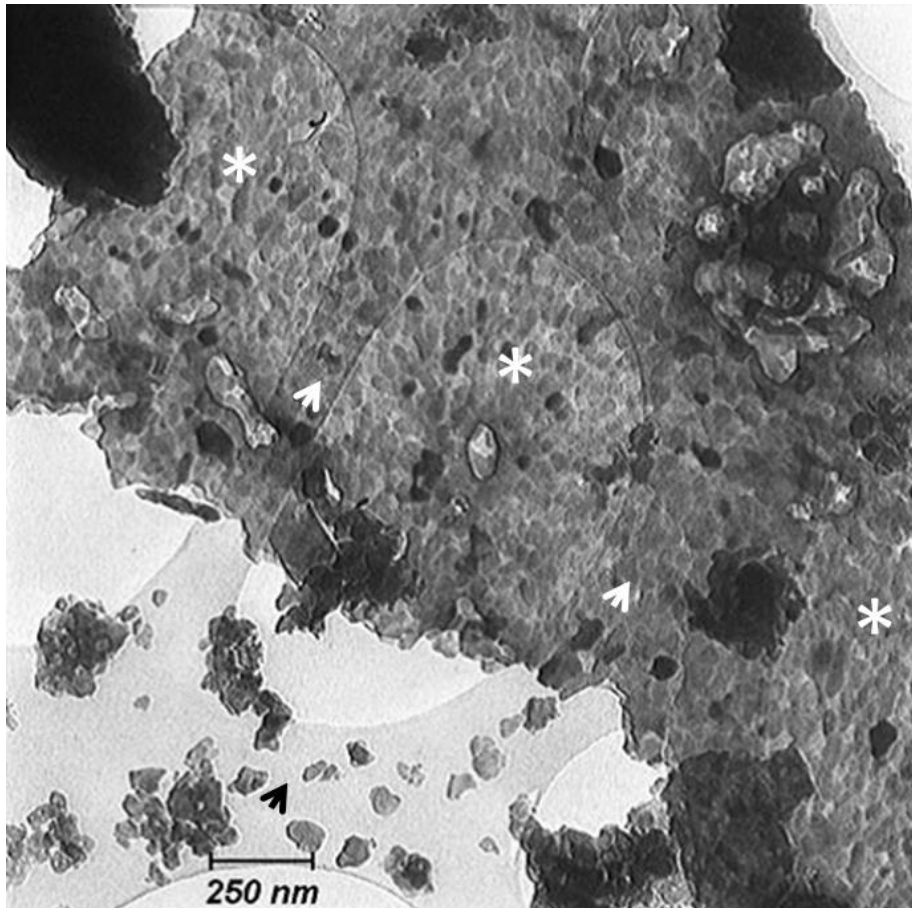


Figure 2. TEM image of GS-Hyd showing the great growth of hydroxyapatite (arrows) and the deposition of silica among its pores (asterisks).

Homing of MSCs in GS-Hyd scaffolds

As mentioned previously, to investigate the biocompatibility of the GS-Hyd complex, scaffolds were seeded with 10^6 BM-MSCs and scaffolds without cells served as negative controls (Figure 3). On days 1, 7 and 14 after cell seeding, scaffolds were collected to be evaluated for cell attachment and proliferation by SEM. Cells were round shaped at the time of seeding (not shown) but adhered to the scaffold, expanded their elongations and obtained a fibroblast-like appearance within 24 h (Figure 4). Moreover, during their cultivation on scaffolds, the BM-MSCs proliferated resulting in the formation of colonies (Figure 5).

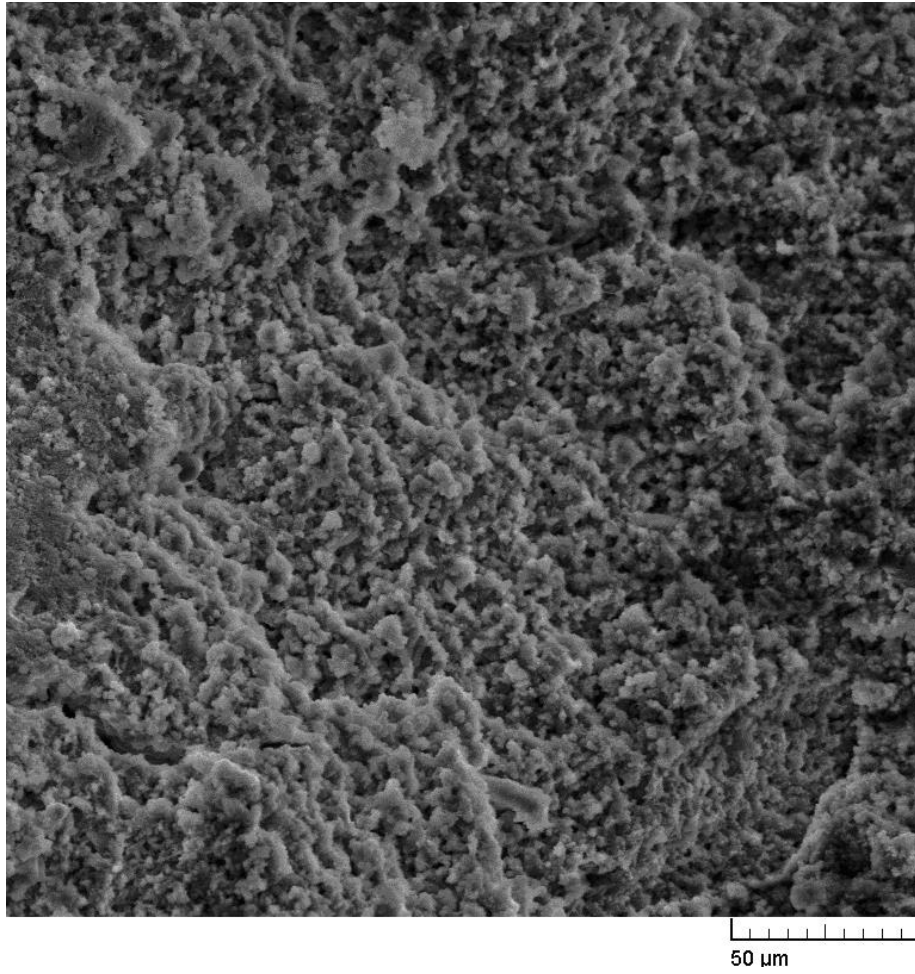


Figure 3. SEM micrograph showing the morphology of the GS-Hyd scaffold without cells.



Figure 4. SEM micrograph showing scattered distribution of MSCs on the surface of the scaffold 24 h after cell seeding.

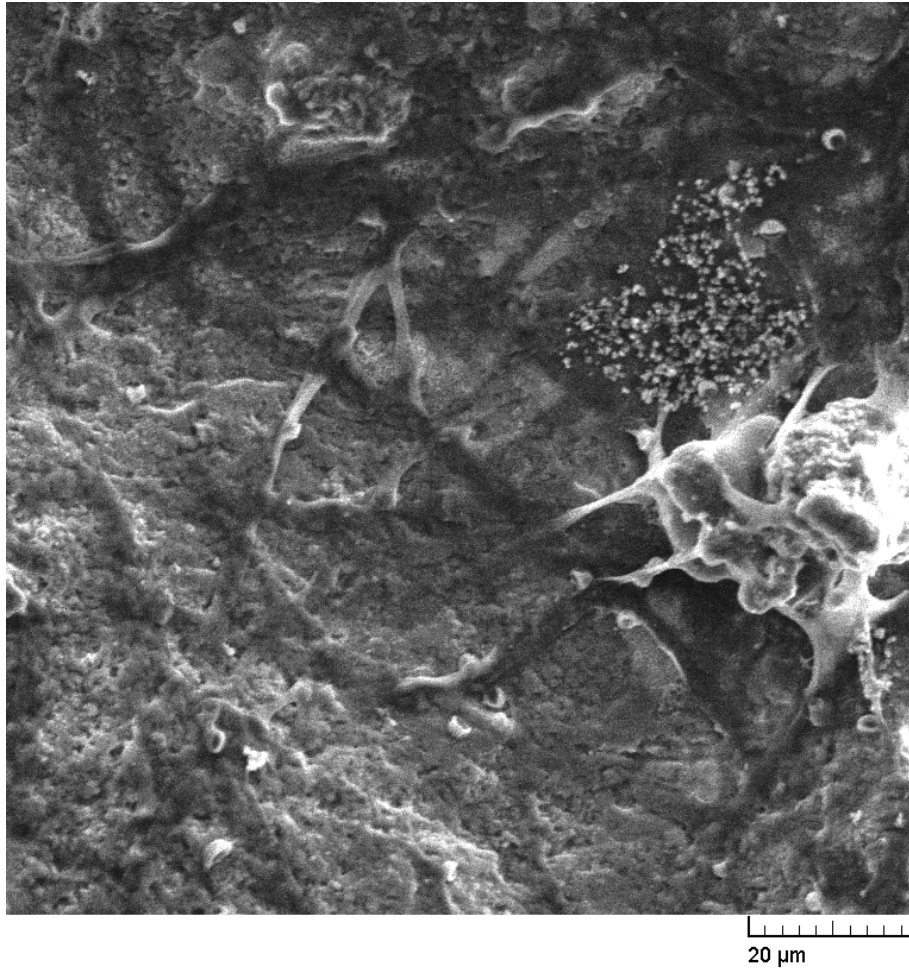


Figure 5. SEM micrograph showing MSC proliferation and colony formation on the scaffold, 7 days after cell seeding.

Cytotoxicity of GS-Hyd scaffold

The MTT assay is a colorimetric method for measuring the activity of enzymes that reduce the colorless MTT to purple colored formazan dyes. Its main application is assessment of the viability and the proliferation of cells. It can also be used to determine cytotoxicity of potential medicinal agents and toxic materials, since those agents would stimulate or inhibit cell viability and growth.

The MTT assay showed that GS-Hyd has no detectable cytotoxic effects on the cells up to concentration of 25.6 mg/ml (128 μ l). Cell viability decreased only at the highest amount of GS-Hyd (200 μ l) as shown in Figure 6.

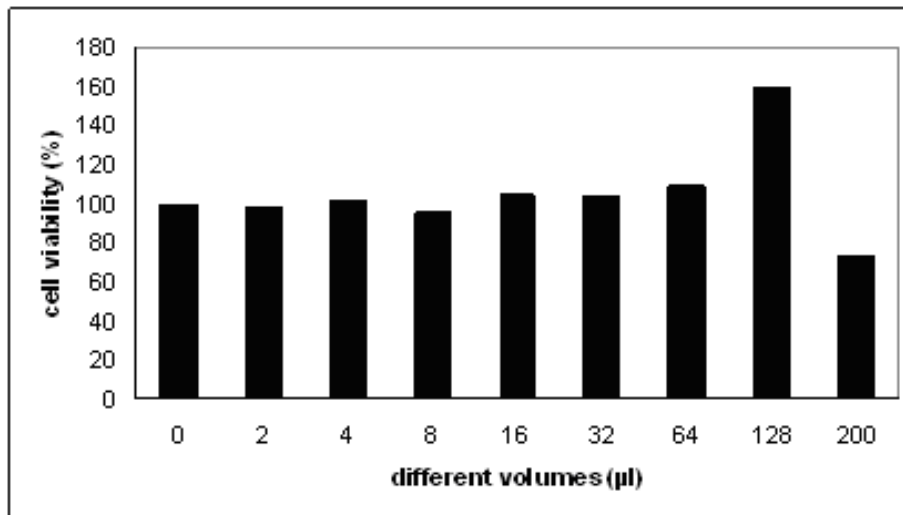


Figure 6. Effects of different volumes of GS-Hyd suspension on the viability of MSCs as measured by MTT assay.

In vivo degradability of GS-Hyd scaffold

The degradation rate of scaffolds implanted at different sites was determined by weighing them following their explantation at 3, 7, 16 and 21 days after transplantation. The weight reduction at day 3 significantly differed from those at day 16 and 21 for scaffolds in all three anatomical sites, but the differences between other days were not significant. At day 7, the differences between thigh muscle and liver ($P < 0.0001$) and between liver and testis were significant ($P < 0.001$), but there was no significant difference between thigh muscle and testicle. The differences between different tissues at other time points were significant (Figure 7).

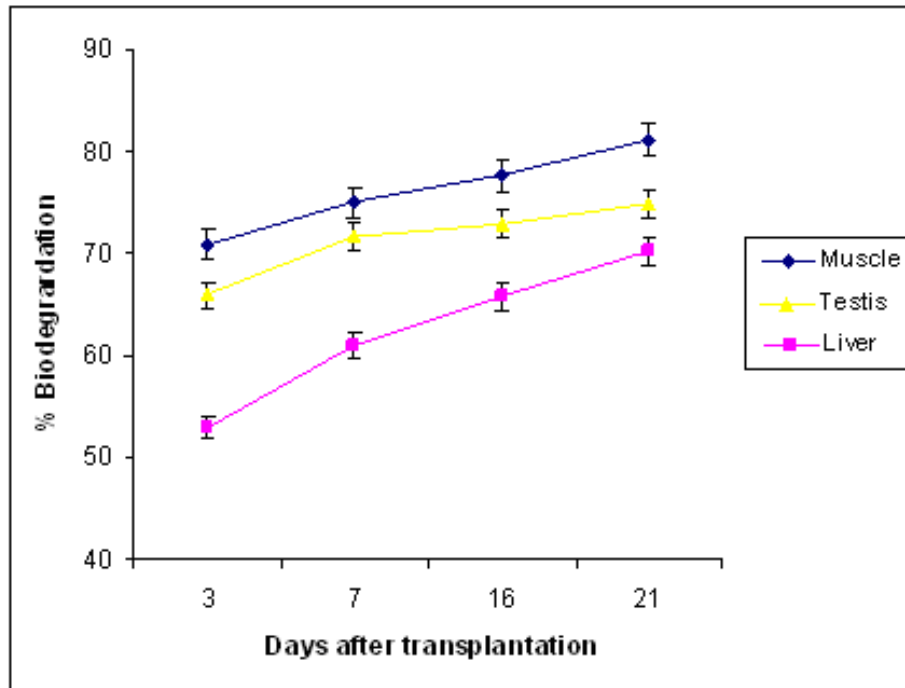


Figure 7. Comparison of the rate of scaffold degradation in various anatomical positions on different days after implantation. There are significant differences in each group during the time period and between groups at the same time point. Vertical bars indicate means \pm SEM in rats of each group at each measurement ($n = 3$, $P \leq 0.05$).

Structural changes of GS-Hyd scaffolds following in vivo implantation

Transplanted GS-Hyd particles underwent clear time-dependent morphological changes on their surface as evinced by SEM micrographs of scaffolds explanted at different times after implantation (Figure 8). These changes in surface structure were accompanied by an increase in diameter of the pores. Consistent with the results presented in Figure 7, degradation of the GS-Hyd scaffold at 21 days post implantation was highest in the thigh and lowest in the liver (Figure 8, B–D).

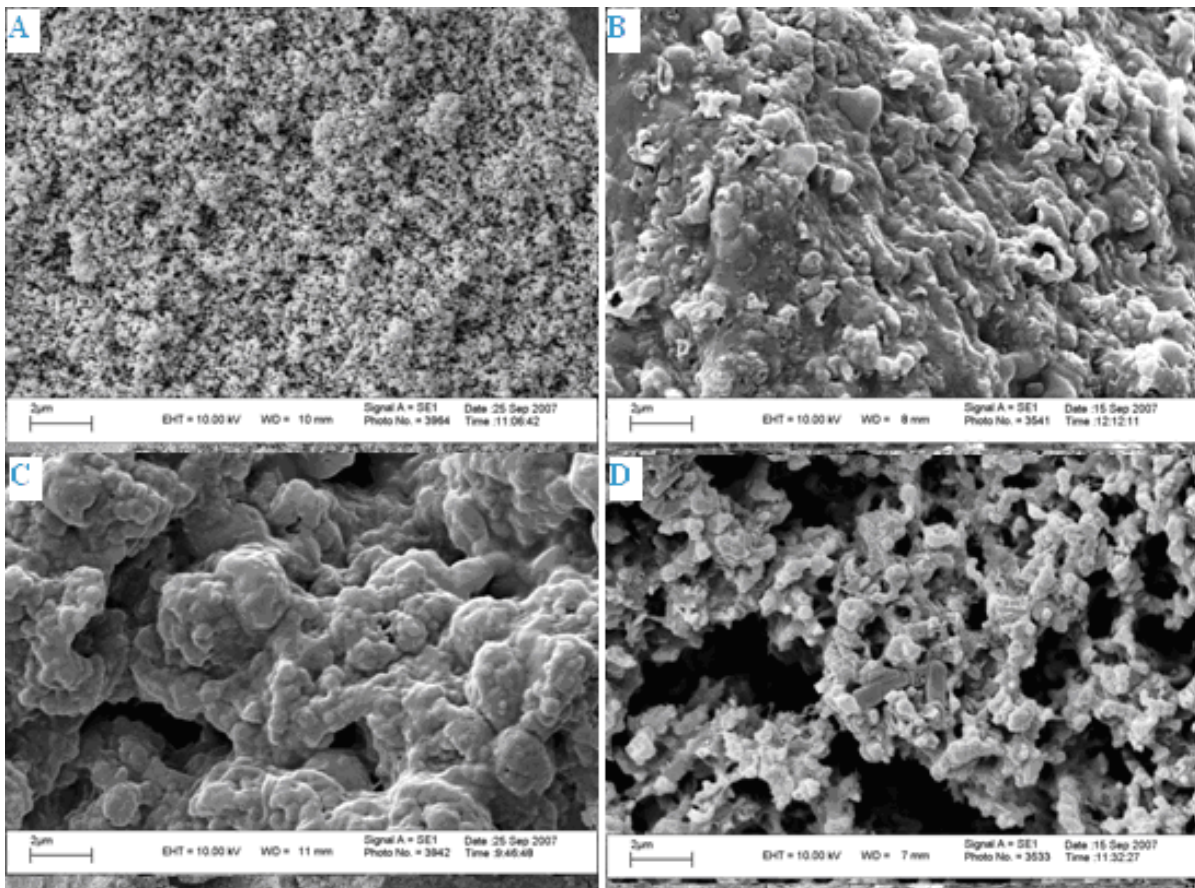


Figure 8. SEM micrographs of the scaffold before (A) and after (B–D) implantation in the liver (B), testicle (C) and thigh muscle (D).

Discussion

One of the main problems in cell therapy is homing of the cells and their maintenance in desired areas, which may be overcome by growing the cells on scaffolds followed by their transplantation at the target sites. The major concerns in applying external scaffolds in tissue engineering are severe immune responses, persistence to degradation, and unexpected side effects. As mentioned before (1) the specific material composition of the scaffold and (2) the cell source are two important elements, which can substantially affect the outcome of tissue engineering.⁵ Application of biodegradable materials is a vital factor in tissue engineering.⁵⁸ Scaffolds should also be mechanically strong, capable of being formed into desired shapes, non-cytotoxic and highly porous for permitting cell adhesion and growth.^{8,9} Development of such an efficient scaffold also involves a

suitable supply of cells such as MSCs, which, due to their specific properties, are attractive candidates for clinical applications. For example, Liu and colleagues cultured anterior cruciate ligament fibroblasts (ACLFs) and BM-MSCs on combined silk scaffolds to determine which of these two cell types would be best suited for ligament tissue engineering applications. Their preliminary results demonstrated that BM-MSCs are superior to ACLFs, with respect to cell proliferation and *in vivo* survival.⁵⁹ Moreover, the safety of MSCs for *in vivo* applications has been shown by numerous studies in animals and humans and the clinical use of MSCs is not associated with major ethical concerns unlike the therapeutic use of embryonic stem cells (ESCs). Although some studies have shown a promotion of tumor growth and metastasis after implantation of MSCs, tumor induction is mostly described for embryonic stem cells (ESCs).^{60,61}

Cell adhesion to substrate is known to affect cell behavior and function in both natural and engineered tissues and plays a key role in morphogenesis and organogenesis.^{62,63} In this study, we used MSCs as candidate stem cells and GS-Hyd scaffold as a cell carrier for adhesion and proliferation of the cells *in vitro*. GS-Hyd is a 3D scaffold which did not show any cytotoxic effects and preserved the cell viability *in vitro*. GS-Hyd also promoted cell adhesion and proliferation. Considering the fact that cells were round shaped at the day of seeding (not shown) but could expand their elongations and obtained a fibroblast-like appearance within 24 h (Figure 4), we conclude that MSCs very well adhere to the GS-Hyd scaffold. Moreover, the fact that more cells were visible on the scaffolds at day 7 than day 2 post seeding and the observation that the MSCs had formed colonies after 7 days of cell seeding indicate that the GS-Hyd complex supports cell proliferation (Figures 3, 4 and 5). The interconnected pores of the scaffold may further promote cellular adherence. Additionally, the pore size (1–2 μm) of the scaffolds seems to be large enough to allow medium flow which would provide ideal conditions for cell proliferation on the scaffolds.

The composition of the scaffold and the speed of scaffold degradation in its biological environment, are important factors for their applicability *in vivo*. However, this is not the case for GS-Hyd scaffold, because its rate of degradation can be manipulated during the synthesis. In previous studies on similar scaffolds, they were kept in the body of rats for 30–90 days after surgery.^{64,65} In our study, we implanted and kept the scaffolds for 21 days. During this period, the speed of scaffold

degradation was much higher shortly after implantation than at later times. This could be explained by the fact that gelatin, the main component of the scaffold, is easily degraded and could hence account for the major weight lost observed in the beginning. However, additional experiments are required to identify the cause(s) for the large loss in scaffold weight early after *in vivo* implantation. At 21 days after implantation about 30% of the initial weight of the scaffolds remained. The SEM analyses revealed that the loss of scaffold weight is accompanied by the disappearance of the interconnections between pores inside the scaffold which suggests a direct link between compound degradation and inter-junction loss. Structural degradation rates at the three examined anatomical sites proved that the degradative capacities are tissue-specific and according to our SEM micrographs the thigh muscle has the highest capacity for the scaffold degradation. During the whole *in vivo* study, the rats did not display any signs of scaffold-related toxicity, other than a mild inflammation.

In conclusion, this study showed that GS-Hyd scaffolds are degraded *in vivo* at rates compatible with their application in tissue engineering. It was also shown that GS-Hyd did not have any cytotoxic effects and also could promote cell adhesion and proliferation *in vitro*, but to reach to a definite conclusion about the toxic effects of the scaffold *in vivo*, further experiments are needed. Therefore, we suggest that GS-Hyd scaffolds can be used for tissue engineering, but still more assays and *in vivo* studies are required to investigate other characteristics of this scaffold which are important for its clinical use.

Acknowledgments

This work was partly supported by grant Sci-1385-21145 from Ferdowsi University of Mashhad, Iran and the GS-Hyd scaffold was filed as a patent (Number 51213).

References

1. Fuchs JR, Nasser BA, Vacanti JP. Tissue engineering: a 21st century solution to surgical reconstruction. *Ann Thorac Surg.* 2001;72:577-591.
2. Langer R, Vacanti JP. Tissue engineering. *Science.* 1993;260:920-926.
3. Nerem RM, Sambanis A. Tissue engineering: from biology to biological substitutes. *Tissue Eng.* 1995;1:3-13.
4. Kim KM, Evans GRD. Tissue engineering: The future of stem cells. In: Ashammakhi N, Reis RL, eds. *Topics in tissue engineering.* USA; 2005:1-21.
5. Katz AJ, Lull R, Hedrick MH, Futrell JW. Emerging approaches to the tissue engineering of fat. *Clin Plast Surg.* 1999;26:587-603.
6. Stock UA, Vacanti JP. Tissue engineering: current state and prospects. *Annu Rev Med.* 2001;52:443-451.
7. Robert L. Matrix biology: past, present and future. *Pathol Biol (Paris).* 2001;49:279-283.
8. Rahaman MN, Mao JJ. Stem cell-based composite tissue constructs for regenerative medicine. *Biotechnol Bioeng.* 2005;91:261-284.
9. Choi YS, Park SN, Suh H. Adipose tissue engineering using mesenchymal stem cells attached to injectable PLGA spheres. *Biomaterials.* 2005;26:5855-5863.
10. Ifkovits JL, Wu K, Mauck RL, Burdick JA. The influence of fibrous elastomer structure and porosity on matrix organization. *PLoS One.* 2010;5:e15717.
11. Soliman S, Sant S, Nichol JW, Khabiry M, Traversa E, Khademhosseini A. Controlling the porosity of fibrous scaffolds by modulating the fiber diameter and packing density. *J Biomed Mater Res A.* 2011;96:566-574.
12. Heller J, Sparer RV, Zentner GM. Poly (ortho esters). In: Chasin M LR, ed. *Biodegradable polymers as drug delivery systems.* New York: Marcel Dekker; 1990:121-161.
13. Agrawal CM, Ray RB. Biodegradable polymeric scaffolds for musculoskeletal tissue engineering. *J Biomed Mater Res.* 2001;55:141-150.
14. Ishaug SL, Crane GM, Miller MJ, Yasko AW, Yaszemski MJ, Mikos AG. Bone formation by three-dimensional stromal osteoblast culture in biodegradable polymer scaffolds. *J Biomed Mater Res.* 1997;36:17-28.

15. Lowry KJ, Hamson KR, Bear L, Peng YB, Calaluce R, Evans ML, Anglen JO, Allen WC. Polycaprolactone/glass bioabsorbable implant in a rabbit humerus fracture model. *J Biomed Mater Res.* 1997;36:536-541.
16. Niklason LE, Gao J, Abbott WM, Hirschi KK, Houser S, Marini R, Langer R. Functional arteries grown *in vitro*. *Science.* 1999;284:489-493.
17. Freed LE, Vunjak-Novakovic G, Biron RJ, Eagles DB, Lesnoy DC, Barlow SK, Langer R. Biodegradable polymer scaffolds for tissue engineering. *Biotechnology (N Y).* 1994;12:689-693.
18. Takahara A, Coury AJ, Hergenrother RW, Cooper SL. Effect of soft segment chemistry on the biostability of segmented polyurethanes. I. *In vitro* oxidation. *J Biomed Mater Res.* 1991;25:341-356.
19. Kim BS, Mooney DJ. Development of biocompatible synthetic extracellular matrices for tissue engineering. *Trends Biotechnol.* 1998;16:224-230.
20. Peter SJ, Miller MJ, Yasko AW, Yaszemski MJ, Mikos AG. Polymer concepts in tissue engineering. *J Biomed Mater Res.* 1998;43:422-427.
21. Dorozhkin SV, Epple M. Biological and medical significance of calcium phosphates. *Angew Chem Int Ed Engl.* 2002;41:3130-3146.
22. Roseberry HH, Hastings AB, Morse JK. X-ray analysis of bone and teeth. *J Biol Chem.* 1931;90:395-407.
23. Klein CP, de Blicke-Hogervorst JM, Wolke JG, de Groot K. Studies of the solubility of different calcium phosphate ceramic particles *in vitro*. *Biomaterials.* 1990;11:509-512.
24. Daculsi G. Biphasic calcium phosphate concept applied to artificial bone, implant coating and injectable bone substitute. *Biomaterials.* 1998;19:1473-1478.
25. LeGeros RZ, Lin S, Rohanizadeh R, Mijares D, LeGeros JP. Biphasic calcium phosphate bioceramics: preparation, properties and applications. *J Mater Sci Mater Med.* 2003;14:201-209.
26. Pasteris JD, Wopenka B, Freeman JJ, Rogers K, Valsami-Jones E, van der Houwen JA, Silva MJ. Lack of OH in nanocrystalline apatite as a function of degree of atomic order: implications for bone and biomaterials. *Biomaterials.* 2004;25:229-238.
27. Koerten HK, van der Meulen J. Degradation of calcium phosphate ceramics. *J Biomed Mater Res.* 1999;44:78-86.

28. Horvath L, Smit I, Sikiric M, Filipovic-Vincekovic N. Effect of cationic surfactant on the transformation of octacalcium phosphate. *J Cryst Growth*. 2000;219:91-97.
29. Koumoulidis GC, Katsoulidis AP, Ladavos AK, Pomonis PJ, Trapalis CC, Sdoukos AT, Vaimakis TC. Preparation of hydroxyapatite via microemulsion route. *J Colloid Interface Sci*. 2003;259:254-260.
30. Sarda S, Heughebaert M, Lebugle A. Influence of the type of surfactant on the formation of calcium phosphate in organized molecular systems. *Chem Mater*. 1999;11:2722-2727.
31. Yan L, Li Y, Deng ZX, Zhuang J, Sun X. Surfactant-assisted hydrothermal synthesis of hydroxyapatite nanorods. *Int J Inorg Mater*. 2001;3:633-637.
32. Yao J, Tjandra W, Chen YZ, Tam KC, Ma J, Soh B. Hydroxyapatite nanostructure material derived using cationic surfactant as a template. *J Mater Chem*. 2003;13:3053-3057.
33. Phan PV, Grzanna M, Chu J, Polotsky A, el-Ghannam A, Van Heerden D, Hungerford DS, Frondoza CG. The effect of silica-containing calcium-phosphate particles on human osteoblasts *in vitro*. *J Biomed Mater Res A*. 2003;67:1001-1008.
34. Porter AE, Best SM, Bonfield W. Ultrastructural comparison of hydroxyapatite and silicon-substituted hydroxyapatite for biomedical applications. *J Biomed Mater Res A*. 2004;68:133-141.
35. Kokubo T, Kim HM, Kawashita M. Novel bioactive materials with different mechanical properties. *Biomaterials*. 2003;24:2161-2175.
36. Ohtsuki C, Kokubo T, Yamamuro T. Mechanism of apatite formation on CaOsingle bondSiO2single bondP2O5 glasses in a simulated body fluid. *J Non-Cryst Solids*. 1992;143.
37. Hench LL. Bioceramics: from concept to clinic. *J Am Ceram Soc*. 1991;74:1487-1510.
38. Hench LL, Splinter RJ, Allen WC, Greenlee TK. Bonding mechanisms at the interface of ceramic prosthetic materials. *J Biomed Mater Res* 1971;5:117-141.
39. Krikorian V, Pochan DJ. Poly (l-lactic acid)/layered silicate nanocomposite: fabrication, characterization, and properties. *Chem Mater*. 2003;15:4317-4324.

40. Villacampa AI, Garcia-Ruiz JM. Synthesis of a new hydroxyapatite-silica composite material. *J Cryst Growth*. 2000;211:111-115.
41. Kang HW, Tabata Y, Ikada Y. Fabrication of porous gelatin scaffolds for tissue engineering. *Biomaterials*. 1999;20:1339-1344.
42. TenHuisen KS, Brown PW. The formation of hydroxyapatite-gelatin composites at 38 degrees C. *J Biomed Mater Res*. 1994;28:27-33.
43. Ren L, Tasura S, Hayakawa A. Synthesis and characterization of gelatin-siloxane hybrids derived through solgel procedure. *Chem Mater Sci*. 2001;21:115-121.
44. Silva TS, Primo BT, Silva Junior AN, Machado DC, Viezzer C, Santos LA. Use of calcium phosphate cement scaffolds for bone tissue engineering: *In vitro* study. *Acta Cir Bras*. 2011;26:7-11.
45. Koh CJ, Atala A. Therapeutic cloning and tissue engineering. *Curr Top Dev Biol*. 2004;60:1-15.
46. Naughton GK. From lab bench to market: critical issues in tissue engineering. *Ann N Y Acad Sci*. 2002;961:372-385.
47. Van Eijk F, Saris DB, Riesle J, Willems WJ, Van Blitterswijk CA, Verbout AJ, Dhert WJ. Tissue engineering of ligaments: A comparison of bone marrow stromal cells, anterior cruciate ligament, and skin fibroblasts as cell source. *Tissue Eng*. 2004;10:893-903.
48. Pittenger MF, Mackay AM, Beck SC, Jaiswal RK, Douglas R, Mosca JD, Moorman MA, Simonetti DW, Craig S, Marshak DR. Multilineage potential of adult human mesenchymal stem cells. *Science*. 1999;284:143-147.
49. Colter DC, Class R, DiGirolamo CM, Prockop DJ. Rapid expansion of recycling stem cells in cultures of plastic-adherent cells from human bone marrow. *Proc Natl Acad Sci U S A*. 2000;97:3213-3218.
50. Jiang Y, Jahagirdar BN, Reinhardt RL, Schwartz RE, Keene CD, Ortiz-Gonzalez XR, Reyes M, Lenvik T, Lund T, Blackstad M, Du J, Aldrich S, Lisberg A, Low WC, Largaespada DA, Verfaillie CM. Pluripotency of mesenchymal stem cells derived from adult marrow. *Nature*. 2002;418:41-49.
51. Amin EM, Reza BA, Morteza BR, Maryam MM, Ali M, Zeinab N. Microanatomical evidences for potential of mesenchymal stem cells in amelioration of striatal degeneration. *Neurol Res*. 2008;30:1086-1090.

52. Bruder SP, Jaiswal N, Ricalton NS, Mosca JD, Kraus KH, Kadiyala S. Mesenchymal stem cells in osteobiology and applied bone regeneration. *Clin Orthop Relat Res.* 1998:S247-256.
53. Fan H, Hu Y, Zhang C, Li X, Lv R, Qin L, Zhu R. Cartilage regeneration using mesenchymal stem cells and a PLGA-gelatin/chondroitin/hyaluronate hybrid scaffold. *Biomaterials.* 2006;27:4573-4580.
54. Ouyang HW, Goh JC, Thambyah A, Teoh SH, Lee EH. Knitted poly-lactide-co-glycolide scaffold loaded with bone marrow stromal cells in repair and regeneration of rabbit achilles tendon. *Tissue Eng.* 2003;9:431-439.
55. Ge Z, Goh JC, Lee EH. The effects of bone marrow-derived mesenchymal stem cells and fascia wrap application to anterior cruciate ligament tissue engineering. *Cell Transplant.* 2005;14:763-773.
56. Edalatmanesh MA, Matin MM, Neshati Z, Bahrami AR, Kheirabadi M. Systemic transplantation of mesenchymal stem cells can reduce cognitive and motor deficits in rats with unilateral lesions of the neostriatum. *Neurol Res.* 2010;32:166-172.
57. Neshati Z, Matin MM, Bahrami AR, Moghimi A. Differentiation of mesenchymal stem cells to insulin-producing cells and their impact on type 1 diabetic rats. *J Physiol Biochem.* 2010;66:181-187.
58. Xie H, Yang F, Deng L, Luo J, Qin T, Li X, Zhou GQ, Yang Z. The performance of a bone-derived scaffold material in the repair of critical bone defects in a rhesus monkey model. *Biomaterials.* 2007;28:3314-3324.
59. Liu H, Fan H, Toh SL, Goh JC. A comparison of rabbit mesenchymal stem cells and anterior cruciate ligament fibroblasts responses on combined silk scaffolds. *Biomaterials.* 2008;29:1443-1453.
60. Arnhold S, Klein H, Semkova I, Addicks K, Schraermeyer U. Neurally selected embryonic stem cells induce tumor formation after long-term survival following engraftment into the subretinal space. *Invest Ophthalmol Vis Sci.* 2004;45:4251-4255.
61. Tang DQ, Cao LZ, Burkhardt BR, Xia CQ, Litherland SA, Atkinson MA, Yang LJ. *In vivo* and *in vitro* characterization of insulin-producing cells obtained from murine bone marrow. *Diabetes.* 2004;53:1721-1732.

62. Lakard S, Herlem G, Propper A, Kastner A, Michel G, Valles-Villarreal N, Gharbi T, Fahys B. Adhesion and proliferation of cells on new polymers modified biomaterials. *Bioelectrochemistry*. 2004;62:19-27.
63. Thiery JP. Cell adhesion in development: a complex signaling network. *Curr Opin Genet Dev*. 2003;13:365-371.
64. Piao H, Kwon JS, Piao S, Sohn JH, Lee YS, Bae JW, Hwang KK, Kim DW, Jeon O, Kim BS, Park YB, Cho MC. Effects of cardiac patches engineered with bone marrow-derived mononuclear cells and PGCL scaffolds in a rat myocardial infarction model. *Biomaterials*. 2007;28:641-649.
65. Kim M, Choi YS, Yang SH, Hong HN, Cho SW, Cha SM, Pak JH, Kim CW, Kwon SW, Park CJ. Muscle regeneration by adipose tissue-derived adult stem cells attached to injectable PLGA spheres. *Biochem Biophys Res Commun*. 2006;348:386-392.

Chapter 4

Investigation of the Pro-arrhythmic Features of Pathological Cardiac Hypertrophy in Neonatal Rat Ventricular Cardiomyocyte Cultures

Zeinab Neshati, Brian O. Bingen, Saïd F.A. Askar, Martin J. SchaliJ, Daniël A. Pijnappels, Antoine A.F. de Vries

To be submitted

Abstract

Background: Different factors may trigger arrhythmias in diseased hearts including fibrosis, cardiomyocyte hypertrophy, hypoxia and inflammation. This makes it difficult to establish the relative contribution of each of them to the occurrence of arrhythmias. Accordingly, in this study, we used an *in vitro* model of pathological cardiac hypertrophy (PCH) to investigate its pro-arrhythmic features and the underlying mechanisms independent of fibrosis or other PCH-related processes.

Methods and Results: Neonatal rat ventricular cardiomyocyte (nr-vCMC) monolayers were treated with phorbol 12-myristate 13-acetate (PMA) to create an *in vitro* model of PCH. Electrophysiological properties of PMA-treated and control monolayers were analyzed by optical mapping at day 9 of culture. PMA treatment led to a significant increase in cell size and total protein content. It also caused a reduction in sarcoplasmic/endoplasmic reticulum Ca^{2+} ATPase 2 level (32%) and an increase in natriuretic peptide A (42%) and α 1-skeletal muscle actin (34%) levels indicating that the hypertrophic response induced by PMA was indeed pathological in nature. PMA-treated monolayers showed increases in action potential duration (APD) and APD dispersion, and a decrease in conduction velocity (CV; APD_{30} of 306 ± 39 vs 148 ± 18 ms, APD_{30} dispersion of 85 ± 19 vs 22 ± 7 and CV of 10 ± 4 vs 21 ± 2 cm/s in controls). Upon local 1-Hz stimulation, 53.6% of the PMA-treated cultures showed focal tachyarrhythmias based on triggered activity (n=82), while control group showed 4.3% tachyarrhythmias (n=70).

Conclusion: Following PMA treatment, nr-vCMC cultures acquire features of pathologically hypertrophied hearts and show a high incidence of focal tachyarrhythmias associated with APD prolongation and an increase in APD dispersion. PMA-treated nr-vCMC cultures may thus represent a well-controllable *in vitro* model for testing new therapeutic interventions targeting specific aspects of hypertrophy-associated arrhythmias.

Key words: phorbol 12-myristate 13-acetate, pathological cardiac hypertrophy, triggered activity, cell culture

Introduction

An increase in cardiac demand triggers the heart to respond in several ways, including by the enlargement of cardiomyocytes. Such cardiac hypertrophy is essentially a beneficial compensatory process as it decreases wall stress, while increasing cardiac output.¹ This adaptation by growth occurs under physiological conditions like exercise and pregnancy, but also in response to myocardial infarction and other cardiac pathologies. Whereas physiological cardiac hypertrophy is usually reversible and contributes to optimal heart function, hypertrophy due to cardiac disease (*i.e.* pathological cardiac hypertrophy [PCH]) is typically associated with several irreversible time-dependent detrimental changes, including maladaptive remodeling of cardiac structure, metabolism, electrophysiology and ion homeostasis, which may ultimately culminate in heart failure.^{2,3} Electrophysiological remodeling, especially if sustained, imposes an increased risk of developing cardiac arrhythmias. The relationship of PCH with ventricular tachyarrhythmias has been investigated in whole heart mapping studies.⁴⁻⁷ However, the complexity of three-dimensional (3D) myocardial tissue and the presence in pathologically hypertrophied hearts of various other changes in cardiac structure and function including fibrosis, inflammation and metabolic remodeling,^{7,8} complicates assessment of the specific contribution of PCH to the development of heart rhythm disturbances. This problem can be overcome by using two-dimensional (2D) cell culture models of defined composition to study PCH-related pro-arrhythmic changes. Induction of hypertrophy-related pathological changes in cardiomyocyte cultures can be accomplished by exposure of the cells to a variety of different peptide and non-peptide hormones and growth factors including angiotensin II (AngII), endothelin 1 (ET-1) and certain natural and synthetic catecholamines.⁹ Many of these molecules exert their pro-hypertrophic effects through the activation of phospholipase C leading to the production of inositol 1,4,5-trisphosphate (IP₃) and diacylglycerol (DAG). Binding of IP₃ to specific receptors located in the membranes of the sarcoplasmic reticulum and in the nuclear envelope causes Ca²⁺ release into the cytosol and nucleus and activation of several pro-hypertrophic factors including calcineurin, nuclear factor of activated T cells (NFAT) and Ca²⁺/calmodulin-dependent protein kinase II (CaMKII).¹⁰ DAG, on the other hand, stimulates cardiac hypertrophy mainly by acting as stimulatory cofactor of protein kinase C (PKC) and protein kinase D (PKD).^{11,12} The pro-hypertrophic effects of DAG can be mimicked by phorbol 12-myristate 13-acetate (PMA). Indeed,

treatment of neonatal rat ventricular cardiomyocytes (nr-vCMCs) with PMA has been shown to induce a gene expression program in these cells sharing many features with that of pathologically hypertrophied hearts.¹³⁻¹⁵ Prominent among the PMA-induced changes are those involving the expression level, cellular localization and specific activity of ion channels and transporters,^{16,17} connexins,^{18,19} and Ca²⁺-handling proteins²⁰⁻²² similar to what happens in pathologically hypertrophied hearts. Still, relatively little is known about the possible pro-arrhythmic consequences of these changes, which are commonly referred to as electrical remodeling. Therefore, the purpose of the present study was to investigate in PMA-treated nr-vCMC cultures the contribution of PCH to the development of cardiac arrhythmias independent of fibrosis, inflammation and hypoxia.

Materials and Methods

All animal experiments had the approval of the Animal Experiments Committee of the Leiden University Medical Center and complied with the Guide for the Care and Use of Laboratory Animals as stated by the US National Institutes of Health.

Cardiomyocyte isolation

nr-vCMCs were isolated and cultured essentially as described previously.²³ In brief, 2-day-old Wistar rats were anaesthetized with 4–5% isoflurane. After confirmation of anesthesia, the chest was opened, the heart was excised and the ventricles were separated from the remainder of the cardiac tissue. Next, the ventricular myocardium was cut into small pieces (~1 mm) and further dissociated by incubation at 37°C with a buffer solution containing 0.01 mM CaCl₂, 5 mM MgCl₂, 450 units/ml of collagenase 1 (Worthington, Lakewood, NJ, USA) and 18.75 Kunitz units/ml DNase I (Sigma-Aldrich, St. Louis, MO, USA). Cells and remaining tissue fragments were pelleted by centrifugation at 161 × *g* and room temperature (RT) for 10 min and resuspended in growth medium (Ham's F10 medium supplemented with 10% fetal bovine serum [FBS] and 10% horse serum [HS; all from Life Technologies, Bleiswijk, the Netherlands]). The cell suspension was then applied to Primaria culture dishes (Corning Life Sciences, Amsterdam, the Netherlands) and incubated for 75 min in a humidified incubator at 37°C and 5% CO₂ to allow preferential attachment of non-

myocytes. The unattached cells (mainly cardiomyocytes) were collected, passed through a cell strainer (70- μm mesh pore size; BD Biosciences, Breda, the Netherlands) to obtain a single cell suspension and applied at a density of 6×10^5 cells/well of a 24-well cell culture plate (Corning Life Sciences) to fibronectin (Sigma-Aldrich)-coated, round glass coverslips (15-mm diameter). One day later (*i.e.* at culture day 1), the cells were treated in growth medium with mitomycin C (10 $\mu\text{g}/\text{ml}$; Sigma-Aldrich) for 2 h to inhibit proliferation of remaining non-myocytes. The growth medium was subsequently replaced by a 1:1 mixture of Dulbecco's modified Eagle's medium [DMEM; Life Technologies] and Ham's F10 medium supplemented with 5% HS, 2% bovine serum albumin (BSA) and sodium ascorbate to a final concentration of 0.4 mM. This so-called maintenance medium was refreshed daily. To induce pathological hypertrophy cultures were exposed to 1 μM PMA (BioVision, Milpitas, CA, USA) for 24 h at day 3 and 8 of culture.

Optical mapping

Optical mapping was done at day 9 of culture. Prior to optical mapping, the cells were incubated for 10 min in maintenance medium containing 8 μM of the voltage-sensitive dye di-4-ANEPPS (Life Technologies) and given fresh medium consisting of DMEM/HAM's F12 (Life Technologies) without phenol red and serum. Immediately afterwards, cultures were optically mapped at 37°C using a MiCAM ULTIMA-L imaging system (SciMedia, Costa Mesa, CA, USA). To allow for a fair comparison of action potential duration (APD) and conduction velocity (CV), all cultures were locally stimulated at 1 Hz using an epoxy-coated bipolar platinum electrode with square suprathreshold (*i.e.* 8 V) electrical stimuli of 10 ms. Parameters of interest were calculated using Brain Vision Analyzer 1208 software (Brainvision, Tokyo, Japan). Optical signals of 9 pixels were averaged to minimize noise artifacts. To calculate CV, two 3 by 3 pixel grids located 2-8 mm apart on a line perpendicular to the activation wavefront were used. APD was calculated at 30% (APD₃₀) and 80% (APD₈₀) of repolarization. CV and APD values were averages of values obtained from 6 different positions equally distributed across the cell cultures. APD₃₀ and APD₈₀ dispersion were expressed as the standard deviation (SD) of the mean of the APDs. For determining CV, APD and APD dispersion only nr-vCMC cultures with uniform activation patterns were used. Occurrence of pro-arrhythmic features was

also evaluated after 1-Hz local stimulation. An early afterdepolarization (EAD) was defined as a reversal of repolarization during phase 2 or 3 of the AP of more than 10% of the maximum optical signal amplitude. A focal tachyarrhythmia was defined as an activation pattern in which an EAD was followed by 2 or more uninterrupted oscillations in membrane potential without giving rise to a reentrant circuit.

Immunocytology

For immunostaining, 8×10^4 cells were seeded on fibronectin-coated, round glass coverslips (15-mm diameter) in wells of 12-well cell culture plates (Corning Life Sciences). At day 9 of culture, cells were fixed by incubation for 30 min in phosphate-buffered 4% formaldehyde (Klinipath, Duiven, the Netherlands) and permeabilized by a 20-min treatment with 0.1% Triton X-100 in phosphate-buffered saline (PBS) both at RT. Next, cells were incubated overnight at 4°C with mouse anti-sarcomeric α -actinin (clone: EA-53; Sigma-Aldrich), mouse anti-sarcoplasmic/endoplasmic reticulum Ca^{2+} ATPase 2 (Serca2; clone: 2A7-A1; Thermo Fisher Scientific, Waltham, MA, USA), rabbit anti-natriuretic peptide precursor type A (Nppa; Merck Millipore, order number: AB5490) and rabbit anti- α 1-skeletal muscle actin (Acta1; Abcam, Cambridge, United Kingdom, order number: ab52218) primary antibodies diluted 1:200 in PBS + 0.1% donkey serum (Santa Cruz Biotechnology, Dallas, TX, USA) followed by a 2-h incubation at RT with appropriate Alexa Fluor 488- or 568-conjugated donkey IgG (H+L) secondary antibodies (Life Technologies) diluted 1:400 in PBS + 0.1% donkey serum. Nuclei were counterstained with 10 $\mu\text{g}/\text{ml}$ Hoechst 33342 (Life Technologies) in PBS. Cells were washed three times with PBS after fixation, permeabilization and incubation with primary antibody, secondary antibody and DNA-binding fluorochrome. To minimize photobleaching, coverslips were mounted in VECTASHIELD mounting medium (Vector Laboratories, Burlingame, CA, USA). Pictures were taken with a fluorescence microscope equipped with a digital color camera (Nikon Eclipse 80i; Nikon Instruments Europe, Amstelveen, the Netherlands) using NIS Elements software (Nikon Instruments Europe). Cell surface area (CSA) and fluorescent intensity were measured using dedicated software (ImageJ, version 4.1 National Institutes of Health, USA).

Statistical analysis

Different experimental groups were compared using the unpaired samples *t*-test. Data represented as mean±SD. Differences among means were considered significant at $P\leq 0.05$. Graphs were prepared in GraphPad Prism version 6 (GraphPad Software, La Jolla, CA, USA).

Results

PMA induces a hypertrophic response in nr-vCMCs

Immunostaining of control and PMA-treated nr-vCMC cultures for sarcomeric α -actinin showed the presence of ~13% non-myocytes in the cultures (Figure 1A). PMA treatment of nr-vCMC cultures increased mean CSA by 30% (3.5 ± 1.5 [n=81] vs 2.6 ± 1.0 pixels in control cultures [n=54], $P<0.0005$) (Figure 1B) and total protein content by 80% (1.3 ± 0.1 vs 0.7 ± 0.1 mg/ 10^7 cells in control cultures [n=9 for both experimental groups], $P<0.0001$) (Figure 1C), confirming that PMA is a hypertrophy inducer.

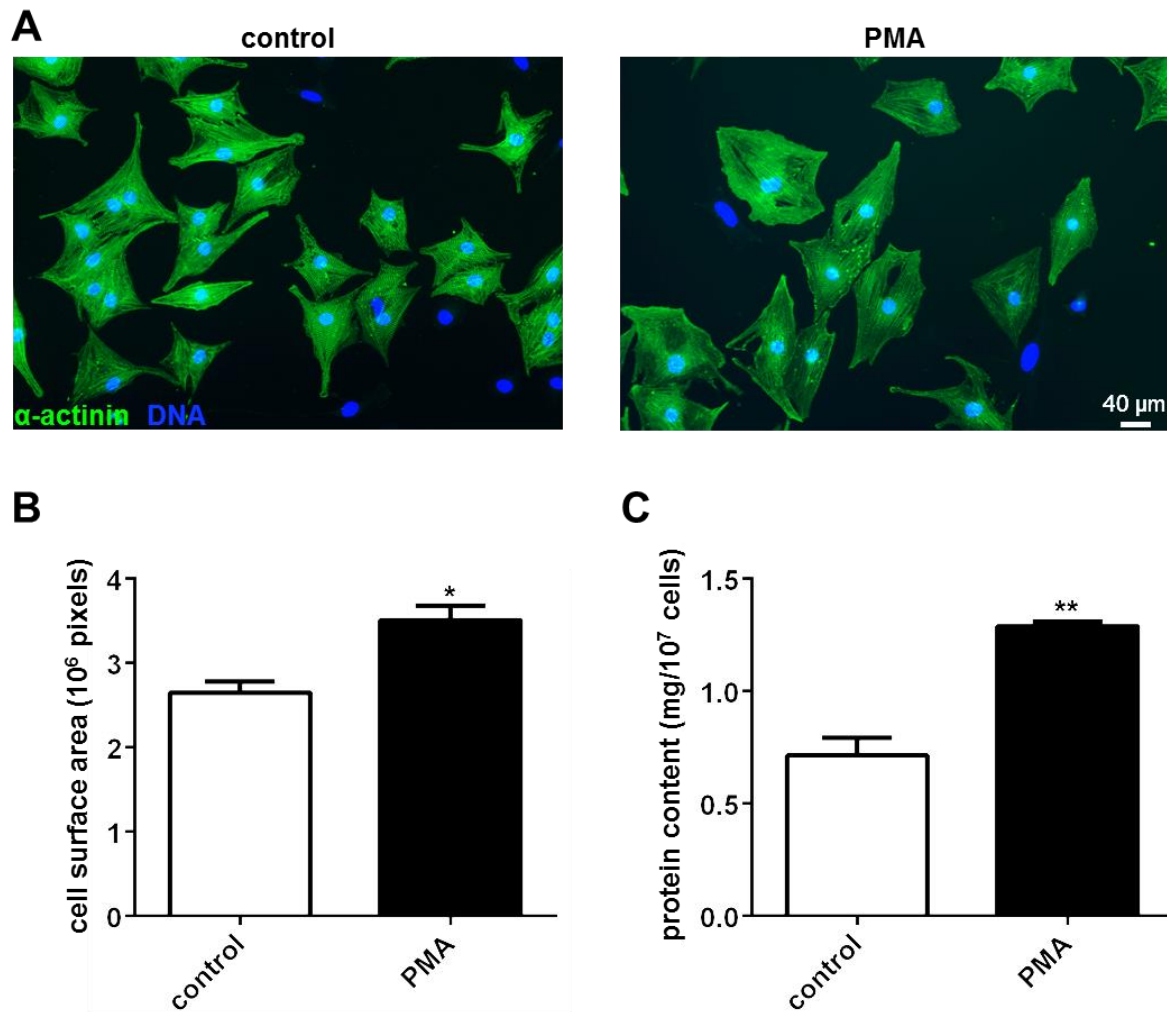


Figure 1. Characterization of PMA-treated nr-vCMC cultures. (A) α -actinin staining showing the presence of 13% non-myocytes in the nr-vCMCs cultures. Quantification of (B) CSA and (C) protein content of control and PMA-treated nr-vCMCs. CSA and protein level were increased in cultures treated with PMA indicative of a hypertrophic response. * $P < 0.0005$ and ** $P < 0.0001$.

PMA-treated nr-vCMCs acquire a pathological hypertrophy-related phenotype

To investigate the nature of the hypertrophic response induced by PMA, control and drug-treated nr-vCMC cultures were immunostained for markers distinguishing physiological from pathological hypertrophy. The PMA-treated nr-vCMC cultures displayed a 42% increase in Nppa level (17.8 ± 2.0 vs 12.5 ± 4.4 arbitrary units, $P < 0.005$) (Figure 2A), a 34% increase in Acta1 expression (22.0 ± 4.1 vs 16.4 ± 2.6 arbitrary units, $P < 0.0005$) (Figure 2B) and a 32% decrease in Serca2a level (15.9 ± 2.5 vs 21.1 ± 3.5 arbitrary units, $P < 0.0001$) (Figure 2C) as compared to those in

control cultures. This indicates that PMA-treated nr-vCMCs obtain properties of pathologically hypertrophic cardiac muscle cells.

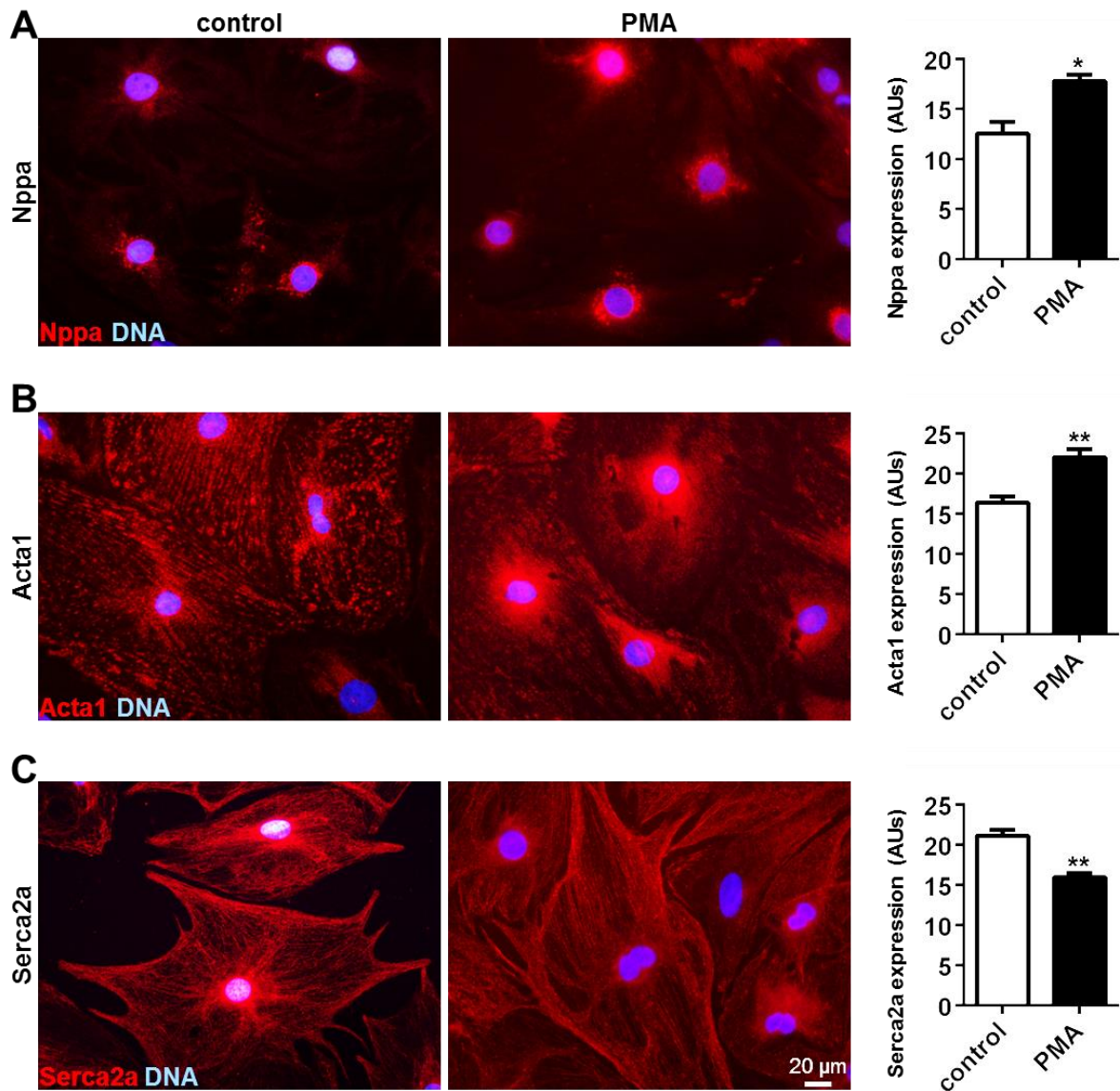


Figure 2. PMA treatment endows nr-vCMCs with features of pathological hypertrophied ventricular myocardium including an increase in (A) Nppa (42%) and (B) Acta1 levels (34%) and a decrease in (C) Serca2a expression (32%). * $P < 0.005$ and ** $P < 0.0005$. AUs, arbitrary units.

Conduction and repolarization are slowed by PMA treatment of nr-vCMCs cultures

Optical mapping recordings in 1 Hz-paced, uniformly propagating nr-vCMC cultures showed that PMA treatment causes a strong reduction in CV (10 ± 4 vs 21 ± 2 cm/s in control cultures, $P < 0.0001$) (Figure 3A). Moreover, the PMA-treated nr-vCMC

cultures displayed a large increase in APD_{30} (306 ± 39 vs 148 ± 18 ms in control cultures, $P<0.0001$) and APD_{80} (516 ± 53 vs 225 ± 34 ms in control cultures, $P<0.0001$) (Figure 3B,C and Figure 4A). Spatial APD dispersion was also increased in PMA-treated cultures (APD_{30} dispersion of 85 ± 19 vs 22 ± 7 ms in control cultures, $P<0.0001$ and APD_{80} dispersion of 50 ± 9 vs 25 ± 2 ms in control cultures, $P<0.0001$) implying increased heterogeneity of repolarization (Figure 3B,C).

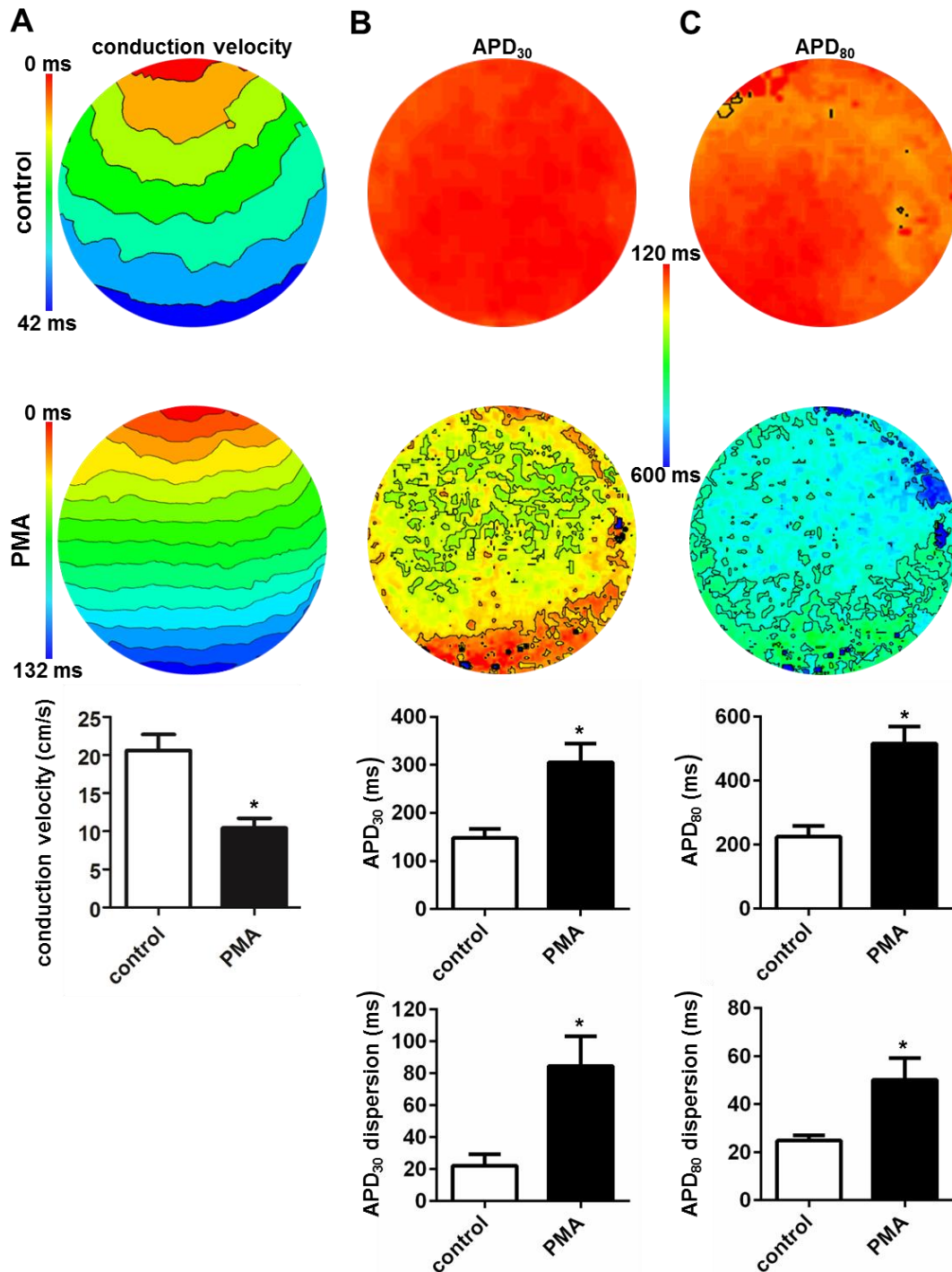


Figure 3. PMA treatment of nr-vCMC cultures causes conduction slowing and heterogeneous APD prolongation. **(A)** Typical activation maps with 6-ms isochronal spacing and corresponding quantitative assessment of control and PMA-treated nr-vCMC cultures showing slowing of conduction upon PMA treatment. Typical APD₃₀ **(B)** and APD₈₀ **(C)** map of control and PMA-treated nr-vCMC cultures and corresponding quantitative assessments of APD and APD dispersion showing PMA-induced increases in APD and APD dispersion. Cultures were subjected to electrical point stimulation at a frequency of 1-Hz. * $P < 0.0001$.

Focal triggered activity is a prominent pro-arrhythmic feature of PMA-treated nr-vCMC cultures

The PMA-induced APD prolongation and increase in APD dispersion provided enough time and depolarizing force, respectively, for formation of EADs in the drug-treated cultures, which could oscillate repetitively resulting in focal tachyarrhythmias. The incidence of this type of arrhythmias following local 1-Hz stimulation was 53.6% in the PMA-treated nr-vCMC cultures (n=82) while control nr-vCMC cultures showed 4.3% arrhythmias (n=70) (Figure 4A, B). During focal tachyarrhythmias, repolarization halted at the initiation site of the EAD (Figure 4C, point 1) followed by slow repolarization in areas in the vicinity of the region of sustained depolarization, which favored EAD formation (Figure 4,C point 2).

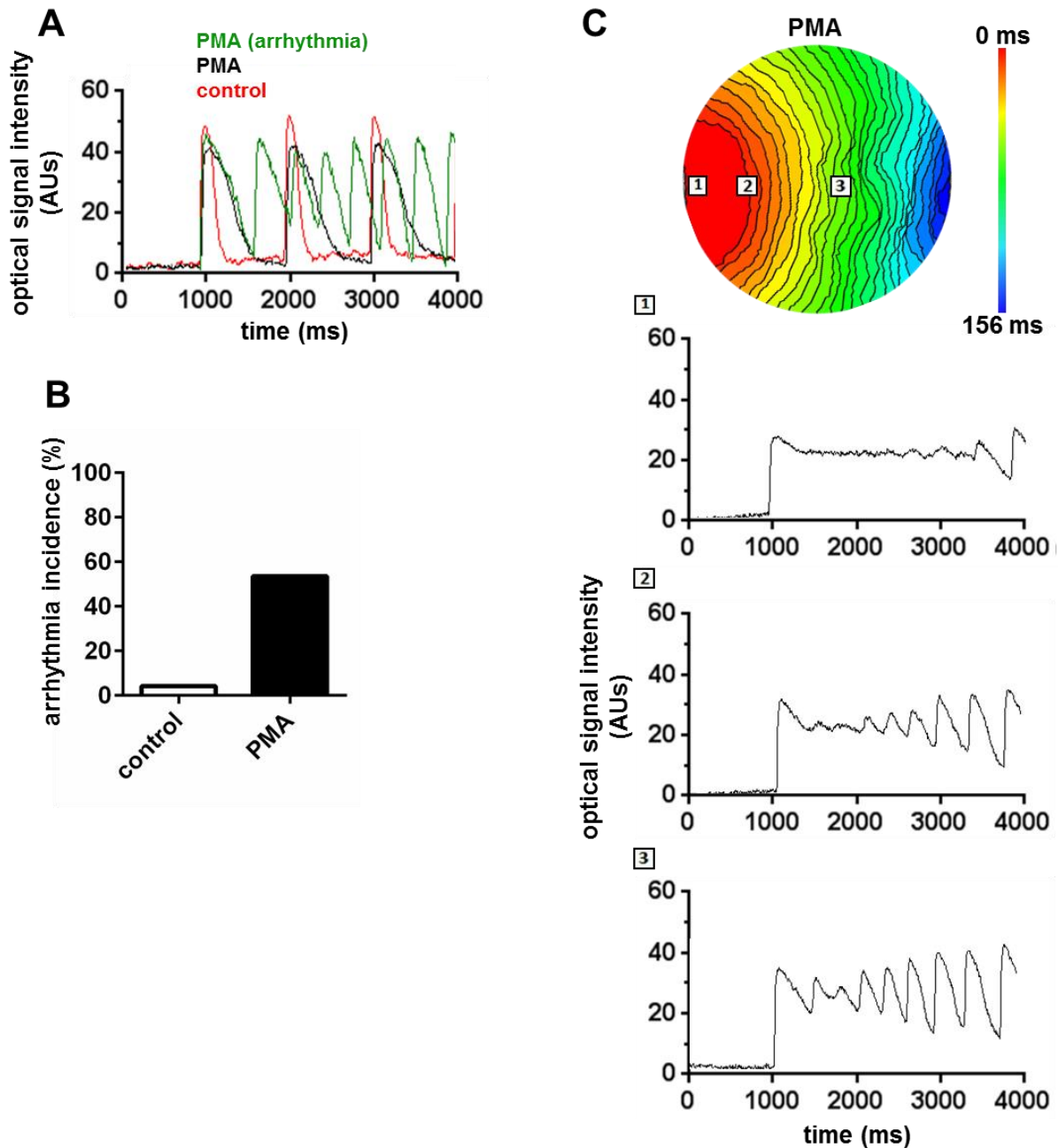


Figure 4. PMA-treated nr-vCMC cultures show a high incidence of focal tachyarrhythmias. **(A)** Typical optical signals from control (red) and PMA-treated cultures showing APD prolongation (black) and onset of tachyarrhythmia (green). **(B)** Quantification of arrhythmia incidence (*i.e.* incidence of focal tachyarrhythmias) in control and PMA-treated nr-vCMC cultures. **(C)** Activation map of a PMA-treated nr-vCMC culture displaying triggered activity. Corresponding optical signals showing ceased repolarization (point 1), EAD initiation (point 2) and EAD propagation (point 3). AUs, arbitrary units.

Discussion

The major findings of this study are: (i) Exposure of nr-vCMC cultures for 2 times 24 hours to PMA induces a hypertrophic response in the cardiac myocytes with hallmarks of pathological hypertrophied ventricular myocardium; (ii) Following prolonged PMA treatment nr-vCMC cultures undergo electrical remodeling as evinced by a decrease in CV and an increase in APD and APD dispersion; (iii) PMA-treated nr-vCMC cultures display a high incidence of triggered activity causing focal tachyarrhythmias; (iv) Mechanistically, the arrhythmias observed in nr-vCMC cultures rendered pathologically hypertrophic by prolonged PMA treatment are probably a direct consequence of the electrical remodeling process.

In vitro models of PCH

In recent years much has been learned about the signaling pathways orchestrating both physiological and pathological heart growth.²⁴ Through extensive molecular, genetic and pharmacological studies, G protein-coupled receptors (GPCRs) and their ligands (e.g. AngII, ET-1, noradrenaline [NE]) have been identified as key regulators of PCH.²⁵ This has led researchers to use these ligands or synthetic analogs hereof (e.g. isoproterenol, phenylephrine [PE]) to develop *in vitro* and *in vivo* models of PCH and heart failure.^{9,26-28} In the *in vitro* models of pathological ventricular hypertrophy, an increase in CSA, mRNA and protein content, cell capacitance and/or protein synthesis rate was taken as proof of cell growth while increases in the expression of Nppa, natriuretic peptide precursor B (Nppb), Acta1, β -myosin heavy chain (Myh7) and/or decreases in α -myosin heavy chain (Myh6) and Serca2a levels were considered indicative of a pathological rather than a physiological hypertrophic response.

The pro-hypertrophic effects of AngII-, ET-1- and catecholamine-binding GPCRs in the heart are for a large part attributable to the activation of phospholipase C, which converts phosphatidylinositol 4,5-bisphosphate (PIP₂) into the second messengers IP₃ and DAG. In this study, PCH was induced by using PMA as a synthetic analogue of the second messenger DAG instead of by agonist-induced GPCR activation. Possible pro-hypertrophic effects caused by direct ligand-induced

IP₃ receptor (IP₃R) activation and subsequent Ca²⁺ release are therefore expected to be absent in our nr-vCMC-based PCH model. The PMA-treated nr-vCMC cultures nevertheless show a very robust hypertrophic response with hallmarks of PCH (Figures 1 and 2), which is consistent with the results of previous studies that employed (prolonged) PMA treatment to render cardiomyocyte cultures hypertrophic.^{17,20,29,30} This suggests that either IP₃R signaling is not necessary for inducing PCH-related phenotypic changes in cultured nr-vCMCs or that IP₃Rs get activated by DAG-dependent signaling. Indeed, several studies have identified the DAG receptors PKC and PKD as important mediators of (pathological) cardiac hypertrophy and fetal cardiac gene reactivation.^{14,21,31-34} Consequently, overexpression of PKC α ³⁵ or PKD3³⁶ in nr-vCMCs induced pathological hypertrophic growth with increased fetal cardiac gene expression in these cells.

Pro-arrhythmic mechanisms of PCH

Despite the rapidly increasing knowledge about the molecular pathways involved in the development of PCH and heart failure, the mechanisms underlying electrical remodeling of the diseased heart are still poorly understood. This is partially due to the disparate results obtained in different *in vivo* studies focusing on PCH-related changes in cardiac electrophysiology.³⁷⁻³⁹ A confounding factor in these studies has been the use of different experimental conditions, animal models and/or patient groups with distinct contributions of other factors besides PCH to the electrophysiological remodeling process. In this study, using a well-defined *in vitro* model system, heterogeneous APD prolongation and EAD-triggered activity were identified as likely key players in the development of PCH-associated arrhythmias. These findings are consistent with the results of animal and clinical studies attributing a prominent role of EADs to the development of ventricular tachyarrhythmias.⁴⁰⁻⁴³ In our study, we did not investigate the ionic basis of the EADs. However, given the pronounced elongation of phase 2 of the AP in the PMA-treated nr-vCMCs, L-type Ca²⁺ channels and delayed rectifier K⁺ channels⁴³ are probably involved. In support of this idea, Puglisi *et al.* recently showed that chronic exposure (*i.e.* for 48-72 hours) of nr-vCMCs to PMA caused a strong decrease in normalized I_{Ks} .¹⁷ The same researchers also reported a significant decrease in I_{to} and a substantial increase in $I_{Na+/Ca2+}$ while the normalized $I_{Ca,L}$ did not change

significantly. A decrease in I_{to} following overnight exposure of nr-vCMCs to PMA has also been documented by Walsh *et al.*⁴⁴ Another important result was the PMA-induced 32% decrease in Serca2a protein level. Similar findings were made by Porter *et al.* and Qi *et al.* following prolonged treatment of nr-vCMCs with PMA.^{20,21} In their study, Qi and co-workers found that the reduction in Serca2a expression led to a slowing of diastolic Ca^{2+} uptake into the sarcoplasmic reticulum with possible pro-arrhythmic consequences. Besides the reduced repolarization reserve at the earlier phases of repolarization (*i.e.* between -40 and 0 mV) and the increased APD dispersion, also the conduction slowing observed in our PMA-treated nr-vCMC cultures is a major risk factor for the development of ventricular tachyarrhythmias.⁴⁵ The most likely explanation for this conduction slowing is gap junctional remodeling in combination with a downregulation of connexin 43 protein level as has been observed in patients with PCH or heart failure.^{46,47}

PCH versus heart failure model

In response to hemodynamic stress and/or myocardial injury (*i.e.* when cardiac load exceeds cardiac output) the heart engages in a process called compensatory hypertrophy through the enlargement of cardiomyocytes by the parallel (concentric hypertrophy) or serial (eccentric hypertrophy) addition of sarcomeres. This process is under neurohormonal control of the adrenergic nervous system and renin-angiotensin system. At the molecular level, the changes in cardiomyocyte phenotype are accompanied by reinduction of the so-called fetal gene program, because patterns of gene expression mimic those observed during cardiac development. In the continued presence of pathologically stimuli, excessive cardiomyocyte death will provoke transition to dilated cardiomyopathy leading to heart failure. The latter process is associated with functional perturbations of cellular Ca^{2+} homeostasis and ionic currents resulting in impaired force generation and the development of malignant arrhythmias.^{38,48} The PMA-treated nr-vCMC cultures display many of the same electrophysiological changes found in failing ventricular myocardium including a reduction in CV, heterogeneous APD prolongation and a high incidence of triggered electrical impulses.³ This may suggest that the PMA-treated nr-vCMC cultures represent a relatively late stage in the transition from PCH to heart failure. Further evidence for this presupposition should come from a comparison of the

contractile force-generating capacity of control and PMA-treated nr-vCMC cultures and from comparative transcriptome analyses.

Conclusion

In the present study, treatment of nr-vCMCs for 2 times 24 hours with PMA not only promoted cardiomyocyte hypertrophy but also led to the reactivation of fetal cardiac genes as evinced by PMA-dependent increases in *Nppa* and *Acta1* levels and a decrease in *Serca2a* expression. PMA-treated nr-vCMCs showed a high incidence of triggered tachyarrhythmias associated with increases in APD and APD dispersion caused by electrical remodeling. To the best of our knowledge, this is the first study in which the pro-arrhythmic features of PCH per se have been investigated. Since this *in vitro* model of PCH is highly controllable and provides reproducible results, it is ideally suited for testing, in proof-of-concept studies, new therapeutic interventions (genetic modifications or pharmacological treatments) targeting specific aspects of hypertrophy/heart failure-associated arrhythmias.

Study limitations

In this study, PCH-related arrhythmias were investigated in 2D cultures of nr-vCMCs. Although this *in vitro* model system has greatly contributed to our current understanding of heart structure and function and lends itself very well to pharmacological and genetic manipulation, the electrophysiological properties of PMA-treated nr-vCMCs will only partially resemble those of cardiomyocytes in the pathologically hypertrophied human heart. Also, in isolation, pathological hypertrophy may have a different impact on cardiomyocytes' behaviour than in combination with other cardiac pathologies like inflammation, hypoxia and fibrosis. Accordingly, discoveries made in PMA-treated nr-vCMC cultures will always have to be verified in more clinically relevant settings. Even so, due to the relative ease with which nr-vCMCs can be obtained, cultured and manipulated they represent a highly useful model system for mechanistic and therapy-directed cardiac research.

Funding

This work was supported by an unrestricted research grant from the Iranian Ministry of Science, Research and Technology.

Author contributions

Conceived and designed the experiments: ZN, BOB, DAP, AAF. Performed the experiments: ZN. Analyzed the data: ZN, BOB, DAP, AAF. Contributed reagents/materials/analysis tools: BOB, MJS, DAP, AAF. Wrote the paper: ZN, MJS, DAP, AAF.

References

1. Grossman W, Jones D, McLaurin LP. Wall stress and patterns of hypertrophy in the human left ventricle. *J Clin Invest.* 1975;56:56-64.
2. Weber KT, Brilla CG. Pathological hypertrophy and cardiac interstitium. Fibrosis and renin-angiotensin-aldosterone system. *Circulation.* 1991;83:1849-1865.
3. Burchfield JS, Xie M, Hill JA. Pathological ventricular remodeling: Mechanisms: Part 1 of 2. *Circulation.* 2013;128:388-400.
4. Galinier M, Balanescu S, Fourcade J, Dorobantu M, Albenque JP, Massabuau P, Doazan JP, Fauvel JM, Bounhoure JP. Prognostic value of arrhythmogenic markers in systemic hypertension. *Eur Heart J.* 1997;18:1484-1491.
5. Haider AW, Larson MG, Benjamin EJ, Levy D. Increased left ventricular mass and hypertrophy are associated with increased risk for sudden death. *J Am Coll Cardiol.* 1998;32:1454-1459.
6. Arnol M, Starc V, Knap B, Potocnik N, Bren AF, Kandus A. Left ventricular mass is associated with ventricular repolarization heterogeneity one year after renal transplantation. *Am J Transplant.* 2008;8:446-451.
7. McLenachan JM, Dargie HJ. Determinants of ventricular arrhythmias in cardiac hypertrophy. *J Cardiovasc Pharmacol.* 1991;17 Suppl 2:S46-49.
8. Amano Y, Kitamura M, Tachi M, Takeda M, Mizuno K, Kumita S. Delayed enhancement magnetic resonance imaging in hypertrophic cardiomyopathy with basal septal hypertrophy and preserved ejection fraction: Relationship with ventricular tachyarrhythmia. *J Comput Assist Tomogr.* 2014;38:67-71.
9. Schaub MC, Hefti MA, Harder BA, Eppenberger HM. Various hypertrophic stimuli induce distinct phenotypes in cardiomyocytes. *J Mol Med (Berl).* 1997;75:901-920.
10. Hohendanner F, McCulloch AD, Blatter LA, Michailova AP. Calcium and IP3 dynamics in cardiac myocytes: Experimental and computational perspectives and approaches. *Front Pharmacol.* 2014;5:35.
11. Sin YY, Baillie GS. Protein kinase D in the hypertrophy pathway. *Biochem Soc Trans.* 2012;40:287-289.
12. Steinberg SF. Cardiac actions of protein kinase C isoforms. *Physiology (Bethesda).* 2012;27:130-139.

13. Dunnmon PM, Iwaki K, Henderson SA, Sen A, Chien KR. Phorbol esters induce immediate-early genes and activate cardiac gene transcription in neonatal rat myocardial cells. *J Mol Cell Cardiol.* 1990;22:901-910.
14. Shubeita HE, Martinson EA, Van Bilsen M, Chien KR, Brown JH. Transcriptional activation of the cardiac myosin light chain 2 and atrial natriuretic factor genes by protein kinase C in neonatal rat ventricular myocytes. *Proc Natl Acad Sci U S A.* 1992;89:1305-1309.
15. Prasad AM, Inesi G. Regulation and rate limiting mechanisms of Ca²⁺ ATPase (SERCA2) expression in cardiac myocytes. *Mol Cell Biochem.* 2012;361:85-96.
16. Shigekawa M, Katanosaka Y, Wakabayashi S. Regulation of the cardiac Na⁺/Ca²⁺ exchanger by calcineurin and protein kinase C. *Ann N Y Acad Sci.* 2007;1099:53-63.
17. Puglisi JL, Yuan W, Timofeyev V, Myers RE, Chiamvimonvat N, Samarel AM, Bers DM. Phorbol ester and endothelin-1 alter functional expression of Na⁺/Ca²⁺ exchange, K⁺, and Ca²⁺ currents in cultured neonatal rat myocytes. *Am J Physiol Heart Circ Physiol.* 2011;300:H617-626.
18. Kwak BR, van Veen TA, Analbers LJ, Jongsma HJ. TPA increases conductance but decreases permeability in neonatal rat cardiomyocyte gap junction channels. *Exp Cell Res.* 1995;220:456-463.
19. Doble BW, Ping P, Fandrich RR, Cattini PA, Kardami E. Protein kinase C-epsilon mediates phorbol ester-induced phosphorylation of connexin-43. *Cell Commun Adhes.* 2001;8:253-256.
20. Qi M, Bassani JW, Bers DM, Samarel AM. Phorbol 12-myristate 13-acetate alters SR Ca(2+)-ATPase gene expression in cultured neonatal rat heart cells. *Am J Physiol.* 1996;271:H1031-1039.
21. Porter MJ, Heidkamp MC, Scully BT, Patel N, Martin JL, Samarel AM. Isoenzyme-selective regulation of SERCA2 gene expression by protein kinase C in neonatal rat ventricular myocytes. *Am J Physiol Cell Physiol.* 2003;285:C39-47.
22. Blum JL, Samarel AM, Mestral R. Phosphorylation and binding of AUF1 to the 3'-untranslated region of cardiomyocyte SERCA2a mRNA. *Am J Physiol Heart Circ Physiol.* 2005;289:H2543-2550.

23. Pijnappels DA, Schalij MJ, Ramkisoensing AA, van Tuyn J, de Vries AA, van der Laarse A, Ypey DL, Atsma DE. Forced alignment of mesenchymal stem cells undergoing cardiomyogenic differentiation affects functional integration with cardiomyocyte cultures. *Circ Res*. 2008;103:167-176.
24. Bernardo BC, Weeks KL, Pretorius L, McMullen JR. Molecular distinction between physiological and pathological cardiac hypertrophy: Experimental findings and therapeutic strategies. *Pharmacol Ther*. 2010;128:191-227.
25. Salazar NC, Chen J, Rockman HA. Cardiac GPCRs: GPCR signaling in healthy and failing hearts. *Biochim Biophys Acta*. 2007;1768:1006-1018.
26. Lijnen P, Petrov V. Renin-angiotensin system, hypertrophy and gene expression in cardiac myocytes. *J Mol Cell Cardiol*. 1999;31:949-970.
27. Wollert KC, Drexler H. The renin-angiotensin system and experimental heart failure. *Cardiovasc Res*. 1999;43:838-849.
28. Osadchii OE. Cardiac hypertrophy induced by sustained beta-adrenoreceptor activation: Pathophysiological aspects. *Heart Fail Rev*. 2007;12:66-86.
29. Allo SN, Carl LL, Morgan HE. Acceleration of growth of cultured cardiomyocytes and translocation of protein kinase C. *Am J Physiol*. 1992;263:C319-325.
30. Hartong R, Villarreal FJ, Giordano F, Hilal-Dandan R, McDonough PM, Dillmann WH. Phorbol myristate acetate-induced hypertrophy of neonatal rat cardiac myocytes is associated with decreased sarcoplasmic reticulum Ca²⁺ ATPase (SERCA2) gene expression and calcium reuptake. *J Mol Cell Cardiol*. 1996;28:2467-2477.
31. Vega RB, Harrison BC, Meadows E, Roberts CR, Papst PJ, Olson EN, McKinsey TA. Protein kinases C and D mediate agonist-dependent cardiac hypertrophy through nuclear export of histone deacetylase 5. *Mol Cell Biol*. 2004;24:8374-8385.
32. Fielitz J, Kim MS, Shelton JM, Qi X, Hill JA, Richardson JA, Bassel-Duby R, Olson EN. Requirement of protein kinase D1 for pathological cardiac remodeling. *Proc Natl Acad Sci U S A*. 2008;105:3059-3063.
33. Palaniyandi SS, Sun L, Ferreira JC, Mochly-Rosen D. Protein kinase C in heart failure: a therapeutic target? *Cardiovasc Res*. 2009;82:229-239.
34. Ellwanger K, Hausser A. Physiological functions of protein kinase D *in vivo*. *IUBMB Life*. 2013;65:98-107.

35. Braz JC, Bueno OF, De Windt LJ, Molkenin JD. PKC alpha regulates the hypertrophic growth of cardiomyocytes through extracellular signal-regulated kinase1/2 (ERK1/2). *J Cell Biol.* 2002;156:905-919.
36. Li C, Li J, Cai X, Sun H, Jiao J, Bai T, Zhou XW, Chen X, Gill DL, Tang XD. Protein kinase D3 is a pivotal activator of pathological cardiac hypertrophy by selectively increasing the expression of hypertrophic transcription factors. *J Biol Chem.* 2011;286:40782-40791.
37. Liu HB, Yang BF, Dong DL. Calcineurin and electrical remodeling in pathologic cardiac hypertrophy. *Trends Cardiovasc Med.* 2010;20:148-153.
38. Wang Y, Hill JA. Electrophysiological remodeling in heart failure. *J Mol Cell Cardiol.* 2010;48:619-632.
39. Cutler MJ, Jeyaraj D, Rosenbaum DS. Cardiac electrical remodeling in health and disease. *Trends Pharmacol Sci.* 2011;32:174-180.
40. Yan GX, Rials SJ, Wu Y, Liu T, Xu X, Marinchak RA, Kowey PR. Ventricular hypertrophy amplifies transmural repolarization dispersion and induces early afterdepolarization. *Am J Physiol Heart Circ Physiol.* 2001;281:H1968-1975.
41. Cosin Aguilar J, Hernandez Martinez A, Andres Conejos F. Mechanisms of ventricular arrhythmias in the presence of pathological hypertrophy. *Eur Heart J.* 1993;14 Suppl J:65-70.
42. Antoons G, Volders PG, Stankovicova T, Bito V, Stengl M, Vos MA, Sipido KR. Window Ca^{2+} current and its modulation by Ca^{2+} release in hypertrophied cardiac myocytes from dogs with chronic atrioventricular block. *J Physiol.* 2007;579:147-160.
43. Weiss JN, Garfinkel A, Karagueuzian HS, Chen PS, Qu Z. Early afterdepolarizations and cardiac arrhythmias. *Heart Rhythm.* 2010;7:1891-1899.
44. Walsh KB, Sweet JK, Parks GE, Long KJ. Modulation of outward potassium currents in aligned cultures of neonatal rat ventricular myocytes during phorbol ester-induced hypertrophy. *J Mol Cell Cardiol.* 2001;33:1233-1247.
45. van Rijen HV, Eckardt D, Degen J, Theis M, Ott T, Willecke K, Jongsma HJ, Opthof T, de Bakker JM. Slow conduction and enhanced anisotropy increase the propensity for ventricular tachyarrhythmias in adult mice with induced deletion of connexin43. *Circulation.* 2004;109:1048-1055.

46. Severs NJ, Bruce AF, Dupont E, Rothery S. Remodelling of gap junctions and connexin expression in diseased myocardium. *Cardiovasc Res*. 2008;80:9-19.
47. Kanno S, Saffitz JE. The role of myocardial gap junctions in electrical conduction and arrhythmogenesis. *Cardiovasc Pathol*. 2001;10:169-177.
48. Diwan A, Dorn GW, 2nd. Decompensation of cardiac hypertrophy: Cellular mechanisms and novel therapeutic targets. *Physiology (Bethesda)*. 2007;22:56-64.

Chapter 5

An *In Vitro* Model of Early- or No-Reperfusion Scars to Explain How Clinical Reentrant Arrhythmia Characteristics May Relate to Therapeutic Efficacy

Säid F. A. Askar*, **Zeinab Neshati***, Brian O. Bingen, Sebastiaan R.D. Piers, Katja Zeppenfeld, Martin J. Schalij, Antoine A.F. de Vries, Daniël A. Pijnappels

* Equal contribution

To be submitted

Abstract

Purpose: Early-reperfusion during acute myocardial infarction causes scars with a patchy aspect, whereas no reperfusion causes compact scars. Patchy scars show a lower inducibility and shorter cycle length of arrhythmias compared to compact scars. Despite increasing numbers of early-reperfused patients, little data on arrhythmic mechanisms is available. We therefore developed an *in vitro* model of patchy and compact scar patterns to gain a mechanistic understanding of associated arrhythmia characteristics and how these affect the efficacy of anti-arrhythmic interventions.

Methods: Neonatal rat Ventricular monolayers were locally ablated at day 6-7 of culture by a laser-cut plexiglass stamp that produced an anatomical obstruction to mimic a compact scar or a stamp that produced multiple smaller anatomical obstructions with an equal total outer obstruction diameter to mimic patchy scars. One day later, optical mapping was performed.

Results: Inducibility of reentry was slightly lower in patchy cultures compared to compact cultures (41%, n=34 vs 52%, n=23, $P<0.05$) and cycle length of reentry was shorter (234 ± 52 vs 288 ± 38 ms, $P<0.05$). Reentry was less frequently sustained in patchy cultures (40% vs 88% in compact cultures) while the percentage of complex arrhythmias was higher (31% vs 11%). Meandering was only found in patchy cultures and could result in local polymorphic pseudo-electrograms. A gradient of excitability during reentrant arrhythmias was only detectable in patchy cultures. Termination of reentry by electrical stimulation was more easily achieved in compact cultures (82% vs 20% in patchy cultures) while Nav1.5 blockade by tetrodotoxin only induced meandering in patchy cultures (67% of arrhythmic cultures). In smaller cultures, this resulted in more frequent termination of reentry in patchy cultures.

Conclusions: An *in vitro* model of patchy and compact obstructions reproduces arrhythmic characteristics observed after early- and non-reperfused myocardial infarctions. Furthermore, it may provide mechanistic insights into the efficacy of anti-arrhythmic interventions in different anatomical substrates.

Introduction

Over the past decades, treatment of acute myocardial infarction (AMI) has become increasingly effective by focusing on restoring cardiac blood supply as early as possible. During AMI, time-to-reperfusion is not only a critical determinant of survival, but also ultimately affects scar composition and size.¹⁻³ By early reperfusion, cardiomyocyte (CMC) survival is improved and as a result, post-infarction scars are smaller and contain surviving myocardial fibers that gives the scars a patchy aspect.² This is opposed to the compact, fibrous scars that are rich in fibroblasts and extracellular matrix that do not contain large amounts of CMCs. As early reperfusion is becoming increasingly widespread due to adherence to constantly improving guidelines that focus on early treatment of AMI, the patient population with patchy scars is vastly growing.⁴⁻⁶ Nevertheless, how scar composition affects arrhythmogenicity and arrhythmic phenotype is not completely clear. Recent clinical evidence suggests that inducibility of arrhythmias in early-reperfused patients was lower compared to non-reperfused patients.⁷ Moreover, reentrant cycle length (CL) is shorter in early-reperfused patients. However, the electrophysiological mechanisms for these observations have not been fully elucidated. More importantly, it is there unknown whether these different scar compositions can influence the efficacy of pharmacological or electrical defibrillatory treatment modalities. Therefore, the current study set out to 1) develop a simplified *in vitro* model to reproduce clinical findings of these different scar compositions and 2) utilize this model to investigate the mechanisms behind the different clinical findings to subsequently 3) investigate how these mechanisms influence therapeutic efficacy of electrical or pharmacological defibrillation as this is more difficult to investigate in a clinical setting.

Methods

All animal experiments were approved by the Animal Experiments Committee of the Leiden University Medical Center and conformed to the Guide for the Care and Use of Laboratory Animals as stated by the US National Institutes of Health.

Cell isolation and culture

Neonatal cardiomyocytes were isolated from 2-day old wistar rats as described previously.^{8,9} Animals were anesthetized by inhalation of 4-5% isoflurane. After pain reflexes were assured to be absent, hearts were rapidly excised and the ventricular tissue was minced and digested with collagenase I (450 units/ml; Worthington, NJ, USA) under gentle agitation. After a pre-plating step to minimize fibroblast contamination of cardiac cultures, cells were plated out on fibronectin-coated, round glass coverslips (22 mm) at a cell density of 1×10^6 cells/well in 12-well plates (Corning Life Sciences, Amsterdam, the Netherlands). In another subset of experiments, 15 mm coverslips were used in 24-wells plates (Corning Life Sciences) and cell density was 5×10^5 cells/well. Proliferation of endogenously present myofibroblasts was inhibited by administration of 10 $\mu\text{g}/\text{mL}$ Mitomycin-C (Sigma-Aldrich, St. Louis, MO, USA) at day 1 for 2 hours.⁸

Preparation of anatomical obstructions

To produce pre-defined configurations of cardiac tissue, a method of inducing local cell death using specialized stamps was utilized to mimic scar compositions from early or non-reperfused myocardium. Stamps were designed using CAD-software (Solidworks, Dassault Systèmes, Velizy-Villacoublay, France). Designs were laser-cut into plexiglass using a PLS3.60 Laser (Universal Lasersystems, Scottsdale, AZ, USA). Bottom surfaces were gently polished with 9 μm polishing paper to equalize surfaces. By carefully pressing these stamps onto cardiac cultures at day 6-7 of culture, these stamps formed the desired pattern in the cardiac cultures. Cultures were allowed to adjust for $\geq 6\text{h}$ after ablation before optical mapping was performed. Stamps that mimicked the compact scar composition had an outer diameter of 11.5 mm and lacked any clefts in order to ablate cells over the entire surface area of the stamp. In contrast, stamps to mimic patchy composition had the same outer diameter of 11.5 mm, but were comprised of smaller circles with a diameter of 1 mm and interpositioned clefts that allowed for the survival of myocardial cells throughout the ablated area.

Optical mapping

Arrhythmogenicity of cultures was evaluated using optical mapping as described previously.^{8,9} At day 7-8, cultures were loaded with 6 $\mu\text{mol}/\text{L}$ of the voltage-sensitive dye Di-4-ANEPPS (Invitrogen, Breda, the Netherlands) diluted in DMEM/Hams' F12

(Invitrogen) for 10 minutes at 37°C. Next, cultures were refreshed with warm (37°C) DMEM/HAMS F12 and immediately mapped. Cultures were never exposed to mapping conditions for >30 minutes, and cumulative exposure time to excitation light never exceeded 1 minute. Electrical stimulation was delivered for 10 ms at $\geq 1.5x$ diastolic threshold using custom-made platinum electrodes spaced either 1 mm (narrow bipolar) or 20 mm (wide bipolar) apart. Narrow bipolar stimulation was used to investigate conduction velocity (CV) and action potential duration (APD), while wide bipolar stimulation was used to induce or terminate reentry. To investigate the inducibility of reentry, burst stimulation was performed by wide bipolar 14 Hz 10 ms pulses. Reentry was defined as at least 3 consecutive circular activations. Reentry was considered not inducible after 6 unsuccessful attempts at induction with burst stimulation. Electrical termination of reentry was performed by wide bipolar burst stimulation. Optical signals were recorded using a 100 by 100 pixels CMOS camera (MiCAM Ultima-L, Scimedia Ltd, Costa Mesa, CA, USA) and several parameters were analyzed offline with Brainvision Analyze 1201 (Brainvision, Scimedia, Tokyo, Japan). CV was determined at least 3 times, directly perpendicular to the activation wavefront. Pharmacological interventions (tetrodotoxin (TTX), Alomone Labs, Jerusalem, Israel) were pipetted directly into the middle of the well, after which wells were gently agitated for 5 seconds to enhance distribution of the pharmacological agent. Excitability gradients were determined as the difference between CV at the spiral tip during an arrhythmia and the CV at the periphery.

Statistical analysis

Student t-tests were performed where appropriate. Statistical analyses were performed using SPSS 11.0 for Windows (SPSS, Inc., Chicago, IL, USA). Differences were considered statistically significant if $P < 0.05$.

Results

Partial or complete conduction block in cultures with patchy or compact obstructions

Neonatal rat ventricular monolayers were confluent and spontaneously beating by day 2 of culture and contained roughly 15% of non-myocytes as described previously.⁸ At day 5, cultures were ablated with custom-made probes to form either patchy or compact obstructions (Figure 1A). These ablations produced local areas of

cell death with smooth, circular edges and often removed the ablated cells altogether (Figure 1B). Cultures are referred to as “patchy” or “compact” cultures depending on the obstruction pattern produced by the ablations. Optical mapping at day 8 of culture showed that APD_{80} did not significantly differ between any of the groups (233 ± 76 ms and 249 ± 31 ms for patchy and compact cultures, respectively, $P>0.05$, Figure 1D). In addition, CV was similar for patchy and compact cultures (21.5 ± 2.1 cm/s and 21.1 ± 1.7 cm/s, respectively, $P>0.05$, Figure 1E). Therefore, the basic electrophysiology of these cultures was considered to be equal. However, the structural differences as produced by the ablations did cause different degrees of dyssynchrony across the ablated areas, as conduction was possible across the ablated area in patchy cultures but not in compact cultures. This resulted in a conduction delay of 70 ± 8 ms in patchy cultures vs 89 ± 6 ms in compact cultures across equal distances ($P<0.05$, Figure 1F). Thereby, partial or complete local conduction block was established in this culture model to mimic scar compositions after early- or no reperfusion of myocardial infarctions, respectively.

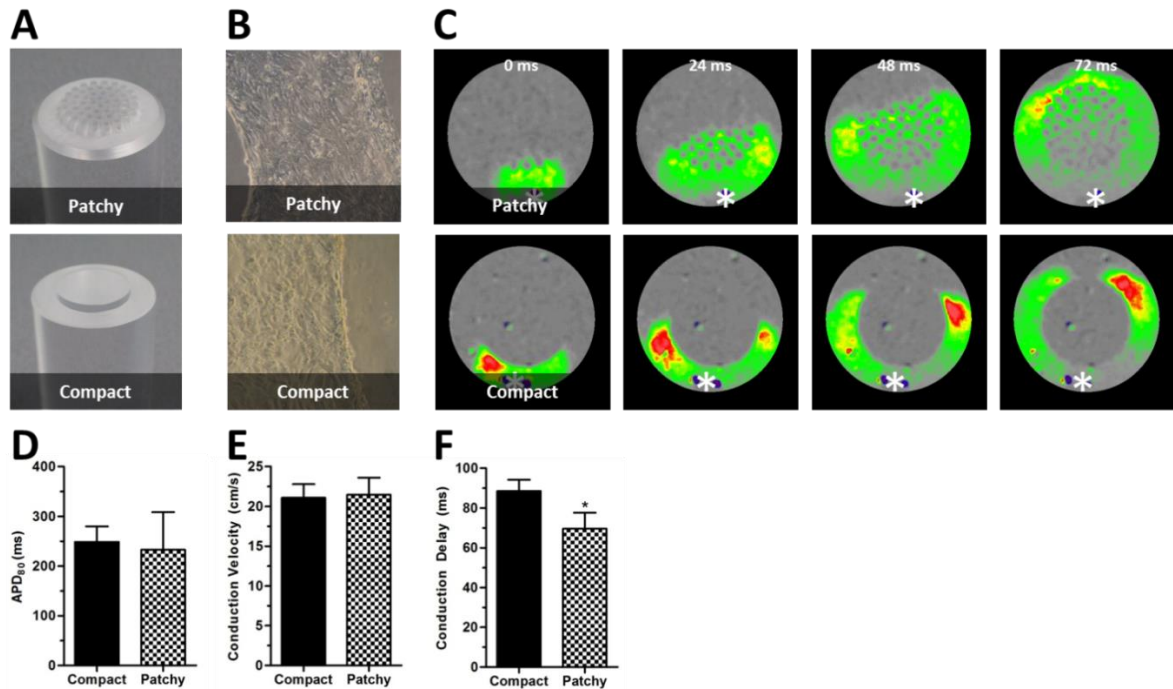


Figure 1. Local ablations in neonatal rat monolayers cause anatomical obstructions of conduction that do not affect basic electrophysiological parameters. **(A)** Pictures of the laser-cut plexiglass stamp that are used to perform **(B)** ablations of neonatal rat ventricular cardiomyocyte monolayers that produce surviving strands of cardiomyocytes and **(C)** non-conducting local anatomical obstructions as visualized by optical mapping. The (*) marks the site of electrical stimulation. Green, yellow and red signify activating tissue while gray marks inactive tissue. **(D)** APD₈₀ and **(E)** CV do not significantly differ between cultures treated with the compact probe and cultures treated with the patchy probe. **(F)** Conduction delay between edges across the ablated area is significantly higher in the cultures treated with the compact probe. *: $P < 0.05$ vs patchy cultures.

Patchy or compact obstructions reproduce clinical findings of differing inducibility, reentrant cycle length and complexity

In vivo, reentry in early reperfused hearts with patchy scars is less frequently inducible but has a shorter cycle. To investigate reproducibility of these findings in the current *in vitro* model, we performed burst stimulation during optical mapping experiments to induce reentrant tachyarrhythmias (Figure 2A, B). Inducibility of reentry was 41% in patchy (n=34) and 52% in compact scar cultures (n=23, Figure 2C). Moreover, while most of the reentry episodes in compact scar cultures were sustained (7 out of 8 reentry induction episodes), reentry in patchy scars was less frequently sustained (6 out of 15 episodes). Reentrant CL was shorter in patchy scar

cultures compared to compact scar cultures (234 ± 52 ms vs 288 ± 38 ms, $P < 0.05$, Figure 2D). Of these CLs, 62% of reentry in patchy cultures was < 250 ms, whereas in compact cultures, 24% was faster than 250 ms. Furthermore, CL adaptation was most pronounced in patchy cultures (decrease in CL within 1 minute of 50 ± 29 ms versus 24 ± 17 ms in compact scar cultures, $P < 0.05$).

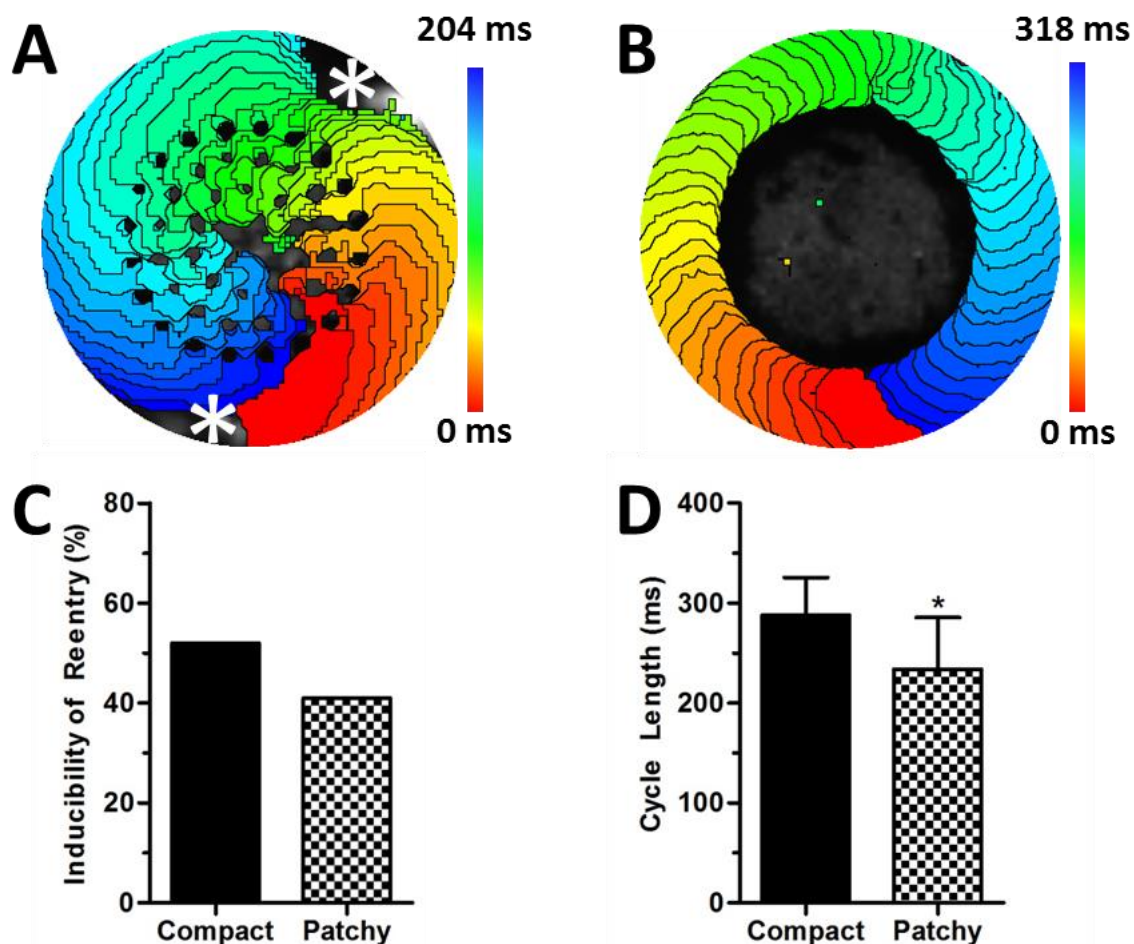


Figure 2. Reentrant tachyarrhythmias in cultures with patchy or compact obstructions. (A) Typical activation map of induced reentry in a culture with patchy obstructions. Isochronal spacing = 6 ms. The (*) marks the positions of the electrodes used to induce reentry by burst stimulation. (B) Typical activation map of induced reentry in a culture with a compact obstruction. Isochronal spacing = 6 ms. (C) Inducibility of reentry was slightly lower in patchy cultures. (D) Reentrant cycle length is shorter during reentry in cultures with patchy obstructions. *: $P < 0.05$.

Excitability gradient from core to periphery is only present during arrhythmias in patchy cultures

Next, to utilize the model and investigate electrophysiological parameters that are difficult to measure *in vivo*, more in-depth analyses of arrhythmias were performed. Complexity of arrhythmias was assessed within the first minute of induction. Interestingly, complexity of observed reentry in compact cultures rarely consisted of more than one activating wavefront (1 out of 9 reentry episodes, Figure 3A). In contrast, reentrant arrhythmias in patchy cultures could consist of multiple wavefronts (5 out of 16 reentry episodes, Figure 3B, C). Moreover, reentrant arrhythmias within patchy cultures were shown to meander following induction (15 reentry induction episodes with meandering found in 11 episodes, Figure 4A) while none out of 8 reentry induction episodes in compact cultures revealed any meandering as reentrant arrhythmias immediately stabilized. During meandering in patchy cultures, local pseudo-electrograms had a polymorphic appearance (Figure 4B). In contrast, all observed reentrant arrhythmias in compact cultures showed a monomorphic pseudo-electrogram (Figure 4C). Out of 9 non-sustained episodes of reentry induction in patchy cultures, 7 showed meandering which implied a role of meandering in the termination of these arrhythmias.

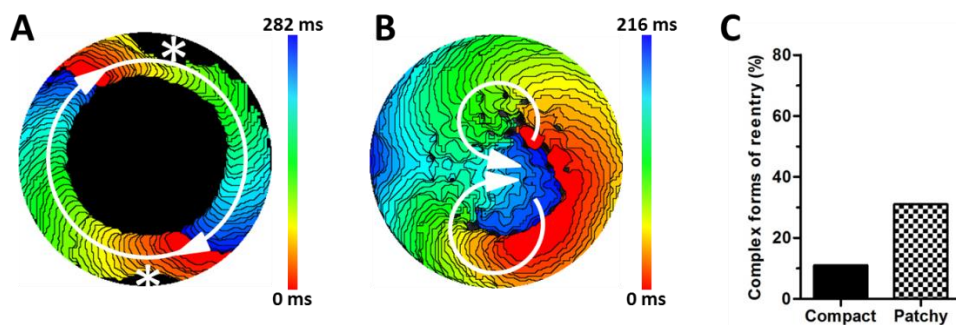


Figure 3. Complexity of reentrant arrhythmias. **(A)** Typical example of a complex reentrant arrhythmia in a culture with a compact obstruction showing multiple activational fronts. The (*) marks the locations of the electrodes that were used to induced reentry. **(B)** Typical activation map of a complex reentrant arrhythmia in a culture with patchy obstructions. Isochronal spacing = 6 ms. **(C)** Incidence of complex forms of reentrant arrhythmias was higher in cultures with patchy obstructions.

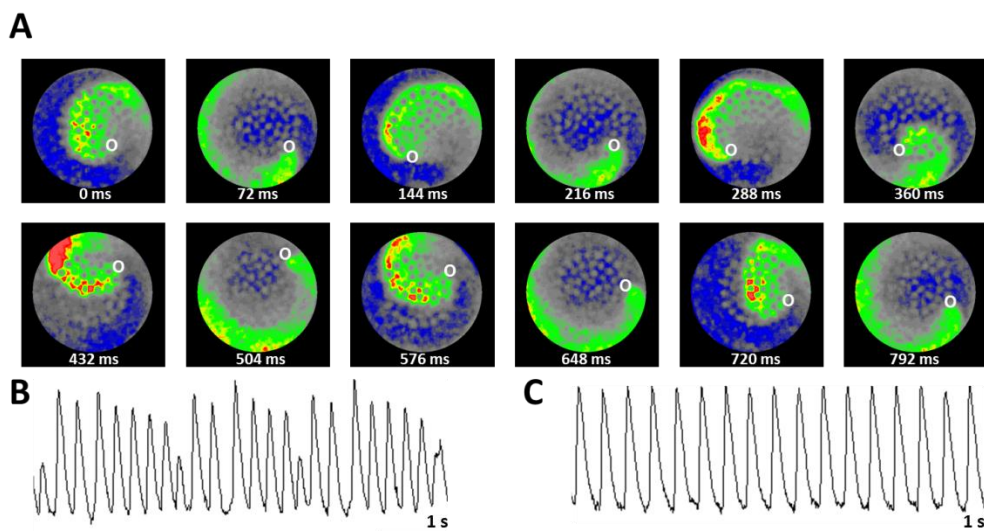


Figure 4. Rotor meandering in cultures with patchy obstructions gives rise to polymorphic pseudo-electrograms. **(A)** High-pass filtered pseudo-voltage map sequence showing meandering of a reentrant arrhythmia through the culture. The (O) marks the pivot point of reentry. Green, yellow and red signify activating tissue while gray signifies inactive tissue. Blue marks depolarizing tissue. **(B)** High-pass filtered pseudo-electrogram during meandering reentry in a culture with patchy obstructions shows a polymorphic appearance. **(C)** High-pass filtered pseudo-electrogram during non-meandering reentry, the only type of sustained reentry in compact cultures. These pseudo-electrograms were typically monomorphic.

During reentrant arrhythmias in patchy cultures, it was observed that the amplitude of the optical pseudo-voltage differed throughout the culture (Figure 5A). As changes in fluorescence of the used voltage-sensitive dye are an indication of changes in membrane potential, it appeared there was an excitability gradient during reentry in patchy cultures that was absent during reentry in compact cultures (Figure 5B).¹⁰ To substantiate this claim, CV was determined at locations nearest to the pivot point of reentry and peripheral to the pivot point in reentry, as CV is highly dependent on the excitability of cardiac tissue. A significant difference between these values was only detected for reentrant arrhythmias in patchy cultures. Moreover, values of these differences were (5.8 ± 0.3 cm/s) in patchy cultures vs (0.8 ± 1.1 cm/s) in compact cultures ($P < 0.05$, Figure 5C).

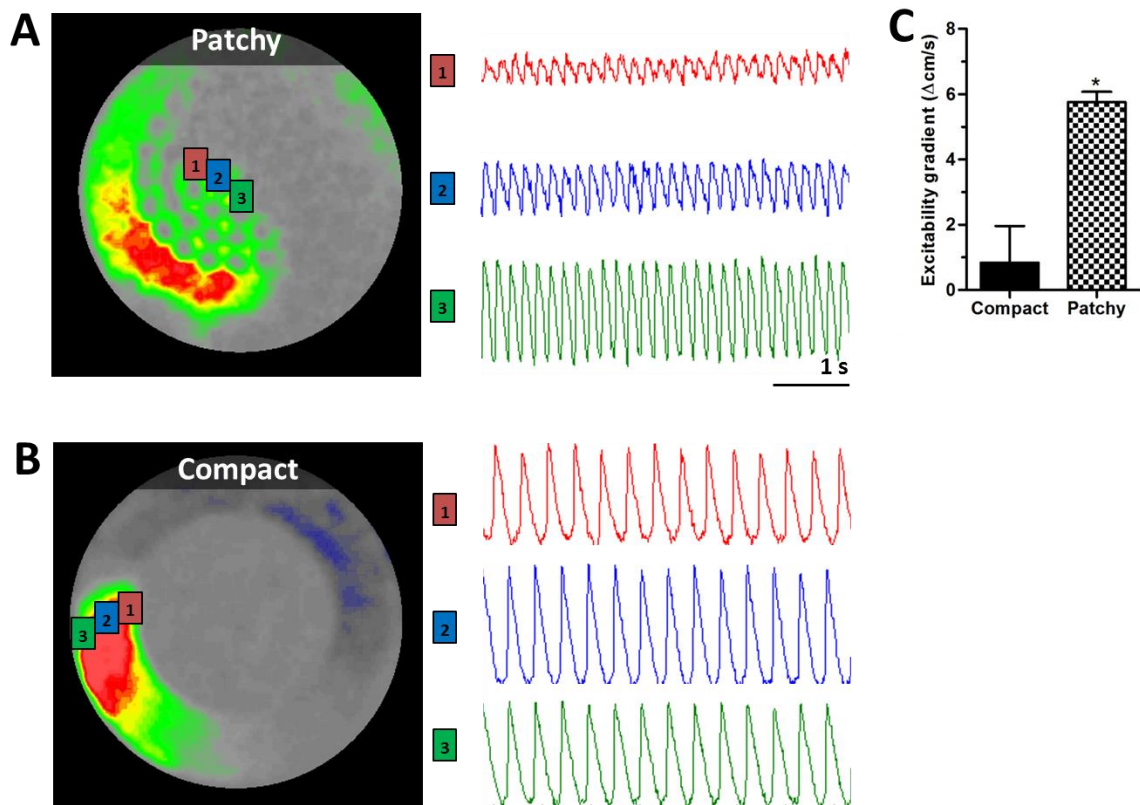


Figure 5. An excitability gradient during reentrant arrhythmias is only found in cultures with patchy obstructions. **(A)** Typical example of a high-pass filtered pseudo-voltage map with corresponding optical signals shows that optical signal amplitude increases from core to periphery during reentry in a patchy culture. Green, yellow and red signify activating tissue while gray marks inactive tissue. **(B)** Typical example of a high-pass filtered pseudo-voltage map with corresponding pseudo-voltage signals show that optical signal amplitude does not differ between the tissue nearest to the core of reentry or outer ring of tissue during reentry in a compact culture. Green, yellow and red signify activating tissue while gray marks inactive tissue. **(C)** During reentry, only patchy cultures showed a significant difference between the CV at the tissue nearest to the core of reentry and CV at the periphery. * $P < 0.05$.

Anti-arrhythmic efficacy of fast-sodium channel blockade and electrical stimulation depends on the anatomical configuration

To investigate the efficacy of fast sodium channel blockade, 20 μM TTX was administered during arrhythmias. After arrhythmias were confirmed to be stable and sustained for at least 30 seconds, TTX was directly pipetted in the middle of the culture. After such an intervention in patchy cultures, reentry started to wander

throughout the culture in 67% of 12 cultures, whereas 14 compact cultures did not show such an activity (Figure 6A). Interestingly, only 1 out of 12 arrhythmias terminated in patchy cultures despite strong meandering. Moreover, 2 out of 14 arrhythmias terminated in compact cultures after TTX administration. To investigate whether this may have been due to the size of the culture and multitude of small obstructions in these cultures that provide re-anchoring points for these arrhythmias, we performed the same intervention in smaller cultures (15 mm in diameter) with smaller and less obstructions (6 mm outer diameter). In these smaller patchy cultures, TTX administration often resulted in termination (88%, n=8 arrhythmias, Figure 6B). In contrast, TTX was less effective in compact cultures (25% terminated arrhythmias, n=8 arrhythmias).

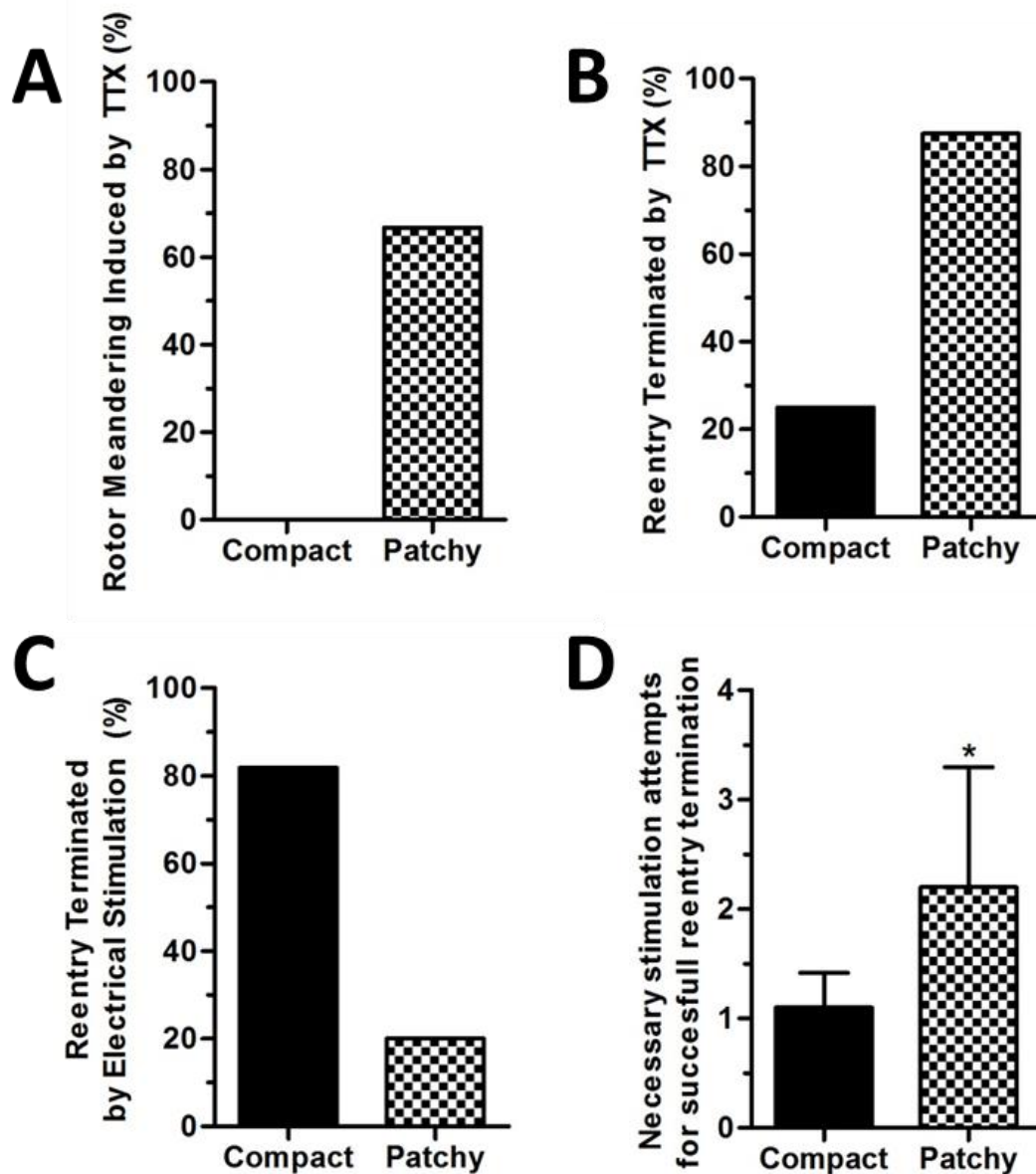


Figure 6. Effect of obstruction pattern on termination of reentry by sodium channel blockade or electrical stimulation. **(A)** Quantification of the percentage of arrhythmias that meander after TTX administration. **(B)** Quantification of the percentage of arrhythmias that terminate after administration of TTX in smaller cultures (total diameter of 15 mm and 6 mm outer diameter of the area of ablation) which shows that the induced meandering by TTX can be important for terminating arrhythmias. **(C)** Quantification of the percentage of reentrant arrhythmias that could be terminated by application of a bipolar 14 Hz electrical stimulation protocol. **(D)** Quantification of the number of attempts necessary to terminate reentry. *: $P < 0.05$.

Alternatively, electrical stimulation was investigated for its anti-arrhythmic efficacy. In compact cultures, reentry was terminated by burst stimulation in 9 out of 11 cultures (Figure 6C). In patchy cultures, 1 out of 5 reentrant arrhythmias terminated by a single attempt at burst stimulation. Overall, 2.2 ± 1 attempts of reentry termination by burst stimulation were necessary for successful reentry termination in patchy cultures, whereas 1.1 ± 0.3 attempts were necessary in compact cultures ($P < 0.05$, Figure 6D).

Discussion

Key findings of this study are 1) patchy or compact obstructions in a 2D cardiac model can reproduce clinical arrhythmic findings of early or non-reperused myocardial scars and 2) reveal an excitability gradient that is only present during reentrant arrhythmias in patchy scar cultures and 3) the absence or presence of this excitability gradient is responsible for differences in anti-arrhythmic outcome of electrical and pharmacological defibrillation.

Reproducibility of clinical findings in a simplified in vitro model

Over the past decades, timely reperfusion during AMI has been proven to be crucial in improving acute but also chronic survival.^{1,3} Duration of coronary artery occlusion is directly related to myocardial cell death, the transmural extent and size of the myocardial scar that develops.^{11,12} As early reperfusion strongly limits myocardial damage, the subsequent myocardial scar contains a lower collagen density than non-reperused scars. Importantly, early reperfusion also increases the amount of surviving cardiomyocytes within the infarction area which results in a patchy aspect of the scar.² Moreover, the pro-arrhythmic substrate that is formed by post-MI scars is altered in such a way that different arrhythmic characteristics are present in early- or non-reperused patients.⁷ However, it is unknown how early reperfusion affects the efficacy of electrical and pharmacological anti-arrhythmic interventions, despite a growing patient population due to better care and management of AMI. In the current study, an *in vitro* model of these patchy or compact scar compositions was developed to gain more insight into the mechanisms of differing arrhythmogenicity. By locally inducing cell death, anatomical obstructions were prepared in 2D neonatal rat cultures that allowed for surviving myocardial strands capable of conduction

through the scar in the patchy group but formed a solid, compact obstruction that blocked conduction in the compact scar group. As a result, dyssynchrony across the scar was higher in the compact group than in the patchy group. In the clinical setting, dyssynchrony also corresponds to obstruction size.¹³ Moreover, this model reproduced the difference in reentrant CL and due to the use of optical mapping, showed that this difference in CL can be explained by differing path lengths.⁷ While non-reperfused and early-reperfused patients without prior arrhythmias do not show a difference in the inducibility of reentry, inducibility is lower for early-reperfused patients that had prior arrhythmic episodes compared to non-reperfused patients with prior arrhythmic episodes.⁷ Remarkably, the inducibility of reentry in the current study can be positioned in between these findings as the inducibility of reentry in patchy cultures was slightly lower than in compact cultures. However, the electrophysiological equality of both groups in our model regarding APD and CV at 1Hz activation rate, and the observation that arrhythmic episodes can modify the electrical behavior of myocardial tissue to favor arrhythmias¹⁴ are arguments that suggest our model may be most relevant to patients without prior arrhythmias. Though the current model is based on neonatal rat cardiomyocytes and any direct comparison of parameters may appear arbitrary, it is peculiar that the clinically established criterion of “fast VT” with a CL below 250 ms can be applied to our model with similar outcomes.⁷ Besides the high degree of reproducibility of clinical findings in this *in vitro* model, the most promising implications of such a model lie in the potential for in-depth investigation of arrhythmic mechanisms.

Anatomical versus functional reentry and the relevance of an excitability gradient

Using the optical mapping technique, arrhythmic dynamics can be studied in detail with a high spatial and temporal resolution.^{15,16} Therefore, this technique was perfectly suited to further investigate arrhythmic mechanisms of reentry in cultures with patchy or compact obstructions in a manner that is currently difficult to realize *in vivo*. By visualizing conduction, it was found that reentry in patchy cultures exhibited features of a functional type of reentry, as wandering of the arrhythmia throughout the culture was observed in a relatively large portion of the cultures.^{17,18} In contrast, reentry in compact cultures did not show meandering and adhered more to the specifications of anatomical reentry.¹⁹ These differences can be explained by the differences in minimal obstacle size to which these arrhythmias pin to in patchy or in

compact cultures.²⁰ Therefore, the distinction between functional and anatomical reentry is based on a gradient rather than strictly separate phenomena.²¹ The smaller the object, the higher the degree of head-to-tail wave interaction and the more the arrhythmia resembles functional reentry. Moreover, the degree of head-to-tail wave interaction determines the excitability of the affected tissue by interfering with recovering ion channel dynamics. This also explains the presence of the excitability gradient in patchy cultures and its absence in compact cultures, as during functional reentry, the head-to-tail wave interaction is maximal at the pivot point of reentry and decreases towards the periphery. The relevance of such a gradient was demonstrated in the current study, as Nav1.5 blockade using TTX altered culture excitability and increased the probability of meandering in patchy cultures, but did not strongly affect arrhythmias in compact cultures apart from increasing the CL. The mechanism behind this destabilization depends on the altered source-sink relationships due to decreased excitability of the tissue by Nav1.5 blockade, which forces an increase in the minimal pivoting radius of the reentrant arrhythmia and detachment of the anatomical obstruction.²²⁻²⁵ By inducing meandering, reentry may be terminated as the core encounters inexcitable boundaries.^{20,26} Indeed, this was confirmed in the current study by repeating the same experiment in smaller cultures that made it more likely for the arrhythmia to encounter inexcitable boundaries. In addition, the excitability gradient also determines the excitable state of a culture. Due to the absence of a fully excitable gap during functional reentry, electrical stimulation during reentry in patchy cultures was less successful at termination than in compact cultures.¹⁹ This electrical stimulation was delivered with bipolar electrodes at a high frequency, so that it bears resemblance to anti-tachycardia pacing and defibrillation protocols. Taken together, this model may provide a useful tool to improve our current understanding of reentrant arrhythmia dynamics and to know how they influence therapeutic efficacy in early or non-reperfused patients.

Future perspectives and limitations

Despite the high reproducibility of clinical findings with the currently presented *in vitro* model, the authors recognize that its relevance to clinical situations needs to be substantially increased. While the current study made a clear distinction between the patchy anatomical composition after early reperfusion or the clear-cut compact scar composition without reperfusion for standardization purposes, the *in vivo* setting is

more complex, with for example borderzones that may exhibit features of both patchy and compact fibrosis. By gradually increasing the complexity of the anatomical configurations in this model, the model can be more tailored to such specific clinical situations in the future. Currently, ventricular cardiomyocytes from neonatal rats have been used to create a 2D monolayer of cells in which arrhythmic dynamics can be more easily interpreted than in 3D tissue preparations. These cells were utilized due to their ability to stay in culture for extended periods of time, to form confluent beating monolayers and their availability, as human adult CMCs cannot, despite their superior clinical relevance. However, with the recent discovery of induced pluripotent stem cells (iPS cells) that allow for the genetic reprogramming of somatic cells into cell types of different lineages such as cardiomyocytes, future studies will benefit from utilizing iPS-derived CMCs for their confluent monolayers.²⁷ Despite reported impurities and inefficiencies of cardiac differentiation of such reprogrammed cells,²⁸ very recent technological advancements²⁹ make it likely that purified human cardiac monolayers can be utilized to increase the relevance of *in vitro* models for the clinical setting in the near future. As these iPS-derived human cardiomyocytes may more accurately represent the patient-specific ion channel expression profile, such cells have already been used to demonstrate the feasibility of patient-specific drug-screening techniques.³⁰ The combination of human cardiomyocytes in monolayers with the anatomical compositions of their respective pro-arrhythmic substrate may therefore not only elucidate pro-arrhythmic mechanisms, but also provide a very powerful patient-specific anti-arrhythmic drug-screening tool in the near future.

Conclusions

An *in vitro* model of early- or non-reperfused post-myocardial infarction scars reproduces clinical arrhythmic findings. Importantly, this model allows for the investigation of arrhythmic mechanisms such as meandering and complexity of arrhythmias that is more difficult to realize in a clinical setting. Finally, this model may provide mechanistic insight in how these arrhythmic mechanisms influence the therapeutic efficacy of anti-arrhythmic interventions.

Acknowledgements

We wish to thank H. van der Stadt and R. van Leeuwen for excellent technical support.

Sources of Funding

This work was supported by the Dutch Heart Foundation (2008/B119) and the Netherlands Organization for Scientific Research (NWO; VENI grant (91611070), D.A.P).

Conflicts of Interest

None declared.

References

1. The effects of tissue plasminogen activator, streptokinase, or both on coronary-artery patency, ventricular function, and survival after acute myocardial infarction. The GUSTO Angiographic Investigators. *N Engl J Med.* 1993;329:1615-1622.
2. Wijnmaalen AP, Schalij MJ, von der Thusen JH, Klautz RJ, Zeppenfeld K. Early reperfusion during acute myocardial infarction affects ventricular tachycardia characteristics and the chronic electroanatomic and histological substrate. *Circulation.* 2010;121:1887-1895.
3. Lambert L, Brown K, Segal E, Brophy J, Rodes-Cabau J, Bogaty P. Association between timeliness of reperfusion therapy and clinical outcomes in ST-elevation myocardial infarction. *JAMA.* 2010;303:2148-2155.
4. Filardo G, Nicewander D, Ballard DJ. Changes over six years in administration of aspirin and beta blockers on arrival and timely reperfusion and in in-hospital and 30-day postadmission mortality in patients with acute myocardial infarction. *Am J Cardiol.* 2011;107:1421-1425.
5. Bassand JP, Danchin N, Filippatos G, Gitt A, Hamm C, Silber S, Tubaro M, Weidinger F. Implementation of reperfusion therapy in acute myocardial infarction. A policy statement from the European Society of Cardiology. *Eur Heart J.* 2005;26:2733-2741.
6. Schiele F, Hochadel M, Tubaro M, Meneveau N, Wojakowski W, Gierlotka M, Polonski L, Bassand JP, Fox KA, Gitt AK. Reperfusion strategy in Europe: temporal trends in performance measures for reperfusion therapy in ST-elevation myocardial infarction. *Eur Heart J.* 2010;31:2614-2624.
7. Piers SR, Wijnmaalen AP, Borleffs CJ, van Huls van Taxis CF, Thijssen J, van Rees JB, Cannegieter SC, Bax JJ, Schalij MJ, Zeppenfeld K. Early reperfusion therapy affects inducibility, cycle length, and occurrence of ventricular tachycardia late after myocardial infarction. *Circ Arrhythm Electrophysiol.* 2011;4:195-201.
8. Askar SF, Ramkisoensing AA, Schalij MJ, Bingen BO, Swildens J, van der Laarse A, Atsma DE, de Vries AA, Ypey DL, Pijnappels DA. Antiproliferative treatment of myofibroblasts prevents arrhythmias *in vitro* by limiting myofibroblast-induced depolarization. *Cardiovasc Res.* 2011; 90(2):295-304.

9. Askar SF, Bingen BO, Swildens J, Ypey DL, van der Laarse A, Atsma DE, Zeppenfeld K, Schalij MJ, de Vries AA, Pijnappels DA. Connexin43 silencing in myofibroblasts prevents arrhythmias in myocardial cultures: role of maximal diastolic potential. *Cardiovasc Res.* 2012;93:434-444.
10. Loew LM, Cohen LB, Dix J, Fluhler EN, Montana V, Salama G, Wu JY. A naphthyl analog of the aminostyryl pyridinium class of potentiometric membrane dyes shows consistent sensitivity in a variety of tissue, cell, and model membrane preparations. *J Membr Biol.* 1992;130:1-10.
11. Reimer KA, Lowe JE, Rasmussen MM, Jennings RB. The wavefront phenomenon of ischemic cell death. 1. Myocardial infarct size vs duration of coronary occlusion in dogs. *Circulation.* 1977;56:786-794.
12. Miyazaki S, Fujiwara H, Onodera T, Kihara Y, Matsuda M, Wu DJ, Nakamura Y, Kumada T, Sasayama S, Kawai C. Quantitative analysis of contraction band and coagulation necrosis after ischemia and reperfusion in the porcine heart. *Circulation.* 1987;75:1074-1082.
13. Nucifora G, Bertini M, Marsan NA, Delgado V, Scholte AJ, Ng AC, van Werkhoven JM, Siebelink HM, Holman ER, Schalij MJ, van der Wall EE, Bax JJ. Impact of left ventricular dyssynchrony early on left ventricular function after first acute myocardial infarction. *Am J Cardiol.* 2010;105:306-311.
14. Rostock T, Steven D, Lutomsky B, Servatius H, Drewitz I, Klemm H, Mullerleile K, Ventura R, Meinertz T, Willems S. Atrial fibrillation begets atrial fibrillation in the pulmonary veins on the impact of atrial fibrillation on the electrophysiological properties of the pulmonary veins in humans. *J Am Coll Cardiol.* 2008;51:2153-2160.
15. Chang MG, Zhang Y, Chang CY, Xu L, Emokpae R, Tung L, Marban E, Abraham MR. Spiral waves and reentry dynamics in an *in vitro* model of the healed infarct border zone. *Circ Res.* 2009;105:1062-1071.
16. Entcheva E, Lu SN, Troppman RH, Sharma V, Tung L. Contact fluorescence imaging of reentry in monolayers of cultured neonatal rat ventricular myocytes. *J Cardiovasc Electrophysiol.* 2000;11:665-676.
17. Pertsov AM, Davidenko JM, Salomonsz R, Baxter WT, Jalife J. Spiral waves of excitation underlie reentrant activity in isolated cardiac muscle. *Circ Res.* 1993;72:631-650.

18. Fenton FH, Cherry EM, Hastings HM, Evans SJ. Multiple mechanisms of spiral wave breakup in a model of cardiac electrical activity. *Chaos*. 2002;12:852-892.
19. Rudy Y. Reentry: insights from theoretical simulations in a fixed pathway. *J Cardiovasc Electrophysiol*. 1995;6:294-312.
20. Lim ZY, Maskara B, Aguel F, Emokpae R, Jr., Tung L. Spiral wave attachment to millimeter-sized obstacles. *Circulation*. 2006;114:2113-2121.
21. Xie F, Qu Z, Garfinkel A. Dynamics of reentry around a circular obstacle in cardiac tissue. *Phys Rev E*. 1998;58:6355-6358.
22. Cabo C, Pertsov AM, Davidenko JM, Jalife J. Electrical turbulence as a result of the critical curvature for propagation in cardiac tissue. *Chaos*. 1998;8:116-126.
23. Cabo C, Pertsov AM, Davidenko JM, Baxter WT, Gray RA, Jalife J. Vortex shedding as a precursor of turbulent electrical activity in cardiac muscle. *Biophys J*. 1996;70:1105-1111.
24. Athill CA, Ikeda T, Kim YH, Wu TJ, Fishbein MC, Karagueuzian HS, Chen PS. Transmembrane potential properties at the core of functional reentrant wave fronts in isolated canine right atria. *Circulation*. 1998;98:1556-1567.
25. Karagueuzian HS, Athill CA, Yashima M, Ikeda T, Wu TJ, Mandel WJ, Chen PS. Transmembrane potential properties of atrial cells at different sites of a spiral wave reentry: cellular evidence for an excitable but nonexcited core. *Pacing Clin Electrophysiol*. 1998;21:2360-2365.
26. Takemoto Y, Takanari H, Honjo H, Ueda N, Harada M, Kato S, Yamazaki M, Sakuma I, Opthof T, Kodama I, Kamiya K. Inhibition of intercellular coupling stabilizes spiral-wave reentry, whereas enhancement of the coupling destabilizes the reentry in favor of early termination. *Am J Physiol Heart Circ Physiol*. 2012;303:H578-H586.
27. Lee P, Klos M, Bollensdorff C, Hou L, Ewart P, Kamp TJ, Zhang J, Bizy A, Guerrero-Serna G, Kohl P, Jalife J, Herron TJ. Simultaneous voltage and calcium mapping of genetically purified human induced pluripotent stem cell-derived cardiac myocyte monolayers. *Circ Res*. 2012;110:1556-1563.
28. Chen JX, Krane M, Deutsch MA, Wang L, Rav-Acha M, Gregoire S, Engels MC, Rajarajan K, Karra R, Abel ED, Wu JC, Milan D, Wu SM. Inefficient

- reprogramming of fibroblasts into cardiomyocytes using Gata4, Mef2c, and Tbx5. *Circ Res.* 2012;111:50-55.
29. Zhang J, Klos M, Wilson GF, Herman AM, Lian X, Raval KK, Barron MR, Hou L, Soerens AG, Yu J, Palecek SP, Lyons GE, Thomson JA, Herron TJ, Jalife J, Kamp TJ. Extracellular matrix promotes highly efficient cardiac differentiation of human pluripotent stem cells: the matrix sandwich method. *Circ Res.* 2012;111:1125-1136.
 30. Malan D, Friedrichs S, Fleischmann BK, Sasse P. Cardiomyocytes obtained from induced pluripotent stem cells with long-QT syndrome 3 recapitulate typical disease-specific features *in vitro*. *Circ Res.* 2011;109:841-847.

Chapter 6

Atrium-Specific Kir3.x Determines Inducibility, Dynamics, and Termination of Fibrillation by Regulating Restitution-Driven Alternans

Brian O. Bingen, **Zeinab Neshati**, Saïd F.A. Askar, Ivan V. Kazbanov, Dirk L. Ypey, Alexander V. Panfilov, Martin J. Schalij, Antoine A.F. de Vries, Daniël A. Pijnappels

Circulation. 2013;128:2732-2744.

Abstract

Background—Atrial fibrillation is the most common cardiac arrhythmia. Ventricular proarrhythmia hinders pharmacological atrial fibrillation treatment. Modulation of atrium-specific Kir3.x channels, which generate a constitutively active current ($I_{K,ACH-c}$) after atrial remodeling, might circumvent this problem. However, it is unknown whether and how $I_{K,ACH-c}$ contributes to atrial fibrillation induction, dynamics, and termination. Therefore, we investigated the effects of $I_{K,ACH-c}$ blockade and Kir3.x downregulation on atrial fibrillation.

Methods and Results—Neonatal rat atrial cardiomyocyte cultures and intact atria were burst paced to induce reentry. To study the effects of Kir3.x on action potential characteristics and propagation patterns, cultures were treated with tertiapin or transduced with lentiviral vectors encoding *Kcnj3*- or *Kcnj5*-specific shRNAs. Kir3.1 and Kir3.4 were expressed in atrial but not in ventricular cardiomyocyte cultures. Tertiapin prolonged action potential duration (APD; 54.7 ± 24.0 to 128.8 ± 16.9 milliseconds; $P < 0.0001$) in atrial cultures during reentry, indicating the presence of $I_{K,ACH-c}$. Furthermore, tertiapin decreased rotor frequency (14.4 ± 7.4 to 6.6 ± 2.0 Hz; $P < 0.05$) and complexity (6.6 ± 7.7 to 0.6 ± 0.8 phase singularities; $P < 0.0001$). Knockdown of *Kcnj3* or *Kcnj5* gave similar results. Blockade of $I_{K,ACH-c}$ prevented/terminated reentry by prolonging APD and changing APD and conduction velocity restitution slopes, thereby altering the probability of APD alternans and rotor destabilization. Whole-heart mapping experiments confirmed key findings (eg, $>50\%$ reduction in atrial fibrillation inducibility after $I_{K,ACH-c}$ blockade).

Conclusions—Atrium-specific Kir3.x controls the induction, dynamics, and termination of fibrillation by modulating APD and APD/conduction velocity restitution slopes in atrial tissue with $I_{K,ACH-c}$. This study provides new molecular and mechanistic insights into atrial tachyarrhythmias and identifies Kir3.x as a promising atrium-specific target for antiarrhythmic strategies.

Keywords: action potentials, arrhythmia, atrial fibrillation, cardiomyocyte, G protein-coupled inwardly rectifying potassium channels, RNA interference, voltage-sensitive dye imaging

Introduction

Atrial fibrillation (AF), the most common cardiac rhythm disorder in humans, contributes substantially to morbidity, mortality, and healthcare costs.¹⁻³ Ablation techniques, breaking up AF circuits or triggers, have improved the outcome of AF in the past decades.⁴ Although the success rate of AF ablation is relatively high in paroxysmal AF, in permanent AF, ablation restores sinus rhythm in only a fraction of patients by altering the underlying mechanisms and structural changes of the atrial myocardium. Importantly, there is a lack of consensus on the optimal ablation strategy in these patients, and this population is vastly growing.^{5,6} In addition, ablation procedures are associated with a risk of complications because of their invasive nature.⁷ Furthermore, long-term maintenance of sinus rhythm requires repeated procedures or continuation of antiarrhythmic drugs in a significant proportion of chronic AF patients.⁸ Hence, the first-line treatment of AF is still pharmacological.⁴ However, the use of antiarrhythmic agents is hampered by potentially lethal ventricular proarrhythmia, lack of efficacy, and serious side effects.⁹⁻¹³ Thus, research on AF treatment has focused on finding atrium-selective drugs with higher efficacy in AF rhythm control but fewer side effects such as ventricular proarrhythmia.

In the heart of most mammals, including humans, the acetylcholine-activated potassium current ($I_{K,ACh}$) is found exclusively in the atrium.¹⁴ Hence, $I_{K,ACh}$ is one of the novel candidates for atrium-specific drug treatment. Activation of $I_{K,ACh}$ by acetylcholine has been shown to shorten action potential (AP) duration (APD) in the atria.¹⁵ In patients suffering from persistent AF and atrial remodeling, $I_{K,ACh}$ can become constitutively active.^{16,17} Whether this constitutively active acetylcholine-inducible current ($I_{K,ACh-c}$) affects AF induction, dynamics, or termination, the mechanisms by which it could do so, and the channels involved in this process remain to be elucidated.

To test whether and how $I_{K,ACh-c}$ affects fibrillation, a 2-dimensional *in vitro* model of atrial tissue and a whole-heart model of AF were developed using atrial neonatal rat cardiomyocytes (nrCMCs) and hearts with endogenous $I_{K,ACh-c}$. With these models, fibrillation could be systematically and reproducibly studied. Inhibition of Kir3.1 or Kir3.4 activity by the highly specific drug tertiapin or lentiviral vector (LV)-mediated RNA interference (RNAi) was used to study the role of $I_{K,ACh-c}$ in AF initiation, dynamics, and termination.

Clinical Perspective

Noninvasive atrial fibrillation (AF) therapies are based on 2 separate strategies: rate or rhythm control aiming to slow ventricular rate to normal or to restore sinus rhythm, respectively. Hence, in rate control, AF itself is not resolved, whereas the curtailment of ventricular frequency reduces exercise tolerance. Rhythm control, on the other hand, is hampered by adverse effects such as ventricular proarrhythmia. Therefore, better insight into the contribution of ion channels, present in the atria but not the ventricles, to AF and the concordant exploration of possible atrium-specific therapies are essential if we are to diminish the burden of adverse effects in AF treatment. Previous studies showed that the acetylcholine-dependent potassium current ($I_{K,ACH}$), governed by the atrium-specific Kir3.x channels, can become constitutively active ($I_{K,ACH-C}$) in patients with AF. In the present study, we demonstrate the contribution of $I_{K,ACH-C}$ and Kir3.x to the initiation, maintenance, and termination of AF. We show for the first time that $I_{K,ACH-C}$ increases the chance of AF initiation through its steepening effects on the action potential duration and conduction velocity restitution curves, causing action potential duration and amplitude alternans. In addition, $I_{K,ACH-C}$ is shown to facilitate AF maintenance by stabilizing rotor dynamics, whereas AF termination can be elicited by blockade of $I_{K,ACH-C}$, causing alternans-mediated rotor destabilization. Our findings provide evidence for a causal relationship between $I_{K,ACH-C}$, alternans, and the initiation, maintenance, and termination of AF. Thus, not only $I_{K,ACH-C}$ or Kir3.x but also its consequent alternans might be an interesting atrium-specific target for future AF rhythm control or pharmacological cardioversion.

Methods

A detailed description of materials and methods can be found in the online-only Data Supplement.

All animal experiments were approved by the Animal Experiments Committee of the Leiden University Medical Center and conformed to the *Guide for the Care and Use of Laboratory Animals* as stated by the US National Institutes of Health.

Cell Isolation and Culture

After careful separation of the atria and ventricles of neonatal Wistar rat hearts, cardiomyocytes were isolated by collagenase digestion and plated on fibronectin-coated, round glass coverslips (15-mm diameter) at a density of 2 to 8×10^5 cells per well in 24-well cell culture plates, as described previously.¹⁸ To restrict unwanted expansion of the remaining nonmyocytes, cell proliferation was inhibited by incubation with mitomycin-C (10 $\mu\text{g}/\text{mL}$; Sigma-Aldrich, St. Louis, MO) for 2 hour at day 1 of culture.¹⁹

Western Blotting

Cardiomyocytes were lysed in 50 mmol/L Tris-HCl (pH 8.0), 150 mmol/L NaCl, 1% Triton X-100, 0.5% sodium deoxycholate, and 0.1% sodium dodecyl sulfate. Three 15-mm wells, each seeded with 8×10^5 cells, were used for each sample, and each experiment consisted of at least 4 samples. The proteins in the lysate were size fractionated in NuPage Novex 12% Bis-Tris gels (Life Technologies, Bleiswijk, the Netherlands) and transferred to Hybond polyvinylidene difluoride membranes (GE Healthcare, Diegem, Belgium). Membranes were blocked in Tris-based saline, 0.1% Tween-20, and 5% BSA (Sigma-Aldrich) for 1 hour. Next, membranes were incubated with antibodies directed against Kir3.1 (Alomone Labs, Jerusalem, Israel), Kir3.4 (Santa Cruz Biotechnology, Dallas, TX), or GAPDH (loading control; Merck Millipore, Billerica, MA) and corresponding horseradish peroxidase-conjugated secondary antibodies (Santa Cruz Biotechnology) for 1 hour. Chemiluminescence was detected with the ECL Prime Western Blotting Detection Reagent (GE Healthcare).

Optical Mapping

At day 9 of culture, investigation of AP propagation on a whole- culture scale by optical mapping (with di-4-ANEPPS [Life Technologies] as a voltage-sensitive dye) and subsequent data analyses were performed as described previously.¹⁸ During optical mapping, cells were stimulated electrically with a custom-made, epoxy-coated unipolar platinum electrode with square suprathreshold electric stimuli at 1 and 2 to 20 Hz (2-Hz increments). Burst pacing with a cycle length of 20 to 100 milliseconds was used to induce reentry. Complexity was defined as the number of phase singularities (PSs) per 1 cm^2 , determined by using the phase space method, as

described previously.¹⁸ The effect of several drugs (100 nmol/L tertiapin [Alomone Labs], 200 nmol/L atropine [Sigma-Aldrich], and 2 μ mol/L carbachol [Sigma-Aldrich])¹⁶ was studied by pipetting them directly into the medium and dispersing them by gentle agitation, followed immediately by optical mapping.

Whole-heart mapping was performed by incubating neonatal rat hearts with 2 μ mol/L di-4-ANEPPS in a tissue bath containing oxygenated Tyrode solution (comprising [in mmol/L] NaCl 130, CaCl₂ 1.8, KCl 4.0, MgCl₂ 1.0, NaH₂PO₄ 1.2, NaHCO₃ 24, and glucose 5.5, pH 7.4). Before excision of the heart, the left ventricle was injected with Tyrode solution supplemented with 20 mmol/L 2,3-butanedione monoxime (Sigma-Aldrich) to minimize motion artifacts with or without 200 nmol/L tertiapin to block the Kir3.x channels. During whole-heart mapping, AF was induced by burst pacing at a cycle length of 20 to 100 milliseconds with a custom-made bipolar platinum electrode.

RNA Interference

Kir3.1 and Kir3.4 expression in neonatal rat atrial cell cultures was selectively inhibited with self-inactivating LVs encoding shRNAs specific for rat *Kcnj3* (LV-Kir3.1 \downarrow) and *Kcnj5* (LV-Kir3.4 \downarrow), respectively. The shuttle constructs to generate these LVs are derivatives of plasmid SHC007 from the Mission shRNA library (Sigma-Aldrich) in which the *Photinus pyralis luciferase* (*PpLuc*)-specific shRNA-coding sequence was replaced by a rat *Kcnj3*- or *Kcnj5*-specific shRNA-coding sequence, and the marker gene cassette consisting of the human *phosphoglycerate kinase 1* gene promoter and the puromycin-*N*-acetyltransferase-coding sequence was substituted by the human *eukaryotic translation elongation factor 1 alpha 1* gene promoter and the *Aequorea victoria* enhanced green fluorescent protein-coding sequence. The negative control vector (LV-PpLuc \downarrow) had the same genetic makeup except that it contained the aforementioned *PpLuc*-specific shRNA-coding sequence.

Statistical Analysis

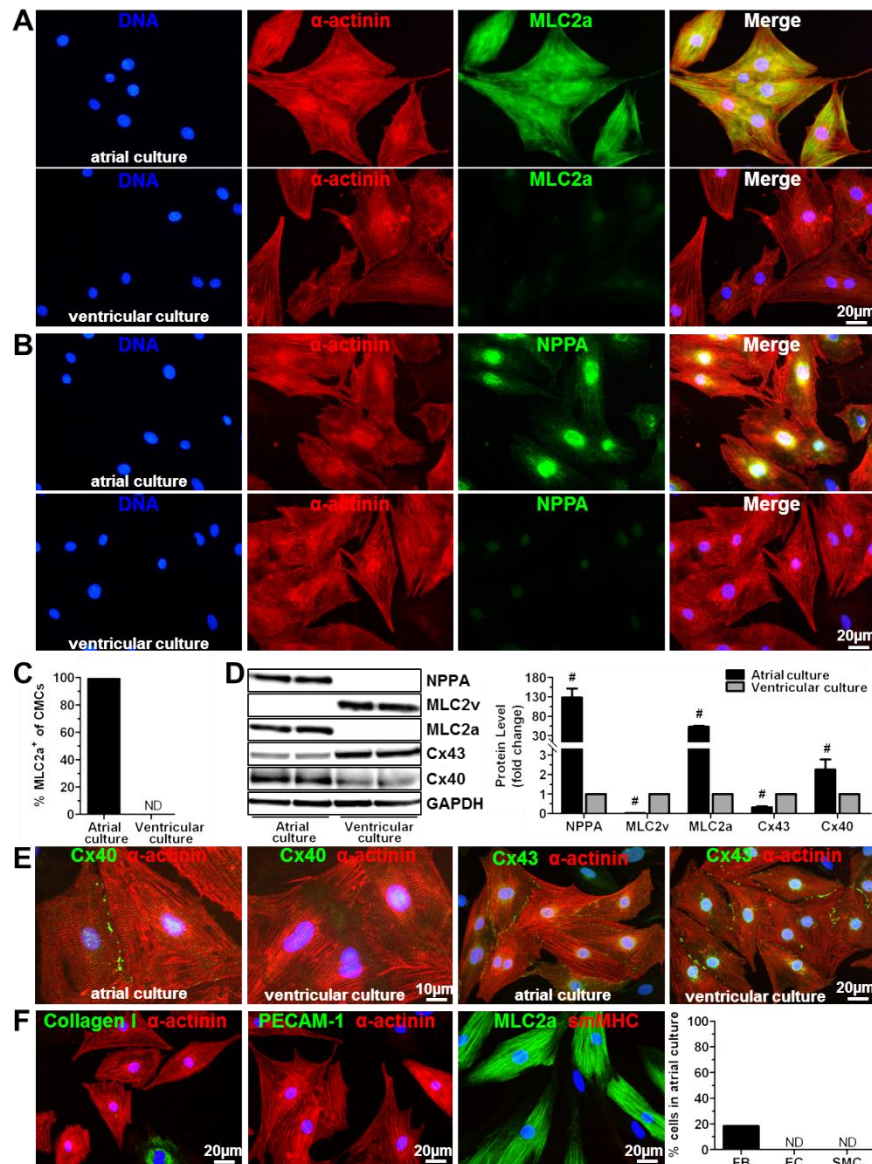
Statistical analyses were performed with SPSS11.0 for Windows (SPSS, Chicago, IL). Comparison between 2 groups was performed with the Mann-Whitney *U* test, the Wilcoxon signed-rank test, or the Fisher exact test as appropriate. Kruskal-Wallis testing with Bonferroni post hoc correction was used for multiple groups and comparisons. Data were expressed as mean \pm SD for a number of observations.

Differences were considered statistically significant at $P < 0.05$. Nonlinear regression curves were constructed by using a robust exponential 1-phase decay curve fit. Accuracy of these curves was expressed as the coefficient of determination (R^2). R^2 was calculated by the formula $R^2 = 1 - (SS_{\text{reg}}/SS_{\text{tot}})$, where SS_{reg} is the regression sum of squares (the sum of the square vertical distances of individual points to the regression curve) and SS_{tot} is the total sum of squares (the sum of the square vertical distances to the mean of all Y values).

Results

Cell Culture Characteristics

A detailed characterization of atrial and ventricular nrCMC cultures by immunocytology and Western blotting can be found in Supplemental Figure I in the online-only Data Supplement.



Supplemental Figure I. Typical examples of immunocytological double staining of (A) MLC2a (green) and α -actinin (red) and (B) NPPA (green) and α -actinin (red) in atrial (upper panels) and ventricular (lower panels) neonatal rat CMC cultures. (C) Quantification of MLC2a and α -actinin double-positive cells in atrial and ventricular neonatal rat CMC cultures. (D) Western blot analysis (left) and quantification (right) of NPPA, MLC2v, MLC2a, Cx43 and Cx40 levels in atrial and ventricular neonatal rat CMC cultures using GAPDH as loading control. (E) Immunocytological double staining of Cx40 (green) and α -actinin (red) and of Cx43 (green) and α -actinin (red) in atrial (1st and 3rd panel from the left, respectively) and ventricular (2nd and 4th panel from the left, respectively) neonatal rat CMC cultures. (F) Immunocytological double staining of collagen type I (green, left) and PECAM-1 (green, middle) with α -actinin (red) and of MLC2a (green, right) with smMHC (red, right). The corresponding quantification of fibroblasts (FB), endothelial cells (EC) and smooth muscle cells (SMC) is depicted on the far right. #: p < 0.05 vs ventricular cultures, ND: not detected.

Activation Pattern Characteristics in Atrial nrCMC Cultures

During optical mapping, atrial cultures showed uniform, convex, and fast activation originating from the electrode on 1-Hz stimulation (Figure 1A). After burst pacing, reentry was induced in the vast majority of atrial cultures. In 46 of 49 of these arrhythmic cultures, the activation patterns remained stable during each cycle of reentry, and the number and spatial dispersion of PSs did not change during 6 seconds of mapping (Figure 1B and Movie 1 in the online-only Data Supplement). Return mapping (plotting a peak-to-peak interval against the subsequent peak-to-peak interval) and time series of the peak-to-peak intervals showed that through such a fixed activation pattern and PS position, these arrhythmias had period-1 (P-1) oscillatory dynamics (ie, all rotor periods had approximately the same length; Figure IIA, IIC, and IIE in the online-only Data Supplement). Interestingly, the remaining 6% of cultures showed changes in activation pattern, PS number, and PS position for each reentrant cycle (Figure 1C and Movie 2 in the online-only Data Supplement). Return mapping and time series of the peak-to-peak intervals in these cultures showed period >1 or aperiodical oscillatory dynamics (ie, the wave front rotation alternated between >1 different periods or showed a different period during each cycle; Supplemental Figure IIB, IID, and IIF in the online-only Data Supplement).

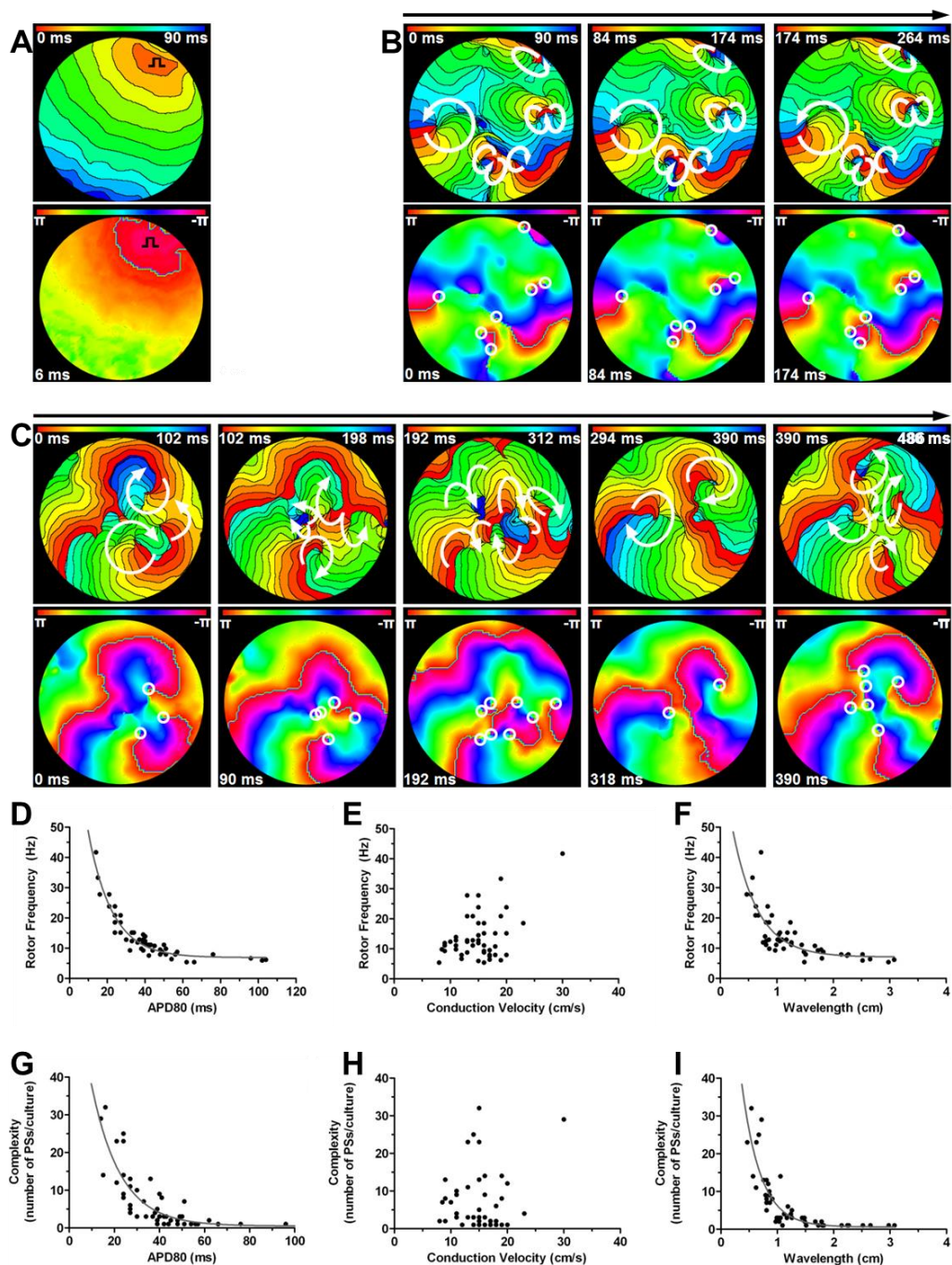
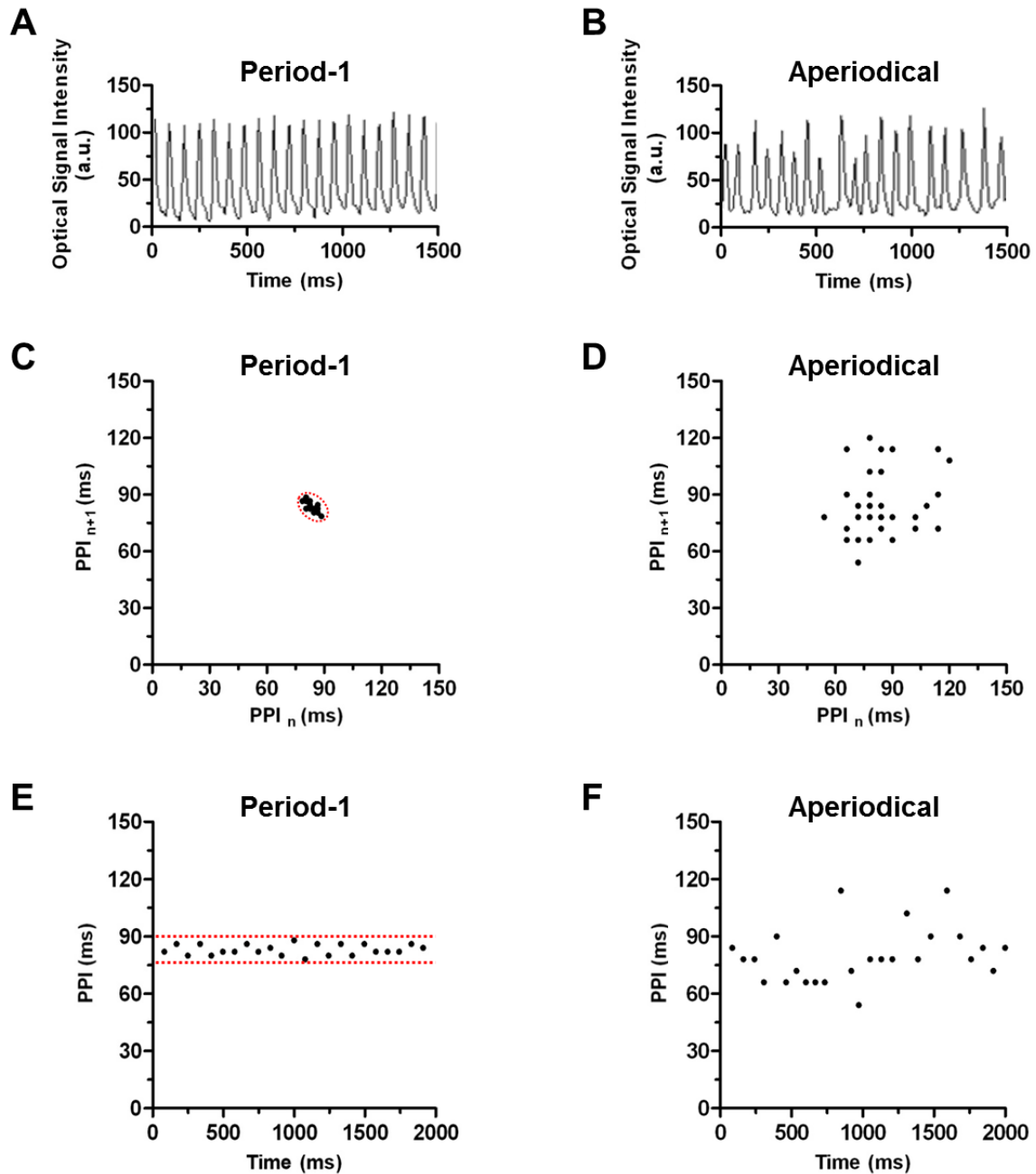


Figure 1. Activation maps (**top**; 6-millisecond isochrone spacing) and corresponding phase maps (**bottom**) of atrial neonatal rat cardiomyocyte cultures during (A) 1-Hz activation showing uniform propagation, (B) 3 subsequent reentrant cycles after burst pacing showing a stable activation pattern and phase singularity (PS) density and localization during each cycle, and (C) 5 subsequent reentrant cycles after burst pacing showing changes in activation pattern and PS density and localization during each cycle. The direction of activation is indicated by the white arrows; PSs are depicted as white circles. Relationship between rotor frequency and (D) APD80, (E) conduction velocity (CV), and (F) wavelength and between complexity of reentry and (G) APD80, (H) CV, and (I) wavelength.



Supplemental Figure II. Typical examples of the optical signal in neonatal rat atrial CMC cultures with (A) period-1 and (B) aperiodical reentry after burst pacing. Return maps of the peak-to-peak interval (PPI) sequences in an atrial CMC culture after burst pacing with (C) period-1 reentry, characterized by monofocal clustering in the return map and (D) aperiodical reentry, characterized by the absence of clustering in the return map. Time series of the PPIs in an atrial CMC culture with (E) period-1 (corresponding with Supplemental Figure IIA,C and Figure 1B in the main manuscript) and (F) aperiodical reentry (corresponding with Supplemental Figure IIB,D and Figure 1C in the main manuscript). The red dotted lines indicate clustering of PPI sequences and PPIs in the return maps and time series, respectively.

During burst pacing–induced reentry (including both the stable and unstable cases of reentry, $n=49$), rotor frequency showed a hyperbolic-like relationship with both APD_{80} ($R^2=0.91$) and wavelength ($R^2=0.63$). No apparent relation was found between rotor frequency and conduction velocity (CV; Figure 1D–1F). Moreover, the number of rotors negatively correlated with wavelength ($R^2=0.73$) and APD_{80} ($R^2=0.70$). Again, CV, other than its effects on wavelength, did not show a strong individual correlation with the number of PSs during reentry (Figure 1G–1I). These results show that fibrillatory activation in this model can be maintained by P-1 or period >1 /aperiodical reentry. Furthermore, the correlation analyses suggest that prolongation of atrial APD and wavelength during AF could decrease rotor frequency and complexity, possibly leading to the prevention or termination of AF.

Blockade of Atrium-Specific $I_{K,ACh}$ Decreases Rotor Frequency, Complexity, and Inducibility of Reentry

Atrial nrCMCs abundantly expressed Kir3.1 and Kir3.4 compared with ventricular nrCMCs ($100.0\pm 6.3\%$ versus $18.3\pm 0.7\%$ and $100\pm 2.8\%$ versus $7.8\pm 2.0\%$, respectively; $P<0.05$; $n=4$ per group) as judged by Western blot analyses (Figure 2A). Therefore, Kir3.x could be a target for blockade in an attempt to selectively prolong atrial APD, thereby preventing or terminating AF. To test this hypothesis, both atrial and ventricular nrCMC cultures were treated with 100 nmol/L tertiapin, a specific blocker of $I_{K,ACh}$.¹⁶ Tertiapin significantly increased APD_{80} in atrial nrCMCs during 1-Hz pacing (from 56.5 ± 12.5 to 145.5 ± 20.6 milliseconds; $P<0.0001$; $n=33$; Figure 2B) in the absence of exogenous acetylcholine, showing the presence of $I_{K,ACh-c}$ in these cells (see also Results and Supplemental Figure III in the online-only Data Supplement). Tertiapin had no significant effect on APD in ventricular nrCMCs ($n=12$; Figure 2C). Hence, the increase in APD_{80} induced by tertiapin was significantly larger in atrial nrCMCs (86.7 ± 19.6 versus 9.5 ± 9.9 milliseconds in ventricular nrCMCs; Figure 2D).

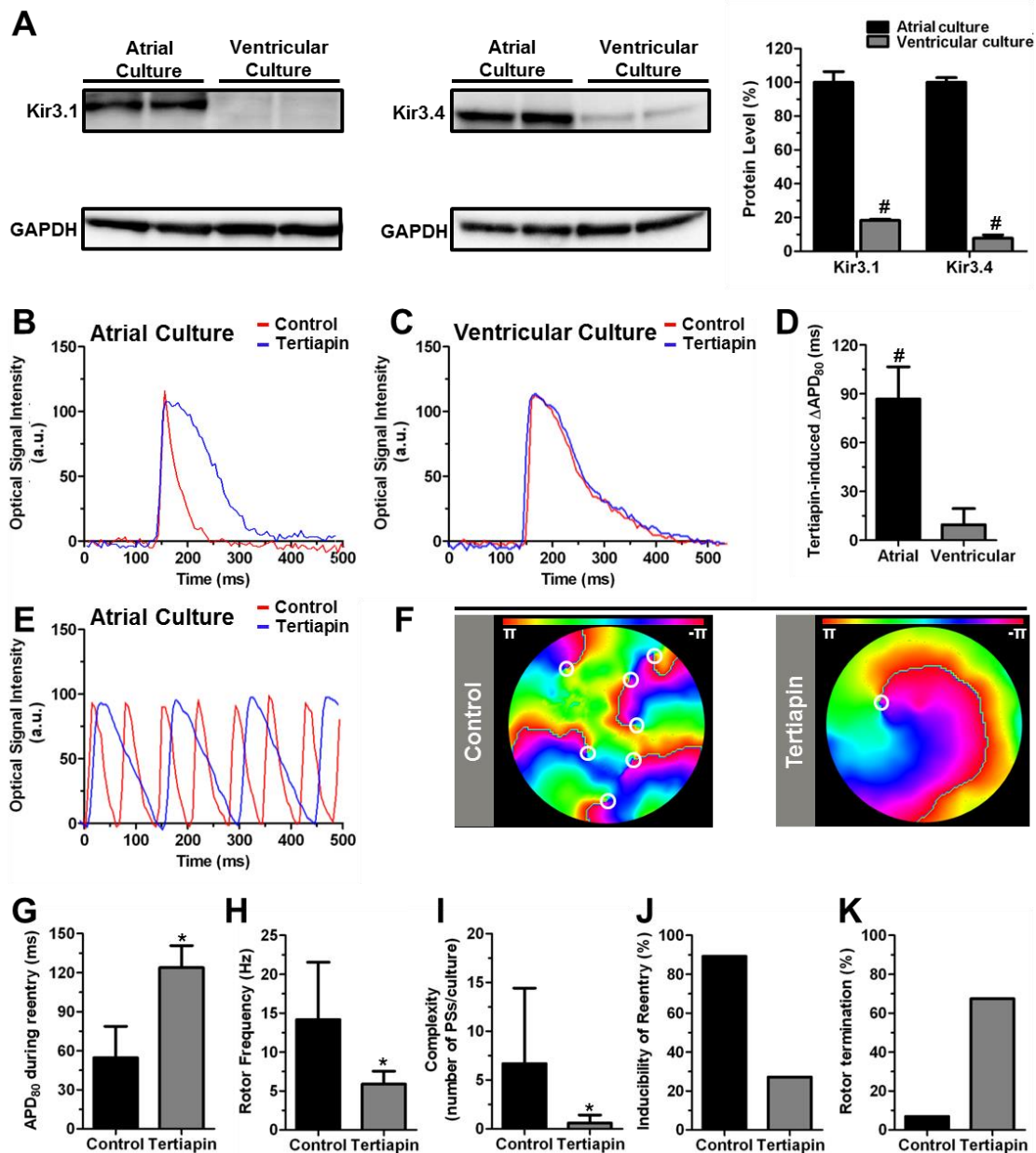
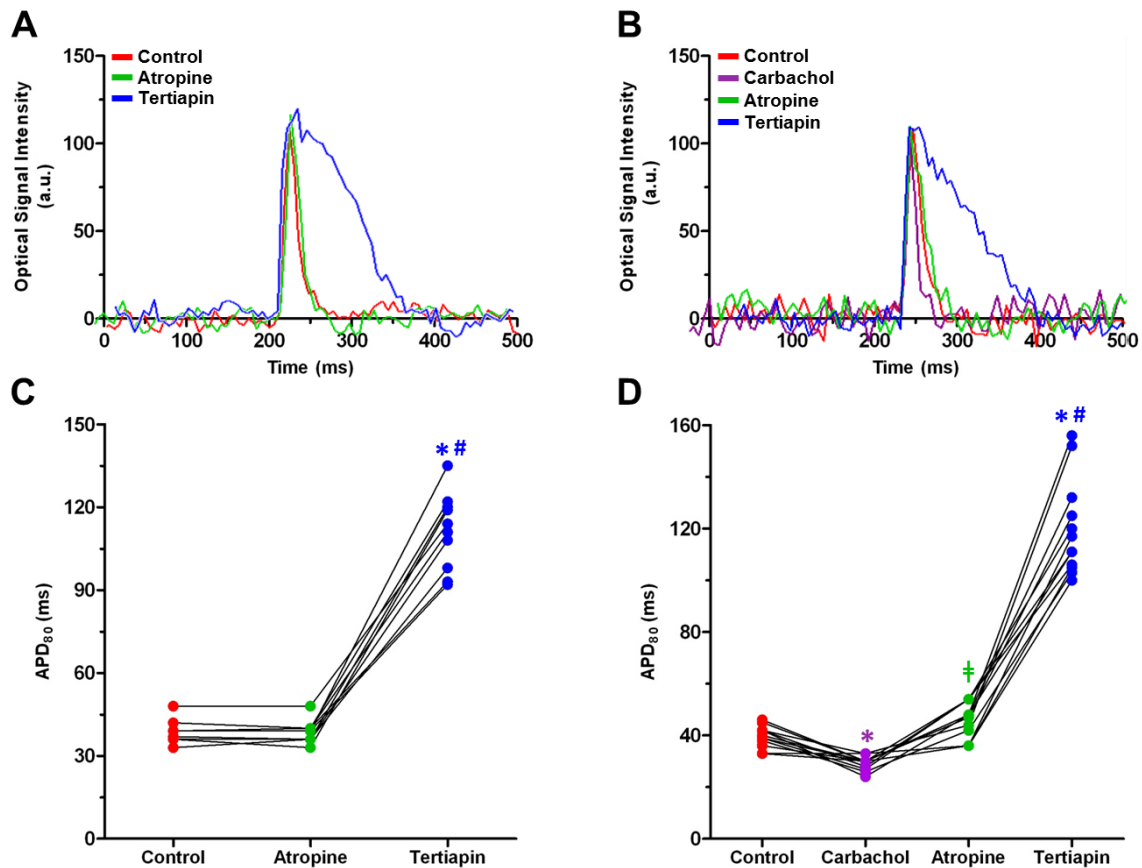


Figure 2. **A**, Western blot analysis of Kir3.1 and Kir3.4 levels in atrial and ventricular neonatal rat cardiomyocyte (nrCMC) cultures using GAPDH as a loading control. **B** and **C**, Typical optical action potential (AP) records of untreated (red) and tertiapin-treated (blue) atrial and ventricular nrCMC cultures, respectively. **D**, Quantification of Δ APD₈₀ after tertiapin treatment in atrial vs ventricular nrCMC cultures. **E**, Typical optical signal records of untreated (red) and tertiapin-treated (blue) atrial nrCMC cultures after induction of atrial fibrillation by burst pacing. **F**, Typical phase maps of untreated (**left**) and tertiapin-treated (**right**) cultures after burst pacing. White circles indicate phase singularities. Quantification of (**G**) APD₈₀ during reentry, (**H**) rotor frequency, (**I**) complexity of reentry, (**J**) inducibility of reentry, and (**K**) complete rotor termination in control and tertiapin-treated atrial nrCMC cultures. a.u. indicates arbitrary units. # $P < 0.05$ vs atrial cultures; * $P < 0.05$ vs control.



Supplemental Figure III. (A) Typical examples of optical signal traces in a neonatal rat atrial CMC culture before (control) and after the cumulative treatment with 200 nmol/L atropine and 100 nmol/L tertiapin during 1-Hz pacing. (B) Typical examples of optical signal traces in a neonatal rat atrial CMC culture before (control) and after the cumulative treatment with 2 μmol/L carbachol, 200 nmol/L atropine and 100 nmol/L tertiapin during 1-Hz pacing. (C) Quantification of APD₈₀ at a 1-Hz pacing frequency in untreated atrial CMC cultures and in atrial CMC cultures treated with atropine and tertiapin, respectively. (D) Quantification of APD₈₀ at a 1-Hz pacing frequency in untreated atrial CMC cultures and in atrial CMC cultures treated with carbachol, atropine and tertiapin, respectively. *: $p < 0.05$ vs control, #: $p < 0.05$ vs atropine, ‡: $p < 0.05$ vs carbachol.

Blockade of $I_{K,ACh-c}$ by tertiapin increased APD₈₀ during reentry (from 54.7 ± 24.0 to 128.8 ± 16.9 milliseconds; $n=42$; Figure 2E–2G), which significantly decreased rotor frequency (from 14.1 ± 7.4 to 5.9 ± 1.7 Hz) and complexity (from 6.7 ± 7.7 to 0.58 ± 0.83 PSs; Figure 2H and 2I). Interestingly, the inducibility of reentry also decreased (from 89.2% to 27.2%) after tertiapin treatment (Figure 2J). Concomitantly, tertiapin led to complete termination of all rotors in 67.4% of cultures, whereas rotor termination occurred in only 7.0% of control cultures (Figure 2K).

Kcnj3/5 Knockdown in Atrial nrCMC Cultures

To investigate the individual contribution of the molecular determinants of $I_{K,ACH-c}$ (Kir3.1 and Kir3.4) to the induction and dynamics of AF, expression of *Kcnj3* and *Kcnj5* was specifically downregulated in atrial nrCMC cultures by means of lentiviral, shRNA-mediated RNAi. Kir3.1 and Kir3.4 protein levels were significantly lowered in cultures transduced with LV-Kir3.1↓ and LV-Kir3.4↓, respectively, compared with those in LV-PpLuc↓-treated control cultures ($20.2 \pm 1.7\%$ versus $100.0 \pm 2.4\%$ and $34.6 \pm 3.5\%$ versus $100.0 \pm 34.6\%$, respectively; $n=4$ per group; Figure 3A–3C). As expected, transduction with LV-Kir3.1↓ ($n=11$) and LV-Kir3.4↓ ($n=20$) resulted in significant APD prolongation compared with LV-PpLuc↓-treated control cultures ($n=11$; Figure 3D). APD_{80} was significantly increased throughout all pacing cycle lengths (PCLs; Figure 3E). In addition, CV was lowered significantly by both *Kcnj3* and *Kcnj5* knockdown (Figure 3F), possibly caused by a depolarizing effect of long-term $I_{K,ACH}$ downregulation on the resting membrane potential.

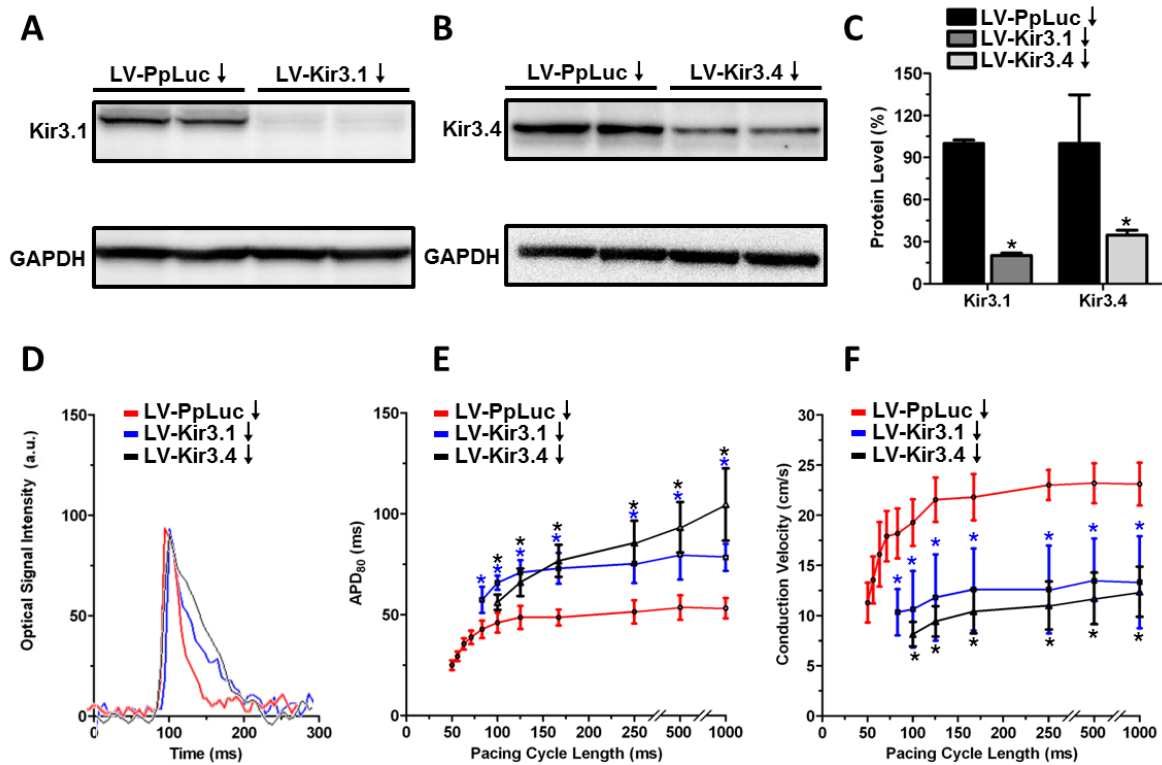


Figure 3. Western blot of (A) Kir3.1 levels in LV-PpLuc \downarrow (ie, control lentiviral vector)- and LV-Kir3.1 \downarrow -transduced atrial neonatal rat cardiomyocyte (nrCMC) cultures and (B) Kir3.4 levels in LV-PpLuc \downarrow - and LV-Kir3.4 \downarrow -transduced atrial nrCMC cultures with GAPDH used as a loading control and (C) their quantification. D, Typical optical signal in atrial nrCMC cultures transduced with the control vector LV-PpLuc \downarrow or with LV-Kir3.1 \downarrow or LV-Kir3.4 \downarrow . Quantification of (E) action potential duration and (F) conduction velocity restitution in atrial nrCMC cultures transduced with the control vector LV-PpLuc \downarrow or with LV-Kir3.1 \downarrow or LV-Kir3.4 \downarrow . a.u. indicates arbitrary units. * P <0.05 vs LV-PpLuc \downarrow .

Effect of Kcnj3/5 Knockdown on Reentry in Atrial nrCMC Cultures

Next, reentry was induced in cultures transduced with LV-Kir3.1 \downarrow (n=14), LV-Kir3.4 \downarrow (n=12), or the control LV (n=19) to investigate the effect of Kir3.x-dependent APD prolongation on spiral waves. As expected, reentrant cycle length was significantly increased after knockdown of either *Kcnj3* or *Kcnj5* (Figure 4A–4D and 4F), consistent with prolongation of APD₈₀ during reentry (Figure 4E). Similarly, activation frequency and complexity were significantly decreased (Figure 4G and 4I and Movie 3 in the online-only Data Supplement). In addition, inducibility of reentry was clearly reduced by *Kcnj3* or *Kcnj5* knockdown (Figure 4H). Together, these results show that the effect of tertiapin on reentry induction and dynamics can be reproduced by RNAi-mediated reduction of Kir3.1 or Kir3.4 protein levels.

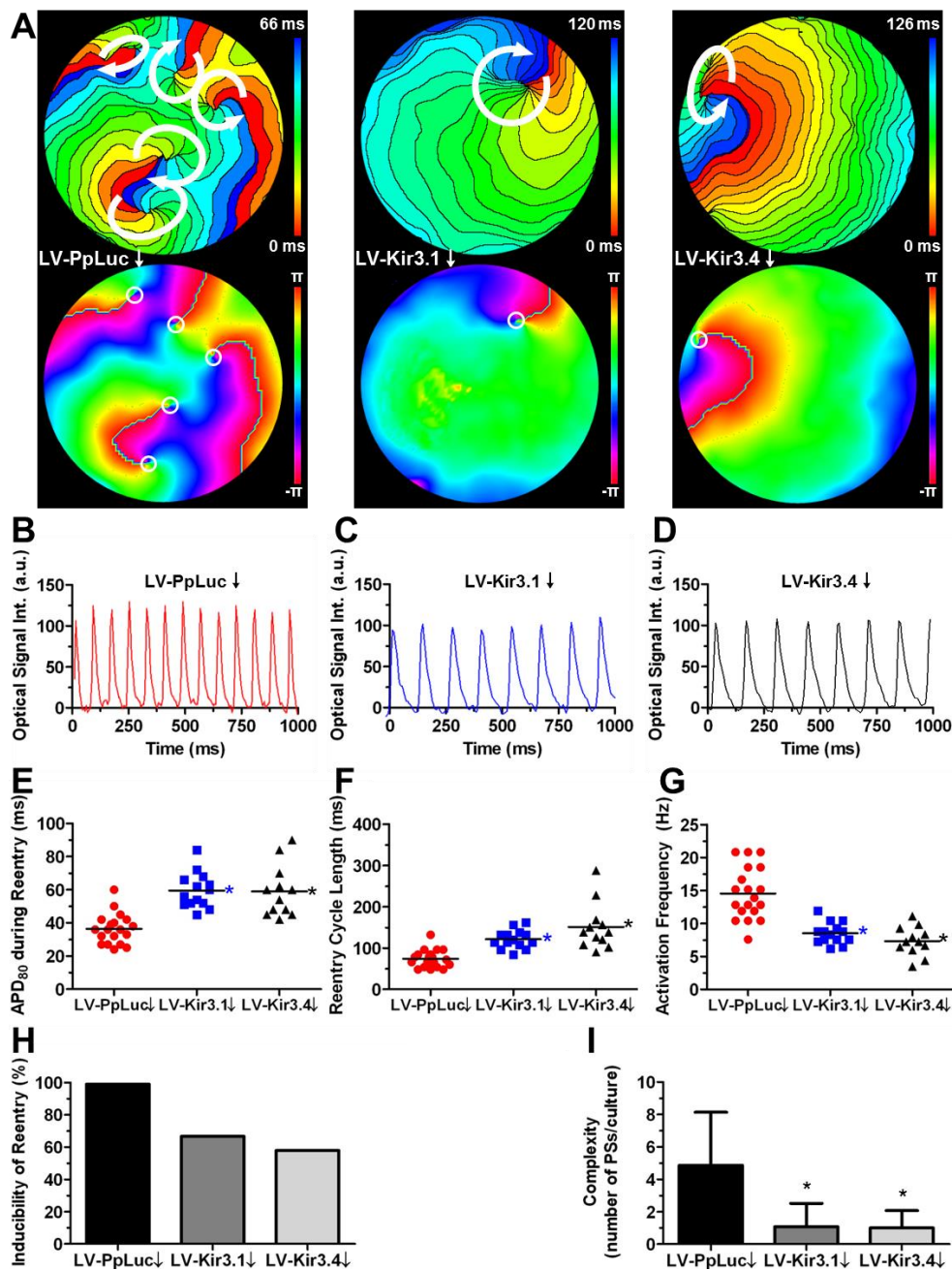


Figure 4. A, Activation maps and corresponding phase maps during reentry in atrial neonatal rat cardiomyocyte (nrCMC) cultures transduced with LV-PpLuc \downarrow (ie, control lentiviral vector), LV-Kir3.1 \downarrow , or LV-Kir3.4 \downarrow . White arrows indicate the direction of action potential (AP) propagation; white circles depict phase singularity position. Optical signal traces during reentry in atrial nrCMC cultures transduced with (B) LV-PpLuc \downarrow , (C) LV-Kir3.1 \downarrow , or (D) LV-Kir3.4 \downarrow . Quantification of (E) AP duration (APD), (F) cycle length, (G) activation frequency, (H) inducibility of reentry, and (I) complexity of reentry after burst pacing in control (red), LV-Kir3.1 \downarrow -transduced (blue), and LV-Kir3.4 \downarrow -treated (black) atrial nrCMC cultures. a.u. indicates arbitrary units. * $P < 0.05$ vs LV-PpLuc \downarrow .

$I_{K,ACH-c}$ Blockade Prevents APD Alternans by Decreasing APD and CV Restitution Slope

To investigate how $I_{K,ACH-c}$ blockade or downregulation prevents reentry induction, we studied the effect of tertiapin on APD and CV restitution. During pacing at 1 to 20 Hz, Kir3.x blockade by tertiapin increased APD₈₀ throughout all PCLs compared with control cultures (n=8 per group; Figure 5A). CV was unaltered after 1- to 2-Hz pacing after tertiapin treatment. However, at higher pacing frequencies, CV was significantly lower in cultures treated with tertiapin (Figure 5B). This was possibly attributable to a change in the maximal diastolic potential, which gets more depolarized at higher pacing frequencies if the APD is prolonged by $I_{K,ACH-c}$ blockade.²⁰ Furthermore, wavelength was significantly increased by tertiapin at all activation frequencies (Figure 5C). Interestingly, the slopes of the APD and CV restitution curves were strongly flattened by tertiapin treatment as a consequence of significantly increased minimal APD₈₀ and decreased maximal activation frequency (Figure 5D and 5E). Because the restitution curves naturally become steeper at shorter diastolic intervals (Figure 5A–5C), prolonging minimal APD (and thereby decreasing maximal activation frequency) prevents steepening in APD and CV restitution. Tertiapin treatment decreased the maximal APD restitution slope from 1.0 ± 0.4 to 0.3 ± 0.2 (Supplemental Figure IVA and IVB in the online-only Data Supplement), whereas the percentage of cultures with a maximal APD restitution slope above the critical value²¹ of 1 decreased from 71.4% to 0% (Supplemental Figure IVC in the online-only Data Supplement).

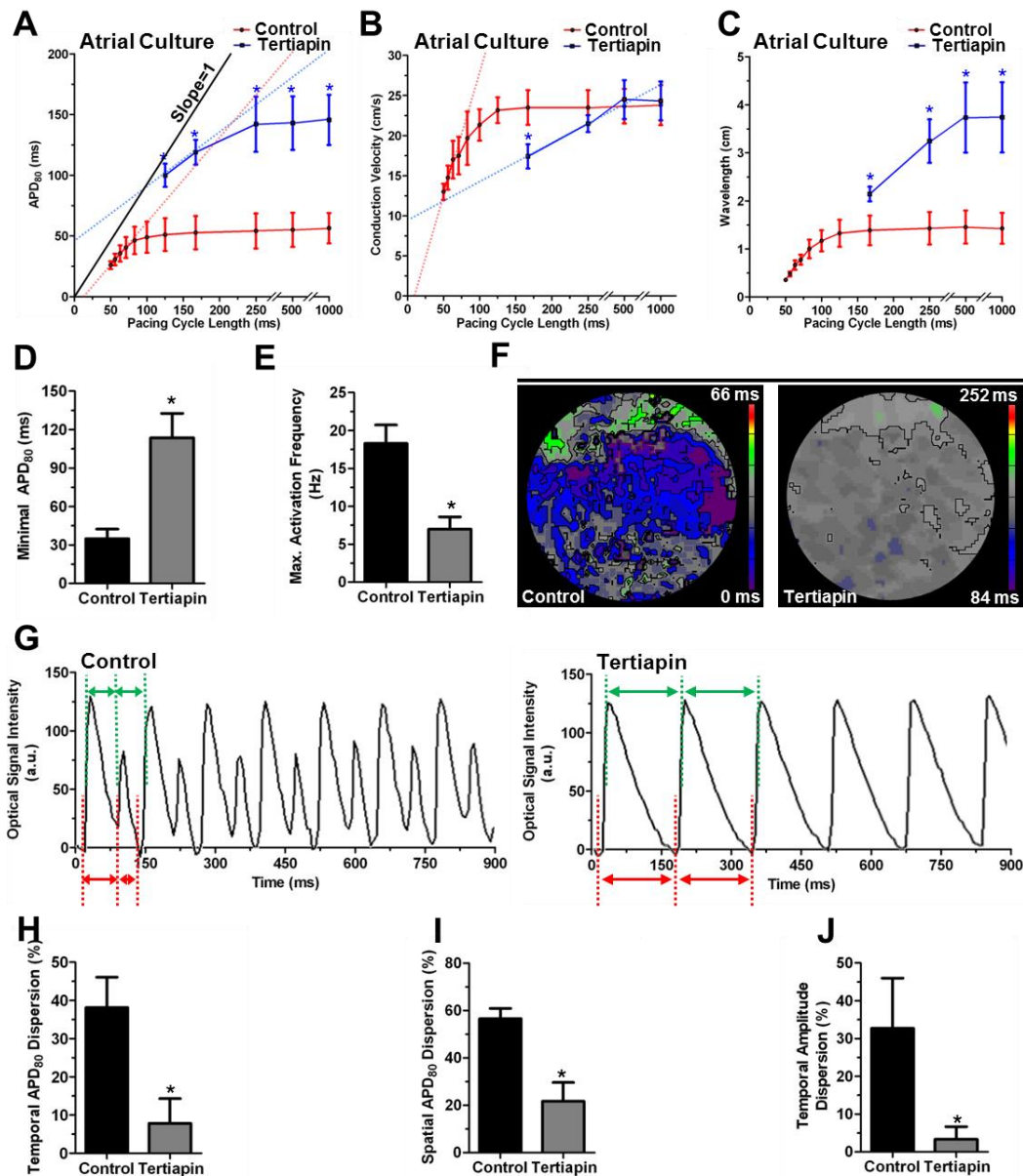
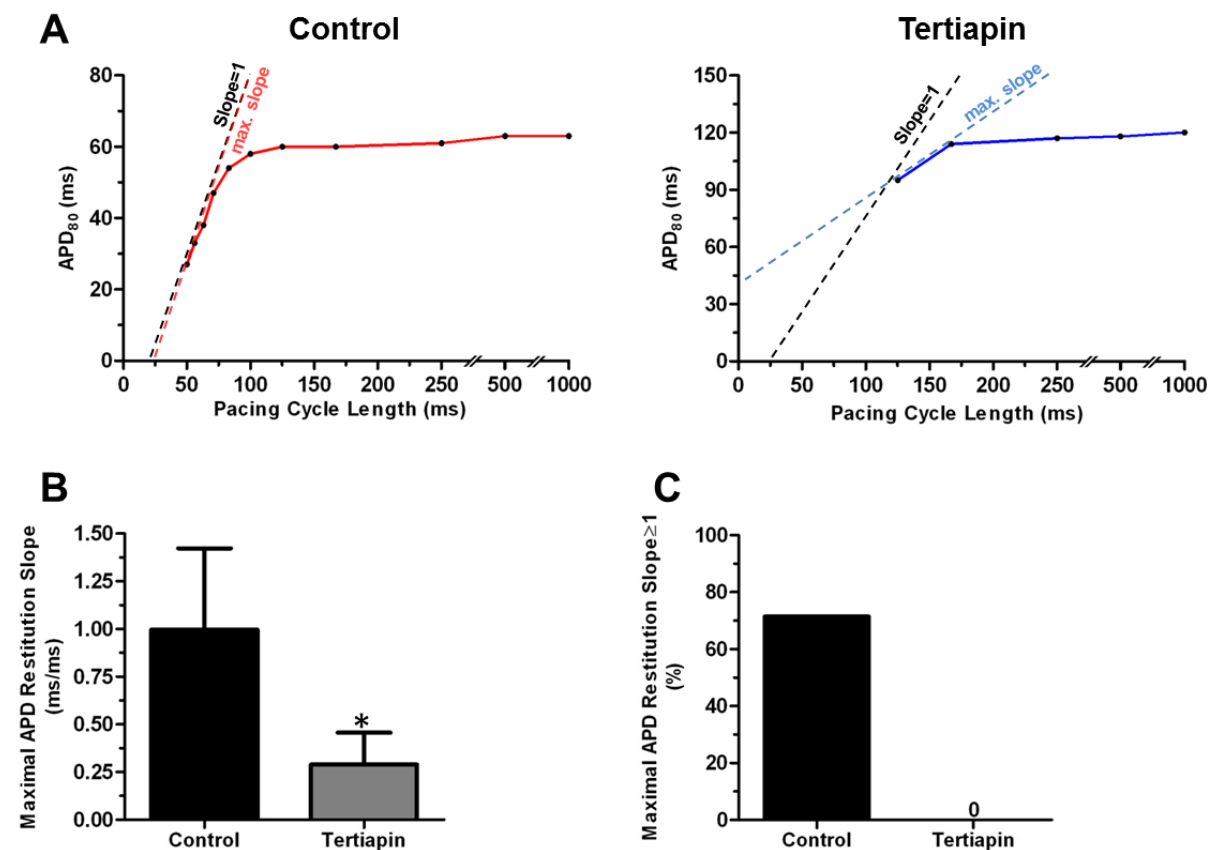


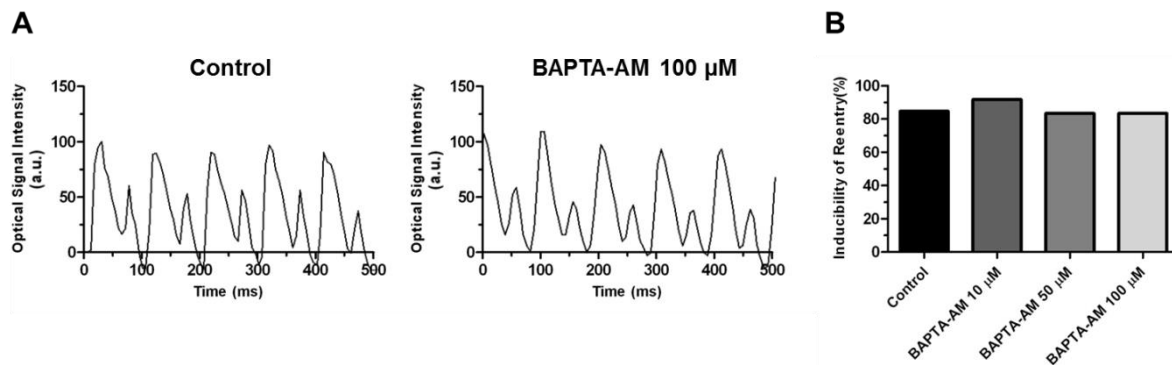
Figure 5. Restitution of (A) APD₈₀, (B) conduction velocity, and (C) wavelength during 1- to 20-Hz pacing in control (red) and tertiapin-treated (blue) atrial neonatal rat cardiomyocyte (nrCMC) cultures. Red and blue dotted lines indicate the maximal slopes in the restitution curves; solid black line indicates slope=1. Quantification of (D) minimal action potential duration (APD) and (E) maximal activation frequency in control and tertiapin-treated atrial nrCMC cultures. F, APD₈₀ maps of untreated (left) and tertiapin-treated (right) atrial nrCMC cultures. G, Typical optical signal traces during pacing at maximal activation frequency in control cultures (left) showing alternating APDs (red double arrows) on equal pacing cycle lengths (PCLs; green double arrows) and tertiapin-treated cultures showing stable APDs (red double arrows) on equal PCLs (green double arrows). Quantification of (H) temporal APD₈₀ dispersion, (I) spatial APD₈₀ dispersion, and (J) temporal amplitude dispersion. a.u. indicates arbitrary units. **P*<0.05 vs control.



Supplemental Figure IV. (A) Typical examples of APD restitution curves of a single control (left) and a single tertiapin-treated (right) culture of neonatal rat atrial CMCs, showing that the maximal slope of the curve in the control culture exceeds 1, while the slope in the tertiapin-treated culture remains well below 1. Black dotted lines indicate slope=1. Colored dotted lines indicate the maximal slope in control (red) and tertiapin-treated (blue) cultures. (B) Quantification of the maximal slope in the APD restitution curve of control and tertiapin-treated cultures. (C) Quantification of the percentage of cultures with a maximal slope in the APD restitution curve ≥ 1 .

As a consequence of restitution moderation, spatial dispersion ($21.7 \pm 8.0\%$ versus $56.5 \pm 4.4\%$ in control cultures) and temporal dispersion ($7.8 \pm 6.5\%$ versus $38.1 \pm 8.0\%$ in control cultures) in APD were significantly decreased by Kir3.x blockade (Figure 5F–5I). Because steepening in APD and CV restitution causes small PCL changes to result in large APD and CV changes, APD alternans occurred in control but not in tertiapin-treated cultures. During APD alternans at stable PCL in a control culture, as a consequence of the relationship between APD and diastolic interval (see also Figure 5A), a long APD was repeatedly followed by a short APD because the diastolic interval is shortened after the long APD (Figure 5G). Since the short APD

follows after incomplete repolarization during the long AP, amplitude alternans was observed (likely because of inactivation of Na^+ channels as a result of incomplete repolarization). Therefore, blockade of $I_{K, \text{ACh-c}}$ leads to a significant decrease in temporal amplitude dispersion (Figure 5G and 5J). Together, these findings suggest that $I_{K, \text{ACh-c}}$ -dependent alternans is linked to restitution kinetics (see also Results and Supplemental Figure V in the online-only Data Supplement).



Supplemental Figure V. (A) Typical examples of optical signal traces of control (left) and BAPTA-AM-treated (right) neonatal rat atrial CMC cultures at maximal activation frequency in areas showing APD alternans **(B)** Quantification of reentry inducibility in control cultures and in cultures treated with 10 $\mu\text{mol/L}$, 50 $\mu\text{mol/L}$ or 100 $\mu\text{mol/L}$ BAPTA-AM showing no difference in the induction of reentry by burst pacing during buffering of intracellular Ca^{2+} .

Role of APD Alternans in Reentry

In control atrial cultures, reentry initiation after burst pacing was found to be a consequence of highly incident APD alternans, during which a long AP was repeatedly followed by a short AP (Figure 6, left). Typically, the long AP was uniformly propagated throughout the culture (Figure 6, right, long AP). However, because of the spatial heterogeneity in APD, the short AP frequently underwent conduction block when propagated from an area with short-long APD to an area with long-long APD. This caused PSs to arise adjacent to the area of conduction block (Figure 6, left and right, short AP). The AP was subsequently propagated around the PS. This could lead to reentry if the area in which the conduction block occurred repolarized before return of the wave front, which then circled the PS in a retrograde fashion (Figure 6, right, short AP). These results show that APD alternans, which can be prevented by blockade of $I_{K, \text{ACh-c}}$, is a major factor in reentry initiation.

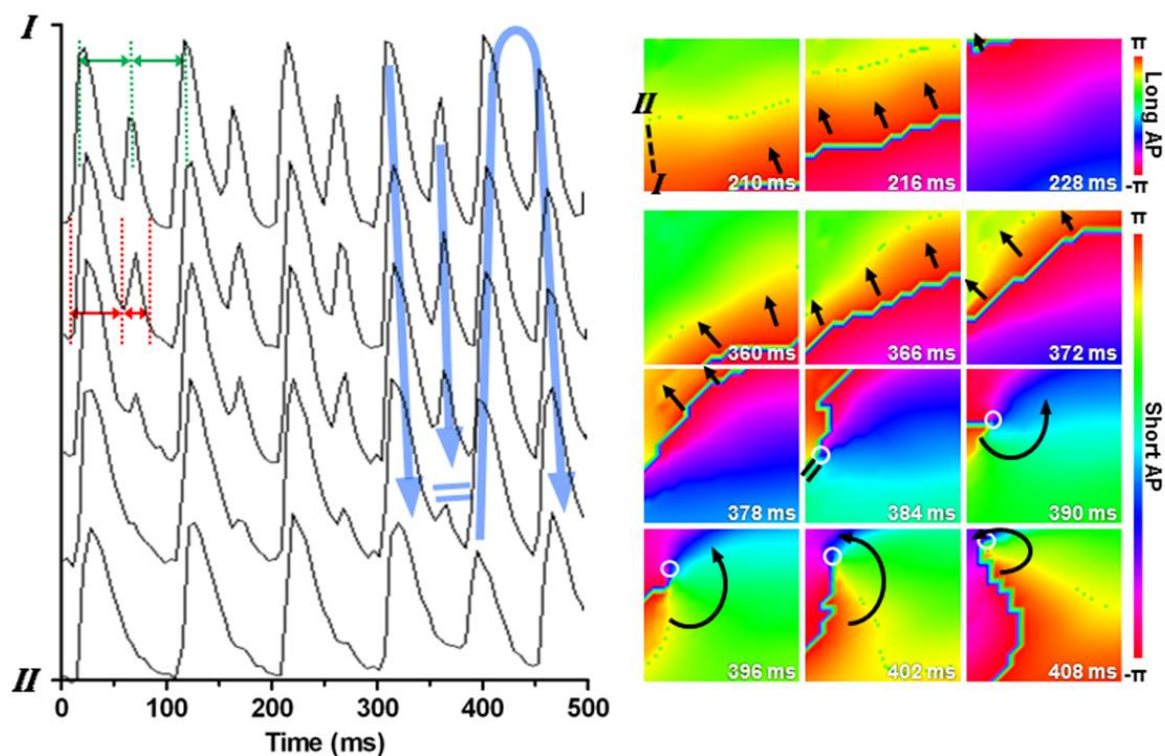


Figure 6. Typical optical signal traces (graph, **left**) in a 9-mm² square in a control atrial neonatal rat cardiomyocyte culture during action potential (AP) duration (APD) alternans leading to reentry. Green and red dotted lines indicate pacing cycle length and alternating APD, respectively. Corresponding phase maps (**right**) during uniform propagation of the long AP (**top**) and conduction block, followed by circular propagation of the short AP (**bottom**). Arrows, double lines (blue in the optical signal traces and black in the phase maps), and white circles indicate the direction of AP propagation, conduction block, and the phase singularity position, respectively. The positions of points I and II in the culture are indicated in the **top left** phase map.

Mechanism of Rotor Termination After $I_{K,ACh}$ Blockade

In addition to preventing reentry induction, blockade of $I_{K,ACh}$ terminated a large portion of rotors initiated by burst pacing. Atrial cultures were mapped during the addition of tertiapin to study how $I_{K,ACh}$ blockade led to rotor termination. Interestingly, during tertiapin incubation, rotors with P-1 oscillatory dynamics destabilized into period-2 (P-2) and aperiodical reentry before termination (Figure 7 and Supplemental Figure VI in the online-only Data Supplement). As shown in Figure 5A, incubation of atrial cultures with tertiapin led to an increase in minimal APD and a decrease in the maximal slope of the APD restitution curve. The increased steepness of the restitution slope at long PCLs in the tertiapin-treated

cultures suggests that this slope becomes critically steep before tertiapin has completely increased minimal APD. This caused APD alternans in vulnerable spots during reentry, leading to P-2 oscillatory dynamics (Figure 7, middle, and Supplemental Figure VIB and VID in the online-only Data Supplement). Subsequently, APD prolonged further and refractory periods around the PSs increased. Consequently, if the refractory period got critically long, the reentrant wave had to alter its path from the previous cycle to be sustained. Therefore, PSs tended to shift position after incubation with tertiapin, leading to aperiodical reentry dynamics (Figure 7, bottom, and Supplemental Figure VIC and VID in the online-only Data Supplement), which simultaneously increased the chance for these PSs to meet a boundary, followed by rotor termination (Figure 7, bottom, and Supplemental Figure VIC and VID in the online-only Data Supplement). Because tertiapin increased wavelength and decreased the incidence of APD alternans after full incubation, new rotors were not formed, resulting in a net decrease in complexity of conduction patterns after tertiapin treatment, ultimately leading to termination of AF (Movie 4 in the online-only Data Supplement). These results show that in addition to affecting reentry initiation and global reentry characteristics, $I_{K,ACH-C}$ determines the period dynamics and propensity toward rotor termination by controlling the onset of APD alternans and PS drift during reentry.

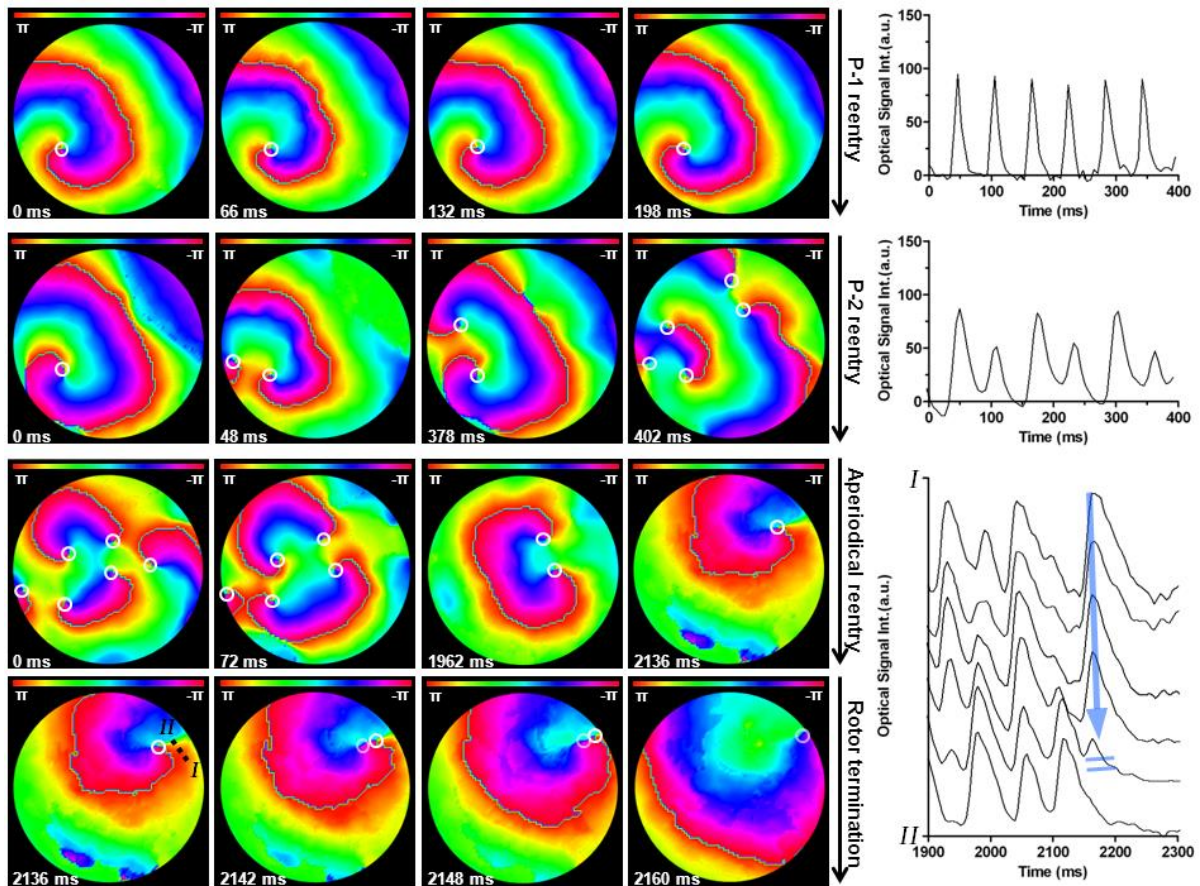
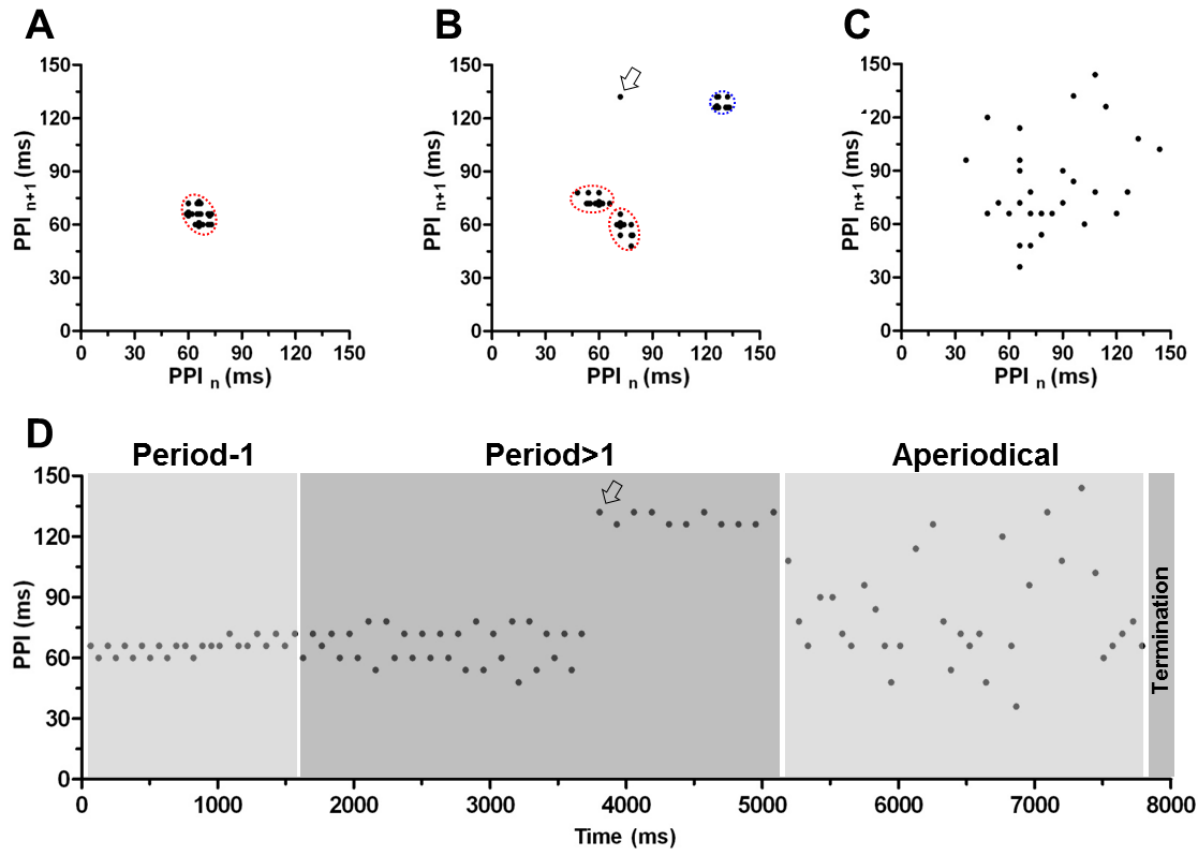


Figure 7. Phase map sequence of an atrial neonatal rat cardiomyocyte culture during tertipin incubation. The top row shows the initial period (P)-1 reentrant arrhythmia rotating around a single stable phase singularity (PS) and its corresponding optical signals. The second row shows the change into a P-2 reentry (≈ 4 seconds after tertipin addition) with meandering, disappearing, and reappearing PSs and its corresponding optical signals showing action potential (AP) duration (APD) alternans in critical areas. The bottom 2 rows show the shift to aperiodical reentry (≈ 9 seconds after tertipin addition) followed by the termination of rotors as a consequence of PS drift toward the edge of the culture as the wave front increasingly meets refractory tissue. The white circles indicate PSs; translucent white circles, the PS position in the previous frame. **Bottom right,** The corresponding AP between points I and II in the culture. The blue arrow indicates the propagation of the final AP leading to conduction block. a.u. indicates arbitrary units.

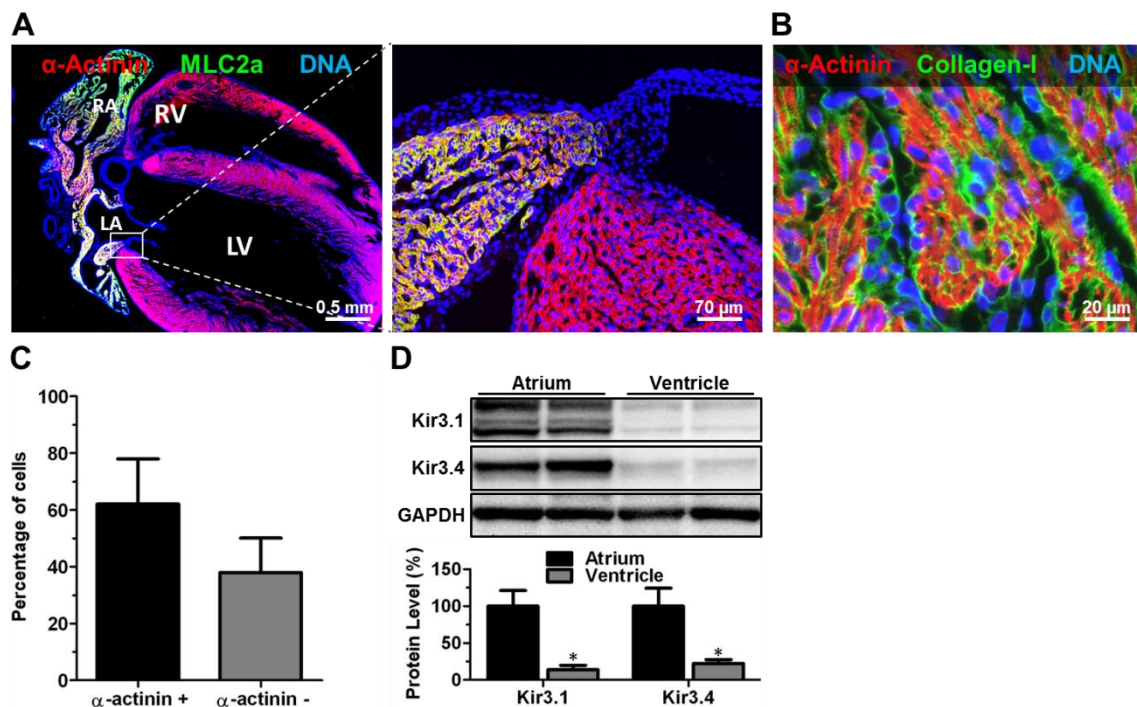


Supplemental Figure VI. Return maps of the PPI sequences in an atrial CMC culture during (A) typical period-1 reentry showing a single cluster in the return map, (B) the early phase of tertiapin incubation leading to a change into period-2 reentry showing two clusters (red) as a result of APD alternans (See Figure 7 in the main manuscript, second row) and a third cluster (blue) corresponding to the subsequent prolonged reentrant cycle length (temporary 2:1 conduction) starting at the arrow in both subfigures B and D, (C) the late phase of tertiapin incubation leading to aperiodical reentry lacking any clustering in the return map. Dotted red circles indicate clustering of PPI sequences. (D) Time series of the PPIs during the incubation with tertiapin, showing the progression of period-1, to period>1, to aperiodical reentry and eventually termination. The return maps in A-C are each based on a part of the time series separated by the gray rectangles.

Kir3.x Blockade in Whole-Heart Mapping

Our novel 2-dimensional model of atrial tissue appeared to be crucial for a mechanistic understanding of the role of $I_{K_{ACh-c}}$ in rotor formation, dynamics, and termination because these events are likely to occur subepicardially in the intact atria, which precludes their direct readout and interpretation. However, whole-heart data are needed to show the effects of $I_{K_{ACh-c}}$ on actual AF in a more complex and

relevant setting. We thus studied the effects of tertiapin in a whole-heart model of AF using neonatal rat hearts. In these hearts, immunocytological analyses confirmed the expression of myosin light chain 2a in the atria only (Supplemental Figure VIIA in the online-only Data Supplement). The atria consisted of $37.9 \pm 12.1\%$ nonmyocytes, which were predominantly fibroblasts as judged by α -actinin/collagen-I double staining (Supplemental Figure VIIB and VIIC in the online-only Data Supplement). Consistent with the in vitro results, Western blot analyses showed a significantly higher expression of Kir3.1 and Kir3.4 in the atrium compared with the ventricle ($100.0 \pm 21.3\%$ versus $13.7 \pm 6.0\%$ [$P < 0.05$] and $100.0 \pm 24.2\%$ versus $22.4 \pm 5.2\%$ [$P < 0.05$], respectively; Supplemental Figure VIID in the online-only Data Supplement).



Supplemental Figure VII. Immunohistological double staining of whole neonatal rat hearts for (A) MLC2a (green) and α -actinin (red) and (B) collagen type I (green) and α -actinin (red). (C) Quantification of the number of α -actinin-positive (i.e. CMCs) and -negative cells (i.e. non-myocytes) as judged by immunohistology. (D) Western blot analysis and quantification of Kir3.1 and Kir3.4 levels in the neonatal rat atrium and ventricle using GAPDH as loading control. LA: left atrium, RA: right atrium, LV: left ventricle, RV: right ventricle, *: $p < 0.05$ vs control.

During optical mapping of whole neonatal rat hearts, blockade of Kir3.x channels by tertiapin significantly increased atrial APD (62.8 ± 20.9 versus 111.0 ± 32.9 milliseconds; $P < 0.05$) in sinus rhythm, whereas the APD in the ventricles was not significantly altered (219.7 ± 57.6 versus 211.8 ± 42.7 milliseconds; $P < 0.05$; $n = 10$ per group; Figure 8A–8C). Atropine treatment had no significant effect on atrial APD (54.7 ± 13.9 versus 62.8 ± 20.9 milliseconds in control hearts; Supplemental Figure VIIIA–VIIC in the online-only Data Supplement), confirming the M2 receptor-independent, constitutive activation of $I_{K,ACH}$ in neonatal rat atria. After burst pacing, AF was maintained by P-1 oscillatory dynamics in both control and tertiapin-treated hearts. In hearts treated with tertiapin, APD during AF was significantly longer compared with control hearts (54.8 ± 14.2 versus 38.8 ± 7.9 milliseconds; $P < 0.05$; Figure 8D and 8E). As a consequence, AF cycle length was significantly increased (106.5 ± 10.3 versus 81.3 ± 11.3 milliseconds; $P < 0.05$; Figure 8F), whereas the inducibility of AF showed a significant decrease after tertiapin incubation (90% versus 40%; $P < 0.05$; Figure 8G). Together, these results support the notion that Kir3.x determines the initiation and maintenance of AF in the whole heart.

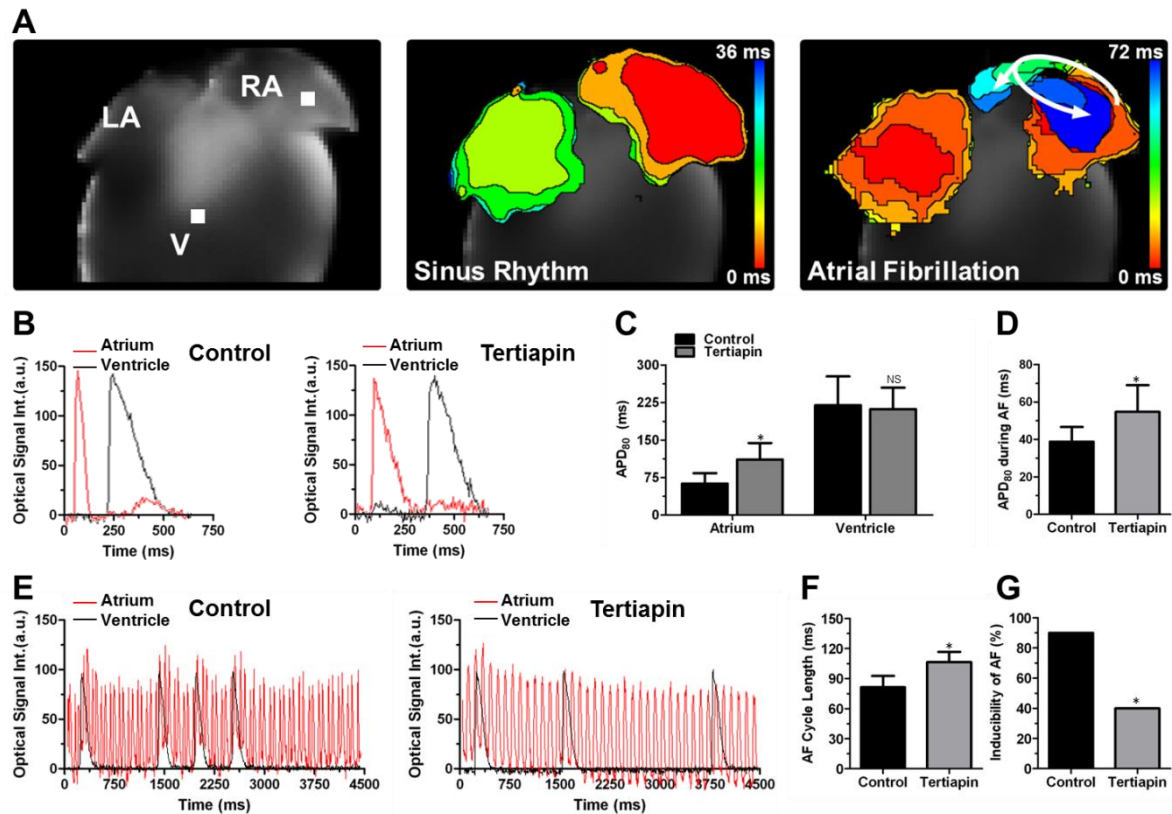
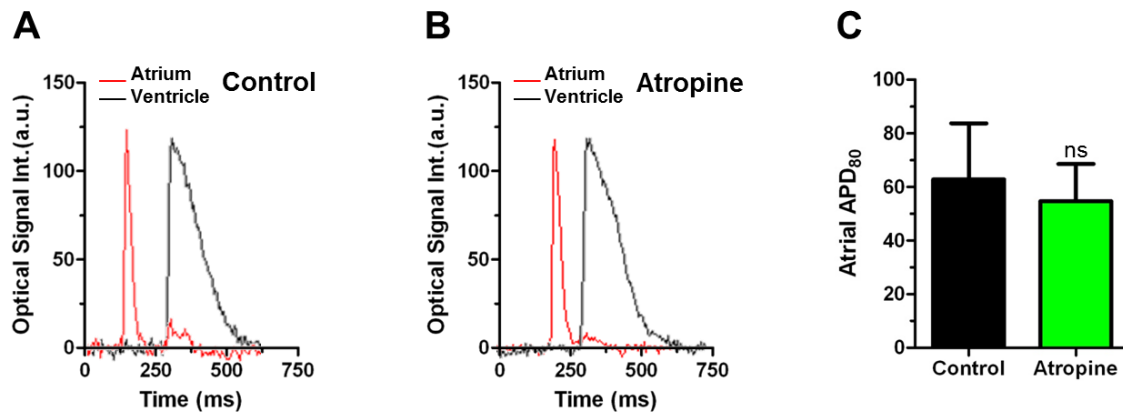


Figure 8. **A**, Typical examples of a control neonatal rat heart during optical mapping showing its orientation (**left**), a map of the atrial activation sequence during sinus rhythm (**middle**; 6-millisecond isochrone spacing), and a map of the atrial activation sequence during atrial fibrillation (AF) induced by burst pacing (**right**; 6-millisecond isochrone spacing) showing circular activation in the atrial epicardium (white arrow). The white squares indicate the areas from which typical optical signals were derived. LA indicates left atrial; RA, right atrial, and V, ventricle. **B**, Examples of the optical signal traces in the atrium (red) and ventricle (black) in control hearts (**left**) and tertiapin-treated hearts (**right**). Quantification of (**C**) APD₈₀ in atria and ventricles of control and tertiapin-treated hearts during sinus rhythm and (**D**) the atrial APD₈₀ during AF. **E**, Examples of the optical signal traces during AF after burst pacing in the atrium (red) and ventricle (black) in control and tertiapin-treated hearts. Irregularly appearing ventricular traces are indicative of AF. Quantification of (**F**) AF cycle length and (**G**) inducibility of AF by burst pacing in control and tertiapin-treated neonatal rat hearts. * $P < 0.05$ vs control.



Supplemental Figure VIII. Typical optical signal traces in the atria (red trace) and ventricles (black trace) of (A) control and (B) atropine-treated neonatal rat hearts. (C) Quantification of APD₈₀ in the atria of control and atropine-treated neonatal rat hearts. NS: non-significant vs control, . a.u.: arbitrary units.

Discussion

The key findings of this study are the following. First, the acetylcholine-inducible potassium current ($I_{K,ACH}$), mediated by Kir3.x, is highly atrium specific and constitutively active in neonatal rat atrial cell monolayers and intact atria. Second, in the presence of this current, sustained reentry can be easily induced electrically ($\approx 90\%$ incidence), whereas the incidence decreases strongly after $I_{K,ACH}$ blockade. Third, after induction, tachyarrhythmias in atrial cultures are maintained by stable P-1 and shifting period >1 or aperiodical rotors and result from restitution-driven alternans, whereas they are terminated by alternans-mediated PS drift. Fourth, mechanistically, it is shown by pharmacological and genetic interventions that Kir3.x is a key regulator of rotor induction, dynamics, and termination by controlling APD and APD alternans through APD restitution steepening. Finally, Kir3.x represents a promising atrium-specific target for antiarrhythmic strategies.

Kir3.x in Models of AF

Previous studies showed that $I_{K,ACH}$ may play an important role in the onset of AF because acetylcholine activates $I_{K,ACH}$ during parasympathetic stimulation and thereby shortens APD.¹⁵ However, after atrial remodeling, which occurs, for instance,

during permanent AF, APD is shortened independently of parasympathetic activation, partly because $I_{K,ACH}$ has become constitutively active.¹⁶ Although alteration of atrial electrophysiology after atrial remodeling has been established, most of the insights into the electrophysiological mechanisms and complex dynamics of wave propagation in AF have come from detailed investigations in computer and animal models of AF, which did not take into account the molecular consequences of atrial remodeling.²² Hence, these results may be applicable to paroxysmal AF, but translation to persistent AF and AF after atrial remodeling remains difficult. In the present study, models have been used that include 1 of these molecular consequences, which is constitutive activation of $I_{K,ACH}$. Therefore, the present models might provide a novel means to link the molecular biology of (persistent) AF to its basic electrophysiological mechanisms.²²

We found that the detrimental effects of $I_{K,ACH-c}$ are strongly dependent on Kir3.x expression, as is the case when $I_{K,ACH}$ is activated by increased parasympathetic tone.^{14,15} Because Kir3.1 homomers do not to form a functional channel,^{23,24} the preventive effect of *Kcnj3* knockdown is likely attributable to diminished density of Kir3.1/Kir3.4 heteromers at the sarcolemma, whereas Kir3.4 downregulation affects both Kir3.4 homomers and Kir3.1/Kir3.4 heteromers. This might explain why a 3-fold reduction in Kir3.4 level produced results similar to the results of a 5-fold decrease in Kir3.1 abundance. Although earlier studies show that there is very little contribution of Kir3.4 homomers to $I_{K,ACH}$,²⁵ our results suggest that after *Kcnj3* knockdown there is still residual $I_{K,ACH-c}$, most likely provided by Kir3.4 homomers, the formation of which is inhibited after *Kcnj5* knockdown. This could imply that the contribution of Kir3.x subunits to $I_{K,ACH}$ and to its constitutively active counterpart differs.

Nevertheless, the effects of tertiapin on APD, rotor frequency, arrhythmia complexity, and inducibility were found to be larger than those of Kir3.1 and Kir3.4 downregulation. Because the atrial nrCMCs have a higher tolerability for short-term $I_{K,ACH-c}$ blockade by tertiapin as opposed to long-term $I_{K,ACH-c}$ blockade by LV-mediated RNAi, tertiapin treatment could provide a somewhat more efficient blockade of $I_{K,ACH-c}$ at the moment of electrophysiological analysis. Furthermore, long-term downregulation of Kir3.1 or Kir3.4 seemed to induce a depolarization of the cardiomyocyte's membrane potential, decreasing CV even at long PCLs. The conduction-slowing effect of *Kcnj3/5* knockdown by shRNAs strongly diminishes its wavelength-prolonging effect. Therefore, we used tertiapin as an alternative means

to study the role of $I_{K,ACH-c}$ in AF in whole hearts. The fact that Kir3.1 and Kir3.4 downregulation still strongly decreased the inducibility of reentry in atrial cell cultures shows that the effects of $I_{K,ACH-c}$ inhibition on the slopes in the restitution curves prevails over its effects on wavelength.

Mechanisms of AF Maintenance

For years, there has been ongoing discussion of whether AF is the consequence of single or multiple ectopic focal discharges or the result of reentrant waves or randomly appearing and disappearing wavelets.²² Isolating the pulmonary veins can be successful in preventing paroxysmal AF, which could be interpreted as evidence for the focal discharge theory.²⁶ Nevertheless, reentrant sources generating fibrillatory conduction as a consequence of a dominant frequency gradient have been demonstrated in chronic AF.²⁷ Importantly, in patients with a long history of AF, pulmonary vein isolation has a low success rate.^{5,6} Therefore, at least in permanent AF, reentry seems to play an important role. The presence of a dominant frequency gradient also makes the multiple wavelet hypothesis less plausible because a hierarchy in frequencies defies randomness as postulated in this theory.²⁸

As demonstrated in our models, constitutive activation of $I_{K,ACH}$ may be one of the determinants of the seemingly increasing role of reentry in the maintenance of AF over time. We show that the constitutively active $I_{K,ACH}$ causes APD alternans, making the atrial tissue prone to wave break and reentry initiation. In most cases, after reentry is initiated, multiple stable rotors maintain fibrillation. Without ongoing electric remodeling, the emergence of such rotors in the left atrium would lead to fibrillatory conduction to the right atrium. However, in several cultures, AF was maintained by shifting aperiodical rotors. Because the APD and CV restitution can become critically steep if the $I_{K,ACH}$ is constitutively active, causing both spatial and temporal heterogeneity in repolarization, rotors can meander and break up. Therefore, in the remodeled atrium (ie, with constitutively active $I_{K,ACH}$), random wavelets (ie, random rotors of which the propagated wave front appears as wavelets at the atrial surface) could maintain AF. This could also explain the possibility of AF originating from a rotor in the right atrium with fibrillatory conduction to the left atrium (eg, after left atrium ablation and permanent AF),²⁸ even though the refractory period is shorter in the left atrium. The fibrillatory aspect of conduction here could be

provided by the seemingly random breakup, appearance, and disappearance of rotors in the right atrium as opposed to an APD gradient.

APD Alternans and AF

Disturbed repolarization is thought to play an important role in producing spatial heterogeneity and causing fibrillation in the ventricles. In theory, if fast ectopic firing occurs, for instance, from the pulmonary veins, spatial heterogeneity in repolarization would also favor reentry initiation in the atria. Hence, it has recently been proposed that repolarization alternans could also play an important role in AF. Indeed, it has been shown that atrial repolarization alternans occurs frequently before the initiation of AF.²⁹⁻³¹ In the diseased atrium, changes in calcium handling have been shown to cause the APD to alternate as a consequence of calcium instabilities.³² During calcium-dependent APD alternans, APD restitution is not necessarily altered. We show here for the first time that APD alternans underlying reentry can be caused by constitutive activation of $I_{K,ACh}$, which steepens APD restitution. Hence, we confirm that disturbed atrial repolarization is associated with the onset of AF. In addition to this association, we show experimentally that wave break and resultant reentry are the direct consequence of APD alternans. Earlier in silico work predicted that discordant APD alternans leads to wave break if the short AP in a long-short sequence reaches the refractory tail of a long AP in a short-long sequence. In accordance with these predictions, we found that propagation of a short AP of an alternating long-short sequence halts when it meets the refractory tail of a long AP. However, in our model, the long AP was usually not the consequence of discordant APD alternans, for example, a short-long sequence. Instead, it was the result of a large APD dispersion causing areas with APD alternans to border areas with solely long APDs. Thus, in our model, we provide an extension to the aforementioned theory by showing that spatial APD dispersion in combination with APD alternans (while not being classically discordant) can cause AF in cells with constitutively active $I_{K,ACh}$.

Atrial Fibrosis in AF

Atrial fibrosis is thought to be an important component of AF substrates.³³ In this study, atrial cell cultures consisted of $\approx 17\%$ cardiac fibroblasts, as deduced by collagen type I immunostaining. Previous studies showed that atrial conduction

abnormalities as a consequence of fibrosis depend strongly on the pattern of fibrosis.³⁴ It was found that long fibrotic strands of tissue could cause significant conduction abnormalities and thereby contribute to AF, whereas diffuse fibrosis only marginally affected conduction. In our in vitro model, fibroblasts are diffusely spread. In addition, the percentage of fibroblasts in this model is lower than in intact neonatal rat atria (see also Figures IF, VIIB, and VIIC in the online-only Data Supplement). Despite this difference in fibroblast content, the atrial cell culture and whole-heart models yielded very similar results in terms of the inducibility of AF and the ability to suppress AF by $I_{K,ACH-c}$ blockade. Furthermore, in both our in vitro and whole-heart models, pathological conditions that promote fibrosis are absent. It thus appears that in our models a possible contribution of fibroblast to AF induction is overshadowed by the strong proarrhythmic effects of $I_{K,ACH-c}$.

Study Limitations

The present study made use of nrCMCs and neonatal rat hearts, which differ electrophysiologically from the more clinically relevant adult human cardiomyocytes and hearts. Use of cardiomyocytes from human adults is hampered by the difficulties in obtaining human cardiac tissue of sufficient quality for the isolation of cardiomyocytes and maintaining human cardiomyocytes in a differentiated state during culture. In addition, healthy atrial nrCMCs were used to facilitate the study of Kir3.x and $I_{K,ACH-c}$. It should be noted, however, that constitutive activation of $I_{K,ACH}$ in human atrial myocytes is usually preceded by significant atrial remodeling and hence may have a different origin than in our model. Therefore, our study focused on a proof of principle, investigating the role of $I_{K,ACH}$ on APD alternans, AF prevention, and AF termination regardless of its onset. Thus, the results may not be directly extrapolatable to the clinical setting.

Conclusions

In neonatal rat atrial cell monolayers and intact atria, the acetylcholine-inducible potassium current is constitutively active and plays a crucial role in the initiation of sustained tachyarrhythmias. Mechanistically, it is shown in atrial cell monolayers that $I_{K,ACH-c}$ is mediated by Kir3.x and regulates not only the initiation but also the maintenance and termination of these arrhythmias by controlling APD and APD alternans through APD restitution steepening. Accordingly, this study provides

insights into the molecular basis of atrium-specific $I_{K,ACH-c}$ and reveals the crucial role it could play in proarrhythmic and antiarrhythmic mechanisms in atrial tissue. These novel insights could contribute to the development of mechanistically driven and atrium-specific, antiarrhythmic strategies.

Acknowledgements

We thank Huybert J.F. van der Stadt for excellent technical support.

Sources of Funding

This work was supported by the Dutch Heart Foundation (E. Dekker grant [2012/T023 to Dr Bingen]) and the Netherlands Organization for Scientific Research (VENI grant [91611070 to Dr Pijnappels]).

Disclosures

None.

References

1. Lloyd-Jones DM, Wang TJ, Leip EP, Larson MG, Levy D, Vasan RS, D'Agostino RB, Massaro JM, Beiser A, Wolf PA, Benjamin EJ. Lifetime risk for development of atrial fibrillation: the Framingham Heart Study. *Circulation*. 2004;110:1042-1046.
2. Miyasaka Y, Barnes ME, Bailey KR, Cha SS, Gersh BJ, Seward JB, Tsang TS. Mortality trends in patients diagnosed with first atrial fibrillation: a 21-year community-based study. *J Am Coll Cardiol*. 2007;49:986-992.
3. Wolowacz SE, Samuel M, Brennan VK, Jasso-Mosqueda JG, Van Gelder IC. The cost of illness of atrial fibrillation: a systematic review of the recent literature. *Europace*. 2011;13:1375-1385.
4. Calkins H, Kuck KH, Cappato R, Brugada J, Camm AJ, Chen SA, Crijns HJ, Damiano RJ, Jr., Davies DW, DiMarco J, Edgerton J, Ellenbogen K, Ezekowitz MD, Haines DE, Haissaguerre M, Hindricks G, Iesaka Y, Jackman W, Jalife J, Jais P, Kalman J, Keane D, Kim YH, Kirchhof P, Klein G, Kottkamp H, Kumagai K, Lindsay BD, Mansour M, Marchlinski FE, McCarthy PM, Mont JL, Morady F, Nademanee K, Nakagawa H, Natale A, Nattel S, Packer DL, Pappone C, Prystowsky E, Raviele A, Reddy V, Ruskin JN, Shemin RJ, Tsao HM, Wilber D. 2012 HRS/EHRA/ECAS Expert Consensus Statement on Catheter and Surgical Ablation of Atrial Fibrillation: recommendations for patient selection, procedural techniques, patient management and follow-up, definitions, endpoints, and research trial design. *Europace*. 2012;14:528-606.
5. Oral H, Knight BP, Tada H, Ozaydin M, Chugh A, Hassan S, Scharf C, Lai SW, Greenstein R, Pelosi F, Jr., Strickberger SA, Morady F. Pulmonary vein isolation for paroxysmal and persistent atrial fibrillation. *Circulation*. 2002;105:1077-1081.
6. Brooks AG, Stiles MK, Laborderie J, Lau DH, Kuklik P, Shipp NJ, Hsu LF, Sanders P. Outcomes of long-standing persistent atrial fibrillation ablation: a systematic review. *Heart Rhythm*. 2010;7:835-846.
7. Cappato R, Calkins H, Chen SA, Davies W, Iesaka Y, Kalman J, Kim YH, Klein G, Packer D, Skanes A. Worldwide survey on the methods, efficacy, and

- safety of catheter ablation for human atrial fibrillation. *Circulation*. 2005;111:1100-1105.
8. Weerasooriya R, Khairy P, Litalien J, Macle L, Hocini M, Sacher F, Lellouche N, Knecht S, Wright M, Nault I, Miyazaki S, Scavee C, Clementy J, Haissaguerre M, Jais P. Catheter ablation for atrial fibrillation: are results maintained at 5 years of follow-up? *J Am Coll Cardiol*. 2011;57:160-166.
 9. Coplen SE, Antman EM, Berlin JA, Hewitt P, Chalmers TC. Efficacy and safety of quinidine therapy for maintenance of sinus rhythm after cardioversion. A meta-analysis of randomized control trials. *Circulation*. 1990;82:1106-1116.
 10. Echt DS, Liebson PR, Mitchell LB, Peters RW, Obias-Manno D, Barker AH, Arensberg D, Baker A, Friedman L, Greene HL, . Mortality and morbidity in patients receiving encainide, flecainide, or placebo. The Cardiac Arrhythmia Suppression Trial. *N Engl J Med*. 1991;324:781-788.
 11. Ehrlich JR and Nattel S. Novel approaches for pharmacological management of atrial fibrillation. *Drugs*. 2009;69:757-774.
 12. Hohnloser SH and Singh BN. Proarrhythmia with class III antiarrhythmic drugs: definition, electrophysiologic mechanisms, incidence, predisposing factors, and clinical implications. *J Cardiovasc Electrophysiol*. 1995;6:920-936.
 13. Waldo AL, Camm AJ, deRuyter H, Friedman PL, MacNeil DJ, Pauls JF, Pitt B, Pratt CM, Schwartz PJ, Veltri EP. Effect of d-sotalol on mortality in patients with left ventricular dysfunction after recent and remote myocardial infarction. The SWORD Investigators. Survival With Oral d-Sotalol. *Lancet*. 1996;348:7-12.
 14. Dobrzynski H, Marples DD, Musa H, Yamanushi TT, Henderson Z, Takagishi Y, Honjo H, Kodama I, Boyett MR. Distribution of the muscarinic K⁺ channel proteins Kir3.1 and Kir3.4 in the ventricle, atrium, and sinoatrial node of heart. *J Histochem Cytochem*. 2001;49:1221-1234.
 15. Liu L and Nattel S. Differing sympathetic and vagal effects on atrial fibrillation in dogs: role of refractoriness heterogeneity. *Am J Physiol*. 1997;273:H805-H816.

16. Dobrev D, Friedrich A, Voigt N, Jost N, Wettwer E, Christ T, Knaut M, Ravens U. The G protein-gated potassium current I(K,ACh) is constitutively active in patients with chronic atrial fibrillation. *Circulation*. 2005;112:3697-3706.
17. Ehrlich JR, Cha TJ, Zhang L, Chartier D, Villeneuve L, Hebert TE, Nattel S. Characterization of a hyperpolarization-activated time-dependent potassium current in canine cardiomyocytes from pulmonary vein myocardial sleeves and left atrium. *J Physiol*. 2004;557:583-597.
18. Bingen BO, Askar SF, Schalij MJ, Kazbanov IV, Ypey DL, Panfilov AV, Pijnappels DA. Prolongation of Minimal Action Potential Duration in Sustained Fibrillation Decreases Complexity by Transient Destabilization. *Cardiovasc Res*. 2012;97:161-170.
19. Askar SF, Ramkisoensing AA, Schalij MJ, Bingen BO, Swildens J, van der Laarse A, Atsma DE, de Vries AA, Ypey DL, Pijnappels DA. Antiproliferative treatment of myofibroblasts prevents arrhythmias in vitro by limiting myofibroblast-induced depolarization. *Cardiovasc Res*. 2011;90:295-304.
20. Kleber AG and Rudy Y. Basic mechanisms of cardiac impulse propagation and associated arrhythmias. *Physiol Rev*. 2004;84:431-488.
21. Nolasco JB and Dahlen RW. A graphic method for the study of alternation in cardiac action potentials. *J Appl Physiol*. 1968;25:191-196.
22. Jalife J. Deja vu in the theories of atrial fibrillation dynamics. *Cardiovasc Res*. 2011;89:766-775.
23. Hedin KE, Lim NF, Clapham DE. Cloning of a *Xenopus laevis* inwardly rectifying K⁺ channel subunit that permits GIRK1 expression of IKACH currents in oocytes. *Neuron*. 1996;16:423-429.
24. Krapivinsky G, Gordon EA, Wickman K, Velimirovic B, Krapivinsky L, Clapham DE. The G-protein-gated atrial K⁺ channel IKACH is a heteromultimer of two inwardly rectifying K(+)-channel proteins. *Nature*. 1995;374:135-141.
25. Bettahi I, Marker CL, Roman MI, Wickman K. Contribution of the Kir3.1 subunit to the muscarinic-gated atrial potassium channel IKACH. *J Biol Chem*. 2002;277:48282-48288.
26. Medi C, Sparks PB, Morton JB, Kistler PM, Halloran K, Rosso R, Vohra JK, Kumar S, Kalman JM. Pulmonary vein antral isolation for paroxysmal atrial

- fibrillation: results from long-term follow-up. *J Cardiovasc Electrophysiol.* 2011;22:137-141.
27. Kalifa J, Jalife J, Zaitsev AV, Bagwe S, Warren M, Moreno J, Berenfeld O, Nattel S. Intra-atrial pressure increases rate and organization of waves emanating from the superior pulmonary veins during atrial fibrillation. *Circulation.* 2003;108:668-671.
 28. Hocini M, Nault I, Wright M, Veenhuyzen G, Narayan SM, Jais P, Lim KT, Knecht S, Matsuo S, Forclaz A, Miyazaki S, Jadidi A, O'Neill MD, Sacher F, Clementy J, Haissaguerre M. Disparate evolution of right and left atrial rate during ablation of long-lasting persistent atrial fibrillation. *J Am Coll Cardiol.* 2010;55:1007-1016.
 29. Narayan SM, Bode F, Karasik PL, Franz MR. Alternans of atrial action potentials during atrial flutter as a precursor to atrial fibrillation. *Circulation.* 2002;106:1968-1973.
 30. Gong Y, Xie F, Stein KM, Garfinkel A, Cuiianu CA, Lerman BB, Christini DJ. Mechanism underlying initiation of paroxysmal atrial flutter/atrial fibrillation by ectopic foci: a simulation study. *Circulation.* 2007;115:2094-2102.
 31. Hiromoto K, Shimizu H, Furukawa Y, Kanemori T, Mine T, Masuyama T, Ohyanagi M. Discordant repolarization alternans-induced atrial fibrillation is suppressed by verapamil. *Circ J.* 2005;69:1368-1373.
 32. Tsai CT, Chiang FT, Tseng CD, Yu CC, Wang YC, Lai LP, Hwang JJ, Lin JL. Mechanical stretch of atrial myocyte monolayer decreases sarcoplasmic reticulum calcium adenosine triphosphatase expression and increases susceptibility to repolarization alternans. *J Am Coll Cardiol.* 2011;58:2106-2115.
 33. Schotten U, Verheule S, Kirchhof P, Goette A. Pathophysiological mechanisms of atrial fibrillation: a translational appraisal. *Physiol Rev.* 2011;91:265-325.
 34. Kawara T, Derksen R, de Groot JR, Coronel R, Tasseron S, Linnenbank AC, Hauer RN, Kirkels H, Janse MJ, de Bakker JM. Activation delay after premature stimulation in chronically diseased human myocardium relates to the architecture of interstitial fibrosis. *Circulation.* 2001;104:3069-3075.

Supplemental Material

Methods

All animal experiments were approved by the Animal Experiments Committee of the Leiden University Medical Center and conformed to the Guide for the Care and Use of Laboratory Animals as stated by the US National Institutes of Health.

Cell isolation and culture

Ventricular and atrial cardiomyocytes (CMCs) were isolated from 2-3 old neonatal Wistar rats by collagenase digestion as described previously.¹ Isoflurane inhalation (4-5%) was used to anaesthetize animals. After adequate anesthesia had been confirmed by the absence of pain reflexes, hearts were excised. Subsequently, large vessels were removed and atria were separated from ventricles. Atrial and ventricular tissue was gently minced and digested using collagenase type 1 (450 U/ml; Worthington, Lakewood, NJ) and DNase I (18,75 Kunitz/ml; Sigma-Aldrich, St. Louis, MO) during 2 subsequent 30-min digestion steps with agitation in a water bath at 37°C. Cell suspensions were pre-plated on Primaria-coated culture dishes (Becton Dickinson, Breda, the Netherlands) for 120 min to allow for preferential attachment of non-myocytes. Next, the unattached cells (mainly CMCs) were passed through a nylon cell strainer with a mesh pore size of 70 µm (Becton Dickinson) to remove cell aggregates and, after counting, the cells were plated isotropically on fibronectin (Sigma-Aldrich)-coated, round glass coverslips (15-mm diameter) in 24-well plates (Corning Life Sciences, Amsterdam, the Netherlands). Cell densities of 2-8×10⁵ cells/well were used depending on the experiment. To restrict unwanted expansion of the remaining non-myocytes, cell proliferation was inhibited by incubation with Mitomycin-C (10 µg/ml; Sigma-Aldrich) for 2 h at day 1 of culture as described previously.^{1,2} All cultures were refreshed daily with Dulbecco's modified Eagle's medium (DMEM)/HAM's F10 (1:1, v/v; both from Life Technologies, Bleiswijk, the Netherlands) supplemented with 5% horse serum (Life Technologies) and cultured in a humidified incubator at 37°C and 5% CO₂.

Immunocytology

Cells were stained for the markers of interest after several rinses with ice-cold **Error! Not a valid link.** to wash out the culture medium, fixation with 1% formaldehyde in PBS and permeabilization with 0.1% Triton X-100 in PBS. Primary antibodies (1:200 dilution in PBS+5% fetal bovine serum [FBS; Life Technologies]) and corresponding Alexa Fluor 488/568-conjugated secondary antibodies (1:400 dilution in PBS+5% FBS; Life Technologies) were left on the cells for 16 and 2 h, respectively, at 4°C. Cultures were stained using antibodies directed against α -actinin (Sigma-Aldrich) as CMC marker, myosin light chain 2a (MLC2a; a gift from Dr. S.W. Kubalak, Charleston, SC) and natriuretic peptide precursor A (NPPA, Merck Millipore, Billerica, MA) as markers for atrial CMCs and myosin light chain 2v (MLC2v; Synaptic Systems, Goettingen, Germany) to identify ventricular CMCs. Non-myocytes were characterized immunostaining using antibodies specific for collagen type I (fibroblasts; Abcam, Cambridge, MA), platelet endothelial cell adhesion molecule-1 (PECAM-1; endothelial cells; Abcam) and smooth muscle myosin heavy chain (smMHC; smooth muscle cells; Abcam). Primary antibodies specific for connexin40 (Cx40; Santa Cruz Biotechnology, Dallas, TX) and connexin43 (Cx43; Sigma-Aldrich) were used to determine expression of gap junction proteins. Counterstaining of the nuclei was performed by a 5-min incubation at room temperature with 10 μ g/ml Hoechst 33342 (Life Technologies) in PBS+5% FBS. Cells were rinsed twice with PBS+5% FBS after incubation with primary antibodies, secondary antibodies and Hoechst 33342. Coverslips were mounted in Vectashield mounting medium (Vector Laboratories, Burlingame, CA) to minimize photobleaching. Images were taken at equal exposure times between compared groups using a fluorescence microscope equipped with a digital color camera (Nikon Eclipse 80i; Nikon Instruments Europe, Amstelveen, the Netherlands). Dedicated software (NIS Elements [Nikon Instruments Europe] and ImageJ [version 1.43; National Institutes of Health, Bethesda, MD]) were used to store and quantify immunofluorescence signals, respectively. All proteins of interest were studied in at least 3 different cultures per experimental group, from which at least 15 representative images were taken.

Immunohistology

Neonatal rat hearts were rinsed with PBS, fixed overnight using 4% formaldehyde in PBS and dehydrated by immersion in 70% ethanol (3 h), 96% ethanol (3 h), 100%

ethanol (3 h) and 1-butanol (overnight), respectively. Hearts were embedded in paraffin, cut in 5- μ m-thick sections and mounted on StarFrost adhesive microscope slides (Knittel Glass, Braunschweig, Germany). Next, sections were deparaffinized in xylene and rehydrated by the subsequent immersion in 100% ethanol, 96% ethanol, 70% ethanol and PBS for 5 min each. Antigen retrieval was performed by incubating the slides with 0.05% trypsin and 0.1% CaCl₂ in demineralized water at pH 7.8 for 15 min at 37°C and 15 min at 20°C, respectively. Sections were immunostained overnight with the aforementioned primary antibodies directed against MLC2a, α -actinin and collagen type I diluted 1:100 in PBS with 1% bovine serum albumin (BSA; Sigma-Aldrich) and 1% Tween-20 (PBSBT). Corresponding secondary antibodies (Alexa Fluor 488/568-conjugated antibodies, Life Technologies) diluted in PBSBT were incubated for 2 hours, after which the nuclei were counterstained with 10 μ g/ml Hoechst 33342 in PBSBT. Image acquisition, processing and analysis were done using the fluorescence microscope and software described above.

Western blotting

CMC cultures were rinsed twice with ice-cold PBS to wash out the culture medium. Next, the cells were lysed in RIPA buffer (50 mM Tris-HCl [pH 8.0], 150 mM NaCl, 1% Triton X-100, 0.5% sodium deoxycholate, 0.1% sodium dodecyl sulfate supplemented with protease inhibitors [cOmplete, Mini Protease Inhibitor Cocktail Tablet; Roche Applied Science, Penzberg, Germany]). Lysates were subsequently flash frozen in liquid nitrogen, thawed and centrifuged at 4°C and 21,130 \times g for 15 min to get rid of undissolved material. The protein concentration in the supernatant was determined using BCA Protein Assay Reagent (Thermo Fisher Scientific, Etten-Leur, the Netherlands). Proteins (10 μ g per sample; \geq 3 samples per group) were then size-fractionated in NuPage Novex 12% Bis-Tris gels (Life Technologies) and transferred to Hybond polyvinylidene difluoride membranes (GE Healthcare, Diegem, Belgium) by wet electroblotting. Membranes were blocked in Tris-based saline, 0.1% Tween-20 (TBST) supplemented with 5% BSA for 1 h at room temperature. Next, the blots were incubated with primary antibodies directed against Cx40 (1:1,000), Cx43 (1:100,000), Kir3.1 (1:1,000; Alomone Labs, Jerusalem, Israel), Kir3.4 (1:1,000; Santa Cruz Biotechnology), MLC2a (1:200,000), MLC2v (1:5,000), NPPA (1:5,000) and glyceraldehyde 3-phosphate dehydrogenase (1:120,000; loading control; Merck Millipore) for 1 h at room temperature in TBST+5% BSA. Following 3 rinses with

TBST, the blots were incubated with appropriate horseradish peroxidase-conjugated secondary antibodies (Santa Cruz Biotechnology) diluted 1:1,000 in TBST+5% BSA for 1 h at room temperature. After another 3 rinses with TBST, membranes were immersed in ECL Prime Western blot detection reagent (GE Healthcare) and chemiluminescence was captured using the ChemiDoc XRS imaging system (Bio-Rad Laboratories, Veenendaal, the Netherlands).

For Western blotting of whole hearts, hearts were excised, atria and ventricles were carefully separated and rinsed in ice-cold PBS before lysis in RIPA buffer using a TissueLyser LT (QIAGEN, Benelux, Venlo, the Netherlands). The whole heart lysates were subsequently processed in the same manner as the lysates of cultured cells.

Construction of self-inactivating lentivirus (SIN-LV) shuttle plasmids

To repress rat *Kcnj3* expression, a SIN-LV shuttle construct encoding a short hairpin (sh) RNA targeting mouse *Kcnj3*, and matching perfectly with the coding sequence of the rat *Kcnj3* gene, was obtained from the MISSION shRNA library (Sigma-Aldrich; clone TRCN0000069736). To knock down rat *Kcnj5* expression, the hybridization product of oligodeoxyribonucleotides

5'

CCGGGACCACAAGAAGATCCCCAAACTCGAGTTTGGGGATCTTCTTGTGGTCTT
TTTG 3' and

5'

AATTCAAAAAGACCACAAGAAGATCCCCAAACTCGAGTTTGGGGATCTTCTTGT
GGTC 3' was inserted in between the unique SgrAI and EcoRI recognition sites of SHC007 (MISSION shRNA library; Sigma-Aldrich) to replace its *Photinus pyralis luciferase (PpLuc)*-specific shRNA-coding sequence. Next, the marker gene cassette in these constructs and in SHC007, which consisted of the human *phosphoglycerate kinase 1* gene promoter and the puromycin-N-acetyltransferase-coding sequence was replaced by the human *eukaryotic translation elongation factor 1 alpha 1* gene promoter and the *Aequorea victoria* enhanced green fluorescent protein (eGFP)-coding sequence. This yielded the SIN-LV shuttle plasmids pLKO.1-mKcnj3-shRNA.hEEF1a1.eGFP, pLKO.1-rKcnj5-shRNA.hEEF1a1.eGFP and pLKO.1-PpLuc-shRNA.hEEF1a1.eGFP, which were used to generate LV-Kir3.1↓, LV-Kir3.4↓ and LV-PpLuc↓ particles, respectively.

SIN-LV production

Vesicular stomatitis virus G protein-pseudotyped SIN-LV particles were generated by transfecting subconfluent monolayers of 293T cells with the packaging plasmids psPAX2 (Addgene, Cambridge, MA; plasmid number: 12260) and pLP/VSVG (Life Technologies) and one of the 3 aforementioned SIN-LV shuttle constructs at a molar ratio of 2:1:1. The 293T cells were cultured in high-glucose DMEM containing 10% FBS. The transfection mixture, which consisted of 40 µg of plasmid DNA and 120 µg of polyethyleneimine (Polysciences Europe, Eppelheim, Germany) in 2 ml of 150 mM NaCl per 175-cm² cell culture flask (Greiner Bio-One, Alphen aan den Rijn, the Netherlands) was directly added to the culture medium. Sixteen hours later, the transfection medium in each flask was replaced by 15 ml of DMEM supplemented with 5% FBS and 25 mM HEPES-NaOH (pH 7.4). At 40-48 h after the start of the transfection procedure, the culture medium was harvested and cleared from cellular debris by centrifugation for 10 min at 3,000×g and filtration through a 33-mm diameter, 0.45-µm pore size polyethersulfone syringe filter (Millex Express; Merck Millipore). To concentrate and purify the SIN-LV particles, 30 ml of vector suspension were layered onto a 5-ml cushion of 20% (wt/vol) sucrose in PBS and centrifuged at 15,000 rotations per min for 2 h at 4°C in an SW32 rotor (Beckman Coulter, Fullerton, CA). Next, the supernatant was discarded and the pellet containing the SIN-LV particles was suspended in 500 µl of PBS-1% BSA by gentle rocking overnight at 4°C. The concentrated vector suspension was divided in 50-100 µl aliquots and stored at -80°C until use. The 3 SIN-LVs were applied to the atrial CMC cultures at doses that resulted in transduction of essentially all cells in the cultures. The transduction level was assessed using a Zeiss Axiovert 200M inverse fluorescence microscopy to visualize eGFP fluorescence.

In vitro optical mapping

At day 9 of culture, action potential (AP) propagation was investigated on a whole-culture scale by optical mapping using the voltage-sensitive dye di-4-ANEPPS (Life Technologies) as described previously.^{1,2} During optical mapping cells were stimulated electrically using a custom-made, epoxy-coated unipolar platinum electrode with square suprathreshold electrical stimuli at 1 and 2-20 Hz (2-Hz increments). Fibrillation was induced by burst pacing with a cycle length of 20-100

ms. A specialized electrical stimulus module with corresponding software (Multichannel Systems, Reutlingen, Germany) was used to perform electrical stimulation. Data analysis and construction of activation maps were performed with specialized software (BrainVision Analyzer 1101; Brainvision, Tokyo, Japan) after pixel signals were averaged with 8 of its nearest neighbors, to minimize noise artifacts. Conduction velocity (CV) in cultures with uniform or reentrant activation patterns was calculated perpendicular to the activation wavefront, between two 3 by 3 pixel grids typically spaced 2-8 mm apart. CV, activation frequency, APD during maximal paced activation frequency (*i.e.* minimal APD) and APD during 1 Hz pacing were determined at 6 different locations equally distributed throughout the culture and averaged before further analysis. APD was determined at 80% of repolarization (APD80) because of the rat AP shape. Wavelength was calculated by multiplying average CV with APD80 (for uniform propagation) or reentrant cycle length.¹ Complexity was defined as the number of phase singularities (PSs) per culture, determined by using the phase space method as described previously.¹

The effect of several drugs (100 nmol/L tertipin [Alomone Labs], 200 nmol/L atropine (Sigma-Aldrich) and 2 μ mol/L carbachol (Sigma-Aldrich)³ was studied by pipetting them directly into the medium, dispersing them by gentle agitation, immediately followed by optical mapping.

Whole heart mapping

Neonatal (2-3 days old) Wistar rats were anesthetized by isoflurane inhalation (4-5%) and adequate anesthesia was confirmed by the absence of pain reflexes. Subsequently, the thoracic wall was cut and lifted to expose the heart. Oxygenated Tyrode's solution (comprising [in mM] NaCl 130, CaCl₂ 1.8, KCl 4.0, MgCl₂ 1.0, NaH₂PO₄ 1.2, NaHCO₃ 24 and glucose 5.5 at pH 7.4) supplemented with 20 mM 2,3-butanedione monoxime (Sigma-Aldrich, BDM) with or without 200 nM tertipin to minimize motion artifacts and to block Kir3.x channels, respectively, was carefully injected in a 200 μ L bolus into the left ventricle using a 30-G needle. The heart was excised just prior to absence of visible contractions, and submersed in Tyrode's solution with BDM and tertipin to remove remaining blood. Next, hearts were incubated in Tyrode's solution with BDM and tertipin containing 2 μ M di-4-ANEPPS for 2 min at 37°C, after which the heart was rinsed and submersed in Tyrode's solution with BDM and tertipin and placed on top of a 37°C heating plate under the

optical mapping camera. AF was induced by burst pacing at a cycle length of 20-100 ms using a custom-made bipolar platinum electrode. Control hearts were treated in an identical manner except that tertiapin was left out during the entire procedure. Typical optical mapping experiments were performed within 6 min after excision of the heart.

Results

Cell culture characterization

Immunocytological analysis at day 9 of culture showed that 100% of the CMCs (*i.e.* α -actinin-positive cells) in the atrial cell cultures were MLC2a-positive (*i.e.* of atrial origin) while in the ventricular cell cultures no MLC2a-positive CMCs were detected (Supplemental Figure IA,C). In addition, NPPA levels were much higher in the atrial than in the ventricular CMC cultures (Supplemental Figure IB). Western blot analyses confirmed these results and showed that MLC2v was exclusively present in the ventricular cell cultures (Supplemental Figure ID). Atrial CMC cultures contained more Cx40 than the ventricular CMC cultures, while Cx43 levels were higher in ventricular CMCs as judged by both Western blotting (Supplemental Figure ID) and immunocytology (Supplemental Figure IE). Atrial cell cultures were also analyzed by collagen type I, PECAM-1 and smMHC staining. While none of the cells contained detectable amounts of PECAM-1 or smMHC, $17.0 \pm 2.5\%$ of the cells stained positive for collagen-I (Supplemental Figure IF) suggesting that the non-myocytes in atrial cell cultures consisted mainly, if not exclusively, of fibroblasts.

Constitutive activation of I_{KACH} in neonatal rat atrial CMC cultures

During constitutive activation I_{KACH} becomes activated independently of acetylcholine or the acetylcholine receptor. Therefore, to confirm constitutive I_{KACH} (I_{KACH-c}) activity in our neonatal rat atrial CMC cultures, atropine (a non-selective muscarinic receptor antagonist) was used to block the acetylcholine receptor during optical mapping to study the dependence of APD on acetylcholine receptor activation. Atropine had no significant effect on the APD80 (38.5 ± 3.9 vs 38.6 ± 3.9 ms in control cultures, $p=ns$), whereas subsequent treatment with tertiapin significantly increased APD80 (to 110.9 ± 13.1 ms, $p < 0.0001$) (Supplemental Figure IIIA,C). This illustrates that after blockade of the acetylcholine receptor there is still current flowing through

Kir3.x channels shortening APD. Thus, our cultures of neonatal rat atrial CMCs indeed possess $I_{K_{ACh-C}}$ activity. Nonetheless, treatment of neonatal rat atrial CMCs with carbachol (a non-selective muscarinergic receptor agonist) induced a significant shortening of APD80 (from 39.6 ± 4.2 to 29.3 ± 3.9 ms, $p < 0.0001$). After subsequent atropine treatment APD80 rose to 45.6 ± 6.9 ms, ($p < 0.0001$ vs carbachol-treated cells) abolishing the carbachol-induced APD shortening, while addition of tertiapin to the carbachol- and atropine-treated CMCs again greatly increased APD80 (to 119.8 ± 18.5 , $p < 0.0001$ vs [carbachol- and] atropine-treated cells) (Supplemental Figure IIIB,D). Together, these results show that the short AP in neonatal rat atrial CMC cultures is caused by a tertiapin-sensitive current which is independent of ligand-induced muscarinergic receptor activation and therefore constitutively active. The cells, however, also still possess muscarinergic receptor stimulation-dependent Kir3.x activity given the APD shortening-effect of carbachol treatment and its inhibition by atropine.

APD alternans in neonatal rat atrial CMCs is independent of intracellular $[Ca^{2+}]$

To confirm the restitution-based nature of APD alternans, neonatal rat atrial CMC cultures were treated with the cell-permeable Ca^{2+} chelator BAPTA-AM (10-100 $\mu\text{mol/L}$; Life Technologies) to rule out the contribution of intracellular Ca^{2+} to APD alternans and reentry induction. Successful buffering of intracellular Ca^{2+} was confirmed by phase contrast microscopy, showing absence of visible contractions after incubation with 10 $\mu\text{mol/L}$ BAPTA-AM during 1-Hz pacing (data not shown). Treatment with BAPTA-AM did not prevent APD alternans (Supplemental Figure VA), while the frequency of reentry induction after burst pacing remained equal for all tested concentrations of BAPTA-AM (84.6% in controls vs 91.7%, 83.3% and 83.3% after treatment of the cells with 10, 50 or 100 $\mu\text{mol/L}$ BAPTA-AM, respectively) (Supplemental Figure VB). This suggests that APD alternans and consequential reentry induction in our model are driven by the $I_{K_{ACh-C}}$ -induced steepness in the APD/CV restitution curve.

Movie 1:

Typical example from an optical mapping experiment in a neonatal rat atrial CMC culture after burst pacing showing period-1 reentry dynamics. The first part shows the high-pass-filtered optical signal exemplifying the repeating activation pattern during period-1 reentry. The second part displays the phase map progression of the same optical mapping experiment, showing the wave propagation around multiple PSs with fixed positioning throughout the experiment.

Movie 2:

Typical example from an optical mapping experiment in a neonatal rat atrial CMC culture after burst pacing showing aperiodical reentry dynamics. The first part shows the high-pass-filtered optical signal exemplifying the transient activation pattern during aperiodical reentry. The second part displays the phase map progression of the same optical mapping experiment, showing multiple instances of PS formation and disappearance leading to aperiodical dynamics.

Movie 3:

Typical example from an optical mapping experiment in neonatal rat atrial cultures investigating the effect of treatment with LV-Kir3.1↓, LV-Kir3.4↓ or the control vector LV-PpLuc↓ after reentry induction by burst pacing. The high-pass-filtered optical signal shows less complex conduction patterns and a lower activation frequency in cell cultures that had been transduced with the *Kcnj3*- or *Kcnj5*-specific shRNA-coding SIN-LV than in those exposed to the control vector.

Movie 4:

Typical movie from optical mapping experiment investigating the effect of tertiapin on reentry dynamics and termination. Part 1 shows the high-pass-filtered optical signal in an atrial culture after burst pacing during the first 500 ms after tertiapin incubation, which is characterized by persisting rotors and period-1 dynamics. The second part shows the high-pass-filtered optical signal in an atrial culture after a few seconds of tertiapin incubation, characterized by drifting rotors and aperiodical dynamics, which is followed by termination (part 3) when the last rotor collides with the culture boundary.

References

1. Bingen BO, Askar SF, Schalij MJ, Kazbanov IV, Ypey DL, Panfilov AV, Pijnappels DA. Prolongation of minimal action potential duration in sustained fibrillation decreases complexity by transient destabilization. *Cardiovasc Res.* 2013;97:161-170.
2. Askar SF, Ramkisoensing AA, Schalij MJ, Bingen BO, Swildens J, van der Laarse A, Atsma DE, de Vries AA, Ypey DL, Pijnappels DA. Antiproliferative treatment of myofibroblasts prevents arrhythmias in vitro by limiting myofibroblast-induced depolarization. *Cardiovasc Res.* 2011;90:295-304.
3. Dobrev D, Friedrich A, Voigt N, Jost N, Wettwer E, Christ T, Knaut M, Ravens U. The G protein-gated potassium current I(K,ACh) is constitutively active in patients with chronic atrial fibrillation. *Circulation.* 2005;112:3697-3706.

Chapter 7

Summary, conclusions and future perspectives

**Samenvatting, conclusies en
toekomstperspectieven**

Summary

The general introduction of this thesis, **chapter I**, starts with a brief comparison of the pathological features of skeletal muscle disorders and cardiac diseases. Furthermore, the lack of (effective) therapies for many cardiac and skeletal muscle diseases is discussed. This paucity in adequate treatment options for (cardio)myopathies is partially explained by the limited knowledge about the precise mechanisms underlying skeletal and cardiac muscle diseases and, related to this, by the non-specific action of many therapeutic interventions. Therefore, the aim of this thesis was to establish cellular models and employ viral vector technology to identify potential targets for future therapeutic interventions in skeletal and cardiac muscle diseases.

Chapter II describes the development of a bipartite lentivirus vector (LV)-based assay to quantify cell fusion in which the cellular fusion partners are transduced with a *Gaussia princeps luciferase* (*GpLuc*) expression unit (acceptor cells) or with a recombinant gene encoding FLPe, a nuclear-targeted and molecularly evolved version of flippase (donor cells). *GpLuc* is a secretory protein allowing repeated analysis of the same study object, a great advantage over cell fusion assays using *Photinus pyralis luciferase* (*PpLuc*), which is not a secretory protein precluding consecutive analysis of the same study object. To investigate whether the spread of FLPe^{NLS+} in myotubes is limited due to its nuclear localization signal (NLS), myoblasts were transduced with LVs encoding either FLPe^{NLS+} or an NLS-less version of FLPe (FLPe^{NLS-}) and subsequently co-cultured in different ratios with myoblasts containing the FLPe-activatable *GpLuc* expression cassette. At different times after induction of cell-to-cell fusion the *GpLuc* activity in the culture medium was determined. In general, *GpLuc* expression increased with increasing fractions of *GpLuc*-transduced myoblasts and both FLPe^{NLS+} and FLPe^{NLS-} activated the latent *GpLuc* gene but when the percentage of *FLPe*-expressing myoblasts was limiting, FLPe^{NLS+} generally yielded slightly higher signals than FLPe^{NLS-} while at low acceptor-to-donor cell ratios FLPe^{NLS-} was usually superior. Thus, it was shown that NLS does not limit the ability of FLPe^{NLS+} to spread through myofibers and to induce reporter gene expression. However, at high fraction of *FLPe*-expressing myoblasts the presence of the NLS negatively affected reporter gene expression. These results

show that a rapid and simple chemiluminescence assay for quantifying cell-to-cell fusion progression based on GpLuc has been developed.

In **chapter III** different properties of Gelatin/Siloxane/Hydroxyapatite (GS-Hyd) scaffolds are investigated such as *in vivo* biodegradability, cytotoxic effects and ability to support cell adhesion. Mesenchymal stem cells (MSCs) were treated with different volumes of the scaffold suspension for evaluation of its cytotoxic effects. MSCs were also cultured on the scaffold for 2 weeks to evaluate the ability of the scaffold to promote cell adhesion and growth. The GS-Hyd scaffold did not exert noticeable cytotoxic effects on the MSCs and these cells could adhere to the scaffold, expand their elongations and form colonies. To study its biodegradability the GS-Hyd scaffolds were implanted in thigh muscle, testicle and liver of Wistar rats. At different times after implantation, scaffolds were excised and their dry weight was measured. The largest reduction in scaffold weight occurred during the first days after implantation and varied from 53% in liver to 71% in thigh muscle at 3 days post implantation. Subsequently, scaffold degradation slowed down with 30%, 25% and 18% of the initial scaffold remaining at 3 weeks after implantation in liver, testis and thigh muscle, respectively. Scanning electron microscopy (SEM) indicated obvious morphological changes on the surface of the scaffold and in the diameter of the pores after 21 days of implantation. In conclusion, the GS-Hyd scaffold seems to be a promising tool for cell-based therapeutic interventions, but additional research is needed to assess its clinical utility.

Chapter IV is dedicated to the development of an *in vitro* model for studying the contribution of pathological cardiac hypertrophy (PCH) per se to arrhythmia independent of fibrosis or other PCH-related processes. Treatment of neonatal rat ventricular cardiomyocyte (nr-vCMC) monolayers with phorbol 12-myristate 13-acetate (PMA) for two times 24 hours, led to increases in cell surface area (CSA) and protein content of the cardiomyocytes. Assessment of the electrophysiological properties of PMA-treated and control nr-vCMC monolayers by optical mapping at day 9 of culture, showed a decrease in conduction velocity (CV) and increases in action potential duration (APD) and APD dispersion upon PMA treatment. It also caused a 32% reduction in sarcoplasmic/endoplasmic reticulum Ca^{2+} ATPase 2 level and an increase in natriuretic peptide A (42%) and α 1-skeletal muscle actin (34%) levels indicating that the hypertrophic response induced by PMA was pathological in nature. Upon local 1-Hz stimulation, 54% of the PMA-treated cultures showed focal

tachyarrhythmias based on triggered activity, while the rate of tachyarrhythmias was only 4% in control nr-vCMC cultures. PMA-treated nr-vCMC cultures may thus represent a well-controllable *in vitro* model for testing new therapeutic interventions targeting specific aspects of hypertrophy-associated arrhythmias.

Chapter V describes the development of *in vitro* models of post-myocardial infarction (MI) compact and patchy fibrosis and the assessment of their pro-arrhythmic features by optical mapping. To this end, either a single large circular anatomical obstruction or multiple smaller circular anatomical obstructions were made in the center of confluent nr-vCMC monolayers by forcefully pressing tailor-made plexiglass stamps onto the cells. To gain mechanistic insight into arrhythmias associated with post-MI scars several parameters such as rate of inducibility, cycle length and maintenance of reentry were compared between these two types of anatomical obstructions. In patchy cultures, reentry was slightly less easily inducible (41% vs 52%) and, when it occurred, had a shorter cycle length (234 ± 52 vs 288 ± 38 ms) than in compact cultures. Sustained reentry was less often observed in patchy cultures (40% vs 88% in compact cultures) while the percentage of complex arrhythmias was higher (31% vs 11%). Meandering of phase singularities and gradients of excitability during reentrant arrhythmias were only detectable in patchy cultures. Reentry could be terminated more easily in compact cultures (82% vs 20% in patchy cultures). Taken together, this *in vitro* model of patchy and compact obstructions reproduced arrhythmic features similar to those observed after early- and non-reperfused MIs, respectively, and may hence provide mechanistic insights into the efficacy of anti-arrhythmic interventions in infarcted hearts with different anatomical substrates.

In **chapter VI** the effects of constitutive acetylcholine-regulated K^+ current ($I_{K,ACh-c}$), which flows through Kir3.1 and Kir3.4 channels, on atrial fibrillation is investigated. Neonatal rat atrial CMC cultures and intact atria were burst paced to induce reentry. Treatment of these cultures with tertiapin prolonged APD, indicating the presence of $I_{K,ACh-c}$. Furthermore, tertiapin decreased rotor frequency and complexity. Reduction of Kir3.1 or 3.4 expression through transduction of cells with LVs encoding Kcnj3- or Kcnj5-specific shRNAs gave similar results. Tertiapin prevented/terminated reentry by prolonging APD and changing APD and CV restitution slopes, thereby lowering the probability of APD alternans and inducing rotor destabilization. Whole-heart mapping experiments confirmed key findings (e.g. >50% reduction in atrial fibrillation

inducibility after $I_{K,ACH-c}$ blockade). This study provided new molecular and mechanistic insights into atrial tachyarrhythmias and identified Kir3.1 and Kir3.4 as promising atrium-specific targets for anti-arrhythmic strategies.

In conclusion, the experiments described in this thesis emphasize the importance of cellular models for (i) elucidating the mechanisms underlying skeletal and cardiac muscle diseases and (ii) identification of novel therapeutic targets. This thesis also underlines the usefulness of viral vector-mediated gene transfer technology for the development of biological assays and the evaluation of therapeutic targets.

Future perspectives

Without a thorough understanding of the mechanisms underlying cardiac and skeletal muscle diseases, their treatment by pharmacological or genetic interventions involve a lot of trial and error. Cellular models are important tools to gain mechanistic insights into skeletal muscle degeneration and cardiac arrhythmias mechanisms allowing the rational design of new treatments. This relates at least in part to their relative simplicity, providing the possibility to investigate a specific pathological feature independent of other complications. Despite of having this and some other advantages, *in vitro* cellular models often do not mimic well enough the *in vivo* situation, which may lead to poor *in vitro-in vivo* correlations. Accordingly, future research should focus on the further improvement of these cellular models in such a way that they better resemble/represent *in vivo* pathological states reducing the need for preclinical and clinical studies. For example, in the case of *in vitro* models of cardiac hypertrophy it is essential to determine which stage in the transition from PCH to heart failure the hypertrophy model represents as this will affect the therapeutic approach. Besides by checking the extent of electrophysiological changes and incidence and nature of arrhythmias, measuring of the contractile force-generating capacity and comparative transcriptome analyses will provide useful information on this issue.

An important hurdle in the development of *in vitro* cellular models arises from the low expansion capability of differentiated cells. For example, postnatal CMCs display very limited proliferation capacity which demands for repetitive isolation and culture of these cells for *in vitro* studies. Therefore, immortalization of atrial or ventricular CMCs from animal or human would circumvent this obstacle. This could be achieved through viral vector-mediated transfer, into these cells, of genes such as those

encoding simian virus 40 large T antigen, B cell-specific Moloney murine leukemia virus integration site 1 (BMI1) or telomerase (TERT) reverse transcriptase.

Genetic manipulations through viral vectors (e.g. overexpression of certain genes or RNA interference) may also help to gain better mechanistic insights into skeletal and cardiac muscle disorders and to further optimize current therapies for these diseases.

Regarding to skeletal muscle wasting, optimization of cell-based therapies may be achieved through enhancement of the fusion of donor cells with each other and with recipient myocytes and by promoting their myogenic differentiation. For instance, forced and controlled expression of fusion-enhancing proteins through transduction of (non-muscle) stem cells with viral vectors encoding these proteins may be beneficial as could be the regulated expression in these cells of myogenic transcription factor genes.

Genetic intervention may also be employed for therapeutic purposes in cardiac arrhythmias. For example, the forced expression of connexins like connexin43 in (myo)fibroblasts present in infarct scars may improve conduction and reduce arrhythmia incidence. This approach could, however, also be deleterious as coupling of CMCs with (myo)fibroblasts would depolarize CMCs and make the tissue susceptible to reentrant tachycardias. The latter problem may be overcome by simultaneously endowing (myo)fibroblasts with a gene like *KCNJ2* whose product is involved in setting the resting membrane potential.

Genetic interventions (overexpression or knockdown) affecting the expression of the genes encoding for ion channels involved in the repolarization phase of the action potential (AP) may also have anti-arrhythmic effects. For example, manipulation of the expression of genes encoding for those ion channels that exert their effect on repolarization in the AP phases at which early afterdepolarizations occur (e.g. adenosine triphosphate (ATP)-sensitive K⁺ channels [K_{ATP} channels]) could provide novel insights into pro- and anti-arrhythmic mechanisms but could also have therapeutic potential.

Effective therapeutic application of viral vectors *in vivo* often requires uniform and near-quantitative transduction of the target tissue and transgene expression at a specific level. This is of particular importance when developing gene therapy for arrhythmias as heterogeneous transduction and inappropriate transgene expression levels may be pro-arrhythmic.

Hence, efficient delivery and high target cell specificity of viral vectors and precise control of transgene expression are of vital importance and deserve further study. Other important topics of future gene therapy research are the further improvement of the safety and reduction of immunogenicity of viral vectors.

Samenvatting

De algemene introductie van dit proefschrift, **hoofdstuk I**, begint met een korte vergelijking van de pathologische kenmerken van skeletspier- en hartspierziekten. Voorts wordt het gebrek aan (effectieve) therapieën voor veel hartspier- en skeletspierziekten bediscussieerd. Deze schaarste aan adequate behandelingsmogelijkheden voor (cardio)myopathieën kan deels worden verklaard door de geringe kennis van de precieze mechanismen die aan skeletspier- en hartspierziekten ten grondslag liggen en, hieraan gerelateerd, door de niet-specifieke werking van veel therapeutische interventies. Het hoofddoel van dit proefschrift was daarom het opzetten van cellulaire modellen en toepassing van virale vectortechnologie ter identificatie van potentiële aangrijpingspunten voor toekomstige behandelmethoden voor skeletspier- en hartspierziekten.

In **hoofdstuk II** wordt de ontwikkeling van een tweedelige lentivirus vector (LV)-gebaseerde analysemethode beschreven voor het kwantificeren van cel fusie waarin de cel fusie-componenten zijn getransduceerd met een *Gaussia princeps luciferase* (*GpLuc*) expressie eenheid (ontvangende cellen) of met een recombinant gen dat codeert voor FLPe, een kerngerichte en moleculair geëvolueerde versie van flippase (donorcellen). *GpLuc* is een secretoir eiwit, waardoor het mogelijk is om herhaalde analyses te verrichten van hetzelfde studieobject, een groot voordeel ten opzichte van cel fusie analyses die gebruik maken van *Photinus pyralis luciferase* (*PpLuc*), wat niet een secretoir eiwit is en daardoor achtereenvolgende analyses van hetzelfde studieobject uitsluit. Om te onderzoeken of de spreiding van FLPe^{NLS+} in gedifferentieerde skeletspiercellen wordt beperkt door het kernlokalisatiesignaal (NLS), werden gedifferentieerde skeletspiercellen getransduceerd met LVs die coderen voor FLPe^{NLS+} of een FLPe versie zonder NLS (FLPe^{NLS-}) en vervolgens in verschillende ratio's in co-cultuur gebracht met myoblasten met een door FLPe activeerbare *GpLuc* expressie cassette. Op verschillende tijdstippen na inductie van fusie tussen cellen werd de *GpLuc* activiteit in het kweekmedium bepaald. In het algemeen nam de *GpLuc* expressie toe met toenemende fracties of *GpLuc*-getransduceerde myoblasten, en zowel FLPe^{NLS+} als FLPe^{NLS-} was in staat om het latente *GpLuc* gen te activeren. Echter, wanneer het percentage myoblasten dat FLPe tot expressie bracht beperkend was, gaf FLPe^{NLS+} over het algemeen iets hogere signalen dan FLPe^{NLS-}; maar bij lage ontvanger:donor celratio's was FLPe^{NLS-}

meestal superieur. Er werd daarmee aangetoond dat het NLS niet beperkend was ten aanzien van het vermogen van $FLPe^{NLS+}$ om zich door gedifferentieerde skeletspiercellen te verspreiden of voor het induceren van reporter-genexpressie. Bij een hoge fractie *FLPe*-expresserende myoblasten heeft de aanwezigheid van het NLS echter een negatief effect reporter-genexpressie. Deze resultaten tonen aan dat het is gelukt om een snelle en simpele analysemethode op basis van GpLuc te ontwikkelen voor de kwantificatie van de progressie van fusie tussen cellen door middel van chemiluminescentie.

In **hoofdstuk III** worden verschillende eigenschappen van Gelatine/Siloxane/Hydroxyapatiet (GS-Hyd) matrices onderzocht zoals *in vivo* biologische afbreekbaarheid, cytotoxische effecten en het vermogen celadhesie te ondersteunen. Mesenchymale stamcellen (MSCs) werden behandeld met verschillende volumes matrixsuspensie voor de evaluatie van de cytotoxische effecten. MSCs werden tevens gedurende 2 weken op de matrix gekweekt ter evaluatie van het vermogen van de matrix om celadhesie en celgroei te bevorderen. De GS-Hyd matrix had geen merkbaar cytotoxisch effect op de MSCs en deze cellen waren in staat om zich te hechten aan de matrix, hun uitlopers uit te breiden en kolonies te vormen. Om de biologische afbreekbaarheid te bestuderen, werden GS-Hyd matrices geïmplantéerd in dijbeenspier, testikel en lever van Wistar ratten. Op verschillende tijdstippen na implantatie werd matrices uitgenomen en werd hun drooggewicht bepaald. De grootste reductie in matrix gewicht vond plaats gedurende de eerste dagen na implantatie en varieerde van 53% in de lever tot 71% in dijbeenspier op dag 3 na implantatie. Vervolgens vertraagde de matrixdegradatie waardoor er 3 weken na implantatie nog 30%, 25% en 18% van de uitgangsmatrix in respectievelijk lever, testis en dijbeenspier resteerde. Scanning elektronmicroscopie liet duidelijke morfologische veranderingen aan het oppervlak van de matrix en in de poriediameter zien 21 dagen na implantatie. Concluderend lijkt de GS-Hyd matrix een veelbelovend hulpmiddel voor celtherapie, maar additioneel onderzoek is nodig om de klinische toepasbaarheid vast te stellen.

Hoofdstuk IV is gewijd aan de ontwikkeling van een *in vitro* model voor het onderzoeken van de specifieke bijdrage van pathologische cardiale hypertrofie (PCH) aan ritmestoornissen, onafhankelijk van fibrose of andere PCH-gerelateerde processen. Behandeling van monolagen van ventriculaire cardiomyocyten geïsoleerd uit neonatale ratten (nr-vCMC) met phorbol 12-myristate 13-acetate

(PMA) gedurende 2 ker 24 uur, leidde tot toenames in celoppervlakte en eiwitinhoud van de cardiomyocyten. Bepaling van de electrofysiologische eigenschappen van PMA-behandelde en controle nr-vCMC monolagen middels optisch mappen op kweekdag 9, lieten een afname van de geleidingssnelheid (CV) en toenames van de actiepotentiaalduur (APD) en APD dispersie zien na PMA behandeling. Verder veroorzaakte de PMA behandeling een 32% afname van het sarcoplasmatisch/endoplasmatisch reticulum Ca^{2+} ATPase 2 gehalte en een toename van de natriuretisch peptide A (42%) en α 1-skeletspier actine (34%) gehaltes, wat aantoonde dat de door PMA-geïnduceerde hypertrofe respons een pathologisch karakter had. Na lokale 1-Hz stimulatie, vertoonden 54% van de PMA-behandelde cultures focale tachyaritmieën op basis van getriggerde activiteit, terwijl de controle nr-vCMCs slechts in 4% van de gevallen tachyaritmieën lieten zien. PMA-behandelde nr-vCMC kweken kunnen derhalve een goed controleerbaar *in vitro* model zijn voor het testen van nieuwe therapeutische interventies voor het bestuderen van specifieke aspecten van hypertrofie-geassocieerde aritmieën.

In **hoofdstuk V** wordt de ontwikkeling van *in vitro* modellen van compacte en fragmentarische fibrose als gevolg van een myocardiaal infarct (MI) beschreven, alsmede de bepaling van hun pro-aritmische eigenschappen door middel van optisch mappen. Hiertoe werd een enkel groot circulair anatomisch obstakel, dan wel multipale kleinere circulaire anatomische obstakels gecreëerd in het midden van confluerende nr-vCMC monolagen door middel van krachtige druk op de cellen met op maat gemaakte plexiglas stempels. Voor het verkrijgen van mechanistisch inzicht in aritmieën die geassocieerd zijn met post-MI littekens werden verschillende parameters vergeleken bij de twee types van anatomische obstakels, zoals de mate van induceerbaarheid, cycluslengte en handhaving van “reentry”. In kweken met fragmentarische fibrose was “reentry” iets minder gemakkelijk induceerbaar (41% vs. 52%) en, als het optrad had het een kortere cycluslengte (234 ± 52 vs. 288 ± 38 ms) dan in cultures met compacte fibrose.

Aanhoudende “reentry” werd minder vaak geobserveerd in fragmentarische culturen (40% vs. 88% in compacte culturen), terwijl het percentage complexe aritmieën hoger was (31% vs. 11%). Meanderende fasesingulariteiten en exciteerbaarheidsgradiënten tijdens aritmieën op basis van “reentry” waren alleen detecteerbaar in fragmentarische culturen. “Reentry” kon gemakkelijker getermineerd worden in compacte cultures (82% vs. 20% in fragmentarische

culturen). Samenvattend konden met de *in vitro* modellen van fragmentarische en compacte obstakels soortgelijke aritmische eigenschappen worden nagebootst als worden gevonden na respectievelijk vroege- en niet-gereperfundeerde MIs. Deze modellen kunnen daarom leiden tot mechanistisch inzicht in de werkzaamheid van anti-aritmische interventies in geïnfarceerde harten met verschillen anatomische substraten.

In **hoofdstuk VI** worden de effecten op atriumfibrilleren onderzocht van constitutief-actieve acetylcholine-gereguleerde K^+ stroom ($I_{K,ACh-c}$), die via Kir3.1 en Kir3.4 kanalen loopt. Culturen van atriale CMCs geïsoleerd uit neonatale ratten en intacte atria werden met hoge frequentie gestimuleerd voor inductie van “reentry”. Behandeling met tertiapin verlengde de APD in atriale culturen tijdens “reentry”, wat duidde op de aanwezigheid van $I_{K,ACh-c}$. Voorts verlaagde tertiapin de frequentie en complexiteit van rotors. Een afname van Kir3.1 of 3.4 expressie door middel van transductie van de cellen met LVs die codeerden voor Kcnj3- of Kcnj5-specifieke shRNAs gaf vergelijkbare resultaten. Tertiapin voorkwam of termineerde “reentry” door verlenging van de APD en door veranderingen van de APD en CV restitutie curves, waardoor de kans op APD alternans verminderde en de kans op rotordestabilisatie toenam. Mapping experimenten van hele harten bevestigden deze bevindingen (b.v. >50% reductie in induceerbaarheid van atriumfibrillatie na $I_{K,ACh-c}$ blokkade). Deze studie heeft nieuwe moleculaire en mechanistische inzichten in atriale tachyarritmieën opgeleverd en heeft geleid tot de identificatie van Kir3.1 en Kir3.4 als veelbelovende atrium-specifieke doelwitten voor anti-aritmische strategieën.

Concluderend benadrukken de experimenten zoals beschreven in dit proefschrift het belang van cellulaire modellen voor (i) het ophelderen van de mechanismen die ten grondslag liggen aan skelet- en hartspierziekten en (ii) het identificeren van nieuwe therapeutische doelwitten. Dit proefschrift onderstreept ook de bruikbaarheid van op virale vectoren gebaseerde genoverdrachttechnologieën voor de ontwikkeling van biologische analysemethoden en de evaluatie van therapeutische doelwitten.

Toekomstperspectieven

Zonder een grondig begrip van de onderliggende mechanismen van hart- en skeletspierziekten, gaan hun behandeling met farmacologische of genetische interventies gepaard met veel praktijkfouten. Cellulaire modellen zijn belangrijke

hulpmiddelen voor het verkrijgen van mechanistische inzichten in skeletspierdegeneratie en cardiale ritmestoornismechanismen als voorwaarde voor het rationele ontwerp van nieuwe behandelingmethoden. Dit is tenminste deels gerelateerd aan hun relatieve eenvoud, wat de mogelijkheid biedt om een specifieke pathologische eigenschap te onderzoeken, onafhankelijk van andere complicaties. Ondanks deze en andere voordelen van *in vitro* cellulaire modellen bootsen zij de *in vivo* situatie vaak onvoldoende na, wat kan leiden tot slechte *in vitro-in vivo* correlaties. Hierdoor dient toekomstig onderzoek zich te richten op de verdere verbetering van deze cellulaire modellen zodat zij een betere weergave vormen van de pathologische status *in vivo*, waardoor de noodzaak voor preklinische en klinische studies kan worden verminderd. Bijvoorbeeld, in het geval van *in vitro* modellen van cardiale hypertrofie is het essentieel om te bepalen welk stadium tijdens de transitie van PCH tot hartfalen door het hypertrofie model wordt weergegeven, aangezien dit de therapeutische aanpak kan beïnvloeden. Naast het bepalen van de mate van electrofysiologische veranderingen en de incidentie en het karakter van aritmieën, kunnen de bepaling van het contractievermogen en transcriptoomanalyses een waardevolle bijdrage leveren.

Een belangrijke hindernis die genomen moet worden voor de verdere ontwikkeling van *in vitro* cellulaire modellen is het overkomen van de lage expansiecapaciteit van gedifferentieerde cellen. Postnatale CMCs vertonen bijvoorbeeld een zeer beperkte proliferatiecapaciteit, wat herhaaldelijke isolatie en kweek van deze cellen noodzakelijk maakt voor *in vitro* studies. Immortalisatie van atriale of ventriculaire CMCs van dierlijk of menselijk weefsel zou dit probleem kunnen omzeilen. Dit kan worden bewerkstelligd door middel van virale overdracht van genen coderend voor eiwitten zoals simian virus 40 large T antigen, B cell-specific Moloney murine leukemia virus integration site 1 (BMI1) of telomerase (TERT) reverse transcriptase.

Genetische manipulaties middels virale vectoren (b.v. overexpressie van bepaalde genen of RNA interferentie) kunnen voorts leiden tot betere mechanistische inzichten in skelet- en hartspierziekten en tot verdere optimalisatie van huidige therapieën voor deze aandoeningen.

Met betrekking tot skeletspieratrofie kan optimalisatie van cellulaire therapieën bereikt worden door verbeterde fusie van donorcellen onderling en met spiercellen van de ontvanger en door verbetering van hun myogene differentiatie. Bijvoorbeeld, geforceerde expressie van fusie-bevorderende eiwitten door transductie van (niet-

myogene) stamcellen met virale vectoren coderend voor deze eiwitten kan bevorderlijk zijn, evenals de gereguleerde expressie van myogene transcriptiefactoren in deze cellen.

Genetische interventie kan ook worden ingezet voor de behandeling van hartritmestoornissen. Bijvoorbeeld, gedwongen expressie van connexines zoals connexine43 in (myo)fibroblasten in infarctlittekenweefsel kan geleiding bevorderen en de incidentie van aritmieën doen afnemen. Deze aanpak zou echter ook negatief kunnen uitpakken aangezien koppeling van CMCs met (myo)fibroblasten kan leiden tot depolarisatie van CMCs, waardoor het weefsel vatbaar wordt voor tachycardieën op basis van “reentry”. Dit probleem kan worden aangepakt door gelijktijdige uitrusting van (myo)fibroblasten met een gen zoals *KCNJ2*, waarvan het product is betrokken bij het instellen van het rustmembraanpotentiaal.

Genetische interventies (overexpressie of knockdown) die invloed uitoefenen op de expressie van genen die coderen voor ionkanalen die betrokken zijn bij de repolarisatiefase van het actiepotentiaal (AP), kunnen ook anti-aritmische effecten hebben. Bijvoorbeeld, manipulatie van de expressie van genen die coderen voor de ionkanalen die betrokken zijn bij de repolarisatie van de AP fases gedurende welke vroege na-depolarisaties optreden (b.v. adenosine trifosfaat (ATP)-gevoelige K^+ kanalen [K_{ATP} kanalen]) zou tot nieuwe inzichten kunnen leiden in pro- en anti-aritmische mechanismen, maar zou ook therapeutische waarde kunnen hebben. Effectieve therapeutische toepassing van virale vectoren *in vivo* vereist uniforme en bijna-kwantitatieve transductie van het doelweefsel en het juiste transgenexpressieniveau. Dit zijn belangrijk punten in de context van aritmiebehandeling, aangezien heterogene transductie of een inadequaat transgenexpressieniveau pro-aritmisches kan zijn.

Daarom zijn efficiënte toediening en een hoge doelcelspecificiteit van virale vectoren, alsmede de precieze beheersing van transgenexpressie van vitaal belang en verdienen verder onderzoek. Andere belangrijke onderwerpen van toekomstig genterapeutisch onderzoek zijn de verdere verbetering van de veiligheid en de reductie van immunogeniciteit van virale vectoren.

List of Publications

Full papers

Neshati Z, Liu J, Zhou G, SchaliJ MJ, de Vries AAF. Development of a lentivirus vector-based assay for non-destructive monitoring of cell fusion activity. PLoS One. 2014;9:e102433.

Bingen BO*, Engels MC*, SchaliJ MJ, Jangsangthong W, **Neshati Z**, Feola I, Ypey DL, Askar SFA, Panfilov AV, Pijnappels DA*, de Vries AAF*. Light-induced termination of spiral wave arrhythmias by optogenetic engineering of atrial cardiomyocytes. Cardiovasc Res. 2014;104:194-205. **Equal contribution*

Bijkerk R*, van Solingen C*, de Boer HC, van der Pol P, Khairoun M, de Bruin RG, van Oeveren-Rietdijk AM, Lievers E, Schlagwein N, van Gijlswijk DJ, Roeten MK, **Neshati Z**, de Vries AAF, Rodijk M, Pike-Overzet K, van den Berg YW, van der Veer EP, Versteeg HH, Reinders MEJ, Staal FJT, van Kooten C, Rabelink TJ, van Zonneveld AJ. Hematopoietic microRNA-126 protects against renal ischemia/reperfusion injury by promoting vascular integrity. J Am Soc Nephrol. 2014;25:1710-1722. **Equal contribution*

Bingen BO, **Neshati Z**, Askar SFA, Kazbanov IV, Ypey DL, Panfilov AV, SchaliJ MJ, de Vries AAF, Pijnappels DA. Atrium-specific Kir3.x determines inducibility, dynamics, and termination of fibrillation by regulating restitution-driven alternans. Circulation. 2013;128:2732-2744.

Ahmadiankia N, Neshati V, **Neshati Z**, Swildens J, de Vries AAF. Generation of Helper Plasmids Encoding Mutant Adeno-associated Virus Type 2 Capsid Proteins with Increased Resistance against Proteasomal Degradation. Iran J Basic Med Sci. 2013;16:813-821.

Neshati Z, Bahrami AR, Eshtiagh-Hosseini H, Matin MM, Housaindokht MR, Tabari T, Edalatmanesh MA. Evaluating the biodegradability of Gelatin/Siloxane/Hydroxyapatite (GS-Hyd) complex in vivo and its ability for adhesion and proliferation of rat bone marrow mesenchymal stem cells. Cytotechnology. 2012;64:485-495.

Ahmadian Kia N, Bahrami AR, Ebrahimi M, Matin MM, **Neshati Z**, Almohaddesin MR, Aghdami N, Bidkhorri HR. Comparative analysis of chemokine receptor's expression in mesenchymal stem cells derived from human bone marrow and adipose tissue. J Mol Neurosci. 2011;44:178-185.

Neshati Z, Matin MM, Bahrami AR, Moghimi A. Differentiation of mesenchymal stem cells to insulin-producing cells and their impact on type 1 diabetic rats. *J Physiol Biochem.* 2010;66:181-187.

Edalatmanesh MA, Matin MM, **Neshati Z**, Bahrami AR, Kheirabadi M. Systemic transplantation of mesenchymal stem cells can reduce cognitive and motor deficits in rats with unilateral lesions of the neostriatum. *Neurol Res.* 2010;32:166-172.

Behnam Rassouli F, Matin MM, Iranshahi M, Bahrami AR, Neshati V, Mollazadeh S, **Neshati Z**. Mogoltacin enhances vincristine cytotoxicity in human transitional cell carcinoma (TCC) cell line. *Phytomedicine.* 2009;16:181-187.

Edalatmanesh MA, Bahrami AR, Behnam Rasuli M, Matin MM, Moghimi A, **Neshati Z**. Microanatomical evidences for potential of mesenchymal stem cells in amelioration of striatal degeneration. *Neurol Res.* 2008;30:1086-1090.

Neshati Z, Bingen BO, Askar SFA, Schalijs MJ, Pijnappels DA, de Vries AAF. Investigation of the pro-arrhythmic features of pathological cardiac hypertrophy in neonatal rat ventricular cardiomyocyte cultures. To be submitted.

Neshati Z, Jangsangthong W, Liu J, Bingen BO, Feola I, Ypey DL, Schalijs MJ, Pijnappels DA, de Vries AAF. Forced NFAT3 expression in hypertrophic myocardial cultures prevents focal tachyarrhythmias by inhibiting triggered activity through reverse L-type calcium channel remodeling. To be submitted.

Askar SFA*, **Neshati Z***, Bingen BO, Piers SRD, Zeppenfeld K, Schalijs MJ, de Vries AAF, Pijnappels DA. An *in vitro* model of early- or no-reperfusion scars to explain how clinical reentrant arrhythmia characteristics may relate to therapeutic efficacy. To be submitted. **Equal contribution*

Engels MC*, Askar SFA*, Jangsangthong W, Bingen BO, **Neshati Z**, Feola I, Liu J, Braun J, Klautz RJM, Ypey DL, Schalijs MJ, de Vries AAF*, Pijnappels DA*. Fusion of cultured human ventricular scar cells with cardiomyocytes reduces arrhythmogenicity by preventing early afterdepolarizations through increased repolarization force. To be submitted. **Equal contribution*

Peer-reviewed abstracts

Neshati Z, Bingen BO, Pijnappels DA, Schalijs MJ, de Vries AAF. NFAT3 gene transfer to counteract the pro-arrhythmic electrophysiological changes accompanying pathological cardiac hypertrophy. *Eur Heart J.* 2014;31:183-184.

Bingen BO, Askar SFA, **Neshati Z**, Feola I, Ypey DL, Schalijs MJ, de Vries AAF, Pijnappels DA. Acetylcholine-dependent potassium current determines atrial defibrillation threshold by regulating post-shock refrillation. *Eur Heart J.* 2014;31:259.

Engels MC, Askar SFA, Jangsangthong W, **Neshati Z**, Feola I, Ypey DL, Klautz RJM, Schalijs MJ, de Vries AAF, Pijnappels DA. Heterocellular fusion of human

ventricular scar cells with neonatal rat cardiomyocytes ameliorates pro-arrhythmia through APD shortening and MDP lowering by enhanced outward potassium current. Eur Heart J. 2014;31:184.

Neshati Z, Bingen BO, Askar SFA, Schalij MJ, Pijnappels DA, de Vries AAF. Development of a new model of cardiac hypertrophy with pro-arrhythmic features to study the role of hypertrophy in arrhythmogenesis. Eur Heart J. 2013;34:916.

Askar SFA, Bingen BO, Schalij MJ, **Neshati Z**, Klautz RJM, de Vries AAF, Pijnappels DA. Forced cellular fusion of human ventricular scar cells with neonatal rat cardiomyocytes ameliorates their arrhythmicity. Europace. 2013;15:S1-S2.

Acknowledgements

This thesis appears in its current form due to the assistance and guidance of several people. Therefore, I would like to offer my thanks to all of them.

I express my sincere gratitude to my promotor Prof. dr. SchaliJ for the continuous support of my PhD training and his great help to accomplish graduation.

I want to express my gratefulness to my copromotores Twan de Vries and Daniel Pijnappels, for the fruitful discussions and valuable advices, their support during the whole period of the PhD and guidance during the writing process.

Twan I would like to thank you for your comprehension, help and support. Thanks for the scientific discussions, especially for your patience and guidance during the writing process.

Thank you very much Daniel for guiding me to come up with a good reason and interesting question for each experiment.

I would like to thank the members of the reading committee, Prof. dr. Goumans, Prof. dr. Atsma and Dr. van der Meer for reviewing of this thesis.

Furthermore, I would like to thank the members of the department of Molecular Cell Biology, especially Kim and Manuel for their advices and support.

I express my gratitude to Arti, Brian and Saïd for their assistance with various problems during experiments. Thanks Arti for helping me with making nice immunocytological images.

A special thank I like to give to my PhD colleagues and friends Marc, Jia, lolanda, Niek, Melina, Annemarie and Sasha with whom I had interesting talks about the science and also life.

I specially thank Marc for translating the “summary and conclusions” into Dutch and accepting to be my paranymph.

Rupa and Yoke thanks for your help and interesting talks. Yoke thanks a lot for all time and effort you put on patch clamp experiments.

Margreet, Cindy and Minka thanks for your excellent technical assistance in the lab and your kindly answers to my questions.

I am grateful to the secretaries Erna and Talitha for assisting me in handling the paperwork.

I would like to thank the members of the department of Immunohaematology and Blood Transfusion for allowing me to use their facilities.

Elham thanks for your valuable friendship, always you made time to hear me.

I also appreciate Mr. Abdollahi and Mr. Nazemi as the scientific representatives of the Iranian government in the Schengen countries.

Thanks to all my close friends and their families, Sarrami, Bahri, Mirnejad, Moshkani, Majlesi and Akbari for the joyful gatherings and all their supports.

Mirnejad’s family (Mohammad and Mehri), thanks for gathering the friend altogether and providing soothing atmosphere for us.

Zeinab and Tanaz thanks for your valuable friendship and accompanying me to Iranian social events. Tanaz I am pleased that you accepted to be my paranymf.

Rahimi’s family, thanks a lot for your great hospitality and providing conditions for me that do not miss my family. Dear Morteza thanks a lot for all administrative work. I do not really know how to thank you and your family.

I warmly thank and appreciate my lovely parents for their exhortation and support in all aspects of my life. I miss proper word and way to thank them.

I also thank my sisters and brothers for their persuasion and encouragements.

I would like to thank my husband’s family; they have provided assistance in numerous ways.

And finally, I would like to thank a person who tolerated being away from each other, my precious husband, dear Mohammad, without his help, support and encouragement I could not have finished this work.

Curriculum Vitae

Zeinab Neshati was born on April 5th 1982 in Mashhad, Iran. She graduated from high school in 2000 and afterwards she obtained her bachelor's degree in general biology in 2004. She started her mastership in 2005 in the field of animal physiology at Ferdowsi University of Mashhad (FUM), Mashhad, Iran. Her thesis was about the differentiation of stem cells to insulin producing cells and their transplantation impact on animal model of type 1 diabetes. She could publish a paper based on this project in Journal of physiology and biochemistry. She obtained her master's degree in 2008. During her studies (2005-2008) she was involved in diverse research projects. She also worked as a demonstrator and teacher-assistant in the Tissue and Cell Culture, Cellular Biology, Molecular Cell Biology and Biotechnology labs of faculty of science of FUM. She also took out a patent entitled "Synthesis and characterization of organic-mineral hybrid gelatin/siloxan/hydroxy apatite". In 2009 she was awarded a scholarship for postgraduate studies from Ministry of Science, Research and Technology of Iran, Tehran, Iran. She was the top candidate for this scholarship. With an invitation of Dr. Antoine A.F. de Vries, she started her PhD training at the Virus and Stem Cell Biology Section of the Molecular Cell Biology Department of the Leiden University Medical Center (LUMC), Leiden, the Netherlands for 1.5 years and then she moved to the Department of Cardiology of LUMC for the last 3 years of her PhD. The work performed during this period is presented here.

